
Numerical Renormalization Group studies of Quantum Impurity Models in the Strong Coupling Limit

Michael Sindel



München 2004

**Numerical Renormalization Group
studies of
Quantum Impurity Models
in the Strong Coupling Limit**

Michael Sindel

Dissertation
an der Fakultät für Physik
der Ludwig-Maximilians-Universität
München

vorgelegt von
Michael Sindel
aus Rothenburg ob der Tauber

München, den 22. Oktober 2004

Erstgutachter: Prof. Dr. Jan von Delft

Zweitgutachter: Prof. Dr. Walter Hofstetter

Tag der mündlichen Prüfung: 27. Januar 2005

Contents

Abstract	xii
I General Introduction	1
1 Introductory remarks	3
2 Quantum dot (QD) basics	7
2.1 Experimental realization of QDs	7
2.2 Level quantization	8
2.3 Charging effects	9
2.4 Tunability of QDs	9
2.5 Experimental consequences on transport	10
2.6 Kondo effect in QDs	12
3 Introduction to the Kondo effect	15
3.1 The Anderson model	15
3.1.1 Unitary transformation of the AM	17
3.1.2 Mapping onto an effective model: Schrieffer-Wolff transformation	18
3.2 The Kondo effect	21
3.2.1 The historical origin - the resistivity minimum in bulk	21
3.2.2 The Kondo model	23
3.2.3 Kondo's explanation	23
3.2.4 General properties of the Kondo effect	29
3.2.5 Poor man's scaling (PMS)	30
4 Wilson's Numerical Renormalization Group (NRG)	33
4.1 Physical quantities computed with NRG	38
4.1.1 Thermodynamic quantities	38
4.1.2 Dynamic quantities: $A(\omega, T)$ and $\chi''(\omega, T)$	39
II NRG-studies of Quantum Impurity Models	44

5	QDs coupled to ferromagnetic leads	47
5.1	Effect of a finite spin polarization in the leads on the Kondo resonance . . .	48
5.1.1	Quantitative determination of the compensation field B_{comp}	54
5.1.2	Experimental relevance	54
5.2	Gate controlled spin splitting in the Kondo regime	57
5.2.1	Comprehensive study dealing with QDs coupled to ferromagnetic leads	64
6	Non-monotonic occupation in two-level QDs	65
7	Frequency-dependent transport in the Kondo regime	71
8	Kondo correlations in optical experiments	77
9	Summary and outlook	91
III	Appendix	93
A	Derivation of the NRG-equations	95
A.1	Manipulation of the CB	96
A.1.1	Transformation of $\hat{\mathcal{H}}_{ld}$	98
A.1.2	Transformation of $\hat{\mathcal{H}}_{CB}$	99
A.2	Mapping of the CB onto a semi-infinite chain	101
A.3	Iterative numerical diagonalization	103
A.4	Results of the iterative diagonalization	105
B	How to obtain continuous dynamic functions	107
B.1	The broadening of the δ -functions	107
B.2	How to combine information from different iterations	109
C	Symmetries in the NRG-scheme	113
D	The density matrix Numerical Renormalization Group (DM-NRG)	115
E	Kramers-Kronig (KK) relation	119
F	Kubo formalism	123
F.1	Derivation of the Kubo formula	124
IV	Miscellaneous	129
	Bibliography	131
	List of Publications	137
	Acknowledgements	138

Table of Contents

vii

Deutsche Zusammenfassung

140

Curriculum vitae

143

List of Figures

2.1	Lateral and vertical QDs	8
2.2	Tunability of QDs	10
2.3	Coulomb oscillations and the Coulomb staircase	11
2.4	Differential conductance of a Kondo QD	12
2.5	Kondo effect in QDs	13
3.1	Relevant parameters of a QD	16
3.2	Unitary transformation	18
3.3	Virtual excitations in a singly occupied QD	20
3.4	Anomaly of the electrical resistivity	22
3.5	First order processes in a Kondo QD	25
3.6	Second order processes in a Kondo QDs	26
3.7	Poor man's scaling	32
4.1	Flow of couplings	35
4.2	Flow diagram of eigenenergies	37
4.3	QD occupation	40
4.4	Dynamic quantities calculated with NRG	42
5.1	Contact between QD and arbitrary material	48
5.2	DoS of a polarized lead	49
5.3	Split Kondo resonance of a QD contacted to ferromagnetic leads	55
5.4	Zero-field splitting of Kondo resonance in a carbon nanotube quantum dot	56
5.5	Gate voltage dependence of the splitting of the Kondo resonance	57
5.6	Spectral function of a Kondo QD in presence of ferromagnetic leads	63
5.7	Sketch of different DoS types	64
8.1	PL-experiment with self assembled QDs	79
8.2	Optical transition between a 'Kondo' and a 'non-Kondo' state	80
A.1	Depiction of arbitrary leads DoS	97
A.2	NRG-iteration	104
B.1	Possible transitions for $T = 0$ and $T \neq 0$	108

B.2	Logarithmic gaussian vs. 'usual' gaussian	109
B.3	Combining different clusters	111
B.4	Matrix elements of neighboring clusters	112
D.1	DM-NRG vs. NRG	117
E.1	KK-transformation	121
F.1	A biased QD	124

List of Tables

9.1 Implemented models in the NRG-code 92

Abstract

In this thesis we summarize a number of theoretical studies dealing with various properties of quantum dots. Small quantum dots with a large level spacing are very well described by the Anderson impurity model. In modern quantum dot experiments all parameters of this model can be tuned via external gate voltages. Thus, it should be possible to check our theoretical findings experimentally. We are particularly interested in temperatures T smaller than the so-called Kondo temperature T_K , $T < T_K$. The Kondo temperature T_K is an energy scale below which a local spin inside the dot interacts strongly with the conduction electrons in its neighboring leads. Consequently we employ Wilson's numerical renormalization group method [1], a numerical technique which allows for an accurate calculation of properties of quantum dots in the Kondo regime.

We start with a general introduction to the physics of quantum dots, an introduction to the Kondo effect and the numerical renormalization group method (Part I).

The main part of this thesis, Part II, is divided into several studies:

- (i) We analyze the properties of the Kondo resonance of a quantum dot that is coupled to leads with a finite spin polarization. We find that this polarization suppresses and splits the Kondo resonance. We extend our study to a dot that is coupled to a lead with an arbitrary density of states and study the gate-voltage dependence of the Kondo resonance.
- (ii) We investigate the filling scheme of a spinless two-level Anderson model as a function of gate voltage. We identify parameters where the two levels do not fill monotonically when being lowered relative to the Fermi energy of the leads. For asymmetrically coupled levels, we even find an occupation inversion of the two levels (i.e. the upper level has a bigger occupation than the lower level) for a specific gate voltage region. We explain this behavior by means of the self consistent Hartree approach.
- (iii) We calculate the finite frequency conductance of a Kondo quantum dot within the Kubo formalism. An analytical formula, which establishes a relation between the frequency dependent conductance and the (local) equilibrium spectral function, is derived. By means of the fluctuation dissipation theorem we establish a relation between current noise and the equilibrium spectral function.
- (iv) Motivated by emission experiments in self-assembled semiconductor quantum dots [2] we study optical transitions between 'Kondo' and 'non-Kondo' states. For this sake the 'standard' Anderson model is extended. We find that the emission and absorption spectrum can be nicely understood by analogy to the X-ray edge absorption problem.

In Part III we summarize technical details that have been of relevance in this thesis.

Part I

General Introduction

Chapter 1

Introductory remarks

Many-body phenomena [3] are of central interest in many fields of modern condensed matter physics. Those phenomena are challenging both from an experimental and from a theoretical point of view.

In typical bulk materials, it can often be difficult to distinguish whether a measured effect stems from single particle physics or is really due to correlation effects. Quantum dots (QDs) (small electron droplets which are confined in all spatial dimensions) on the other hand, are ideally suited to investigate the interplay of single-particle and many-body physics in a controlled fashion. In typical QDs many-body effects become observable at temperatures T below $\sim 1\text{K}$. Consequently, a lot of effort was invested to reach these limits experimentally. In QDs it is possible to study correlation effects systematically. In particular, it is possible to tune QDs such that one of the simplest strongly correlated models, the *Kondo model* (KM), can be realized experimentally.

New theoretical methods need to be used to investigate regimes where many-body effects are important. It turns out that mean-field theories are *not* capable of describing *all* effects that arise from many-body correlations properly. The quest for new theoretical methods, such as the numerical renormalization group method, lead to renormalization techniques which allow for a quantitative description of effects where correlations are important. The fruitful interplay between experimental and theoretical developments allowed for a considerable progress in Kondo physics, the physics related with the Kondo model, within the last years.

This thesis deals with some low-temperature properties of different QD-systems. We are particularly interested in zero-temperature properties of those systems. Since correlation effects are crucial in this regime we employ Wilson's numerical renormalization group (NRG) method to tackle this problem.

The thesis is divided into four parts:

A pedagogical introduction to the field is given in **Part I**. After we provide basic knowledge about QDs in Chapter 2, we give a detailed introduction to the Kondo problem in Chapter 3. In Chapter 4 we discuss the method that is heavily used in this thesis, the NRG-method.

The second part of this thesis, **Part II**, contains several studies that were carried out and published during my PhD-studies.

In Chapter 5 we consider a QD coupled to leads with a finite spin polarization and analyze the delicate effect of a spin polarization in the leads on the Kondo resonance. In the first part of this Chapter we are interested in the consequences of this polarization on the Kondo resonance while keeping the gate voltage fixed (Section 5.1). In the second part (Section 5.2), on the other hand, we focus on the gate voltage dependence of the Kondo resonance for a QD coupled to leads with a particular density of states (DoS). We find that the local spin splitting of a QD coupled to leads of that type can be controlled by means of an external gate voltage.

Chapter 6 deals with the filling of a spinless two-level QD. We observe a non-monotonic filling scheme for a particular region in parameter space and explain this behavior via a simple self-consistent Hartree approach. We identify gate voltage regions where the QD occupation is even inverted, i.e. the occupation of the energetically higher lying level is bigger than the occupation of the energetically lower lying level, given the two levels are coupled with a different strength. The generalization of this study to the spinfull case is currently in preparation.

The finite frequency conductance of a Kondo QD is investigated in Chapter 7. We use the Kubo formalism to compute the frequency-dependent conductance of a QD in the Kondo regime. We identify two possibilities to measure the equilibrium spectral function of a generic QD, namely via (i) a finite frequency conductance measurement or via (ii) a current noise measurement.

We study optical transitions between a 'Kondo' and a 'non-Kondo' state in Chapter 8. Transitions of this type have recently come into experimental reach in self assembled QDs [2]. In contrast to the previous Chapters, where various transport properties of QDs were considered, we focus on optical properties in Chapter 8. We use Fermi's Golden Rule to calculate the line shape related to the transitions mentioned above. The findings can be nicely explained by an analogy to the X-ray edge problem.

Part III, the Appendix, contains technical details relevant for the studies carried out in Part II. In Appendix A, the general NRG-mapping of a single-level QD coupled to a lead with a spin- and energy-dependent DoS is performed.

Dynamic quantities, such as the widely used spectral function, are rather difficult to calculate for the following two reasons: firstly, to realize a continuous function, δ -functions need to be broadened properly. Secondly, the different energy scales of the NRG-iteration have to be combined properly to obtain a function valid on *all* energy scales. Both issues are addressed in Appendix B.

To keep the numerical effort of the NRG-iteration tolerable and to get rid of artificial perturbations, we introduce some relevant and useful symmetries of the NRG-procedure in Appendix C. Their use is crucial as we are usually dealing with a Hilbert space of considerable dimension (its dimension is typically $\sim 10^4$).

Problems that inherit more than a single energy scale (e.g. systems in presence of a magnetic

field B) have to be treated with a generalized NRG-procedure, known as the 'DM-NRG'-method. This method, invented by Hofstetter [4], generalizes the 'traditional' NRG-method which incorporates only a single energy scale. We introduce the 'DM-NRG'-method in Appendix D.

The Kramers-Kronig relations are well established relations for causal functions. Since we are mostly interested in functions that have a sharp feature around the Fermi energy (e.g. the Kondo resonance of width $\sim T_K$), it turns out that their numerical implementation is rather tricky. Following Bulla [5] we introduce an accurate method to perform this transformation in Appendix E.

In Appendix F we present a general way for the calculation of the conductance through an interacting region. We derive equations for the conductance based on the Kubo formalism [6]. In particular, these relations allow for the accurate determination of the frequency-dependent conductance of a 'Kondo-QD' as used in [7] (see also Chapter 7).

The last part, **Part IV**, contains miscellaneous. It contains the bibliography, a list of publications, the acknowledgements, "Deutsche Zusammenfassung" and finally the curriculum vitae.

Chapter 2

Quantum dot (QD) basics

The tunability of QDs makes them ideal devices to study quantum impurity problems experimentally. Due to the small spatial dimensions of QDs the energy levels inside the QDs are quantized. QDs with large charging energies (up to $1.5\text{meV} \simeq 15\text{K}$; see e.g. [8]) can be routinely manufactured, thus charging effects are important below temperatures $T \sim 15\text{K}$. Therefore: QDs reveal both charge and energy quantization.

2.1 Experimental realization of QDs

Quantum mechanical effects occur when the system size L is of the order of the de Broglie wavelength¹ $\lambda_F = \frac{h}{m^*v_F}$ and the thermal wavelength $\lambda_T = \sqrt{\frac{h^2}{2m^*k_B T}}$ of the electrons, i.e. $L \sim \lambda_F, \lambda_T$. Here m^* denotes the effective electron mass (at the Fermi energy) and v_F the Fermi velocity. Due to a much smaller Fermi velocity semiconducting materials have a significantly larger de Broglie wavelength ($\lambda_F \sim 100\text{nm}$) than metallic materials ($\lambda_F \sim 0.1\text{nm}$). Accordingly, quantum mechanical effects are observable in semiconductor QDs with a diameter $L \sim 100\text{nm}$, a length scale that can be routinely realized with today's fabrication techniques.

The most frequently used *tunable* QDs - a property that self-assembled QDs do not share - are *lateral* and *vertical* QDs, see Fig. 2.1.

A lateral QD, see Fig. 2.1(left panel), is defined by metallic gates on top of a semiconductor heterostructure (typically GaAs/AlGaAs). Near the interface of these two semiconducting materials a two-dimensional electron gas (2DEG) forms. When a negative voltage is applied at the top gates a small electron droplet, a QD, is formed in the 2DEG which itself is below the surface of the heterostructure. In addition, the gates allow for an accurate control of the tunnel barriers between the QD and the neighboring reservoirs (i.e. the source and drain region), the shape of the QD and the electro-chemical potential inside the dot.

A vertical QD, on the other hand, is etched out of a double-barrier heterostructure [9] and finally coated by metal gates, see Fig. 2.1(right panel). The number of electrons in a

¹Which is identical to the Fermi wavelength here.

vertical dot can be controlled very accurately by side gates without changing the tunnel barriers. Lateral QDs do not share this property: a variation of the electron number in lateral QDs results in a variation of the tunnel barriers as well.

Transport measurements through a QD can be performed by coupling it (via adjustable

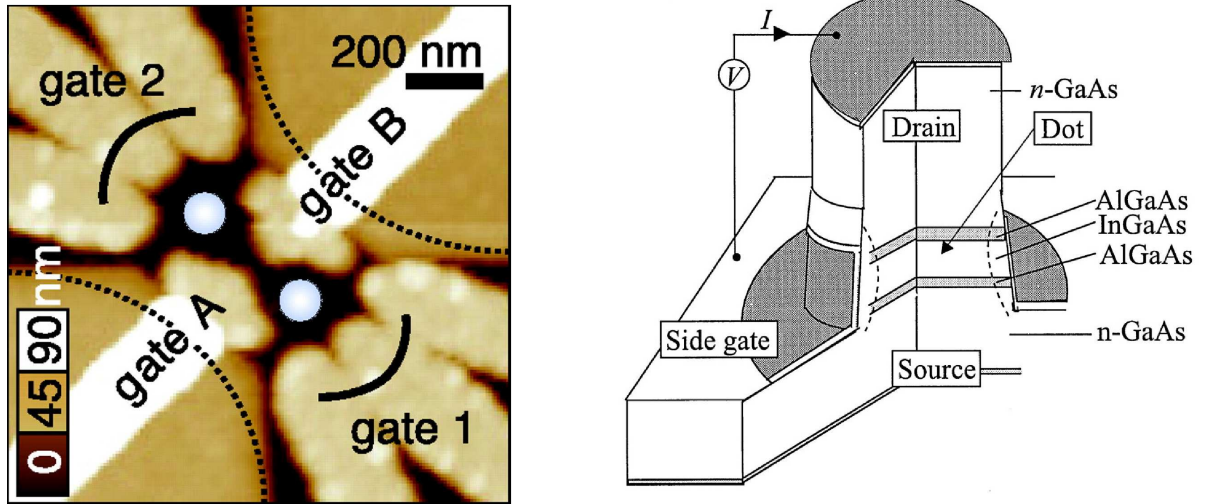


Figure 2.1: Left: Atomic force microscopy picture of two *coupled lateral* QDs (bright central circles), serving as an 'artificial' molecule [10]. A negative voltage in the gates *A* (source), *B* (drain), 1 and 2 leads to a partial depletion of the 2DEG (which is below the surface of the heterostructure). Right: *Vertical* QDs are realized by coating a pillar with metallic gates [11]. The side gates allow for an accurate control of the number of electrons in the island without changing the tunnel barriers. Transport measurements in QDs are performed by applying a finite bias voltage V_{SD} (a source-drain voltage) across the dot.

tunnel barriers) to electron reservoirs whose role it is to feed the QD with electrons. When a finite bias voltage V_{SD} is applied across the QD a current (which depends sensitively on the parameters of the QD) might be driven through the QD.

2.2 Level quantization

The energy difference between neighboring eigenenergies of a system, the *level spacing* δE , is set by the system size L . Qualitatively, a decrease in system size results in an increasing level spacing [12].

A lateral QD traps electrons in a disk of diameter L . A crude approximation of this geometry is a square of side length L , thus the level spacing is $\delta E \propto 1/L^2$. More precisely the level spacing of such a QD [13] is given by

$$\delta E \simeq 1/\rho L^2, \quad (2.1)$$

where $\rho = \frac{k_F}{\hbar v_F}$ is the (material dependent) DoS (at the Fermi energy) of the 2DEG. Note that metallic systems have a much bigger DoS as compared to semiconducting materials. Thus, for fixed L , the level spacing of metallic QDs is much smaller than that of semiconducting QDs.

2.3 Charging effects

Due to the spatial confinement of the electrons inside the QD, Coulomb repulsion between *all* electrons inside the QD is an important energy scale. The energy penalty that has to be paid when an additional electron enters the QD (initially occupied with N electrons), $N \rightarrow N + 1$, is called the charging energy E_C of the QD, $E_C = e^2/2C$ (C denotes the total capacitance of the QD). A good estimate of the total capacitance of a disk of diameter L is $C \sim \varepsilon_0 L$ [13], with the dielectric constant ε_0 , thus

$$E_C \simeq \frac{e^2}{2\varepsilon_0 L}. \quad (2.2)$$

Since the level spacing δE has a different L dependence as the charging energy E_C , see Eqs. (2.1) and (2.2), one can (in principle) tune the ratio of these two energy scales experimentally by choosing L appropriately,

$$\frac{E_C}{\delta E} \simeq \frac{\pi e^2}{\varepsilon_0 \hbar v_F} \left(\frac{L}{\lambda_F} \right). \quad (2.3)$$

In typical QDs, the diameter L is larger than λ_F ($L > \lambda_F$), thus charging energy E_C is the dominant energy scale ($E_C > \delta E$).² Semiconductor QDs with a diameter $L \sim 100\text{nm}$ have typically the following parameters: $E_C \approx 1.5\text{meV}$ (as mentioned before), $\delta E \approx 0.1\text{meV}$. At sufficiently low-temperatures charging effects result in *Coulomb blockade* behavior, i.e. the QD is charged one by one when its local electro-chemical potential is lowered relative to the Fermi energy of the reservoirs.

One remark should be made here: the interaction between electrons inside a QD is not solely due to charging effects. The first correction to E_C is due to exchange interaction E_S , an energy scale that arises from spin-spin interaction. Similar to Hund's rule in atomic physics a QD can lower its energy by maximizing its total spin.

2.4 Tunability of QDs

The success of QDs is associated with their tunability. As mentioned in Section 2.1, different gate voltages allow for a precise control of a variety of relevant parameters of the QD, such as the coupling strength between the QD and its surrounding reservoirs.

Here, we comment on gates that (i) allow for a rigid shift of the discrete levels inside the QD and (ii) enable one to perform transport measurements (as a function of the bias

²The prefactor in Eq. (2.3), $\frac{\pi e^2}{\varepsilon_0 \hbar v_F}$, is of order one in typical materials.

voltage V_{SD}) between the source and drain region. A schematic illustration is given in Fig. 2.2, where the left (right) reservoir plays the role of the source (drain) contact.

A back gate (tunable via the *gate voltage* V_G) influences the electro-chemical potential inside the QD. It can thus be used to realize task (i). Task (ii) can be realized by directly applying a bias voltage between the left/right reservoir, see Fig. 2.1(b). We will henceforth use the word lead synonymous for reservoir. The chemical potentials of the left/right lead, μ_L/μ_R , obey the relation $\mu_L = \mu_R + eV_{SD}$.

Since the electro-chemical potential in a QD (containing N electrons) $\mu_{dot}(N)$ can be tuned by means of V_G , one can control the number of electrons inside the QD for temperatures $T < E_C$. For $V_{SD} = 0$ ($\mu = \mu_L = \mu_R$) and $\mu_{dot}(N+1) > \mu > \mu_{dot}(N)$ the QD is filled with N electrons. The $(N+1)$ -th electron can not enter the QD as long as $\mu_{dot}(N+1) > \mu$, i.e. transport is blocked [*Coulomb blockade*, Fig. 2.2(a)]. In typical semiconductor QDs with $E_C > \delta E$ one can measure the level-spacing δE of a QD by continuously increasing the source-drain voltage V_{SD} , while keeping V_G fixed. Any time a new discrete level of the QD enters the transport window (of width eV_{SD}) a peak in the differential conductance can be observed, see Fig. 2.2(b).

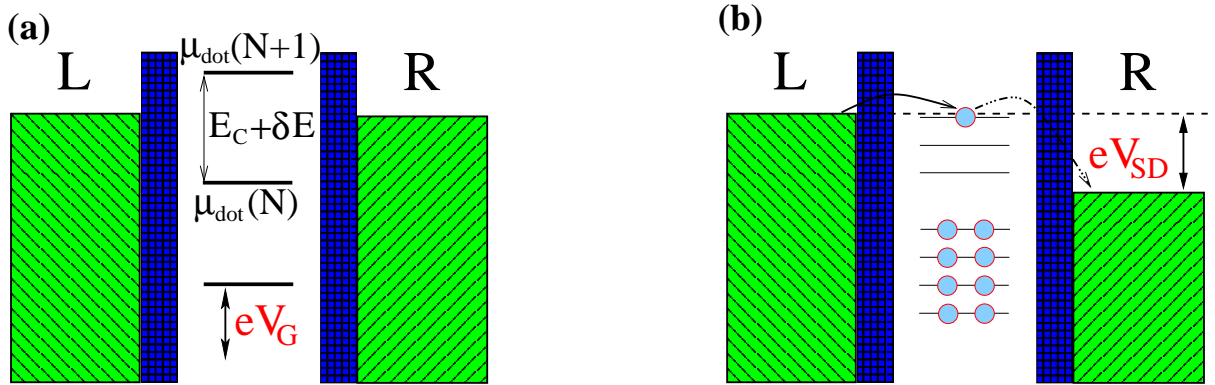


Figure 2.2: (a) The gate voltage V_G allows for a rigid and linear shift of the electro-chemical potential of the n -th electron in the QD $\mu_{dot}(n)$, $n \in \mathbb{N}$. For $T < E_C$ the QD is filled with N electrons, if the corresponding chemical potential $\mu_{dot}(N)$ lies below the lowest chemical potential of the leads $\mu_{dot}(N) < \min\{\mu_L, \mu_R\}$ and $\mu_{dot}(N+1) > \min\{\mu_L, \mu_R\}$, (b) The chemical potential of the left (L) and right (R) lead $\mu_{L/R}$ can be changed relative to each other by tuning the source drain voltage V_{SD} . The sketch shows how the discrete energy levels in a QD can be probed by increasing the bias voltage V_{SD} . The excited states (of spacing δE) can be seen as peaks in differential conductance measurement.

2.5 Experimental consequences on transport

In this Section we show that both energy scales E_C and δE can be extracted from differential conductance measurements. As discussed above, a differential conductance mea-

surement can be used to probe the internal structure of the QD. A measurement of the *Coulomb oscillations* (dI/dV_{SD} vs. V_G , $V_{SD} \rightarrow 0$) allows for the estimation of E_C , see Fig. 2.3(left panel). The level spacing δE , on the other hand, can be determined from a measurement of dI/dV_{SD} vs. V_{SD} (with fixed V_G), known as the *Coulomb staircase*.

Note that the peaks in the differential conductance measurements have a finite width (each local level is broadened) for the following two reasons: the local level (i) is coupled to reservoirs with strength Γ and (ii) it is thermally broadened $\sim k_B T_{\text{exp}}$ as the experiment is carried out at finite temperature T_{exp} . Obviously discrete peaks in differential conductance measurements are no longer observable once the total width of the level $\sim (\Gamma + k_B T)$ exceeds the energy scale of interest (E_C or δE), see Fig. 2.3(left panel). Thus, in weakly coupled QDs ($\Gamma \approx 0.01\text{meV}$) with level spacings $\delta E \approx 0.1\text{meV}$ ($\sim 1\text{K}$) and a charging energy $E_C \approx 1.5\text{meV}$, discrete peaks in the differential conductance are observable up to temperatures of several hundred mK. Note that an increase in the coupling Γ enhances quantum fluctuations in the QD leading to a suppression of the discrete peaks in the differential conductance.

The *charging diagram*, see Fig. 2.3(right panel), gives a compact specification of a QD. To illustrate the differential conductance dI/dV_{SD} as a function of both V_G and V_{SD} one uses a color scheme. From the position of the maxima of the differential conductance in the charging diagram, one can extract the relevant parameters E_C and δE .

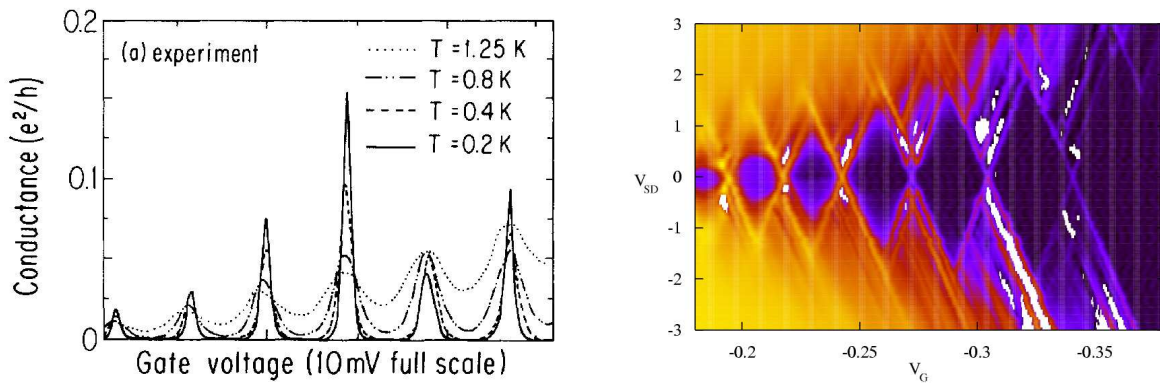


Figure 2.3: Left: Conductance as a function of gate voltage V_G in lateral QDs in the limit $V_{SD} \rightarrow 0$ [14]. The conductance peaks are separated by E_C ($E_C \gg \delta E$). As expected, the Coulomb blockade peaks get washed out when the temperature T is increased towards E_C . Right: Charging diagram of a QD [courtesy of A.K. Hüttel (LMU)]. The differential conductance is plotted as a function of both V_G and V_{SD} . For $V_{SD} = 0$ the Coulomb oscillations (with period $\sim E_C$) can be observed. Fixing V_G and varying V_{SD} , illustrated in Fig. 2.2(b), allows for the determination of δE , known as the Coulomb staircase.

2.6 Kondo effect in QDs

Under certain circumstances (as will be shown below) a many-body resonance, known as the Kondo resonance, can develop in QDs. The following two requirements are necessary for the observation of this resonance: (i) the system is tuned to the local moment regime (LMR)³ and (ii) the experiment is carried out at a temperature smaller than the so-called Kondo temperature T_K , which in turn depends exponentially on the parameters of the QD, cf. Eq. (3.29).

Based on theory, it was predicted in 1988 that the Kondo effect should be observable in QDs [16, 17]. However, it took roughly another ten years before its experimental observation by Goldhaber-Gordon *et al.* [18]. In Fig. 2.4(a) the setup of this experiment is shown. The QD is coupled (with strength Γ) to two (*left* and *right*) leads with identical chemical potential $\mu_L = \mu_R = \mu$. In order to satisfy the condition $T_{\text{exp}} < T_K$, several gates can be used to tune the QD parameters ϵ_d , Γ and U (this quantities that will be explained in Chapter 3) such that this requirement is fulfilled. This tunability allowed for many controlled 'Kondo-experiments' in the course of the last years, e.g. [19, 20]. Consequently, a better understanding of this non-trivial many-body effect was established within the last years.

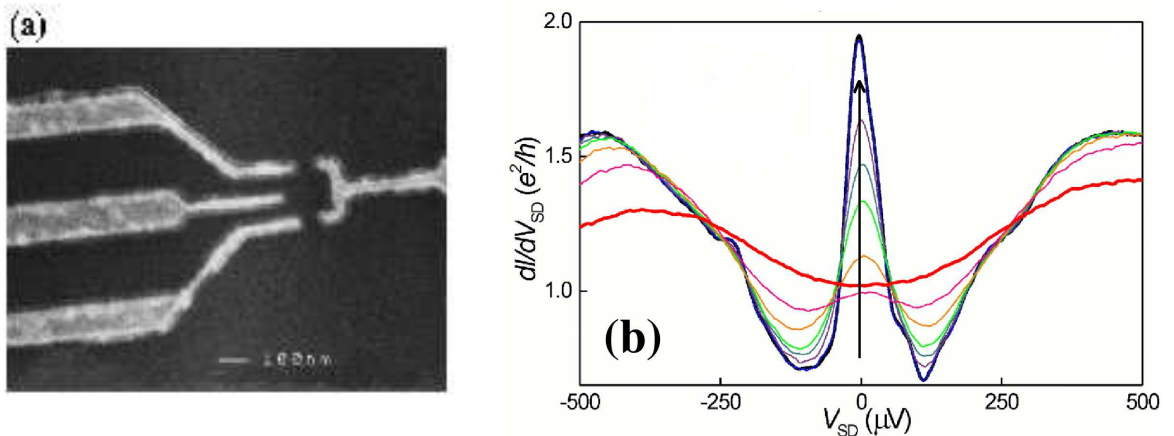


Figure 2.4: (a) Image of the device used by Goldhaber-Gordon *et al.* [19] to measure the Kondo effect in QDs. This experiment can be very well described by the Anderson model, a model that will be introduced in Section 3.1. (b) Differential conductance dI/dV_{SD} vs. V_{SD} of a QD for temperatures ranging from 15mK up to 900mK [20]. The arrow indicates an increase in dI/dV_{SD} at $V_{SD} \simeq 0$ upon lowering the temperature T (a fingerprint of the Kondo effect). Note that the differential conductance dI/dV_{SD} vs. V_{SD} clearly mimics the Kondo resonance in the local DoS for sufficiently low-temperatures.

³The LMR is realized if the topmost nonempty level of the QD contains a single electron, acting like a free spin with $n_{\uparrow} = n_{\downarrow} \sim \frac{1}{2}$ [15].

From a theoretical point of view the key quantity that governs this many-body resonance is the local DoS. In particular, the sharp resonance in the local DoS pinned at the Fermi energy of the leads, is responsible for an increase in the linear conductance (for $T \lesssim T_K$) as found experimentally in Refs. [19, 20]. Fig. 2.4(b) shows the temperature dependence of the differential conductance (which is essentially the local DoS) observed in an experiment carried out at TU Delft (Netherlands) [20].

From the Friedel-sum rule [21], we know that the height of this resonance is $\propto \frac{1}{\Gamma}$. The linear conductance $G(T)$ is consequently expected to saturate in the limit $T \rightarrow 0$ to its theoretical limit, known as the unitary limit (which is $2e^2/h$ as observed in Ref. [20]; see lower inset in Fig. 2.5), resulting in a perfect transmission of an incoming electron.

The Kondo effect in QDs is usually identified by a logarithmic increase in the linear conductance $G(T)$ as a function of decreasing temperature (for temperatures $\sim T_K$), see lower inset in Fig. 2.5. As expected, for temperatures well below T_K , a saturation of $G(T)$ appears. One experiment showing this signature very nicely was carried out at TU Delft [20]. In this experiment the linear conductance through a QD contacted to leads (with a single channel) really reached the unitary limit of $G = 2e^2/h$, see Fig. 2.5.

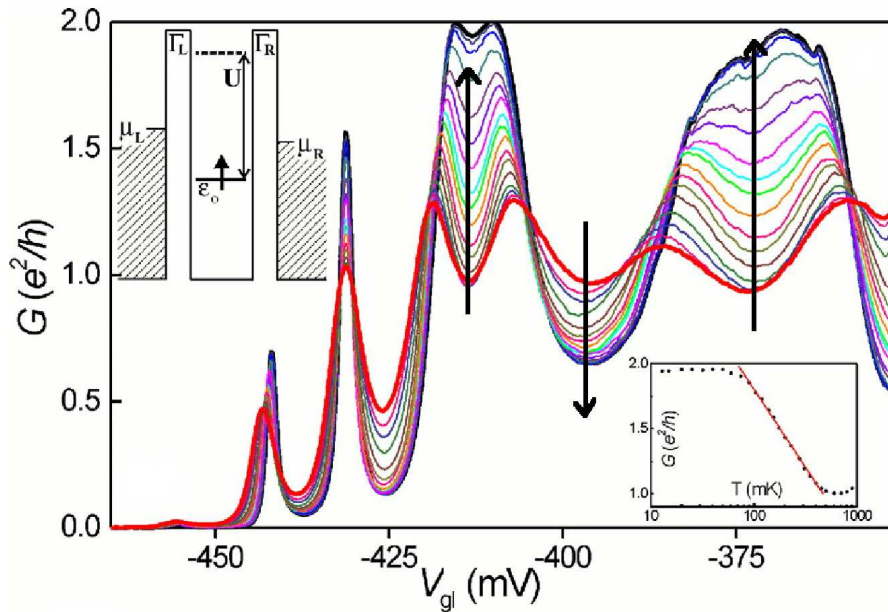


Figure 2.5: A measurement of the linear conductance $G(T)$ vs. gate voltage upon lowering the temperature T_{exp} (carried out by van der Wiel *et al.* [20]). For those gate voltages where the QD is in the LMR (see inset in the top left corner), a monotonic increase in $G(T)$ is observed for a decrease in the temperature T (indicated by two 'up' arrows). In both 'Kondo-valleys' the theoretical maximum of $2e^2/h$ is almost reached. The logarithmic increase in $G(T)$ upon lowering T in a 'Kondo-valley' is shown in the lower inset. The conductance in the valley between the two 'Kondo-valleys', i.e. in a 'non-Kondo' valley, decreases as T is lowered.

In contrast to the Kondo effect in bulk materials, where the resistivity increases below T_K , in QDs the conductivity increases for $T < T_K$. Kondo correlations lead to an *opposite* behavior in QDs as compared to bulk systems.

The reason for this behavior is the following: in presence of magnetic impurities the scattering is strongly enhanced for temperatures $T \lesssim T_K$. Since QDs are contacted to a left and a right lead an increasing scattering enhances the forward scattering drastically. Thus, the transmission through the QD increases, its resistivity decreases. In bulk materials, on the other hand, a magnetic impurity is connected to various 'channels'. Consequently an increasing scattering does *not* result in a decreasing resistivity, as the electrons are scattered in all possible directions.

To summarize the findings of this Chapter: the level quantization that appears in QDs constitutes an analogy between 'real' atomic systems and QDs; consequently QDs are often referred to as 'artificial' atomic systems. Since a detailed understanding of two-level systems is necessary for the realization of recently proposed quantum computing devices [22], QD-physics recently gathered additional interest. In particular, intense studies on coupled QDs, 'artificial molecules' [Fig. 2.1(a)], are carried out at the moment.

The analogy between QDs and 'real' atoms was strengthened when Kondo physics was measured in QDs (1998) [18, 23, 24], roughly ten years after it was predicted theoretically [16, 17]. *Kondo physics* is of central interest throughout this thesis. Modern many-body methods are required to capture the physics of strongly correlated electrons in the Kondo regime properly.

Before we focus on Kondo physics, however, we introduce a theoretical model, the Anderson impurity model, that describes QDs extremely well. It is well-known that this model is capable of Kondo physics. Thus, it allows for an accurate study of various interesting aspects of this many-body phenomenon.

Chapter 3

Introduction to the Kondo effect

This Chapter is divided into two parts: in the first part we introduce a theoretical model that describes the physics of QDs extremely well. The second part of this Chapter is devoted to Kondo physics. Some aspects of the Kondo effect are addressed there.

3.1 The Anderson model

In this Section we introduce the *Anderson model* (AM), a model (suggested by P. W. Anderson in 1961 [25]) that describes the physics of single impurities hosted in a metal. This model had a revival when it was realized, roughly 15 years ago, that it is the effective model in the framework of dynamical mean field theory [26]. As the AM is extremely well suited for the description of QDs, it got an additional boost when the first controlled QD experiments were carried out.

Within this thesis, the AM is of central relevance since (in contrast to the Kondo model) it allows for the calculation of several experimentally accessible quantities, such as the gate voltage dependence of the conductance, see Fig. 2.3(left panel).

A theoretical model that captures the physics of QDs has to consist of three parts: (i) a local part ($\hat{\mathcal{H}}_d$), which describes the isolated QD, (ii) a tunneling part between the QD and its surrounding reservoirs ($\hat{\mathcal{H}}_{ld}$) and (iii) a part that describes the reservoirs ($\hat{\mathcal{H}}_\ell$), in total

$$\hat{\mathcal{H}}_{AM} = \hat{\mathcal{H}}_d + \hat{\mathcal{H}}_{ld} + \hat{\mathcal{H}}_\ell. \quad (3.1)$$

We start analyzing Eq. (3.1) by considering $\hat{\mathcal{H}}_d$: the energetic situation inside the QD, as depicted in Fig. 3.1(a), is determined by the bare energy of the i -th local level ϵ_{di} (with typical level spacing δE between neighboring levels),¹ the charging energy E_C , the exchange energy E_S and the Zeeman energy. An isolated multi-level QD therefore takes the form

$$\hat{\mathcal{H}}_d = \sum_{i\sigma} \epsilon_{di} d_{i\sigma}^\dagger d_{i\sigma} + \sum_i U_i \hat{n}_{i\uparrow} \hat{n}_{i\downarrow} + \sum_{\sigma\sigma', i \neq j} U_{ij} \hat{n}_{i\sigma} \hat{n}_{j\sigma'} - \mu_B g B \sum_i S_i^z + J \sum_{i \neq j} \mathbf{S}_i \cdot \mathbf{S}_j, \quad (3.2)$$

¹The bare level energy ϵ_{di} is measured relative to the chemical potential of the leads μ .

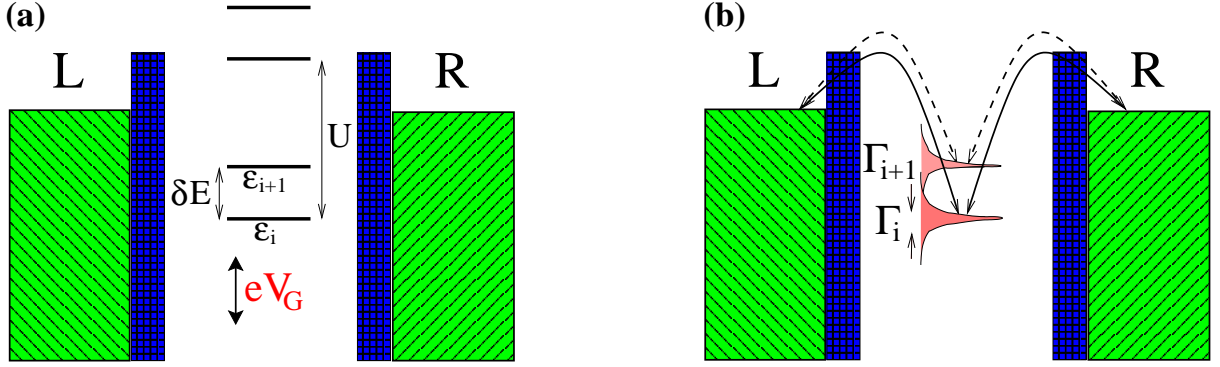


Figure 3.1: (a) Relevant parameters for the theoretical description of a QD: the charging energy U , the local level position of the i -th level ϵ_{di} (adjustable by V_G) separated from its neighboring levels by the level spacing δE . Additionally the QD-Hamiltonian $\hat{\mathcal{H}}_d$, Eq. (3.2), includes a Zeeman and an exchange term. (b) The coupling of the i -th local level to the leads (assumed to be non-interacting) results in a level-broadening of width Γ_i . In general neighboring levels are not expected to have equal width [27], $\Gamma_i \neq \Gamma_{i+1}$.

with the replacement $E_C \rightarrow U$ and $E_S \rightarrow J$. Note that multi-level QDs possess an intra-level U_i and an inter-level charging energy U_{ij} , in contrast to single-level dots that only one possess an (intra-level) charging energy U . Here $d_{i\sigma}$ ($\hat{n}_{i\sigma} = d_{i\sigma}^\dagger d_{i\sigma}$) are the Fermi operators for spin σ electrons in level i of the QD, $S_i^z = (\hat{n}_{i\uparrow} - \hat{n}_{i\downarrow})/2$, and $\mathbf{S}_i = \frac{1}{2} \sum_{\mu\nu} d_{i\mu}^\dagger \boldsymbol{\sigma}_{\mu\nu} d_{i\nu}$ (with the Pauli-matrices $\boldsymbol{\sigma}_{\mu\nu}$)². The fourth term of Eq. (3.2) denotes the Zeeman energy of the local spin with the Bohr magneton μ_B and the gyro-magnetic ratio g (a quantity that characterizes the coupling between the magnetic field and the 'QD-material'). Spins that are aligned parallel to an external magnetic field B are consequently favored. Additionally we included an exchange interaction J (the first correction to pure Coulomb interaction), a term which allows the dot to lower its energy by maximizing its total spin. This term is especially important for QDs close to a singlet-triplet transition [28].

The coupling between the QD and its environment ($\hat{\mathcal{H}}_\ell$ is the Hamiltonian of the environment), see Fig. 3.1(b), is described by the tunneling term $\hat{\mathcal{H}}_{ld}$,

$$\hat{\mathcal{H}}_{ld} = \sum_{k\sigma ir} \left(V_{kir} c_{k\sigma r}^\dagger d_{i\sigma} + V_{kir}^* d_{i\sigma}^\dagger c_{k\sigma r} \right) \quad (3.3)$$

$$\hat{\mathcal{H}}_\ell = \sum_{k\sigma r} \epsilon_{kr} c_{k\sigma r}^\dagger c_{k\sigma r}. \quad (3.4)$$

Here, the operator $c_{k\sigma r}^\dagger$ creates an electron with momentum k (corresponding to an energy ϵ_{kr}) and spin σ in lead $r = L, R$. The leads, described by $\hat{\mathcal{H}}_\ell$, are assumed to be identical,

² Those are given by $\boldsymbol{\sigma}^x = \begin{pmatrix} 0 & 1 \\ 1 & 0 \end{pmatrix}$, $\boldsymbol{\sigma}^y = \begin{pmatrix} 0 & -i \\ i & 0 \end{pmatrix}$ and $\boldsymbol{\sigma}^z = \begin{pmatrix} 1 & 0 \\ 0 & -1 \end{pmatrix}$, in standard representation.

non-interacting and in equilibrium with a dispersion $\epsilon_{kL} = \epsilon_{kR} = \epsilon_k$. Henceforth we will frequently use the phrasing conduction band (CB) electrons instead of lead electrons. We consider the tunneling matrix elements V_{kir} in $\hat{\mathcal{H}}_{ld}$, originating from the overlap of the wave functions that participate in the tunneling process (i.e. wave functions that correspond to 'impurity' and 'lead' electrons, respectively) to be k -independent, $V_{kir} = V_{ir}$ [29]. Note that the system lowers its energy when the impurity hybridizes with its environment, see Eq. (3.3), i.e. when impurity electrons become delocalized.

Below, we focus on a *single-level* AM [30, 31], so the index i will be dropped. This simplification avoids tedious mathematics while the general concepts still apply.

Due to the coupling between the impurity and the conduction band ($V_r \neq 0$), the local level acquires a width Γ , depicted in Fig. 3.1(b). We neglect the additional temperature-dependent level broadening ($\sim k_B T_{\text{exp}}$) here, as we are mostly interested in $T = 0$ quantities in this thesis. One expects, based on second order perturbation theory in the tunneling, that the level width Γ is $\propto |V_r|^2$ and $\propto \rho_r(\omega)$, the DoS in lead r [note: $\rho_L(\omega) = \rho_R(\omega) = \rho(\omega) = \sum_k \delta(\omega - \epsilon_k)$]. More rigorously, this quantity can be computed from the imaginary part of the non-interacting self-energy $\Im[\Sigma_0]$, $\Sigma_0(i\omega) = \sum_{kr} \frac{|V_r|^2}{i\omega - \epsilon_k}$. After analytic continuation, i.e. $i\omega \rightarrow \omega + i\delta$, one immediately³ arrives at $\Im[\Sigma_0] = -\pi \sum_{kr} |V_r|^2 \delta(\omega - \epsilon_k)$. When we assume both leads symmetrically coupled, $V_L = V_R = V$, we obtain the total level-width $\Gamma = -\Im[\Sigma_0]$ [29], or equivalently

$$\Gamma(\omega) = 2\pi\rho(\omega)|V|^2. \quad (3.5)$$

Transport through an interacting single-level QD is therefore characterized by the following five relevant energies: U , Γ , ϵ_d (*all* adjustable by external gates), B (an external magnetic field) and T_{exp} (set by the fridge).

Before we really solve the AM [as introduced in Eq. (3.1)], however, we perform a unitary transformation [16], which reveals that a single-level impurity couples effectively to *one* channel only, the symmetric combination of the left and the right lead.

3.1.1 Unitary transformation of the AM

In this Section a rotation in the 'L-R' basis of lead electrons is introduced. In general a single-level impurity may couple differently to its left and right leads, $V_R \neq V_L$. The basis transformation [16]

$$\begin{pmatrix} \alpha_{sk\sigma} \\ \alpha_{ak\sigma} \end{pmatrix} = \frac{1}{\sqrt{|V_L|^2 + |V_R|^2}} \begin{pmatrix} V_R & V_L \\ -V_L & V_R \end{pmatrix} \begin{pmatrix} c_{k\sigma R} \\ c_{k\sigma L} \end{pmatrix} \quad (3.6)$$

defines fermionic operators, $\alpha_{sk\sigma}/\alpha_{ak\sigma}$, that describe electrons in the symmetric and anti-symmetric channel, respectively. By means of this transformation the single-level Anderson Hamiltonian $\hat{\mathcal{H}}_{AM}$ is rotated such that it couples to the (symmetric) channel only, i.e. $\hat{\mathcal{H}}_{ld} = \sum_{k\sigma} \sqrt{V_L^2 + V_R^2} \left(\alpha_{sk\sigma}^\dagger d_\sigma + d_\sigma^\dagger \alpha_{sk\sigma} \right)$ [32] (the antisymmetric channel decouples from

³ $\lim_{\eta \rightarrow 0} \frac{1}{x \pm i\eta} = \mathcal{P} \left(\frac{1}{x} \right) \mp i\pi\delta(x)$ with \mathcal{P} denoting the principal value.

the impurity).

After this transformation, illustrated in Fig. 3.2, the Hamiltonian takes the more compact form

$$\hat{\mathcal{H}}_{AM} = \sum_{\sigma} \epsilon_d d_{\sigma}^{\dagger} d_{\sigma} + U n_{\uparrow} n_{\downarrow} - \mu_B g B S^z + \sum_{\mathbf{k}\sigma} \epsilon_k \alpha_{s\mathbf{k}\sigma}^{\dagger} \alpha_{s\mathbf{k}\sigma} + \sum_{\mathbf{k}\sigma} \tilde{V} \left(\alpha_{s\mathbf{k}\sigma}^{\dagger} d_{\sigma} + d_{\sigma}^{\dagger} \alpha_{s\mathbf{k}\sigma} \right) \quad (3.7)$$

with $\tilde{V} = \sqrt{V_L^2 + V_R^2}$. Note that we have dropped the uncoupled channel $\sum_{\mathbf{k}\sigma} \epsilon_k \alpha_{a\mathbf{k}\sigma}^{\dagger} \alpha_{a\mathbf{k}\sigma}$

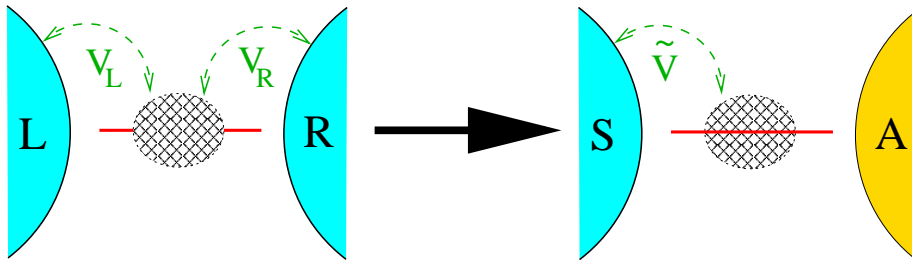


Figure 3.2: The unitary transformation Eq. (3.6) reveals that a single-level impurity couples effectively to one channel only (described by the fermionic operator $\alpha_{s\mathbf{k}\sigma}$), the symmetric linear combination of the left and the right lead [$\sim (V_L c_{\mathbf{k}\sigma L} + V_R c_{\mathbf{k}\sigma R})$]. The strength of this coupling is given by $\tilde{V} = \sqrt{V_L^2 + V_R^2}$.

in Eq. (3.7), which does not influence QD-operators at all.

QDs can be tuned via V_G such that the dot is on average singly occupied [33]; a scenario that is, as noted in Section 2.6, essential for Kondo physics. For this particular choice of V_G the topmost occupied level contains a single, unpaired electron (known as the LMR)⁴, which can be used to mimic a magnetic impurity.

As will be shown below, an AM in the LMR can be projected onto an *effective* model. As charge fluctuations are small in this regime, it suffices to perform this projection via second order perturbation theory in the tunneling (where Γ/ϵ_d is the small parameter). This projection is known as *Schrieffer-Wolff* (SW) transformation [30].

3.1.2 Mapping onto an effective model: Schrieffer-Wolff transformation

To realize a QD in the LMR we fix the gate voltage ϵ_d such that

$$\epsilon_d \ll -|\Gamma| \ll \mu \ll |\Gamma| \ll \epsilon_d + U, \quad (3.8)$$

⁴ For completeness we mention all possible regimes of a single-level AM here: the *mixed valence* regime (MV) is characterized by large charge fluctuations, realized for $\epsilon_d \sim \mu$ or $(\epsilon_d + U) \sim \mu$. That regime where the local level is either empty ($\epsilon_d \gg \mu$) or doubly occupied ($\epsilon_d + U \ll \mu$) is called the *empty orbital* regime (EO).

ensuring that the QD is singly occupied, $\langle \hat{n} \rangle \approx 1$. For this particular choice of ϵ_d the empty and the doubly occupied states in the QD can be disregarded, since they are energetically highly unfavorable. Thus, the impurity is either occupied with an \uparrow or \downarrow electron (for the rest of the first part of this thesis we use the following notation: $\sigma = \uparrow / \downarrow$ corresponds to a spin σ electron in the impurity and $\sigma = \uparrow / \downarrow$ to a spin σ electron in the CB). Thus, the impurity spin can be described by a spin operator $\hat{\mathbf{S}}$, $\hat{\mathbf{S}} \equiv \frac{1}{2} \sum_{\mu\nu} d_{\mu}^{\dagger} \boldsymbol{\sigma}_{\mu\nu} d_{\nu}$.

Due to *virtual excitations*, see Fig. 3.3, there is still a small (but finite) probability for the QD to contain zero or two electrons, even though condition (3.8) is fulfilled. For $|\epsilon_d| \gg \Gamma$, these virtual excitations are appropriately described by second order perturbation theory in the tunneling between the local level and the CB-electrons. Due to the Pauli-principle, virtual processes are only possible between CB and impurity electrons with anti-parallel spin [34]. As these processes lower the energy of the system by an amount ΔE , the effective Hamiltonian - describing the low-energy properties of the system - should include a term that favors anti-parallel alignment between electron spin in the QD and the CB.

There are two types of virtual processes, *hole-like* (excitations to an unoccupied local level; lower middle panel in Fig. 3.3) and *electron-like* (excitations to a double occupied local level; upper middle panel in Fig. 3.3) processes. A hole (electron)-like process lowers⁵ the energy of the system [35] by ΔE_h (ΔE_e)

$$\Delta E_h(\epsilon_k) = \frac{V^2[1 - f(\epsilon_k)]}{\epsilon_k - \epsilon_d} \quad (3.9)$$

$$\Delta E_e(\epsilon_k) = \frac{V^2[f(\epsilon_k)]}{U + \epsilon_d - \epsilon_k}, \quad (3.10)$$

with the Fermi function of the leads $f(\epsilon_k) = 1/(1 + e^{(\epsilon_k - \mu)/k_B T})$.

Fig. 3.3 sketches all relevant virtual processes. The impurity spin might: (i) remain unchanged (either with $\sigma = \uparrow$ or $\sigma = \downarrow$), (ii) flip its spin from $\uparrow \rightarrow \downarrow$ (in two possible ways - corresponding to a transition from the left side to the right side in Fig. 3.3) or (iii) flip its spin oppositely from $\downarrow \rightarrow \uparrow$ (also in two possible ways - corresponding to a transition from the right side to the left side in Fig. 3.3). As the total spin is conserved, the CB electron spin has to flip oppositely to the impurity spin [in the processes (ii) and (iii)] or remain unchanged [in process (i)]. A compact representation of all those processes is realized by rewriting them with spin operators. Consequently, a QD in the LMR shall contain a term $\hat{\mathbf{S}} \cdot \hat{\mathbf{s}}_0 = [S^z s_0^z + \frac{1}{2} (S^+ s_0^- + S^- s_0^+)]$ with the QD spin operator $\hat{\mathbf{S}}$, the CB spin operator $\hat{\mathbf{s}}_0$, $\hat{\mathbf{s}}_0 \equiv \frac{1}{2} \sum_{kk'} \sum_{\mu\nu} \alpha_{sk\mu}^{\dagger} \boldsymbol{\sigma}_{\mu\nu} \alpha_{sk'\nu}$ [with $\alpha_{sk\sigma}$ as defined in Eq. (3.6)] and the usual definition of the ladder operators $S^{+/-}$ and $s_0^{+/-}$, respectively. A spin-flip event between the left and the right ground state shown in Fig. 3.3, for example, is described by the operator $S^- s_0^+$.

Due to the Fermi functions, only states $\epsilon_k > \mu$ [$\epsilon_k \leq \mu$] contribute in Eq. (3.9) [Eq. (3.10)]. As we restricted ourselves to $\epsilon_d \ll \mu \ll \epsilon_d + U$, see Eq. (3.8), we can approximate the denominators in Eqs. (3.9) and (3.10) by their smallest possible values,

⁵Virtual excitations lower the energy by an amount $\Delta E \approx \frac{V^2}{E_{\text{exc}} - E_{\text{ini}}}$.

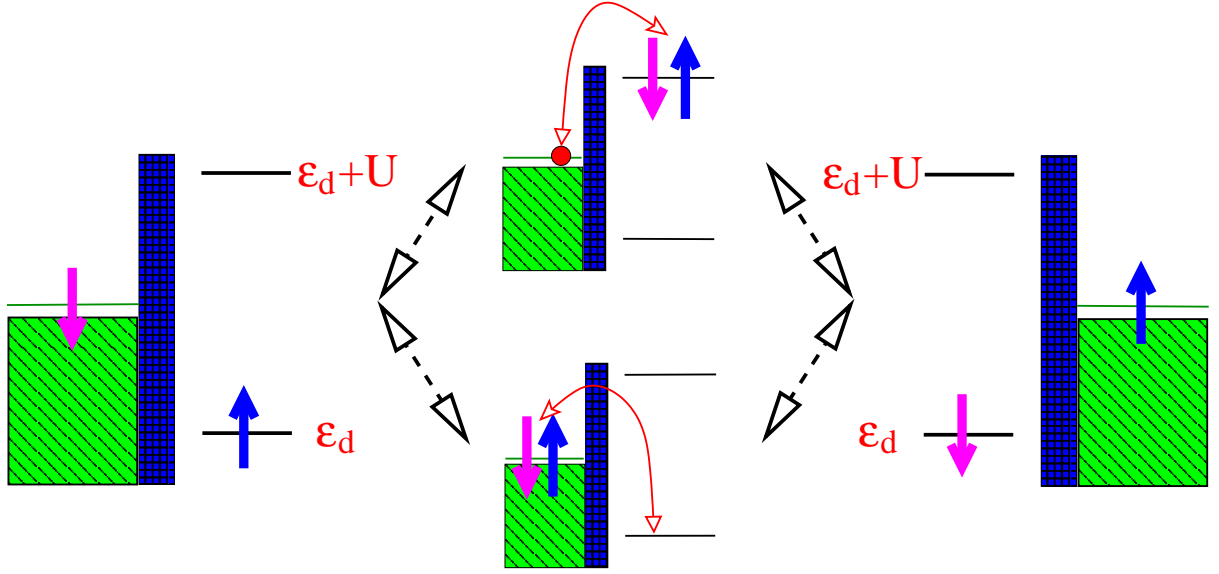


Figure 3.3: Sketch of a QD in the LMR with its two possible ground states: the electron in the QD might either be a spin \uparrow (left side) or a spin \downarrow electron (right side). In the middle of the figure the possible virtual excitations (obeying the Pauli principle), due to hybridization between impurity and lead electrons, are shown. The lower middle panel shows a hole-like excitation, realized by a CB hole that tunnels into the QD. The upper panel in the middle shows an electron-like excitation, where a CB electron tunnels into the QD. The energy gain due to these processes is described in Eq. (3.9) and (3.10). As the left and the right state in the figure are connected by virtual transitions the possibility of a spin-flip inside the QD exists!

i.e. $\epsilon_{k,k>\mu} - \epsilon_d \approx \mu - \epsilon_d$ and $U + \epsilon_d - \epsilon_{k,k\leq\mu} \approx U + \epsilon_d - \mu$.

Thus, virtual processes lower the systems energy by an amount

$$J = \frac{V^2}{\mu - \epsilon_d} + \frac{V^2}{U + \epsilon_d - \mu}. \quad (3.11)$$

Summing up *all* possible virtual transitions sketched in Fig. 3.3, we arrive at an *effective* Hamiltonian for the LMR.

$$\hat{\mathcal{H}}_{\text{eff}} = \hat{\mathcal{H}}_{\ell} + 2J\hat{\mathbf{S}} \cdot \hat{\mathbf{s}}_0, \quad (3.12)$$

with the local (Heisenberg) coupling J between the impurity spin and the conduction electron spins.

This heuristic arguments illustrated the general concept of a Schrieffer-Wolff (SW) transformation. For a detailed, more rigorous discussion, see Ref. [30] or [36]. A SW transformation enables one to project a general Hamiltonian (which is the single-level AM here) into a special subspace of its full Hilbert space (the LMR). The corresponding effective Hamiltonian, Eq. (3.12), describing the LMR is known as the *Kondo* Hamiltonian $\hat{\mathcal{H}}_{\text{eff}} = \hat{\mathcal{H}}_K$.

In this Section we argued, based on a perturbation expansion in the tunneling, how the impurity can lower its energy by means of virtual transitions. In particular processes where the impurity spin flips will become of great interest below, when the Kondo effect will be discussed.

3.2 The Kondo effect

The non-trivial physics associated with the presence of *magnetic* impurities in a solid is referred to as the *Kondo* effect. The experimental discovery of a shallow minimum in the resistivity of metals that contain magnetic impurities (at temperatures $T \sim 10\text{K}$) triggered big interest in this field. Kondo was able to relate this phenomenon to spin-flip scattering events. Kondo could show that this scattering mechanism becomes more and more dominant when the temperature of the system is lowered successively.

3.2.1 The historical origin - the resistivity minimum in bulk

Back in 1934 de Haas, de Boer and van den Berg were measuring the electrical resistivity $\rho^{\text{el}}(T)$ of Au as a function of temperature. They observed an unexpected local minimum of the resistivity at temperatures $T \sim 10\text{K}$, see Fig. 3.4. In several other experiments it was confirmed that the resistivity of 'pure' metallic samples (like gold, silver and copper) passes through a minimum when the temperature is gradually decreased. However, as was found later, the 'pure' samples were not really pure but contained a small concentration of magnetic impurities.

The resistivity of a metal is determined by different scattering mechanisms: (i) the electrical resistivity due to the scattering between conduction electrons and lattice distortions (phonons) $\rho_{\text{Phonon}}^{\text{el}} \propto T^5$ should clearly die out in the limit $T \rightarrow 0$. (ii) The resistivity contribution stemming from electron-electron scattering, $\rho_{\text{e-e}}^{\text{el}} \propto T^2$ (known from Fermi liquid theory), is also expected to vanish for very small temperatures. (iii) The scattering between electrons and static impurities is temperature independent. Consequently also the corresponding resistivity reveals no T -dependence (static impurities are present in a constant concentration, say c_{imp}).⁶ Summing up the contributions stemming from the mechanisms (i)-(iii) suggests a monotonic temperature dependence of the electrical resistivity $\rho^{\text{el}}(T) = ac_{\text{imp}}\rho_0^{\text{el}} + bT^2 + cT^5$ (a , b and c denoting proportionality constants and ρ_0^{el} a characteristic resistivity). Additionally a saturation is expected in the limit $T \rightarrow 0$, $\lim_{T \rightarrow 0} \rho^{\text{el}}(T) = ac_{\text{imp}}\rho_0^{\text{el}}$. Clearly the mechanisms (i)-(iii) can *not* explain the above mentioned anomaly in the electrical resistivity, sketched in Fig. 3.4(a).

It took about thirty years until the puzzle of a minimum in $\rho^{\text{el}}(T)$ was solved by J. Kondo (1964) [38]. He associated the minimum with the presence of *magnetic* impurities, such as Co, in the measured samples.

Magnetic impurities allow for a novel scattering mechanism, spin-flip scattering, not included in the mechanisms (i)-(iii). In particular, one finds that this scattering mechanism

⁶Both magnetic and non-magnetic impurities participate in this scattering mechanism.

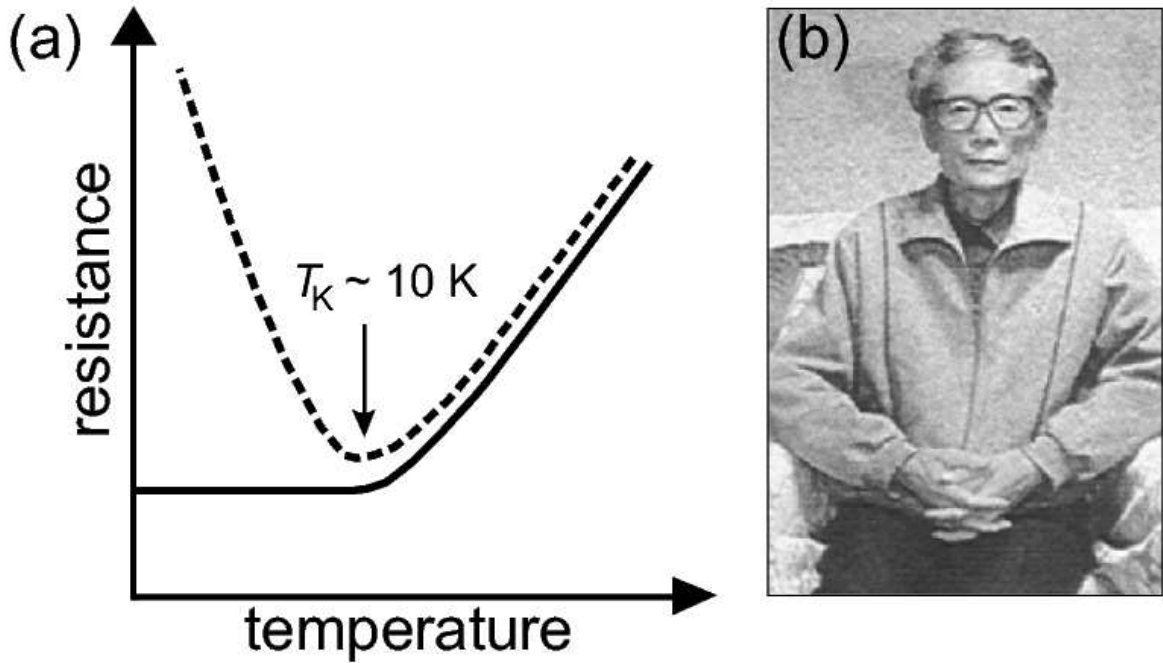


Figure 3.4: (a) Sketch of the temperature dependence of the electrical resistance for pure metals (solid line) and metals that contain a small concentration of magnetic impurities (dashed line). Note the local minimum in the resistivity around $T \sim 10 \text{ K}$ for samples containing magnetic impurities. (b) Picture of Jun Kondo. Figure and picture from [37].

is temperature *dependent*. The spin-flip scattering introduces a new energy scale in the problem, the Kondo temperature T_K . It turns out, that this scattering mechanism starts to dominate for temperatures T that are comparable to T_K . Indeed, the logarithmic increase in the resistivity for temperatures smaller than $\sim 10 \text{ K}$, e.g. observed in the experiments of de Haas *et al.*, can be nicely explained by that type of scattering [$\rho_{\text{Kondo}}^{\text{el}}(T) \propto \ln(T_K/T)$]. The local minimum of $\rho^{\text{el}}(T)$ can naturally be explained by adding up all scattering contributions to the resistivity

$$\rho^{\text{el}}(T) = ac_{\text{imp}}\rho_0^{\text{el}} + bT^2 + cT^5 + c_{\text{imp}}\rho_1^{\text{el}} \ln(T_K/T), \quad (3.13)$$

with an additional characteristic resistivity ρ_1^{el} .

In Section 3.2.3 we give a derivation for the logarithmic temperature dependence of the electrical resistivity due to the scattering of electrons from magnetic impurities. For this sake we examine the Kondo model, the 'LMR-limit' [see Eq. (3.8)] of the more general AM, carefully.

3.2.2 The Kondo model

In 1964 J. Kondo [38] introduced a model that describes the scattering of conduction electrons from a localized magnetic impurity, i.e. a localized spin [39]. This model, the Kondo model [cf. Eq. (3.12)],

$$\hat{\mathcal{H}}_K = \hat{\mathcal{H}}_\ell + 2J\hat{\mathbf{S}} \cdot \hat{\mathbf{s}}_0 = \hat{\mathcal{H}}_\ell + \sum_{kk'} J \left[S^z \left(\alpha_{sk\uparrow}^\dagger \alpha_{sk'\uparrow} - \alpha_{sk\downarrow}^\dagger \alpha_{sk'\downarrow} \right) + S^+ \alpha_{sk\downarrow}^\dagger \alpha_{sk'\uparrow} + S^- \alpha_{sk\uparrow}^\dagger \alpha_{sk'\downarrow} \right], \quad (3.14)$$

was motivated by experiments carried out in the 1930s, as explained in Section 3.2.1. As mentioned before, the operators $\hat{\mathbf{S}}$ and $\hat{\mathbf{s}}_0$ in Eq. (3.14) denote the impurity and conduction electrons spin operators, respectively, with $\hat{S}^+ |\downarrow\rangle = |\uparrow\rangle$ and $\hat{S}^- |\uparrow\rangle = |\downarrow\rangle$ ($\hat{s}_0^{+/-}$ acts accordingly on CB-electrons). In contrast to the AM (parametrized by V , ϵ_d and U), the Kondo model contains only the parameter J , which is related to the parameters of the AM via Eq. (3.11). The parameter J characterizes the coupling strength between the localized spin and the CB electrons. As $\hat{\mathcal{H}}_K$ has non-vanishing matrix elements between the states $\langle \downarrow | \langle \uparrow |$ and $|\downarrow\rangle |\uparrow\rangle$, $\langle \downarrow | \langle \uparrow | \hat{\mathcal{H}}_K | \downarrow \rangle |\uparrow \rangle \neq 0$, the Kondo Hamiltonian obviously contains spin-flip processes. Here the state $|\downarrow\rangle |\uparrow\rangle$, for instance, mimics a state where the impurity contains a spin \uparrow electron and the CB is represented by a spin \downarrow electron.

Kondo calculated the resistivity in a perturbation expansion of $\hat{\mathcal{H}}_K$ in J . He found that the second order contribution (in J) to the scattering amplitude diverges logarithmically for temperatures smaller than a characteristic temperature, the *Kondo temperature* T_K . Therefore the perturbative approach of Kondo is only valid for temperatures $T > T_K$. For temperatures $T \leq T_K$ the proper (theoretical) understanding of the KM arises from 'scaling' ideas, suggested by P.W. Anderson in the late 1960s. This ideas were used to develop an accurate theoretical description for the regime $T < T_K$. The Renormalization group (RG) theory (developed by Anderson and Wilson) is the appropriate theory in this regime.

3.2.3 Kondo's explanation

In metals conduction electrons can be described by plane waves carrying a crystal momentum, say k . The scattering of electrons from magnetic impurities can be described as follows: an incoming spin σ electron of momentum k gets scattered into an outgoing spin σ' electron of momentum k' . Since the total spin is conserved in the scattering event, the localized spin has to flip if $\sigma \neq \sigma'$. One finds, interestingly, that the spin-flip scattering is temperature dependent. We are going to derive that T -dependence here.

Our interest in scattering events between a localized magnetic impurity (of spin S) with electrons of momentum k and spin σ suggests to label the involved conduction electron states as

$$|\Psi\rangle = |k \sigma\rangle \quad (3.15)$$

and to write the impurity spin in terms of the impurity spin operator $\hat{\mathbf{S}}$. After the scattering event the electron carries a momentum k' and a spin σ' . The perturbation expansion of

$\hat{\mathcal{H}}_K$ in J can be performed by rewriting Eq. (3.14) as $\hat{\mathcal{H}}_K = \hat{\mathcal{H}}_\ell + \hat{\mathcal{H}}'$, with $\hat{\mathcal{H}}'$ describing the interaction of the CB electrons with the impurity spin, $\hat{\mathcal{H}}' = 2J\hat{\mathbf{S}} \cdot \hat{\mathbf{s}}_0$.

In order to determine the eigenstates of $\hat{\mathcal{H}}_K$, $\hat{\mathcal{H}}_K |\Psi\rangle = \epsilon |\Psi\rangle$, we rewrite the Schrödinger equation as $(\epsilon - \hat{\mathcal{H}}_\ell) |\Psi\rangle = \hat{\mathcal{H}}' |\Psi\rangle$. The general solution of this equation is a sum of the 'homogeneous' solution and the 'particular' solution. We can immediately identify plane waves $|\Psi_0\rangle$ as eigenstates of $\hat{\mathcal{H}}_\ell$, $\hat{\mathcal{H}}_\ell |\Psi_0\rangle = \epsilon |\Psi_0\rangle$, i.e. as the 'homogeneous' solution.

The formal solution of the full Schrödinger equation is

$$|\Psi\rangle = |\Psi_0\rangle + \frac{1}{\epsilon + i0^+ - \hat{\mathcal{H}}_\ell} \hat{\mathcal{H}}' |\Psi\rangle, \quad (3.16)$$

known as the Lippmann-Schwinger equation (see e.g. [40]). Eq. (3.16) can be solved by substituting the 'new' value of $|\Psi\rangle$ in the r.h.s. of this equation, resulting in $|\Psi\rangle = |\Psi_0\rangle + \frac{1}{\epsilon + i0^+ - \hat{\mathcal{H}}_\ell} \mathcal{T} |\Psi_0\rangle$. The hereby defined \mathcal{T} -matrix takes the form

$$\mathcal{T} = \overbrace{\hat{\mathcal{H}}'}^{\mathcal{T}^{(1)}} + \overbrace{\hat{\mathcal{H}}' \frac{1}{\epsilon + i0^+ - \hat{\mathcal{H}}_\ell} \hat{\mathcal{H}}'}^{\mathcal{T}^{(2)}} + \overbrace{\hat{\mathcal{H}}' \frac{1}{\epsilon + i0^+ - \hat{\mathcal{H}}_\ell} \hat{\mathcal{H}}' \frac{1}{\epsilon + i0^+ - \hat{\mathcal{H}}_\ell} \hat{\mathcal{H}}'}^{\mathcal{T}^{(3)}} + \dots \quad (3.17)$$

Eq. (3.17) shows the first three contributions to the \mathcal{T} -matrix of the perturbation expansion in J .

To first order in J , the \mathcal{T} -matrix consists of six possible scattering events, sketched in Fig. 3.5. Whereas the impurity spin is conserved in Fig. 3.5(a) [two possibilities] and (b) [two possibilities], it flips in Fig. 3.5(c) [one possibility] and (d) [one possibility].

The first-order contributions to the \mathcal{T} -matrix can thus easily be inferred from Fig. 3.5 [34]

$$\begin{aligned} \langle k' \uparrow | \mathcal{T}^{(1)} | k \uparrow \rangle &= JS^z, \\ \langle k' \downarrow | \mathcal{T}^{(1)} | k \downarrow \rangle &= -JS^z, \\ \langle k' \uparrow | \mathcal{T}^{(1)} | k \downarrow \rangle &= JS^-, \\ \langle k' \downarrow | \mathcal{T}^{(1)} | k \uparrow \rangle &= JS^+. \end{aligned} \quad (3.18)$$

Note that we kept the dependence on the impurity spin in terms of the impurity spin operator here. We continue to use this notation below.

The probability to scatter from a plane wave with momentum k to another one with momentum k' , $W_{kk'}$, is related to the amplitude for this scattering event $T_{kk'}$. In particular, $T_{kk'}^{(1)}$, a matrix element of $\mathcal{T}^{(1)}$, contains all possible transitions given in Eq. (3.18). The second order contribution to the scattering probability has the form

$$\begin{aligned} W_{kk'} &= \frac{2\pi N_{\text{imp}}}{\hbar} |T_{kk'}^{(1)}|^2 \\ &= \frac{1}{2} |J|^2 \frac{2\pi N_{\text{imp}}}{\hbar} \left[2S^z (S^z)^\dagger + \overbrace{S^+ (S^+)^\dagger + S^- (S^-)^\dagger}^{2S^z} \right] \\ &= |J|^2 \frac{2\pi N_{\text{imp}}}{\hbar} S(S+1). \end{aligned} \quad (3.19)$$

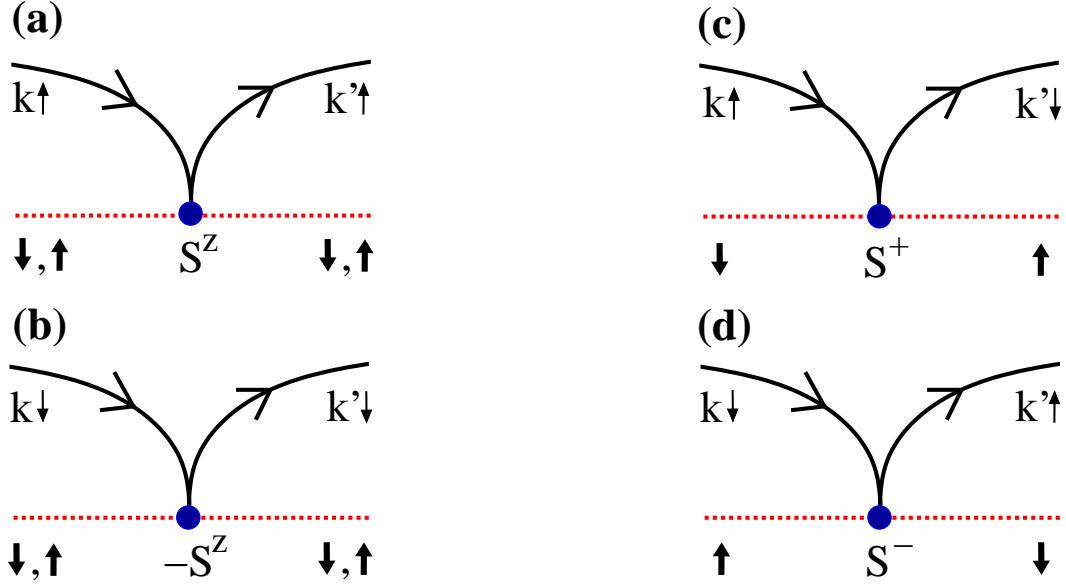


Figure 3.5: Possible processes for the \mathcal{T} -matrix to first order in J . The lower (dashed) line represents the impurity (with corresponding spin S indicated by thick arrows), whereas the curved (solid) lines represent the CB electrons [with initial (final) momentum k (k') and spin σ (σ')]. The impurity spin S (and correspondingly the CB electron spin σ) is conserved in the scattering processes (a) and (b) and it is flipped in processes (c) and (d).

Note that the factor $1/2$ [in the second line of (3.19)] ensures the proper average over the initial impurity spin configurations. Due to our notation, we replaced the impurity spin operators with their expectation values in the third line of Eq. (3.19), $S = \langle S^z \rangle$. The quantity N_{imp} labels the number of magnetic impurities in the sample.

To finally compute the resistivity $\rho_{\text{imp}}^{\text{el}}$, we need to compute the transport relaxation time at the Fermi energy $\tau(k_F)$,

$$\rho_{\text{imp}}^{\text{el}} = \frac{m}{ne^2\tau(k_F)}, \quad (3.20)$$

with the density of conduction electrons at the Fermi energy $n = N/V = k_F^3/3\pi^2$. The transport relaxation time depends sensitively on $W_{kk'}$.⁷ To second order in J this relaxation time for an electron at the Fermi surface, i.e. $k = k_F$, is given as $[\tau(k_F)]^{-1} = \frac{3\pi J^2 S(S+1)c_{\text{imp}}n}{2\epsilon_F\hbar}$, with the Fermi energy $\epsilon_F = \hbar^2 k_F^2/2m$ and the impurity concentration c_{imp} . Finally, we obtain the second order contribution (in J) to the resistivity by inserting $\tau(k_F)$ in Eq. (3.20),

$$\rho_{\text{imp}}^{\text{el},(2)} = \frac{3\pi m J^2 S(S+1)c_{\text{imp}}}{2e^2\epsilon_F\hbar}. \quad (3.21)$$

Note that $\rho_{\text{imp}}^{\text{el},(2)}$ is temperature *independent* indicating that it can not explain the anomalous temperature dependence found in the experiments of de Haas *et al.* .

⁷ $\frac{1}{\tau(\vec{k})} = \sum_{\vec{k}'} W_{\vec{k}\vec{k}'}(1 - \cos\theta')\delta(\epsilon_{\vec{k}} - \epsilon_{\vec{k}'})$ with the angle θ' between \vec{k} and \vec{k}' .

Now, we will go to the next order in perturbation theory, i.e. to $\mathcal{T}^{(2)}$. It will turn out that in this order a prefactor appears that diverges logarithmically in the limit of small temperatures.

When second order processes are considered ($\mathcal{T}^{(2)} = \hat{\mathcal{H}}' \frac{1}{\epsilon + i0^+ - \hat{\mathcal{H}}_\ell} \hat{\mathcal{H}}'$), corresponding diagrams are shown in Fig. 3.6, intermediate states of momentum k_i appear that have to be summed. Fig. 3.6 contains *all* possible second order processes for incoming and outgoing CB electrons with spin \uparrow . For instance, Fig. 3.6(c) describes a virtual process, where first an incoming electron (with momentum k and spin \uparrow) scatters from the impurity, thereby flipping both the impurity and its own spin and changing its momentum to the intermediate value k_i . Afterwards, the virtually excited conduction electron (of momentum k_i and spin \downarrow) scatters again with the impurity by flipping both spins again and finally leaving with final momentum k' and spin \uparrow . This second order process, see Fig. 3.6(c), contributes the

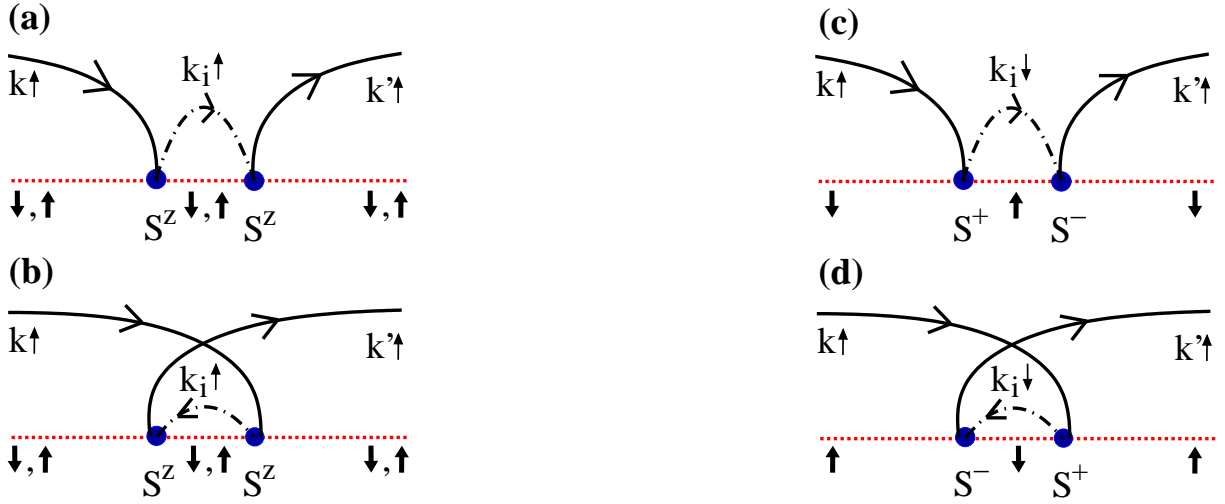


Figure 3.6: All possible second order processes for CB electrons entering and leaving the system with spin \uparrow . The intermediate states can either be electron-like [(a) and (c)] or hole-like [(b) and (d)]. Note that the impurity spin (thick arrows) flips virtually in processes [(c) and (d)] in contrast to processes [(a) and (b)].

following term to $\langle k' \uparrow | \mathcal{T}^{(2)} | k \uparrow \rangle$:

$$\sum_{k_i} J^2 \langle k' \uparrow | \alpha_{sk'\uparrow}^\dagger \alpha_{sk_i\downarrow} S^- \frac{1}{\epsilon + i0^+ - \hat{\mathcal{H}}_\ell} S^+ \alpha_{sk_i\downarrow}^\dagger \alpha_{sk\uparrow} | k \uparrow \rangle = \sum_{k_i} J^2 \frac{S^- S^+ [1 - f(\epsilon_{k_i})]}{\epsilon - \epsilon_{k_i} + i0^+}, \quad (3.22)$$

where the relation $\langle \alpha_{sk_i\downarrow}^\dagger \frac{1}{\epsilon + i0^+ - \hat{\mathcal{H}}_\ell} \alpha_{sk_i\downarrow}^\dagger \rangle = \frac{1 - f(\epsilon_{k_i})}{\epsilon - \epsilon_{k_i} + i0^+}$ was used. Here f is the Fermi-Dirac distribution.

Another second order contribution to $\langle k' \uparrow | \mathcal{T}^{(2)} | k \uparrow \rangle$ is shown in Fig. 3.6(d). The diagram describes a scattering process, where first the impurity spin is flipped ($\uparrow \rightarrow \downarrow$) by creating an electron-hole pair with an outgoing electron of momentum k' and spin \uparrow . After this

event, an incoming electron of momentum k and spin \uparrow scatters with the impurity a second time by flipping its spin back to its original state ($\Downarrow \rightarrow \Uparrow$) and thereby destroying the hole of momentum k_i . Evaluating this diagram results in

$$\begin{aligned} \sum_{k_i} J^2 \langle k' \uparrow | \alpha_{sk_i \downarrow}^\dagger \alpha_{sk \uparrow} S^+ \frac{1}{\epsilon + i0^+ - \hat{\mathcal{H}}_\ell} S^- \alpha_{sk' \uparrow}^\dagger \alpha_{sk_i \downarrow} | k \uparrow \rangle &= - \sum_{k_i} J^2 \frac{S^+ S^- f(\epsilon_{k_i})}{\epsilon - \epsilon_k - \epsilon_{k'} + \epsilon_{k_i} + i0^+} \\ &= \sum_{k_i} J^2 \frac{S^+ S^- f(\epsilon_{k_i})}{\epsilon - \epsilon_{k_i} - i0^+}, \end{aligned} \quad (3.23)$$

where we used $\epsilon \approx \epsilon_k \approx \epsilon_{k'} \approx \mu$ since we are interested in having both values k and k' near the Fermi level.

The two remaining diagrams in Fig. 3.6, namely (a) and (b), can be evaluated analogously and give the following contributions to $\langle k' \uparrow | \mathcal{T}^{(2)} | k \uparrow \rangle$,

$$\sum_{k_i} J^2 \frac{(S^z)^2 [1 - f(\epsilon_{k_i})]}{\epsilon - \epsilon_{k_i} + i0^+} \quad \text{and} \quad \sum_{k_i} J^2 \frac{(S^z)^2 f(\epsilon_{k_i})}{\epsilon - \epsilon_{k_i} - i0^+}, \quad (3.24)$$

respectively. Note that the sum of the two contributions given in Eq. (3.24) is temperature *independent*, since the contributions that include the Fermi function cancel each other⁸. The contributions from Eqs. (3.22) and (3.23), however, do not cancel. Therefore we identify the spin-flip scattering with the mechanism that gives rise to a temperature dependent scattering.

To second order in J , we approximate the \mathcal{T} -matrix with $\mathcal{T} \approx \mathcal{T}^{(1)} + \mathcal{T}^{(2)}$. The second order contribution $\mathcal{T}^{(2)}$ leads to a correction of the scattering probability $W_{kk'}$, see Eq. (3.19), which we call $\delta W_{kk'}$. The correction $\delta W_{kk'}$ is of third order in J . As $W_{kk'} \sim |T_{kk'}|^2 \sim \left| T_{kk'}^{(1)} \right|^2 + \left[T_{kk'}^{(1)} \left(T_{kk'}^{(2)} \right)^* + \left(T_{kk'}^{(1)} \right)^* T_{kk'}^{(2)} \right]$ we obtain the correction $\delta W_{kk'}$ to the transition probability as

$$\frac{\hbar}{2\pi N_{\text{imp}}} \delta W_{kk'} = T_{kk'}^{(1)} \left(T_{kk'}^{(2)} \right)^* + \left(T_{kk'}^{(1)} \right)^* T_{kk'}^{(2)} \sim J^3. \quad (3.25)$$

Adding *all* spin contributions to $\delta W_{kk'}$ leads to

$$\frac{\hbar}{2\pi N_{\text{imp}}} \delta W_{kk'} \sim S(S+1) J^3 \sum_{k_i} \frac{f(\epsilon_{k_i}) - \frac{1}{2}}{\epsilon - \epsilon_{k_i}}. \quad (3.26)$$

The third order contribution to the resistivity, however, requires the tricky determination of the corresponding transport relaxation time $\tau(k)$. To do so, the sum over the intermediate states has to be performed

$$\sum_{k_i} \frac{f(\epsilon_{k_i}) - \frac{1}{2}}{\epsilon - \epsilon_{k_i}} \sim \int d\epsilon_i \rho(\epsilon_i) \frac{f(\epsilon_i) - \frac{1}{2}}{\epsilon - \epsilon_i} = \frac{1}{2} \rho(0) \int_{-D}^D d\epsilon_i \frac{\tanh(\epsilon_i/2kT)}{\epsilon - \epsilon_i}. \quad (3.27)$$

⁸The summation over k_i is taken as a principal value integration.

Here the energy-dependent DoS $\rho(\epsilon_i)$ has been replaced by its value at the Fermi energy $\rho(\mu)$, $\mu = 0$. Moreover, the high-energy divergence has been cut off by restricting the conduction electron states to a band of finite width $2D$ (D is usually referred to as the bandwidth of the conduction band).

We will now consider two limiting cases to obtain an *interpolation formula* for the integral given in Eq. (3.27): (i) for $\epsilon \ll kT$, we approximate the integral with $2 \ln(D/kT)$, whereas (ii) for $\epsilon \gg kT$ we approximate it with $2 \ln(D/|\epsilon|)$. This leads to the compact - *temperature dependent* - approximation $\sum_{k_i} \frac{f(\epsilon_{k_i})^{-1/2}}{\epsilon - \epsilon_{k_i}} \sim \ln\left(\frac{D}{\max(|\epsilon|, kT)}\right)$. Therefore, the third order contribution (in J) to the transport relaxation time, $[\tau(k_F)]^{-1} = \frac{3\pi J^2 S(S+1)c_{\text{imp}n}}{2\epsilon_F \hbar} \left[1 + 4J\rho(0) \ln \frac{D}{\max(|\epsilon|, kT)}\right]$, see also [34], introduces a temperature dependence in the resistivity.

Remarkably $\mathcal{T}^{(2)}$ reveals that the existence of magnetic impurities leads to an enhanced scattering rate for electrons in the close vicinity of the Fermi energy for sufficiently low temperatures. This enhanced scattering, known as the Kondo resonance, explains the temperature dependence of the resistivity observed in bulk materials. Surprisingly, the energy scale that is related to this phenomenon, the Kondo temperature T_K , is *not* an intrinsic energy scale of the problem such as ϵ_d , U or V (in case of the AM). The value of T_K results from an *interplay* between the impurity spin and *all* its surrounding conduction electrons, it is a many-body phenomenon.

Including this order, the resistivity, see Eq. (3.21), becomes temperature dependent. In particular, when we assume $kT > \epsilon$ the resistivity takes the form

$$\rho_{\text{imp}}^{\text{el},(3)} = \frac{3\pi m J^2 S(S+1)c_{\text{imp}}}{2e^2 \epsilon_F \hbar} [1 - 4J\rho(0) \ln(kT/D)]. \quad (3.28)$$

The temperature dependent contribution to the resistivity indeed agrees very well with the resistance minimum found in the experiments of de Haas *et al.*, mentioned in Section 3.2.1. Note that Eq. (3.28) reproduces the logarithmic divergence that was experimentally found, see Eq. (3.13). We are now able to clarify the physical meaning of all contributions to the resistivity, $\rho^{\text{el}}(T) = ac_{\text{imp}}\rho_0^{\text{el}} + bT^2 + cT^5 + c_{\text{imp}}\rho_1^{\text{el}} \ln(T_K/T)$. Whereas ρ_0^{el} is a specific resistivity that includes *magnetic* and *non-magnetic* impurities, ρ_1^{el} includes only *magnetic* impurities. At this point we do not want to specify the dependence of T_K on the parameters of the system further. This will be done in the next Section.

At the end of this Section, we want to allude a new problem, which arises from the perturbation expansion performed above: what happens for small temperatures (in particular in the limit $T \rightarrow 0$)?

Obviously, the behavior suggested in Eq. (3.28) has to be unphysical for $T \rightarrow 0$ since it implies a divergent resistivity in this limit. In fact, the perturbative expansion for the resistivity can not be trusted any more, once the third order contribution becomes of the order of the second order contribution, i.e. for $|4J\rho(0) \ln(kT/D)| \sim \mathcal{O}(1)$ [see Eq. (3.28)]. Clearly this happens for sufficiently small temperatures.

For these temperatures, the perturbative method fails and one needs scaling techniques for a proper solution of the Kondo problem. Therefore a lot of conceptual work was

needed to overcome the breakdown of perturbation theory to properly describe the emerging regime. We investigate this regime, the regime of extremely small temperatures, in the next Section.

3.2.4 General properties of the Kondo effect

It was realized in Section 3.2.3, that the spin-flip scattering introduces a logarithmic temperature dependence to the electrical resistivity. Obviously, a degeneracy between the two spin states of the impurity is necessary for spin-flip scattering to appear. A magnetic field B [of strength T_K (more precisely $\mu_B g B = k_B T_K$), see below] clearly removes this degeneracy and thereby destroys spin-flip scattering and consequently the Kondo effect.

Below the temperature where perturbation theory breaks down, known as the Kondo temperature T_K , an *effective* screening of the unpaired spin (i.e. the magnetic impurity) takes place due to coherent virtual transitions between the impurity spin and its surrounding conduction electrons; the (many-body) ground state [40] of the system is a *singlet* of binding energy T_K .⁹ All conduction electrons are arranged such that the magnetic moment is screened and the singlet can be formed. Thus for $T < T_K$, $k_B T_K \sim D e^{-1/[2\rho(0)J]}$ (see e.g. [40]) with $\rho(0)$ the leads DoS at the Fermi energy, the localized magnetic impurity interacts strongly with its surrounding electrons.

Once T becomes less than T_K the system is in the strong coupling regime, universal scaling sets in. In absence of a magnetic field no other energy scale is left in the problem [40]. This means all measurable quantities, like the conductance $G(T)$, scale as T/T_K or ω/T_K for energies smaller than T_K .

In the framework of the single-level AM [tuned such that the LMR is realized, see Eq. (3.8)] the value of T_K can be estimated in the framework of poor man's scaling (as done by Haldane [41]) or by Bethe-Ansatz [29]

$$k_B T_K = \frac{1}{2} \sqrt{U\Gamma} e^{\pi\epsilon_d(\epsilon_d+U)/\Gamma U}. \quad (3.29)$$

Note the exponential dependence of T_K on the system parameters ϵ_d , U and Γ . According to Eq. (3.29), T_K is minimal for $\epsilon_d = -U/2$. It increases as ϵ_d approaches 0 or $-U$.

For fixed gate voltage V_G (i.e. fixed ϵ_d), on the other hand, T_K can be exponentially enhanced by increasing Γ . This can be achieved by opening the QD.

This knowledge is of experimental relevance, as it allows one to tune T_K to values that are experimentally accessible (i.e. $T_{\text{exp}} < T_K$). However, a continuous increase of Γ has other drawbacks. Once Γ exceeds the level-spacing δE , transport processes involve more than one level. Consequently a multi-level AM has to be considered. We study such a model in Chapter 6, for instance, where we focus on the ϵ_d -dependence of the occupation of a multi-level AM.

The crossover scale T_K , given in Eq. (3.29), can also be extracted from the following dynamic quantity: the imaginary part of the spin susceptibility $\chi''(\omega)$, defined in Eq. (4.9),

⁹In this regime the impurity binds on average one conduction electron to form this singlet. A magnetic field of strength $B \gtrsim T_K$ destroys this singlet.

shows Curie-Weiss behavior for temperatures $T > T_K$, $\chi''(\omega) \sim \frac{1}{\omega + T_K}$, i.e. $\chi''(\omega)$ decays as $\propto \omega^{-1}$ (apart from logarithmic corrections) for $\omega > T_K$. For $T < T_K$, on the other hand, the system behaves like a Fermi liquid, $\chi''(\omega) \propto \omega$ for $\omega < T_K$. Numerically, it is convenient to extract T_K from the (numerically) computed spin susceptibility $\chi''(\omega)$ by identifying it with the maximum of $\chi''(\omega)$.¹⁰ In case of a single-level AM this (numerical) determination of T_K agrees very well with the values for T_K obtained from Eq. (3.29). For more complicated models (such as the two-level AM), however, Eq. (3.29) does not apply any more. Then $\chi''(\omega)$ can still be used to extract the value of T_K .

The fact that the ground state of the system is a singlet for $T < T_K$ results in a sharp resonance in the local DoS $A(\omega)$ pinned at the Fermi energy of characteristic width $\sim T_K$ (see Section 4.1.2). Indeed, a three-peak structure in $A(\omega)$, two broadened peaks (of width Γ) at energies ϵ_d and $\epsilon_d + U$ and the Kondo peak, can nicely be seen in Fig. 4.4(left panel), which was calculated with NRG. The determination of the local DoS is crucial since it is the key quantity for the computation of transport properties.

To summarize: Kondo correlations are established if (i) there are (at least) two degenerate states in the system (like spin-degenerate states), (ii) the degenerate states are coupled to a Fermi sea with finite strength Γ and (iii) the average number of electrons in the system is fixed (U suppresses adding a further electron). Some references to experimental results related to QDs in the Kondo regime were already given in Chapter 2.6.

3.2.5 Poor man's scaling (PMS)

In 1970 P.W. Anderson introduced a method, the poor man's scaling (PMS) method [42], to derive an *effective* Hamiltonian that captures the low-energy properties of a given system. Anderson's idea was to obtain an effective Hamiltonian, say at an energy ω^* , by successively integrating out high energy states of the system until the scale ω^* was reached. He imposed the physical condition that this scaling procedure (equivalent to a decrease in the bandwidth from D to \tilde{D} , see Fig. 3.7) leaves the scattering between conduction electrons and the impurity invariant. One can satisfy this requirement by continuously adapting the physical parameters of the Hamiltonian (say the coupling J in case of $\hat{\mathcal{H}}_K$) under study, i.e. to allocate a cutoff-dependent parameter $\tilde{J}(\tilde{D})$ to the corresponding effective Hamiltonian $\hat{\mathcal{H}}_{\text{eff}}(\tilde{D})$. This adjustment results in a 'flow' of the parameter $\tilde{J}(\tilde{D})$, the coupling becomes cutoff dependent.

PMS for the Kondo model

Here we want to discuss the PMS of the KM. Since this procedure can be easily found in the standard literature, see e.g. Ref. [40] or [43], we keep this discussion short.

A scaling equation for the isotropic KM is obtained, when one successively eliminates the excitations (say of energy k_i) that lie in the band edge $\tilde{D} \leq |k_i| \leq D$. When one restricts all excitations that appear in the second order diagrams discussed in Section 3.2.3 (see

¹⁰In Chapter 4 we introduce the NRG method and explain how to compute $\chi''(\omega)$ in the framework of this method. The right panel of Fig. 4.4 shows $\chi''(\omega)$ calculated with NRG.

especially Fig. 3.6), to this interval¹¹ the scaling equation for the Kondo coupling J can be derived. For a flat band ($\rho = \text{const.}$) the scaling equation of the Kondo has the form

$$\frac{dJ}{d \ln D} = -2\rho J^2. \quad (3.30)$$

A detailed derivation of this equation can, for instance, be found in Section 3.3 of [40].

The consequence of a decrease in the cutoff D can be understood when one integrates Eq. (3.30) from \tilde{D} to D . This integration yields

$$\tilde{J}(\tilde{D}) = \frac{J}{1 + 2\rho J \ln(\tilde{D}/D)} \quad (3.31)$$

with the effective coupling \tilde{J} corresponding to the reduced bandwidth \tilde{D} . Provided we are in the weak coupling regime ($\rho J \ll 1$), we can infer from Eq. (3.31), that \tilde{J} is continuously growing since $1 + 2\rho J \ln(\tilde{D}/D) < 1$ ($\tilde{D} < D$).

The bandwidth is continuously reduced until it reaches the scale of interest, the temperature T , $\tilde{D} \simeq T$. Consequently, the effective coupling at a temperature T is given as $\tilde{J}(T) = \frac{J}{1 + 2\rho J \ln(T/D)}$. One immediately realizes that $\tilde{J}(T)$ diverges, for $1 + 2\rho J \ln(T/D) = 0$. The temperature that is related to the divergence in $\tilde{J}(T)$ is called the Kondo temperature T_K

$$T_K = D e^{-1/(2\rho J)}. \quad (3.32)$$

PMS for the Anderson model

Here we apply the PMS method to the AM. Following Haldane [41] we calculate how the energy levels of the AM are renormalized if high energy states are integrated out.

To illustrate this flow, we consider a single-level AM in the limit $U \rightarrow \infty$, i.e. the relevant energy level is either empty $|0\rangle$ or singly occupied with a spin σ electron $|1, \sigma\rangle$.

The flow of the energy of the empty level $\epsilon_d^{(0)}$ and the singly occupied level $\epsilon_{d\sigma}^{(1)}$ is obtained, as mentioned above, by successively integrating out the 'high energy' band-states (see Fig. 3.7). By this we mean the following: the presence of the highly excited states, of energy $\sim D$, is absorbed by a change of the energies of the empty $\delta\epsilon_d^{(0)}$ and singly occupied levels $\delta\epsilon_{d\sigma}^{(1)}$. Within second order perturbation theory in V we obtain

$$|0\rangle : \delta\epsilon_d^{(0)} = \tilde{\epsilon}_d^{(0)} - \epsilon_d^{(0)} = \sum_{\sigma} \int_{-D}^{-\tilde{D}} \frac{\rho_{\sigma}(\omega) |V_{\sigma}|^2}{\epsilon_d^{(0)} - (\epsilon_{d\sigma}^{(1)} + |\omega|)} d\omega \quad (3.33)$$

$$\begin{aligned} |1, \sigma\rangle : \delta\epsilon_{d\sigma}^{(1)} = \tilde{\epsilon}_{d\sigma}^{(1)} - \epsilon_{d\sigma}^{(1)} = & \int_{\tilde{D}}^D \frac{\rho_{\sigma}(\omega) |V_{\sigma}|^2}{\epsilon_{d\sigma}^{(1)} - (\epsilon_d^{(0)} + |\omega|)} d\omega \\ & + \underbrace{\int_{-D}^{-\tilde{D}} \frac{\rho_{\bar{\sigma}}(\omega) |V_{\bar{\sigma}}|^2}{\epsilon_{d\bar{\sigma}}^{(1)} - U + |\omega|} d\omega}_{\rightarrow 0 \text{ f. } U \rightarrow \infty}. \end{aligned} \quad (3.34)$$

¹¹This means that all k_i 's in expressions like Eq. (3.22) are restricted to the interval $\tilde{D} \leq |k_i| \leq D$.

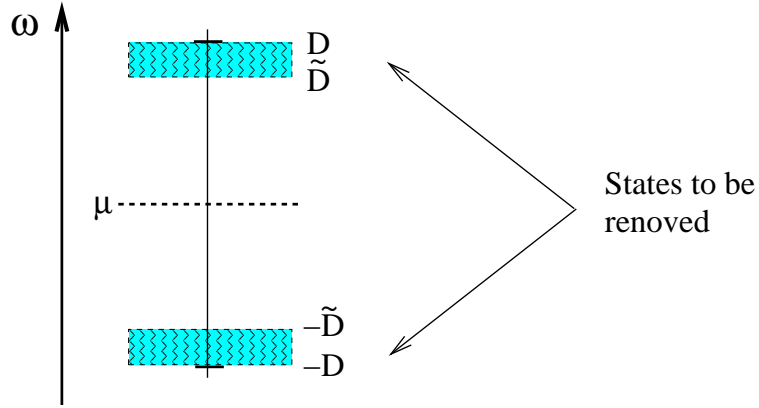


Figure 3.7: The marked high energy states (of width δ , $\delta \rightarrow 0$) are those that are integrated out in the course of the scaling procedure. D denotes the full bandwidth and \tilde{D} the new effective bandwidth after the high energy states have been integrated out. This procedure leads to a 'flow' of the parameters of the considered model so that the derived Hamiltonian describes the low-energy physics of the system properly.

Here the tilde denotes the renormalized local levels and $\bar{\sigma} = \uparrow / \downarrow$ if $\sigma = \downarrow / \uparrow$. When we assume the leads DoS to be constant and spin independent, $\rho_\sigma(\omega) = \rho$, and define $\Gamma_\sigma \equiv 2\pi\rho|V_\sigma|^2$, this leads to

$$\delta\epsilon_d^{(0)} = -\sum_\sigma \left(\frac{\Gamma_\sigma}{2\pi}\right) \int_{-D}^{-\tilde{D}} \frac{d\omega}{|\omega| + \epsilon_{d\sigma}^{(1)} - \epsilon_d^{(0)}} \quad (3.35)$$

$$\delta\epsilon_{d\sigma}^{(1)} = -\left(\frac{\Gamma_\sigma}{2\pi}\right) \int_{\tilde{D}}^D \frac{d\omega}{|\omega| + \epsilon_d^{(0)} - \epsilon_{d\sigma}^{(1)}}. \quad (3.36)$$

As long as $\epsilon_{d\sigma}^{(1)} - \epsilon_d^{(0)} \ll D$ we can approximate $|\omega| + \epsilon_d^{(0)} - \epsilon_{d\sigma}^{(1)} \approx |\omega|$ in the integrals in Eqs. (3.35) and (3.36). Thus the flow of $\epsilon_{d\sigma}$, most easily seen in differential form $\delta\epsilon_{d\sigma} = \delta\epsilon_{d\sigma}^{(1)} - \delta\epsilon_d^{(0)}$, is described via

$$\frac{d\epsilon_{d\sigma}}{d \ln D} = \frac{\Gamma_{\bar{\sigma}}}{2\pi}, \quad (3.37)$$

equivalent to Eq. (2) of [44] [valid for $U \rightarrow \infty$]. Note that the renormalization of $\epsilon_{d\sigma}$ depends on $\Gamma_{\bar{\sigma}}$, i.e. on the coupling of the opposite spin species. The reason is that, the empty level $|0\rangle$ hybridizes with the singly occupied level $|1, \sigma\rangle$ (involving band states of both spin directions), so both spin species contribute (see Eq. 3.33), while for the σ -occupied level $|1, \sigma\rangle$ (which hybridizes only with $|0\rangle$) for $U \gg |\epsilon_d|$ only spin σ electrons contribute (Eq. 3.34), and after a partial cancellation, only the contribution of $\bar{\sigma}$ survives.

Chapter 4

Wilson's Numerical Renormalization Group (NRG)

Naively one might expect that high energy states can be disregarded when one is interested in the low-temperature properties of a system. As the Fermi function f is smoothed around the Fermi energy μ with a width $\sim k_B T$ (known from the Sommerfeld-expansion [45]) one is tempted to consider only states of energy $|\omega - \mu| \leq k_B T$ to be relevant for transport.¹ However, as the intermediate states of momentum k_i in the (second order) perturbation expansion (see Section 3.2.3) are not restricted to this interval, one might already anticipate, that in the Kondo problem states of *all* energies are relevant. To account for all energies of the problem, $|\omega| \leq D$, the idea of the renormalization group (RG) was introduced.

Within the PMS-approach, introduced in Section 3.2.5, high energy states are successively integrated out, leading to an effective 'flow' of the parameters of the model. A prominent example of such a flow, as discussed in Section 3.2.5, is the flow of the parameter J (in case of the Kondo model), see Fig. 4.1. The PMS-method allows one to identify relevant (parameters that are flowing to larger values under a decrease of the cutoff), marginal (... not flowing under a decrease of the cutoff) and irrelevant (... flowing to zero ...) parameters. Once one has identified the irrelevant parameters of a system, one knows, in principle², which mechanisms govern the low-temperature physics of the system, i.e. one has derived an *effective* Hamiltonian. However, PMS breaks down once the relevant parameters start to diverge.

That drawback was overcome by another prominent RG-method, the NRG-method. In this Chapter we introduce this renormalization scheme.

In the early 1970's K.G. Wilson succeeded to construct a *nonperturbative* solution of the KM [46] (which was later extended to the AM by Krishna-murthy *et al.* [31, 47]). Since the "NRG-method does not rely on any assumptions regarding the ground state or

¹Typical transport integrals include the derivative of f .

²The question whether marginal operators are important has to be investigated separately.

leading order divergent couplings" [28] it is superior to a mean-field description or scaling equations. A detailed description of the procedure is given in Appendix A.

Wilson's ingenious idea was to discretize the CB (of bandwidth $2D$) logarithmically [1] via a discretization parameter Λ ($\Lambda > 1$). This discretization enabled him to take *all* CB energies into account. He reached this goal by dividing the CB into energy intervals $[-x_N, -x_{N+1}[$ and $]x_{N+1}; x_N]$ with $x_N = D\Lambda^{-N}$, $N \in \mathbb{N}_0$. Wilson showed that this CB-discretization becomes exact if the discretization parameter approaches 1, $\Lambda \rightarrow 1$. Moreover he was able to show that the method still works extremely well for a moderately large choice of Λ (up to $\Lambda \sim 3$).

Within the NRG-scheme the continuous CB operators are expanded in a Fourier series with fundamental frequency $2\omega_N = \pi\Lambda^N / (1 - \Lambda^{-1})$ in each (logarithmic) interval. Defining a single fermionic degree of freedom $f_{0\sigma}$ [defined in (A.13)] allowed Wilson to rewrite the hybridization $\hat{\mathcal{H}}_{\ell d}$ between the impurity and *all* CB electrons in a compact way, see Eq. (A.14). The Lanczos algorithm, ansatz (A.22) in Appendix A.2, then allows one to tridiagonalize the remaining CB (represented by constant Fourier components within each logarithmic interval). This permits one to solve the problem at hand numerically. Indeed the transformation of the CB onto a semi-infinite chain, the 'Wilson chain', with corresponding fermionic operators $f_{N\sigma}^\dagger$ creating a spin σ electron at the N -th site of the Wilson chain [Eq. (A.24)], allows for an iterative diagonalization and consequently a numerical exact solution of the Kondo problem. Further details of this procedure can be found in Appendix A.

More formally, as can e.g. be found in Ref. [31], the KM is recovered in the limit of an infinite long Wilson chain $\mathcal{H}_K = \lim_{N \rightarrow \infty} \frac{1}{2} (1 + \Lambda^{-1}) \Lambda^{-(N-1)/2} \hat{H}_N$, with

$$\hat{H}_N = \Lambda^{(N-1)/2} \left\{ \hat{H}_0 + \sum_{n=0, \sigma}^{N-1} \left[\Lambda^{-n/2} \xi_n^K \left(f_{n\sigma}^\dagger f_{n+1\sigma} + f_{n+1\sigma}^\dagger f_{n\sigma} \right) \right] \right\}. \quad (4.1)$$

Here $\hat{H}_0 = \hat{H}_0 \left(\frac{2}{1+\Lambda^{-1}} \right)$ and $\xi_n^K = \frac{1-\Lambda^{-n-1}}{\sqrt{(1-\Lambda^{-2n-1})(1-\Lambda^{-2n-3})}}$, cf. Eq. (2.18) of [31]. The ξ_n^K 's are the tunneling matrix elements between two sites along the Wilson chain (which decay $\propto \Lambda^{-N/2}$ [46]) and $\hat{H}_0 = J\mathbf{S}f_{0\mu}^\dagger \boldsymbol{\sigma}_{\mu\nu} f_{0\nu}$ (with \mathbf{S} as defined in Section 3.1.2). The typical energy scale in the N -th iteration, ω_N , is roughly set by ξ_N^K . Wilson showed $\omega_N \sim \Lambda^{-(N-1)/2}$ [46]. Note that a rescaling factor $\frac{1}{2} (1 + \Lambda^{-1})$ has been introduced [31] here. This factor ensures that the recursion relation $\hat{H}_{N+1} = \sqrt{\Lambda} \hat{H}_N + \sum_{\sigma} \left[\xi_N^K \left(f_{N\sigma}^\dagger f_{N+1\sigma} + f_{N+1\sigma}^\dagger f_{N\sigma} \right) \right]$ takes a particular simple form [see Eq. (A.40) for the general case]. In contrast to the more general case, discussed in Appendix A, the leads DoS in Ref. [31] was assumed to be constant and spin independent.

Note that the exponential decrease of ξ_N^K ($\propto \Lambda^{-N/2}$) in Eq. (4.1) ensures that the problem can be solved by iterative diagonalization, as the energy scales of the different iterations separate nicely. Other models like the Hubbard model - where the hopping matrix element are constant - can not be solved by NRG and one needs to use other methods such as the density matrix renormalization group (DMRG) method [48] for tackling problems of this kind.

As expected from PMS the parameter J of the Kondo problem is small at the beginning of the NRG-procedure corresponding to high energies (weak coupling regime). Once the strong coupling regime is reached, i.e. when the NRG-iteration has proceeded far below the energy scale T_K (see Fig. 4.1), however, J diverges. To capture the crossover regime (at an energy T_K) between the weak and the strong-coupling regime well, it is crucial to keep sufficiently many the lowest lying eigenstates of the system in each iteration. Fig. 4.1 shows the crossover of J as a function of decreasing energy (i.e. increasing iteration).

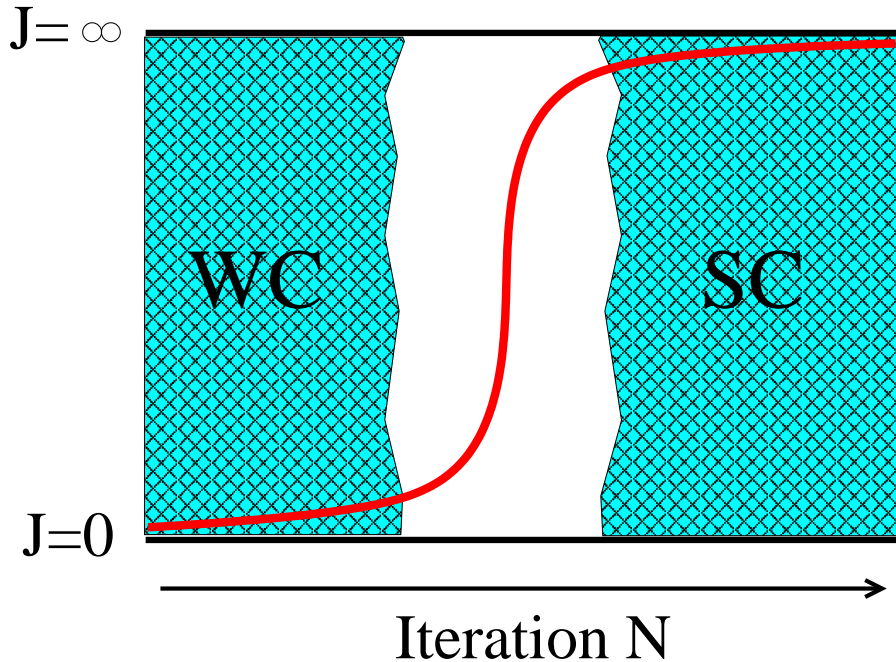


Figure 4.1: In the course of the iteration, i.e. with decreasing energies, the Kondo coupling J ‘flows’ from a small value [weak coupling (WC) regime] to a very big value [strong coupling (SC) regime], a behavior that was already indicated in Eq. (3.31). The shaded regions mark these two regimes. Especially the complicated crossover regime (white region) can only reliably be calculated via NRG.

In summary, the scheme provided by Wilson [46] relates effective Hamiltonians on successive energy scales [40] by a transformation R , $H_{N+1} = R[H_N]$. Due to the separation of energy scales Wilson showed that the Kondo problem can be solved by iterative perturbation theory [meaning the $(N + 1)$ -th site of the Wilson chain can be viewed as a small perturbation of \hat{H}_N].

As an example we shortly show the principle of the numerical procedure for $\hat{\mathcal{H}}_K$: the matrix that describes the initial Hamiltonian of the KM, \hat{H}_0 is a 8×8 matrix which consists of the impurity and the first site of the Wilson chain. We define the eight basis states of this matrix as product states of the two possible impurity states $|\uparrow\rangle$ and $|\downarrow\rangle$ and four possible electronic states at the first site of the Wilson chain $|0\rangle_0$, $f_{0\uparrow}^\dagger |0\rangle_0 = |\uparrow\rangle_0$, $f_{0\downarrow}^\dagger |0\rangle_0 = |\downarrow\rangle_0$

and $f_{0\uparrow}^\dagger f_{0\downarrow}^\dagger |0\rangle_0 = |\uparrow\downarrow\rangle_0$. An arbitrary state in the zeroth-iteration can thus be written as $|\Psi\rangle_0 = |i\rangle_0 |\sigma\rangle$, with $i \in \{0, \uparrow, \downarrow, \uparrow\downarrow\}$ and $\sigma = \{\uparrow, \downarrow\}$. In this basis spanning the Hilbert space \mathcal{H}_0 the Hamiltonian \hat{H}_0 takes the form

$$\hat{H}_0 = \begin{array}{c} |0\rangle |\uparrow\rangle \\ |\uparrow\rangle |\uparrow\rangle \\ |\downarrow\rangle |\uparrow\rangle \\ |\uparrow\downarrow\rangle |\uparrow\rangle \\ |0\rangle |\downarrow\rangle \\ |\uparrow\rangle |\downarrow\rangle \\ |\downarrow\rangle |\downarrow\rangle \\ |\uparrow\downarrow\rangle |\downarrow\rangle \end{array} \begin{pmatrix} 0 & 0 & 0 & 0 & 0 & 0 & 0 & 0 & 0 \\ 0 & \frac{1}{2}J & 0 & 0 & 0 & 0 & 0 & 0 & 0 \\ 0 & 0 & -\frac{1}{2}J & 0 & 0 & J & 0 & 0 & 0 \\ 0 & 0 & 0 & 0 & 0 & 0 & 0 & 0 & 0 \\ 0 & 0 & 0 & 0 & 0 & 0 & 0 & 0 & 0 \\ 0 & 0 & J & 0 & 0 & -\frac{1}{2}J & 0 & 0 & 0 \\ 0 & 0 & 0 & 0 & 0 & 0 & \frac{1}{2}J & 0 & 0 \\ 0 & 0 & 0 & 0 & 0 & 0 & 0 & 0 & 0 \end{pmatrix}.$$

We start the procedure by diagonalizing \hat{H}_0 , $\hat{H}_0 \rightarrow \hat{H}_0^d$. This is achieved by rotating \hat{H}_0 to a proper basis, $\mathcal{U}_0^T \hat{H}_0 \mathcal{U}_0 = \hat{H}_0^d$, where \mathcal{U}_0 is determined numerically. Since we are interested in the low-temperature properties of $\hat{\mathcal{H}}_K$, the eigenenergies of \hat{H}_0 are sorted with respect to increasing energy and in the course of the iteration only the low-energy states are kept. This sorting is important, as the size of the Hilbert-space grows as $\sim 4^N$, indicating that already after a few iterations the Hilbert space has to be truncated. Obviously *all* relevant operators one is interested in, in particular the fermionic operators acting on the zeroth site of the chain $f_{0\sigma}$, have to be transformed to this new basis as well and afterwards sorted w.r.t. increasing eigenenergies of \hat{H}_0 .

In this basis the matrix corresponding to \hat{H}_1 can easily be obtained by connecting the 0-th and 1-st site of the Wilson chain [Eq. (A.40)]

$$\hat{H}_1 = \begin{array}{c} |0\rangle_1 \\ |\uparrow\rangle_1 \\ |\downarrow\rangle_1 \\ |\uparrow\downarrow\rangle_1 \end{array} \begin{pmatrix} \sqrt{\Lambda} \hat{H}_0^d & \xi_0^K f_{0\uparrow}^{*\dagger} & \xi_0^K f_{0\downarrow}^{*\dagger} & 0 \\ \xi_0^K f_{0\uparrow}^* & \sqrt{\Lambda} \hat{H}_0^d & 0 & \xi_0^K f_{0\downarrow}^{*\dagger} \\ \xi_0^K f_{0\downarrow}^* & 0 & \sqrt{\Lambda} \hat{H}_0^d & -\xi_0^K f_{0\uparrow}^{*\dagger} \\ 0 & \xi_0^K f_{0\downarrow}^* & -\xi_0^K f_{0\uparrow}^* & \sqrt{\Lambda} \hat{H}_0^d \end{pmatrix},$$

with $f_{0\sigma}^* = \mathcal{U}_0^T f_{0\sigma} \mathcal{U}_0$. Note: (i) \hat{H}_0^d and $f_{0\sigma}^*$ are 8×8 matrices (from the Hilbert space \mathcal{H}_0), thus the Hilbert-space \mathcal{H}_1 corresponding to \hat{H}_1 has dimension 32. (ii) states including the first site of the Wilson chain are written as $|\Psi\rangle_1 = |i\rangle_1 |\Psi\rangle_0$, with $i \in \{0, \uparrow, \downarrow, \uparrow\downarrow\}$, or more general

$$|\Psi\rangle_{N+1} = |i\rangle_{N+1} |\Psi\rangle_N. \quad (4.2)$$

Analogously to above, we can now determine the eigenspectrum of \hat{H}_1 by diagonalizing \hat{H}_1 . Before we do so, however, we need to determine $f_{1\sigma}^\dagger$ which ensures that the iteration can be continued. In the original (undiagonalized) basis of the Hilbert space \mathcal{H}_1 these

operators are trivially given as

$$f_{1\sigma}^\dagger = \begin{matrix} |0\rangle_1 \\ |\uparrow\rangle_1 \\ |\downarrow\rangle_1 \\ |\uparrow\downarrow\rangle_1 \end{matrix} \begin{pmatrix} |0\rangle_1 & |\uparrow\rangle_1 & |\downarrow\rangle_1 & |\uparrow\downarrow\rangle_1 \\ 0 & 0 & 0 & 0 \\ \mathbb{1}\delta_{\sigma,\uparrow} & 0 & 0 & 0 \\ \mathbb{1}\delta_{\sigma,\downarrow} & 0 & 0 & 0 \\ 0 & -\mathbb{1}\delta_{\sigma,\downarrow} & \mathbb{1}\delta_{\sigma,\uparrow} & 0 \end{pmatrix}, \quad (4.3)$$

where $\mathbb{1}$ denotes 8×8 unit-matrices. This steps [diagonalization, sorting w.r.t. increasing eigenenergies, truncating, adding the next site of the Wilson chain, setting up the fermionic operator that acts on the 'new site' of the Wilson chain, see Eq. (4.3), diagonalization, ...] are repeated until the iteration converges.

Convergence can be checked in a flow diagram (see Fig. 4.2), where the lowest lying eigenstates of the system are plotted as a function of the iteration number. Once the strong coupling fixed point is reached the method has converged.

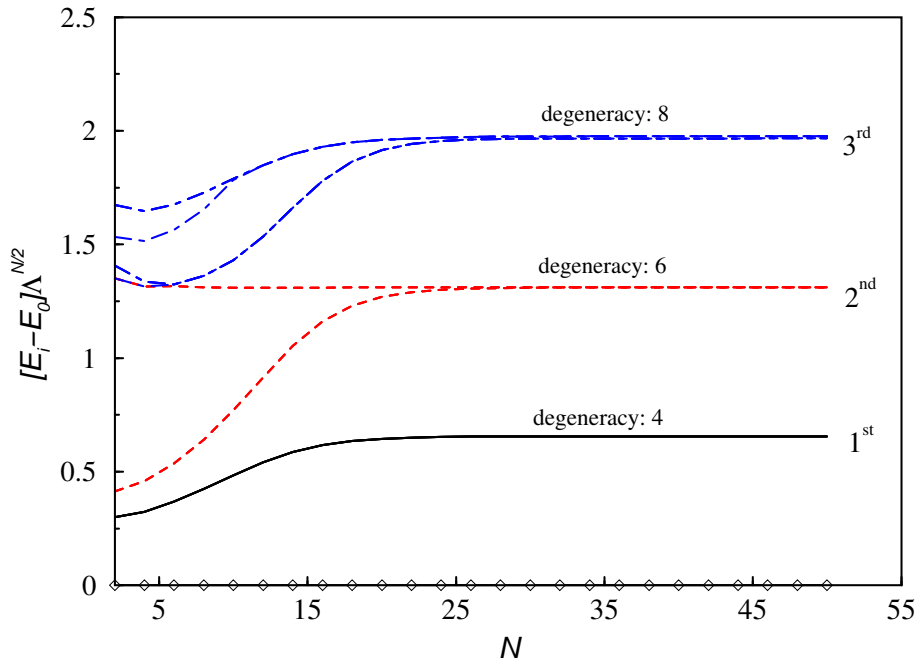


Figure 4.2: Eigenenergies (with corresponding degeneracy) of the KM as a function of the iteration N corresponding to an energy $\sim \Lambda^{-N/2}$. The energies of all levels are drawn with respect to the ground state energy (diamonds on x-axis) and are rescaled by $\Lambda^{N/2}$, as they are exponentially decreasing in the course of the iteration. After ~ 20 iterations the system flows to the strong coupling fixed point. The iteration converged after ~ 35 iterations. Parameters: $J = 0.25$, $\Lambda = 2$.

We would like to make a final remark here: as the size of the Hilbert-space grows

exponentially fast it is crucial to make use of the system's symmetries to speed up the numerical calculation, see Appendix C.

4.1 Physical quantities computed with NRG

There are two classes of quantities we are interested in: (i) thermodynamic quantities, obtained by properly averaging over a given operator, say \hat{A} , $\langle \hat{A} \rangle = \frac{1}{Z} \sum_m e^{-\beta E_m} \langle m | \hat{A} | m \rangle$.³ A typical example of this class is the impurity occupation $\hat{A} = \hat{n}$ (in case of the AM). As will be shown below, another thermodynamic quantity, the impurity specific heat $C_{\text{imp}}(T)$, requires not even the knowledge of matrix elements. (ii) Dynamic quantities, such as the spectral function $A(\omega, T)$, which are harder to compute since, additional to the task of calculating the corresponding energy spectrum and matrix elements of the involved operators, appearing δ -functions have to be combined and broadened properly (see Appendix B).

The energy-dependence (or alternatively temperature-dependence) of the quantities of interest enters via the iteration number N , as in the N -th step of the NRG-iteration physical quantities are computed at a typical energy $\omega_N \sim \Lambda^{-(N-1)/2} D$ (or temperature $k_B T_N \sim \Lambda^{-(N-1)/2} D$).

In contrast to zero-temperature calculations one has to *stop* the NRG-iteration at a specific iteration number in case of finite temperature calculations. Once ω_N reaches the scale $k_B T$, to be precise $k_B T = \frac{1}{2} (1 + \Lambda^{-1}) \Lambda^{-(N-1)/2}$, i.e. after N_T iterations

$$N_T = \left[1 - 2 \frac{\log\left(\frac{2k_B T}{1 + \Lambda^{-1}}\right)}{\log(\Lambda)} \right] \quad (4.4)$$

with $[\dots]$ denoting the integer function, the NRG-iteration has to be stopped. The reason for this is the following: for $N > N_T$ the typical energy scale ω_N is smaller than the thermal energy, i.e. relevant excitations of the system are *not* included any more since they have already been truncated.

4.1.1 Thermodynamic quantities

Using two specific examples we give a rough idea how to compute thermodynamic quantities in this Section.

The knowledge of the energy spectrum is already sufficient for the calculation of the impurity specific heat $C_{\text{imp}}(T)$, $C(T) = -T \frac{\partial^2}{\partial T^2} F(T)$ (with the total free energy of a canonical ensemble $F(T) = -k_B T \ln Z$). $C_{\text{imp}}(T)$ is obtained by subtracting the *free* electron specific heat (corresponding to $J = 0$, i.e. the specific heat in absence of the impurity) from the specific heat of the whole system [47]. This difference can be rewritten as [46]

$$C_{\text{imp}}(T) = \frac{d}{dT} \left[T^2 \frac{d}{dT} \lim_{N \rightarrow \infty} \left(\ln \text{tr}(e^{-\beta \Lambda^{-(N-1)/2} H_N(J)}) - \ln \text{tr}(e^{-\beta \Lambda^{-(N-1)/2} H_N(J=0)}) + \ln 2 \right) \right]$$

³ Z denotes the partition function $Z = \sum_m e^{-\beta E_m}$ with $\beta = (k_B T)^{-1}$.

$$= \frac{d}{dT} \left[T^2 \left(\frac{d \ln F_{imp}(T)}{d \ln T} \right) \right].$$

For the calculation of other thermodynamic quantities, such as the impurity occupation $\hat{n}_0 = \sum_{\sigma} d_{\sigma}^{\dagger} d_{\sigma}$, one has to implement the initial matrix elements of \hat{n}_0 as well. In case of a single-level AM \hat{n}_0 has the form

$$\hat{n}_0 = \begin{array}{c} |0\rangle \\ |\uparrow\rangle \\ |\downarrow\rangle \\ |\uparrow\downarrow\rangle \end{array} \begin{pmatrix} |0\rangle & |\uparrow\rangle & |\downarrow\rangle & |\uparrow\downarrow\rangle \\ \hline 0 & 0 & 0 & 0 \\ 0 & 1 \cdot \mathbb{1} & 0 & 0 \\ 0 & 0 & 1 \cdot \mathbb{1} & 0 \\ 0 & 0 & 0 & 2 \cdot \mathbb{1} \end{pmatrix}$$

where $\mathbb{1}$ denotes 4×4 unit matrices. Obviously \hat{n} has to be transformed in the same manner as the Hamiltonian in the course of the iteration. To finally obtain the expectation value $\langle \hat{n} \rangle$, one has to average over the eigenstates of the system, i.e. a knowledge of the eigenspectrum of \hat{H}_N and of the matrix elements of the operator \hat{n} (in the N -th iteration) is required.

Thermodynamic quantities can be computed rather accurately (more accurate than dynamic quantities, see Section 4.1.2), since they are obtained from the low-energy part of the spectrum (where NRG has, by construction, its highest resolution).

Indeed, a careful comparison of the gate voltage dependence of the zero-temperature occupation between the NRG and the Bethe-Ansatz solution (an analytic exact solution of the problem) allows for an accuracy check of the numerics. In Fig. 4.3(left panel) we plot the local level occupation $n \equiv \langle \hat{n} \rangle$ (for $T = 0$) for a single-level AM as a function of ϵ_d once computed via Bethe-Ansatz [49, 50] and once computed via NRG (see also [33]). We find perfect agreement between both methods.

In contrast to Bethe-Ansatz, however, NRG allows us to study the QD occupation as a function of decreasing temperature as well. Fig. 4.3(right panel) shows how the QD occupation evolves upon lowering the temperature. As already mentioned, in the limit of small temperatures three regimes can be identified (EO: $|n - 1| \sim 1$, MV: $|n - 1| \sim 0.5$, LMR: $|n - 1| \sim 0$).

For $T = 0$ the impurity occupation can be used to compute the phase shift $\Delta\phi_{\sigma}$ a spin σ electron experiences when being scattered off the magnetic impurity, $\Delta\phi_{\sigma} = n_{\sigma}\pi$, known as the Friedel-sum rule [21]. For $T = 0$ a relation between $\Delta\phi_{\sigma}$ and the conductance holds [$G_{\sigma} \sim \sin^2(\Delta\phi_{\sigma})$] which is based on Fermi liquid theory. This relation allows one to determine the conductance G from the knowledge of the occupation of the impurity.

4.1.2 Dynamic quantities: $A(\omega, T)$ and $\chi''(\omega, T)$

Dynamic quantities are harder to compute than thermodynamic ones since they are energy and temperature dependent. Nevertheless we are interested in those quantities, since in most experiments transport properties instead of thermodynamic properties are measured. Transport properties can typically be expressed via a function L_{ml} , $m, l \in \mathbb{Z}$, where

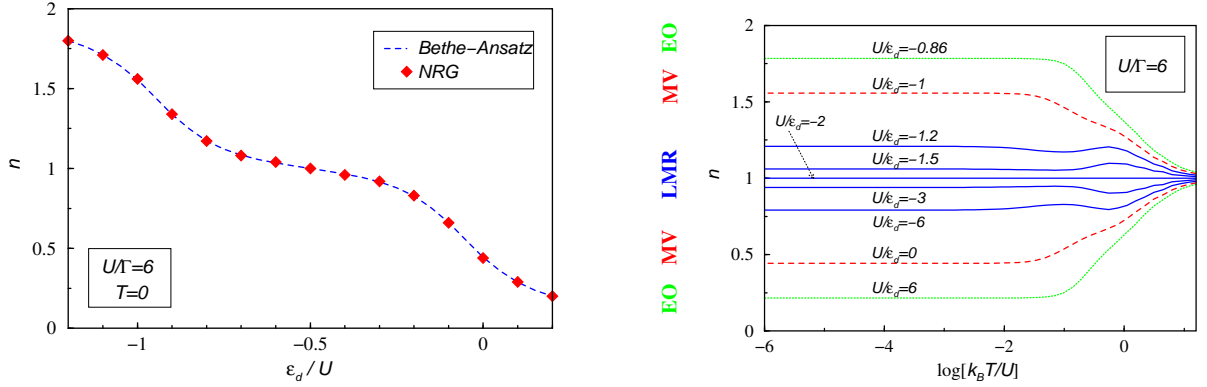


Figure 4.3: Left: Gate voltage dependence of the local occupation n of a single-level AM. We find excellent agreement between the exact Bethe-Ansatz solutions [49, 50] and NRG-calculations, indicating the high accuracy of the numerics. The right panel shows the three possible QD regimes: the Local-moment-regime (LMR) ($n \approx 1$), where Kondo correlations can exist (see also the 'Kondo plateau' in the left panel), the mixed valence (MV) regime ($|n - 1| \approx \frac{1}{2}$) and the empty orbital (EO) regime where the QD is either empty or doubly occupied. For temperatures smaller $\sim 0.01U$ the system reaches the strong coupling limit. Note the particle-hole symmetry around $\epsilon_d = -U/2$. Parameters: $U = 0.12D$, $\Lambda = 2$.

$L_{ml} \propto \int \frac{\partial f}{\partial \omega} \tau^l \omega^m d\omega$ (f labels the Fermi-function of the leads). Examples are the resistivity $\rho(T) = \frac{1}{e^2} L_{01}$ or the thermopower $S(T) = -\frac{1}{eT} \frac{L_{11}}{L_{01}}$.

As such integrals depend crucially on the lifetime $\tau(\omega, T)^{-1} \sim A(\omega, T)$ [51], a good knowledge of the system's spectral function $A(\omega, T)$ is essential to compute transport properties of a given system. Another important dynamical quantity is the spin spectral function $\chi''(\omega, T)$.

Consequently, we introduce these two important dynamical quantities, $A(\omega, T)$ and $\chi''(\omega, T)$ in this Section.

The spectral function $A(\omega, T)$ is defined as

$$A(\omega, T) = -\frac{1}{\pi} \Im [\mathcal{G}^R(\omega, T)], \quad (4.5)$$

where $\mathcal{G}^R(\omega, T)$ is the Fourier-transformed⁴ of the retarded Green's function $\mathcal{G}^R(t, T) \equiv -i\theta(t)\langle\{d(t), d^\dagger(0)\}\rangle$. Obviously the calculation of $A(\omega, T)$ requires the determination of the matrix elements of d . Consequently one has to implement the matrix elements of the operator d in the zeroth step of the NRG-iteration, d_0 .

For arbitrary temperatures the retarded Green's function can be written (in Lehmann representation) as

$$\mathcal{G}^R(t, T) = -i\theta(t) \sum_{nm} \frac{e^{-\beta E_n} + e^{-\beta E_m}}{Z(\beta)} \langle n| d(t) |m\rangle \langle m| d^\dagger |n\rangle, \quad (4.6)$$

⁴ $\mathcal{G}^R(\omega, T) = \int_{-\infty}^{\infty} dt e^{i\omega t} \mathcal{G}^R(t, T)$

where $Z(\beta) = \sum_i e^{-\beta E_i}$ denotes the partition function and $|n\rangle$ an eigenstate with corresponding eigenenergy E_n of \hat{H} .

When we insert the time evolution⁵ $d(t) = e^{i\hat{H}t}d(0)e^{-i\hat{H}t}$ into Eq. (4.6) and finally perform the Fourier transformation we arrive at the spectral function [51]

$$A(\omega, T) = \sum_{nm} \frac{e^{-\beta E_n} + e^{-\beta E_m}}{Z(\beta)} |\langle m | d^\dagger | n \rangle|^2 \delta(\omega - (E_m - E_n)). \quad (4.7)$$

In particular, the $T = 0$ limit (in which we are mostly interested in) can easily be obtained from Eq. (4.7),

$$A(\omega, T = 0) = \overbrace{\sum_n |\langle n | d^\dagger | 0 \rangle|^2 \delta(\omega - (E_n - E_0))}^{\omega > 0} + \overbrace{\sum_n |\langle 0 | d^\dagger | n \rangle|^2 \delta(\omega - (E_0 - E_n))}^{\omega < 0}, \quad (4.8)$$

where $|0\rangle$ denotes the ground state of the system. As finite temperature spectral functions $A(\omega, T)$ involve transitions between excited states $|\langle m | d^\dagger | n \rangle|^2$, they are more difficult to calculate than $A(\omega, T = 0)$ (see e.g. Fig. B.1). We already pointed out in Eq. (4.4) that it is crucial to stop the iteration after N_T steps when one is interested in a finite temperature calculation.

In Fig. 4.4 we plot the (properly renormalized) spectral function $A(\omega, T = 0)$ for different values of ϵ_d for a single-level AM obtained from NRG. The accuracy of the numerics can be checked by comparing the numerically obtained value of $A(\omega = 0, T = 0)$ with that known from the Friedel-sum-rule [21], $A(0, 0) = \frac{\sin^2(\pi n/2)}{\pi\Gamma/4}$ [with $n = \sum_\sigma \langle d^\dagger_\sigma d_\sigma \rangle$; here we took $\Gamma_\sigma = \frac{1}{2}\Gamma$ and $n_\sigma = \frac{1}{2}n$ (since $B = 0$)]. A further check of the numerical accuracy of the calculation of the spectral function $A(\omega, T = 0)$ can be achieved by comparing its integrated weight $\int_{-\infty}^0 d\omega A(\omega, T = 0)$ with the thermodynamically calculated occupation n . As high energy features in $A(\omega, T = 0)$ are dominantly responsible for the occupation obtained via $\int_{-\infty}^0 d\omega A(\omega, T = 0)$, we do not expect a perfect agreement between $\int_{-\infty}^0 d\omega A(\omega, T = 0)$ and n . Remember that the NRG-method is designed to describe low-energy properties of the system accurately. A trick due to Bulla [52], that involves the self-energy of the AM, can slightly cure this problem.

In the Kondo regime, the spectral function shows a three peak structure: (i) two atomic resonances of width $\sim \Gamma$ near ϵ_d and $\epsilon_d + U$ and (ii) the Kondo resonance of width $\sim T_K$ (pinned at the Fermi energy). It was already pointed out before that a finite magnetic field of strength $B \lesssim T_K$ leads to a suppression and splitting of the Kondo resonance. An even bigger magnetic field completely destroys the Kondo effect. As shown by Hofstetter [4], the 'traditional' NRG-procedure has even to be changed for $B \neq 0$. In this case the "density-matrix NRG" (DM-NRG) method should be used. A detailed description of the DM-NRG-method is given in Appendix D.

⁵Here the time evolution operator has the form $\hat{U}(t, 0) = e^{-\frac{i}{\hbar}\hat{H}t}$.

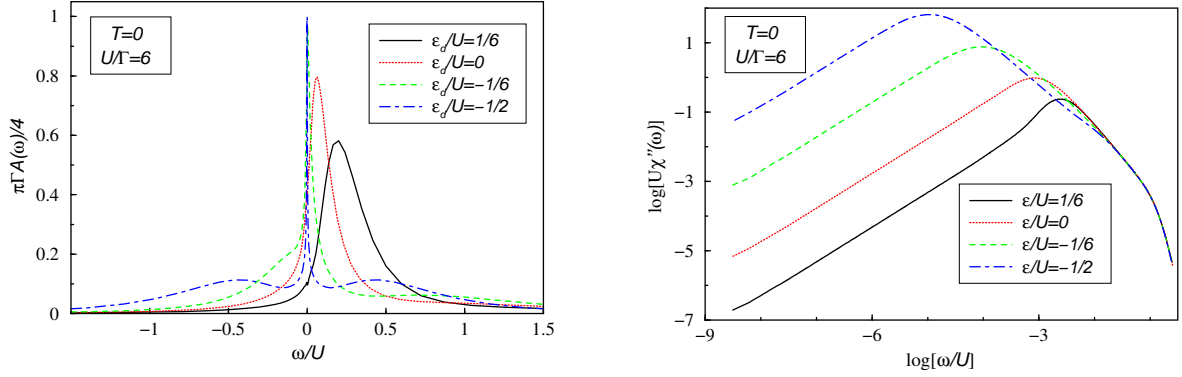


Figure 4.4: Left: Spectral function $A(\omega, T = 0)$ for different values of ϵ_d . The Kondo resonance (of width $\sim T_K$) can be nicely seen for that values of ϵ_d (namely $\epsilon_d = -U/6$ and $\epsilon_d = -U/2$) where the impurity is roughly singly occupied, i.e. in the LMR. Note that the Friedel-sum rule [21] is fulfilled extremely well (with a deviation less than 3%). Additional side peaks of width Γ appear in the spectral function which are due to the discrete (atomic) levels at ϵ_d and $\epsilon_d + U$. Right: Spin spectral function χ'' for the same values of ϵ_d as in the left panel. The maximum in $\chi''(\omega, T = 0)$ appears at a frequency $\omega \sim T_K$ (given the Kondo effect exists); for frequencies below T_K the system behaves like a Fermi liquid, i.e. $\chi''(\omega, T = 0) \propto \omega$.

In some cases, e.g. when one is interested in the transmission phase shift $\phi(\omega, T)$, $\tan[\phi(\omega, T)] = \frac{\Im[\mathcal{G}^R(\omega, T)]}{\Re[\mathcal{G}^R(\omega, T)]}$, it is necessary to calculate *both* the imaginary part $\Im[\mathcal{G}^R(\omega, T)]$ and the real part $\Re[\mathcal{G}^R(\omega, T)]$ of \mathcal{G}^R . For causal functions, such as the retarded Green's function, this can be achieved by a Kramers-Kronig transformation [7], see Appendix E.

The spin susceptibility $\chi(t) = \chi'(t) + i\chi''(t)$, a second dynamic quantity we briefly want to explain here, describes the response of a system, which is a magnetization $\vec{m}(t)$ at a time t , after a magnetic field $\vec{h}(0)$ was applied at $t = 0$

$$\vec{m}(t) = \chi(t, 0)\vec{h}(0). \quad (4.9)$$

It was pointed out before, that it is convenient to define T_K as the maximum of the spin susceptibility $\chi''(\omega)$ [29], see Fig. 4.4.

In linear response theory the spin susceptibility is given by $\chi(t) \equiv i\theta(t)\langle[\hat{S}_{imp}^z(t), \hat{S}_{imp}^z(0)]\rangle$. For a single-level AM S_{imp}^z has the following matrix elements in the zeroth iteration

$$(S_{imp}^z)_0 = \begin{matrix} & |0\rangle & |\uparrow\rangle & |\downarrow\rangle & |\uparrow\downarrow\rangle \\ \begin{matrix} |0\rangle \\ |\uparrow\rangle \\ |\downarrow\rangle \\ |\uparrow\downarrow\rangle \end{matrix} & \begin{pmatrix} 0 & 0 & 0 & 0 \\ 0 & \frac{1}{2} \cdot \mathbb{1} & 0 & 0 \\ 0 & 0 & -\frac{1}{2} \cdot \mathbb{1} & 0 \\ 0 & 1 & 0 & 0 \end{pmatrix} \end{matrix}.$$

When we write $\chi(t)$ in Lehmann representation, achieved by inserting a complete set of states, we obtain (for $t > 0$ and $T = 0$):

$$\chi(t) = i \sum_n \langle 0 | e^{i\hat{H}t} \hat{S}_{imp}^z e^{-i\hat{H}t} | n \rangle \langle n | \hat{S}_{imp}^z | 0 \rangle = i \sum_n |\langle n | S_{imp}^z | 0 \rangle|^2 e^{i(E_0 - E_n)t}.$$

Its Fourier-transformed then takes the form

$$\begin{aligned} \chi(\omega) &= i \sum_n |\langle n | S_{imp}^z | 0 \rangle|^2 \lim_{\eta \rightarrow 0^+} \int_0^\infty e^{i[\omega - (E_n - E_0) + i\eta]t} dt = \\ &= i^2 \sum_n |\langle n | S_{imp}^z | 0 \rangle|^2 \left[\mathcal{P} \left(\frac{1}{\omega - (E_n - E_0)} \right) - i\pi \delta(\omega - (E_n - E_0)) \right]. \end{aligned}$$

Thus the $T = 0$ spin-susceptibility $\chi''(\omega)$ has the form

$$\chi''(\omega) = \pi \sum_n |\langle n | S_{imp}^z | 0 \rangle|^2 \delta(\omega - (E_n - E_0)). \quad (4.10)$$

To summarize: additional to the knowledge of the eigenstates $|n\rangle$ (with corresponding eigenenergies E_n) and matrix elements (e.g. $\langle n | S_{imp}^z | 0 \rangle$) of a system, the computation of a dynamical quantity involves a (proper) broadening of appearing δ -functions. In Appendix B we focus on this issue.

Part II

NRG-studies of Quantum Impurity Models

Chapter 5

QDs coupled to ferromagnetic leads

In Chapter 2 we stressed that lateral semiconductor QDs, commonly used in transport experiments, are defined by depleting a 2DEG (via negatively charged gates). An example of such a structure is shown in Fig. 5.1(left panel). In absence of an external magnetic field the local interacting region, the source and the drain region (all these regions consist of the *same* material) do not have a preferred spin direction, i.e. they are unpolarized. Consequently, for $B = 0$ the electrons of the leads screen a localized spin in the QD for $T < T_K$. As explained in Chapter 3 this results in an enhanced linear conductance (due to the Kondo resonance in the local DoS).

Leads that consist of one spin species only (half-metallic leads), are obviously *not* able to screen a local moment, no Kondo correlations can develop in this scenario. This way of thought brings one to an interesting theoretical question, namely whether Kondo correlations do exist for a local moment which is coupled to a reservoir with a finite spin polarization (partially polarized leads). In this scenario it is not obvious what kind of consequences the leads' polarization on the Kondo effect has.

Experimentally the idea of contacting a QD to a lead that consists of a different material than the QD itself came into reach when Liang *et al.* [53] managed to contact a divanadium-molecule (serving as QD) to gold electrodes, see Fig. 5.1(right panel). Usually the contacting between the QD and its surrounding leads is rather difficult. In conductance experiments through this device, however, the Kondo effect was observed, indicating that Liang *et al.* managed to realize a sufficiently good contact between the molecule and its leads. If one replaced the gold electrodes by manganese, the model we are studying in this chapter would be realized.

In the following papers [15, 54] we discuss the effect of a finite spin polarization in the leads on the Kondo resonance. In Section 5.1 we study the consequence of a finite leads polarization $P \neq 0$ on Kondo physics (with fixed gate voltage ϵ_d). It turns out that a finite spin polarization $P \neq 0$ results in a splitting and a suppression of the Kondo resonance.

In Section 5.2 we address the question how the splitting of the Kondo resonance varies upon changing ϵ_d for QDs coupled to leads with a 'realistic' DoS. We find a strong gate voltage dependence of the splitting of the Kondo resonance that depends crucially on the particular band-structure in the leads. Surprisingly the suppression and splitting of the

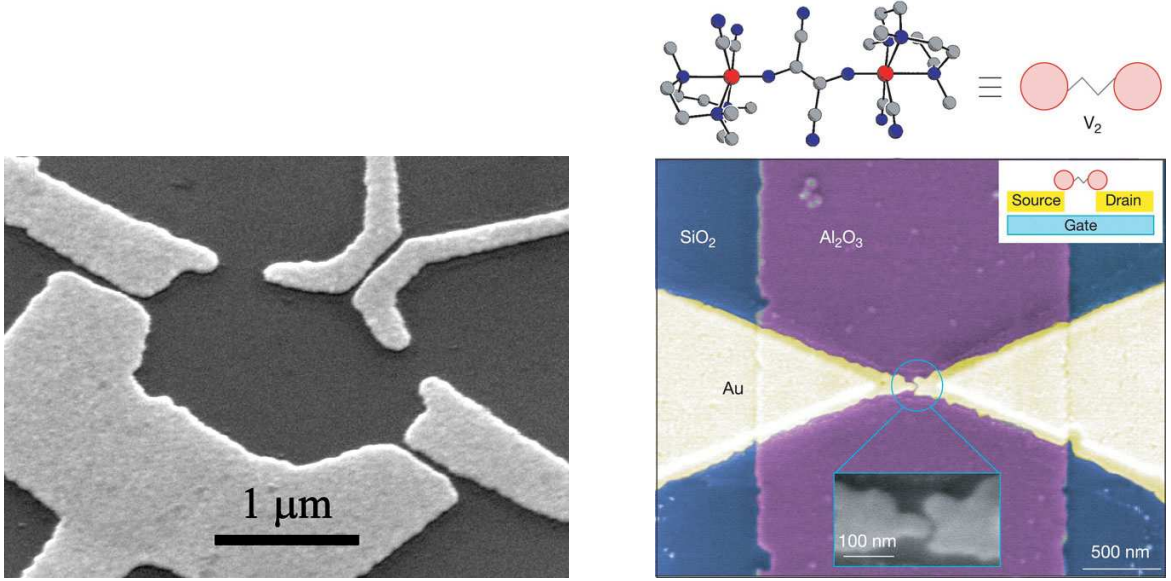


Figure 5.1: Left: 'Traditional' way of realizing a QD, coupled to leads which consist of the same material as the QD itself (Photo from: <http://www.unibas.ch/phys-meso/>). Right: Liang *et al.* [53] managed to contact a divanadium-molecule, depicted above the image, to gold contacts. This opens up the exciting possibility to contact QDs to *arbitrary* leads.

Kondo resonance, which usually appears in case of a QD contacted to polarized leads, can be compensated by an appropriately tuned gate voltage ϵ_d .

5.1 Effect of a finite spin polarization in the leads on the Kondo resonance

In this Section we study the effect of a finite spin polarization P in the leads on the Kondo resonance. To ensure that the QD is in the local moment regime, i.e. it is roughly singly occupied, we fix the gate voltage at $\epsilon_d = -U/3$ throughout this study.

We assume the DoS in the leads ρ_σ to be flat and normalized $\sum_\sigma \int_{-D_0}^{D_0} \rho_\sigma d\omega = 1$ but *spin-dependent*, as shown in Fig. 5.2(left panel).¹ Correspondingly, the spin polarization P of the leads is determined by the DoS at the Fermi energy $P = \frac{\rho_\uparrow(E_F) - \rho_\downarrow(E_F)}{\rho_\uparrow(E_F) + \rho_\downarrow(E_F)}$. For flat bands, as considered here, the full information about spin asymmetry in the leads can be parameterized by a *spin-dependent* hybridization function $\Gamma_\sigma \equiv \frac{1}{2}\Gamma(1 \pm P)$.² Based on second order perturbation theory in the tunneling one expects a *spin-dependent* shift and

¹Here we disregard an additional spin splitting at the edge of the bands (Stoner-splitting), which leads to a logarithmically suppressed effective magnetic field.

² $\sigma = \uparrow (\downarrow)$ corresponds to $+(-)$.

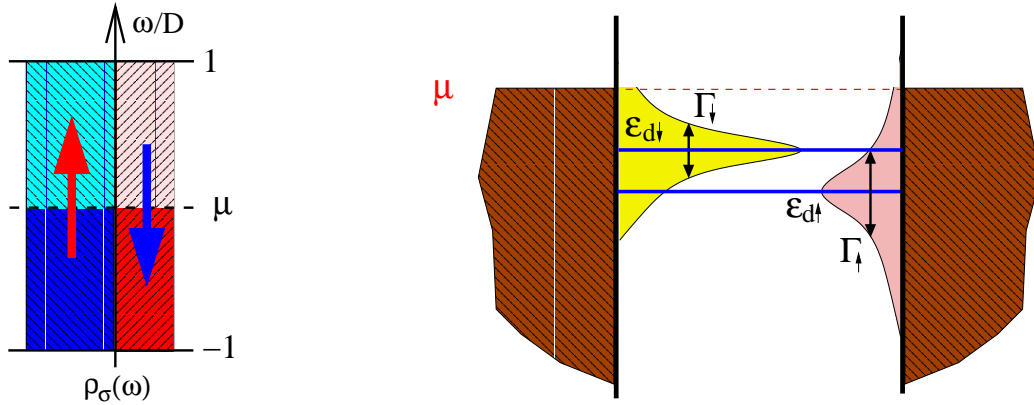


Figure 5.2: Left: Spin-resolved leads DoS $\rho_\sigma(\omega)$ ($\omega \in [-D; D]$) for a flat band with $P > 0$. The imbalance of available \uparrow - and \downarrow -electron states determines the spin polarization P of the leads. Right: The cartoon illustrates the consequence of a finite spin polarization in the leads, namely a spin splitting of the local level $\epsilon_{d\sigma}$ (here: $P > 0$ and $\epsilon_d > -U/2$).

consequently a spin splitting of the local level³ for a finite spin polarization of the leads ($P \neq 0$), see Fig. 5.2(right panel). Consequently one expects the Kondo resonance of a QD contacted to spin polarized leads to be suppressed and split, similar to a QD in presence of a magnetic field.

Below we present a careful NRG-study of the problem outlined above. We find that the full Kondo resonance of a QD that is coupled to spin polarized leads can be recovered (with a reduced value of T_K) given an appropriately tuned external magnetic field is applied.

³For $\epsilon_d \neq -U/2$ and $\Gamma_\uparrow \neq \Gamma_\downarrow$ one expects a spin-dependent shift of the local level $\delta\epsilon_{d\sigma}$, $\delta\epsilon_{d\uparrow} \sim \frac{\Gamma_\downarrow}{\epsilon_d+U} - \frac{\Gamma_\uparrow}{\epsilon_d} \neq \frac{\Gamma_\uparrow}{\epsilon_d+U} - \frac{\Gamma_\downarrow}{\epsilon_d} \sim \delta\epsilon_{d\downarrow}$.

Kondo Effect in the Presence of Itinerant-Electron Ferromagnetism Studied with the Numerical Renormalization Group Method

J. Martinek,^{1,4} M. Sindel,² L. Borda,^{2,3} J. Barnaś,^{4,5} J. König,^{1,6} G. Schön,¹ and J. von Delft²

¹*Institut für Theoretische Festkörperphysik, Universität Karlsruhe, 76128 Karlsruhe, Germany*

²*Sektion Physik and Center for Nanoscience, LMU München, Theresienstrasse 37, 80333 München, Germany*

³*Hungarian Academy of Sciences, Institute of Physics, TU Budapest, H-1521, Hungary*

⁴*Institute of Molecular Physics, Polish Academy of Sciences, 60-179 Poznań, Poland*

⁵*Department of Physics, Adam Mickiewicz University, 61-614 Poznań, Poland*

⁶*Institut für Theoretische Physik III, Ruhr-Universität Bochum, 44780 Bochum, Germany*

(Received 15 April 2003; published 10 December 2003)

The Kondo effect in quantum dots (QDs)—artificial magnetic impurities—attached to ferromagnetic leads is studied with the numerical renormalization group method. It is shown that the QD level is spin split due to the presence of ferromagnetic electrodes, leading to a suppression of the Kondo effect. We find that the Kondo effect can be restored by compensating this splitting with a magnetic field. Although the resulting Kondo resonance then has an unusual spin asymmetry with a reduced Kondo temperature, the ground state is still a locally screened state, describable by Fermi liquid theory and a generalized Friedel sum rule, and transport at zero temperature is spin independent.

DOI: 10.1103/PhysRevLett.91.247202

PACS numbers: 75.20.Hr, 72.15.Qm, 72.25.-b, 73.23.Hk

The prediction [1] and experimental observation of the Kondo effect in artificial magnetic impurities—semiconducting quantum dots (QDs) [2,3]—renewed interest in the Kondo effect and opened new opportunities of research. The successful observation of the Kondo effect in molecular QDs such as carbon nanotubes [4,5] and single molecules [6] attached to metallic electrodes opened the possibility to study the influence of many-body correlations in the leads (superconductivity [7] or ferromagnetism) on the Kondo effect. Recently, the question arose whether the Kondo effect in a QD attached to ferromagnetic leads can occur or not. Several authors have predicted [8–11] that the Kondo effect should occur. However, it was shown recently [12] that the QD level will be spin split due to the presence of ferromagnetic electrodes leading to a suppression of the Kondo effect, and that the Kondo resonance can be restored only by applying an external magnetic field. The analyses of Refs. [8–12] were all based on approximate methods.

In this Letter, we resolve the controversy by adapting the numerical renormalization group (NRG) technique [13,14], one of the most accurate methods available to study strongly correlated systems in the Kondo regime, to the case of a QD coupled to ferromagnetic leads with parallel magnetization directions. We find that, in general, the Kondo resonance is split, similar to the usual magnetic-field-induced splitting [15,16]. However, we find that, by appropriately tuning an external magnetic field, this splitting can be fully compensated and the Kondo effect can be restored [17] (confirming Ref. [12]). We point out that precisely at this field the occupancy of the local level is the same for spin-up and -down, $n_{\uparrow} = n_{\downarrow}$, a fact that follows from the Friedel sum rule [19]. Moreover, we show that the Kondo effect then has unusual properties such as a strong spin polarization of the Kondo

resonance and, just as for ferromagnetic materials, for the density of states (DOS). Nevertheless, despite the spin asymmetries in the DOS of the QD and the leads, the symmetry in the occupancy $n_{\uparrow} = n_{\downarrow}$ implies that the system's ground state can be tuned to have a fully compensated local spin, in which case the QD conductance is found to be the *same* for each spin channel, $G_{\uparrow} = G_{\downarrow}$.

The model.—For ferromagnetic leads, electron-electron interactions in the leads give rise to magnetic order and spin-dependent DOS $\rho_{r\uparrow}(\omega) \neq \rho_{r\downarrow}(\omega)$, ($r = L, R$). Magnetic order of typical band ferromagnets such as Fe, Co, and Ni is mainly related to electron correlation effects in the relatively narrow $3d$ subbands, which only weakly hybridize with $4s$ and $4p$ bands [20]. We can assume that, due to a strong spatial confinement of d electron orbitals, the contribution of electrons from d subbands to transport across the tunnel barrier can be neglected [21]. In such a situation, the system can be modeled by noninteracting [22] s electrons, which are spin polarized due to the exchange interaction with uncompensated magnetic moments of the completely localized d electrons. In the mean-field approximation, one can model this exchange interaction as an effective molecular field, which removes spin degeneracy in the system of noninteracting conducting electrons, leading to a spin-dependent DOS. The Anderson model (AM) for a QD with a single energy level ϵ_d , which is coupled to ferromagnetic leads, is given by

$$\tilde{H} = \sum_{rk\sigma} \epsilon_{rk\sigma} c_{rk\sigma}^{\dagger} c_{rk\sigma} + \epsilon_d \sum_{\sigma} \hat{n}_{\sigma} + U \hat{n}_{\uparrow} \hat{n}_{\downarrow} + \sum_{rk\sigma} (V_{r,k} d_{\sigma}^{\dagger} c_{r,k\sigma} + V_{r,k}^{*} c_{r,k\sigma}^{\dagger} d_{\sigma}) - g \mu_B B S_z. \quad (1)$$

Here $c_{rk\sigma}$ and d_{σ} ($\hat{n}_{\sigma} = d_{\sigma}^{\dagger} d_{\sigma}$) are the Fermi operators for

electrons with momentum k and spin σ in the leads and, in the QD, V_{rk} is the tunneling amplitude, $S_z = (\hat{n}_\uparrow - \hat{n}_\downarrow)/2$, and the last term is the Zeeman energy of the dot. All information about spin asymmetry in the leads can be modeled by the spin-dependent hybridization function $\Gamma_{r\sigma}(\omega) = \pi \sum_k \delta(\omega - \epsilon_{k\sigma}) V_{r,k}^2 = \pi \rho_{r\sigma}(\omega) V_r^2$, where $V_{r,k} \equiv V_r$ and $\rho_{r\sigma}(\omega)$ is the spin-dependent DOS.

In order to understand the Kondo physics of a QD attached to two identical ferromagnetic electrodes with parallel configurations, it suffices to study, instead of the above general model [Eq. (1)], a simpler one, which captures the same essential physics, namely, the fact that $\Gamma_{r\uparrow}(\omega) \neq \Gamma_{r\downarrow}(\omega)$ will generate an effective local magnetic field, which lifts the degeneracy of the local level (even for $B = 0$). A simple (but not unique) way of modeling this effect is to take the DOS in the leads to be constant and spin independent, $\rho_{r\sigma}(\omega) \equiv \rho$, the bandwidths to be equal $D_\uparrow = D_\downarrow$, and lump all spin dependence into the spin-dependent hybridization function, $\Gamma_{r\sigma}(\omega)$, which we take to be ω independent, $\Gamma_{r\sigma}(\omega) \equiv \Gamma_{r\sigma}$. By means of a unitary transformation [1], the AM [Eq. (1)] can be mapped onto a model in which the correlated QD level couples only to one electron reservoir described by Fermi operators $\alpha_{k\sigma}$ with strength $\Gamma_\sigma = \sum_r \Gamma_{r\sigma}$:

$$H = \sum_{k\sigma} \epsilon_k \alpha_{k\sigma}^\dagger \alpha_{k\sigma} + \epsilon_d \sum_\sigma \hat{n}_\sigma + U \hat{n}_\uparrow \hat{n}_\downarrow + \sum_{k\sigma} \sqrt{\Gamma_\sigma / (\pi\rho)} (d_\sigma^\dagger \alpha_{k\sigma} + \alpha_{k\sigma}^\dagger d_\sigma) - g \mu_B B S_z. \quad (2)$$

Finally, we parametrize the spin dependence of Γ_σ in terms of a spin-polarization parameter $P \equiv (\Gamma_\uparrow - \Gamma_\downarrow)/\Gamma$, by writing $\Gamma_{\uparrow(\downarrow)} \equiv \frac{1}{2}\Gamma(1 \pm P)$, where $\Gamma \equiv \Gamma_\uparrow + \Gamma_\downarrow$.

In the model of Eq. (2), we allowed for $\Gamma_\uparrow \neq \Gamma_\downarrow$ but not for $D_\uparrow \neq D_\downarrow$, as would be appropriate for real ferromagnets, whose spin-up and -down bands always have a Stoner splitting $\Delta D \equiv D_\uparrow - D_\downarrow$, with typical values $\Delta D/D_\uparrow \lesssim 20\%$ (for Ni, Co, and Fe). However, no essential physics is thereby lost, since the consequence of taking $D_\uparrow \neq D_\downarrow$ is the same as that of taking $\Gamma_\uparrow \neq \Gamma_\downarrow$, namely, to generate an effective local magnetic field [25].

The occurrence of the Kondo effect requires spin fluctuations in the dot as well as zero-energy spin-flip excitations in the leads. Indeed, a Stoner ferromagnet without full spin polarization $-1 < P < 1$ provides zero-energy Stoner excitations [26], even in the presence of an external magnetic field.

Method.—The model [Eq. (2)] can be treated by Wilson's NRG method. This method, with recent improvements related to high-energy features and finite magnetic field [15,16], is a well-established method to study the Kondo impurity (QD) physics. It allows one to calculate the level occupation $n_\sigma \equiv \langle \hat{n}_\sigma \rangle$ (a static property), the QD spin spectral function, $\text{Im} \chi_s^z(\omega) = \mathcal{F}\{i\Theta(t)\langle [S_z(t), S_z(0)] \rangle\}$, where \mathcal{F} denotes the Fourier transform, and the spin-resolved single-particle spectral

density $A_\sigma(\omega, T, B, P) = -\frac{1}{\pi} \text{Im} \mathcal{G}_{d,\sigma}^R(\omega)$ for arbitrary temperature T , magnetic field B , and polarization P [where $\mathcal{G}_{d,\sigma}^R(\omega)$ denotes a retarded Green function]. From this we can find the spin-resolved conductance $G_\sigma = (e^2/\hbar)(2\lambda)/(\lambda+1)^2 \Gamma_\sigma \int_{-\infty}^{\infty} d\omega A_\sigma(\omega) \times \{-\partial f(\omega)/\partial \omega\}$, where $f(\omega)$ is the Fermi function and $\lambda = \Gamma_{L\sigma}/\Gamma_{R\sigma}$ denotes the coupling asymmetry. We choose $\lambda = 1$ below.

Generation and restoration of spin splitting.—In this Letter, we focus exclusively on the properties of the system at $T = 0$ in the local moment regime, where the total occupancy of the QD, $n = \sum_\sigma n_\sigma \approx 1$. The occurrence of charge fluctuations broadens and shifts the position of the QD levels (for both spin-up and -down), and, hence, changes their occupation. For $P \neq 0$, the charge fluctuations and, hence, level shifts and level occupations become *spin dependent*, causing the QD level to split [12] and the dot magnetization $n_\uparrow - n_\downarrow$ to be finite (Fig. 1). As a result, the Kondo resonance is also spin split [28,29] and weakened (Fig. 2), similarly to the effect of an applied magnetic field [15,16]. This means that Kondo correlations are reduced or even suppressed in the presence of ferromagnetic leads. However, for any fixed P , it is possible to compensate the splitting of the Kondo resonance [Figs. 2(c) and 3(c)] by fine-tuning the magnetic field to an appropriate value, $B_{\text{comp}}(P)$, defined as the field which maximizes the height of the Kondo resonance. This field is found to depend linearly [27] on P [Fig. 1(c)] (as predicted in [12] for $U \rightarrow \infty$). Remarkably, we also find (throughout the local moment regime) that at B_{comp} the local occupancies satisfy $n_\uparrow = n_\downarrow$ [Fig. 1(b)]. The fact that this occurs simultaneously with the disappearance of the Kondo resonance splitting suggests that the local spin is fully screened at B_{comp} .

Spectral functions.—We henceforth fix the magnetic field at $B = B_{\text{comp}}(P)$. To learn more about the properties of the corresponding ground state, we computed the spin spectral function $\text{Im}\{\chi_s^z(\omega)\}$ for several values of P at $T = 0$ (Fig. 3). Its behavior is characteristic for the formation of a local Kondo singlet: As a function of decreasing frequency, the spin spectral function shows a

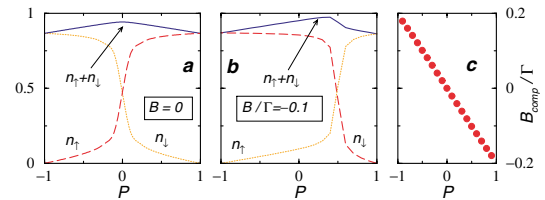


FIG. 1 (color online). Spin-dependent occupation of the dot level at (a) $B = 0$ and (b) $B = -0.1\Gamma$, as a function of spin polarization P . (a) For $B = 0$, the condition $n_\uparrow = n_\downarrow$ holds only at $P = 0$. (b) For finite P , it can be satisfied if a finite, fine-tuned magnetic field, $B_{\text{comp}}(P)$, is applied, whose dependence on P is shown in (c). As expected, it is approximately linear [12,27]. Here $U = 0.12D$, $\epsilon_d = -U/3$, $\Gamma = U/6$, and $T = 0$.

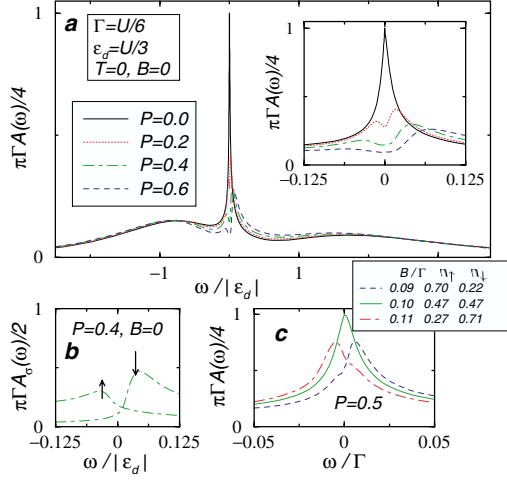


FIG. 2 (color online). (a) QD spectral function $A(\omega) = \sum_\sigma A_\sigma(\omega)$ for several values of spin polarization P ; inset: expanded scale of $A(\omega)$ around ϵ_F . (b) The spin-resolved spectral function for fixed P . For $P \rightarrow -P$, we have $A_\sigma \rightarrow A_{-\sigma}$. (c) Compensation of the spin splitting by fine-tuning an external magnetic field. Parameters U , ϵ_d , Γ , and T as in Fig. 1.

maximum at a frequency ω_{\max} which we associate with the Kondo temperature [i.e., $k_B T_K \equiv \hbar \omega_{\max}$ at $B = B_{\text{comp}}(P)$], and then decreases linearly with ω , indicating the formation of the Fermi liquid state [14]. By determining $T_K(P)$ (from ω_{\max}) for different P values, we find that T_K decreases with increasing P [Fig. 3(b)]. For metals such as Ni, Co, and Fe, where $P = 0.24, 0.35$, and 0.40 , respectively, the decrease of T_K is weak, so the Kondo effect should be experimentally accessible. Remarkably, both $\text{Im}\{\chi_s^z(\omega)\}$ and the $A_\sigma(\omega)$ collapse rather well onto a universal curve if plotted in appropriate units [Figs. 3(a) and 3(c)]. This indicates that an applied magnetic field B_{comp} restores the universal behavior characteristic for the isotropic Kondo effect, in spite of the presence of spin-dependent coupling to the leads. Figure 4(a) shows that the amplitude of the Kondo resonance is now strongly spin dependent, which is unusual and unique. The nature of this asymmetry is related to the asymmetry of the DOS in the leads, and its value is exactly proportional to $\sim 1/\Gamma_\sigma$. As a result, the total conductance G_σ is not spin dependent [Fig. 4(b)]. This indicates the robustness of the Kondo effect in this system: If the external magnetic field has been tuned appropriately, it is able to compensate the presence of a spin asymmetry in the leads by creating a proper spin asymmetry in the dot spectral density, thereby conserving a fully compensated local spin and achieving perfect transmission.

Friedel sum rule.—Further insights can be gained from the Friedel sum rule, an exact $T = 0$ relation [19] that holds for arbitrary values of P and B [30]. The interacting Green's function can be expressed as [14] $\mathcal{G}_{d,\sigma}^R(\omega) = [\omega - \epsilon_{d\sigma} + i\Gamma_\sigma - \Sigma_\sigma(\omega)]^{-1}$, with spin de-

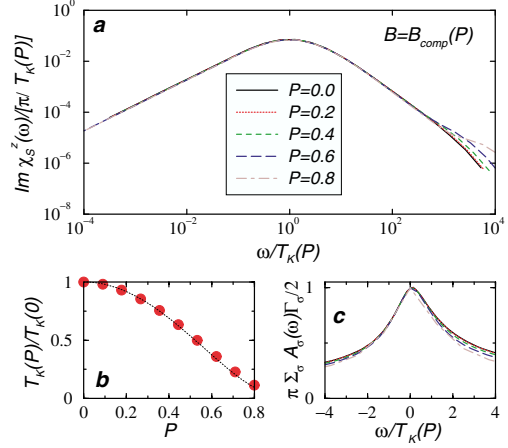


FIG. 3 (color online). (a) The spin spectral function $\text{Im}\{\chi_s^z(\omega)\}$. (b) Dependence of T_K on spin polarization P . The dotted line shows the prediction from Ref. [12]—namely, $T_K(P)/T_K(0) = \exp[C \text{arctanh}(P)/P]$, where the best fit is obtained for $C = -5.98$. Equation (6) from Ref. [12] with $(\rho_\uparrow + \rho_\downarrow)J_0 = (\Gamma/\pi)U/[\epsilon_d(U + \epsilon_d)]$ would lead to $C = -4.19$. (c) QD spectral function for several values of P . Parameters U , ϵ_d , Γ , and T are as in Fig. 1, $B = B_{\text{comp}}(P)$.

pendent $\epsilon_{d\sigma}$ and Γ_σ ; the former due to Zeeman splitting ($\epsilon_{d\sigma} = \epsilon_d - 1/2 \sigma g \mu_B B$) and the latter due to the ferromagnetic leads. Here $\Sigma_\sigma(\omega)$ denotes the spin-dependent self-energy. Now, the Friedel sum rule [19] implies that, at $T = 0$, the following relations hold:

$$n_\sigma = \phi_\sigma/\pi = \frac{1}{2} - \frac{1}{\pi} \tan^{-1} \left(\frac{\epsilon_{d\sigma} - \epsilon_F + \Sigma_\sigma^R(\epsilon_F)}{\Gamma_\sigma} \right), \quad (3)$$

$$A_\sigma(\epsilon_F) = \frac{\sin^2(\pi n_\sigma)}{\pi \Gamma_\sigma}, \quad (4)$$

where $\Sigma_\sigma^R(\omega) \equiv \text{Re} \Sigma_\sigma(\omega)$, and $\phi_\sigma(\omega)$ is the phase of $\mathcal{G}_{d,\sigma}^R(\omega)$. Since $\Sigma_\uparrow^R(\epsilon_F) \neq \Sigma_\downarrow^R(\epsilon_F)$, an equal spin occupation, $n_\uparrow = n_\downarrow$, is possible only for $(\epsilon_{d\uparrow} - \epsilon_F + \Sigma_\uparrow^R(\epsilon_F))/\Gamma_\uparrow = (\epsilon_{d\downarrow} - \epsilon_F + \Sigma_\downarrow^R(\epsilon_F))/\Gamma_\downarrow$, which can be obtained only for an appropriate external magnetic field $B = B_{\text{comp}}$. For the latter, in the local moment regime ($n \approx 1$), we have $n_\uparrow = n_\downarrow \approx 0.5$, so that $\phi_\uparrow = \phi_\downarrow \approx \pi/2$, which implies that the peaks of A_\uparrow and A_\downarrow are aligned. Thus, the Friedel sum rule clarifies why the magnetic field B_{comp} , at which the splitting of the Kondo resonance disappears, coincides with that for which $n_\uparrow = n_\downarrow$. For $B = B_{\text{comp}}$, the spin-dependent amplitude $A_\sigma(\epsilon_F)$ of Eq. (4) and the conductance $G_\sigma \sim \Gamma_\sigma A_\sigma(\epsilon_F)$ agree well with the above-mentioned NRG results [Figs. 4(a) and 4(b)].

In conclusion, we showed that the Kondo effect in a QD attached to ferromagnetic leads is in general suppressed, because the latter induce a spin splitting of the QD level, which leads to an asymmetry in the occupancy $n_\uparrow \neq n_\downarrow$. Remarkably, the Kondo effect may nevertheless be restored by applying an external magnetic field B_{comp} , tuned

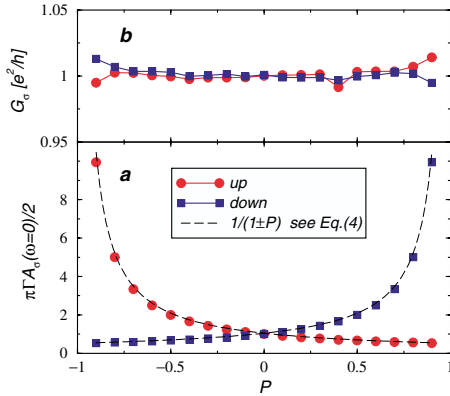


FIG. 4 (color online). (a) Spin resolved QD spectral function amplitude $A_\sigma(\omega=0)$ at the Fermi level, and (b) the QD conductance G_σ , as functions of the spin polarization P , for $B = B_{\text{comp}}(P)$ and symmetric couplings ($\Gamma_{L\sigma} = \Gamma_{R\sigma}$), with U , ϵ_d , Γ , and T as in Fig. 1, implying $n_\sigma \approx 0.5$. The dashed line in (a) is $1/(1 \pm P)$ [Eq. (4) with $n_\sigma = 0.5$]. As expected, we find $G_\sigma = e^2/h$, with a numerical error less than 1%.

such that the splitting of the Kondo resonance is compensated and the condition $n_\uparrow = n_\downarrow$ is fulfilled. Although the Kondo resonance is strongly spin polarized, it then features a locally screened state, a spin-independent conductance, and a Kondo temperature which decreases with increasing spin asymmetry.

We thank R. Bulla, T. Costi, L. Glazman, W. Hofstetter, H. Imamura, B. Jones, S. Maekawa, A. Rosch, M. Vojta, and Y. Utsumi for discussions. This work was supported by the DFG under the CFN, ‘‘Spintronics’’ Network RTN2-2001-00440, Project No. PBZ/KBN/044/P03/2001, OTKA T034243, and the Emmy-Noether program.

Note added.—After submission of our paper, a preprint [31] studying a similar problem using the NRG technique appeared, with conclusions consistent with ours.

- [1] L. I. Glazman and M.E. Raikh, JETP Lett. **47**, 452 (1988); T.K. Ng and P.A. Lee, Phys. Rev. Lett. **61**, 1768 (1988).
- [2] D. Goldhaber-Gordon *et al.*, Nature (London) **391**, 156 (1998).
- [3] S.M. Cronenwett *et al.*, Science **281**, 540 (1998); F. Simmel *et al.*, Phys. Rev. Lett. **83**, 804 (1999); J. Schmid *et al.*, Phys. Rev. Lett. **84**, 5824 (2000); W.G. van der Wiel *et al.*, Science **289**, 2105 (2000).
- [4] J. Nyg ard *et al.*, Nature (London) **408**, 342 (2000).
- [5] M.R. Buitelaar *et al.*, Phys. Rev. Lett. **88**, 156801 (2002).
- [6] J. Park *et al.*, Nature (London) **417**, 722 (2002); W. Liang *et al.*, Nature (London) **417**, 725 (2002).
- [7] M.R. Buitelaar *et al.*, Phys. Rev. Lett. **89**, 256801 (2002).
- [8] N. Sergueev *et al.*, Phys. Rev. B **65**, 165303 (2002).
- [9] P. Zhang *et al.*, Phys. Rev. Lett. **89**, 286803 (2002).

- [10] B.R. Bulka *et al.*, Phys. Rev. B **67**, 024404 (2003).
- [11] R. Lopez *et al.*, Phys. Rev. Lett. **90**, 116602 (2003).
- [12] J. Martinek *et al.*, Phys. Rev. Lett. **91**, 127203 (2003).
- [13] K.G. Wilson, Rev. Mod. Phys. **47**, 773 (1975); T.A. Costi *et al.*, J. Phys. Condens. Matter **6**, 2519 (1994).
- [14] A.C. Hewson, *The Kondo Problem to Heavy Fermions* (Cambridge University Press, Cambridge, England, 1993).
- [15] W. Hofstetter, Phys. Rev. Lett. **85**, 1508 (2000).
- [16] T.A. Costi, Phys. Rev. Lett. **85**, 1504 (2000); Phys. Rev. B **64**, 241310 (2001).
- [17] The remarkable full recovery of the Kondo effect should be contrasted to the competition between Kondo physics and magnetic RKKY interactions in heavy-fermion systems [18]. There, depending on the relation between the relevant energy scales T_{RKKY} and T_{K} , either the local spin is quenched and no magnetic order occurs (for $T_{\text{K}} > T_{\text{RKKY}}$), or the local molecular field removes spin degeneracy and suppresses the Kondo effect (for $T_{\text{K}} < T_{\text{RKKY}}$).
- [18] A.H. Castro Neto and B.A. Jones, Phys. Rev. B **62**, 14975 (2000), and references therein.
- [19] D.C. Langreth, Phys. Rev. **150**, 516 (1966).
- [20] W. Nolting *et al.*, Z. Phys. B **96**, 357 (1995).
- [21] E.Yu. Tsybal and D.G. Pettifor, J. Phys. Condens. Matter **9**, L411 (1997).
- [22] We expect that a finite s -electron interaction, $U_s > 0$, will lead only to a slight renormalization of T_{K} . Recently, an Anderson impurity embedded in a correlated host (without magnetic order) was studied [23,24], and an enhancement of T_{K} was found for weak s -electron interaction, $U_s/D < 1$, whereas, for intermediate and strong interactions, T_{K} was found to be reduced.
- [23] T. Schork and P. Fulde, Phys. Rev. B **50**, 1345 (1994); G. Khaliullin and P. Fulde, Phys. Rev. B **52**, 9514 (1995).
- [24] W. Hofstetter *et al.*, Phys. Rev. Lett. **84**, 4417 (2000).
- [25] A lowest-order perturbation calculation shows that for $|U + \epsilon_d|, |\epsilon_d| \ll D_\sigma$ the spin splitting of the bottom of the band ΔD (for s bands we consider no spin splitting for the band top) generates an effective local magnetic field $B_{\text{Stoner}} \approx \pi\Gamma/2 \ln(1 - \Delta D/D_\uparrow)$. To account for this in our model of Eq. (2), one could renormalize P (or else use a shifted compensation field B_{comp} below).
- [26] K. Yosida, *Theory of Magnetism* (Springer, New York, 1996).
- [27] A poor man’s scaling analysis [12] yields a renormalization $\delta\epsilon_{\text{dir}}$ of the level ϵ_{dir} proportional to Γ_σ , i.e., $B_{\text{comp}} \propto (\delta\epsilon_{\text{dir}} - \delta\epsilon_{\text{dl}}) \propto (\Gamma_\downarrow - \Gamma_\uparrow) = -P\Gamma$.
- [28] A similar splitting was predicted [D. Boese, *et al.*, Phys. Rev. B **64**, 125309 (2001); W. Hofstetter, cond-mat/0104297] for a two-level QD system which, in a special situation, can be mapped on our model.
- [29] For certain special (nongeneric) cases, the spin-up and -down level positions and, hence, also the Kondo resonance do not split up in two, even for $P \neq 0$: This occurs, for example, at the symmetry point $\epsilon_d = -U/2$ of the Anderson model, provided the bands are also symmetric around ϵ_F (but this is unrealistic for ferromagnets).
- [30] Our NRG confirms Eq. (4) for arbitrary P and B .
- [31] M.S. Choi *et al.*, cond-mat/0305107.

5.1.1 Quantitative determination of the compensation field B_{comp}

After finishing the work presented above we became particularly interested (motivated by questions of D. Ralph) in (i) a quantitative determination of the compensation field B_{comp} and (ii) why the condition $n_{\uparrow} = n_{\downarrow}$ implies an unsplit Kondo resonance.

We use poor man's scaling to derive the total shift of the local level $\delta\epsilon_{d\sigma}$, which is due to electrons at the band edges, i.e. at energies $\omega \sim \pm D$. For the case of finite U the scaling starts at U and breaks down when ϵ_d is reached, thus Eq. (3.37) has to be adjusted correspondingly. The shift of the level $\epsilon_{d\sigma}$ is given as

$$\delta\epsilon_{d\sigma} = \frac{\ln\left(\frac{U}{|\epsilon_d|}\right)}{2\pi}\Gamma_{\bar{\sigma}}. \quad (5.1)$$

Note that Eq. (5.1) holds only for $\epsilon_d > -U/2$ (with finite ϵ_d), as Eq. (3.37) was derived in the limit $U \rightarrow \infty$. The case $\epsilon_d < -U/2$ produces opposite signs, as one expects from particle-hole symmetry. For $P > 0$, i.e. $\Gamma_{\uparrow} > \Gamma_{\downarrow}$, and in absence of an additional applied magnetic field one obtains from Eq. (5.1) $\epsilon_{d\uparrow} < \epsilon_{d\downarrow}$, so $n_{\uparrow} > n_{\downarrow}$ [see Fig. 5.2(right panel)]. Obviously, one can apply an additional local magnetic field, which decreases n_{\uparrow} somewhat faster than n_{\downarrow} is increased (since the former is broader than the latter). It turns out that a compensation field B_{comp} , tuned such that the condition $n_{\uparrow} = n_{\downarrow}$ is fulfilled, realizes the case where the QD-spin is perfectly screened even though the leads have a finite polarization. Note that the condition $n_{\uparrow} = n_{\downarrow}$ implies $\phi_{\uparrow} = \phi_{\downarrow}$ (due to the Friedel sum rule [21]) which results in $n_{\sigma} \sim \frac{1}{2}$ or $\phi_{\sigma} \sim \pi/2$ for $\sigma = \uparrow / \downarrow$ as ϵ_d is fixed such that $n \sim 1$. At $T = 0$, in strong coupling (the opposite limit to poor man's scaling), the interacting Green's function can be written as $G_{\sigma}(\omega) = \frac{1}{\omega - \epsilon_{d\sigma} + i\Gamma_{\sigma} - \Sigma_{\sigma}(\omega)} = |G_{\sigma}(\omega)|e^{i\phi_{\sigma}}$. Therefore the condition $n_{\uparrow} = n_{\downarrow}$ implies that both spin-resolved spectral functions are on resonance - the Kondo resonance is not split [see question (ii) above]. To have a resonance at the Fermi energy the real part of the self-energy has to fulfill $\Sigma_{\sigma}^R(0) = -(\epsilon_{d\sigma} - \epsilon_F)$, which means that the self-energy term Σ is *not small*, indicating the importance of correlation effects. One can get an approximation about the dependence of B_{comp} by means of PMS, Eq. (5.1), via

$$B_{\text{comp}} \approx \delta\epsilon_{d\uparrow} - \delta\epsilon_{d\downarrow} = -\frac{\ln\left(\frac{U}{|\epsilon_d|}\right)}{2\pi}\Gamma P. \quad (5.2)$$

That B_{comp} should be linear in P and Γ can be understood from poor man's scaling (coming from weak coupling) and is confirmed by the numerics presented before [see question (i) above].

5.1.2 Experimental relevance

The theoretical study presented in this Section was recently confirmed in an experiment of Pasupathy *et al.*, “*The Kondo Effect in the Presence of Ferromagnetism*”, [55]. It was confirmed in this experiment that C_{60} molecules (serving as QDs) can be strongly coupled to nickel electrodes (serving as ferromagnetic leads) so as to exhibit the Kondo effect.

The shapes of the nickel electrodes were designed such that the two electrodes have different magnetic anisotropies. Consequently, these electrodes undergo a magnetic reversal at different values of the magnetic field. This design has the fundamental advantage that the relative orientation of the magnetic moments in the two electrodes can be controlled (via an external magnetic field) between parallel and antiparallel alignment.

Pasupathy *et al.* found, that ferromagnetism suppresses Kondo-assisted tunneling, but Kondo correlations are still present in QDs contacted to ferromagnetic leads. In agreement with our prediction they observed a split conductance, see Fig. 5.3, for the case of the parallel aligned nickel electrodes. For antiparallel aligned electrodes, on the other hand, the strong-coupling Kondo effect was recovered, in agreement with a prediction of Martinek *et al.* [44] (see Fig. 5.3 for $B \approx 15\text{mT}$).

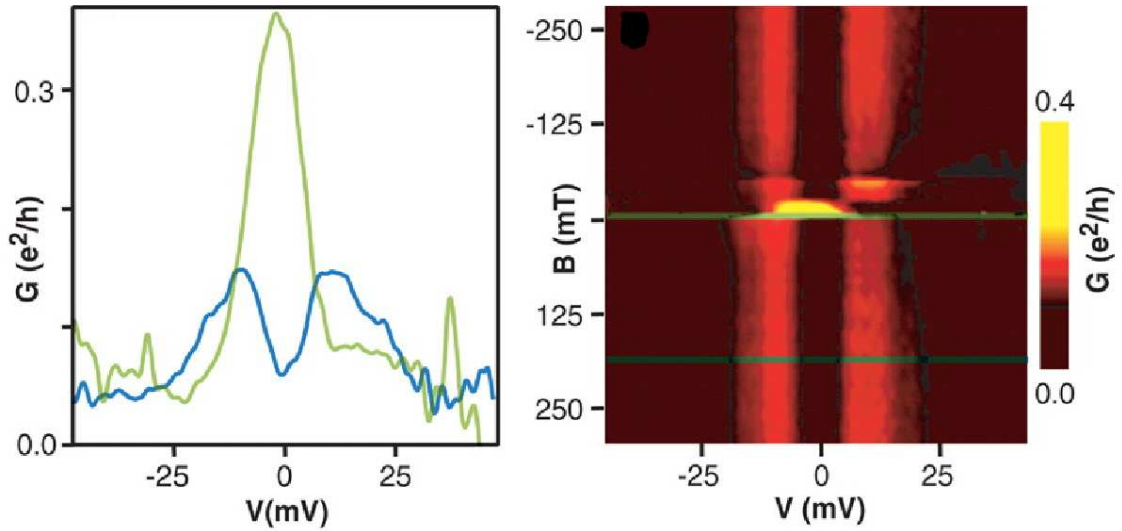


Figure 5.3: Conductance curves for a $Ni-C_{60}-Ni$ device. An external magnetic field allows to switch the magnetic orientation of the electrodes between parallel and antiparallel alignment. For $B \approx 15\text{mT}$ (see right panel) the alignment between the electrodes is approximately antiparallel, the strong-coupling Kondo effect (with an enhanced conductance at $V = 0$ as shown in the right panel) is recovered even in presence of ferromagnetic electrodes. The peak in the conductance at $V = 0\text{mV}$, shown in the left panel, corresponds to this particular magnetic field. For a different magnetic field (a magnetic field $B \approx 175\text{mT}$ is marked in the right panel) the electrodes are essentially parallel oriented and the conductance is split and suppressed (the split conductance in the left panel corresponds to this magnetic field). This observation was predicted in the study presented in this Section. Figure taken from 5.3.

Currently the group of D. Ralph [56], Cornell University, is also trying to contact Mn-atoms (serving as QDs) to ferromagnetic leads, made of Mn as well. Unfortunately, the contacting between the Mn-atoms and the Mn-leads turns out to be extremely difficult.

Another possibility to realize QDs contacted to polarized leads is to use QDs based on single wall carbon nanotubes (SWNT), instead of semiconductor QDs. These systems allow for various studies of Kondo effects in devices with magnetic or superconducting electrodes [57].

SWNT are usually grown on iron catalysts. If this (ferromagnetic) catalyst is by accident close to the contact between a non-magnetic lead and the SWNT, it can evidently appear that the tunneling between the SWNT and the leads becomes *spin*-dependent [58], a scenario that directly applies to the study presented in Section 5.1.

In a recent study Nygaard *et al.* [59] presented experimental data on a SWNT based QD, where the Kondo resonance was split at zero magnetic field, see Fig. 5.4. This splitting was interpreted, in agreement with the findings presented in this Section, as evidence for the coupling of the dot to a ferromagnetic impurity.

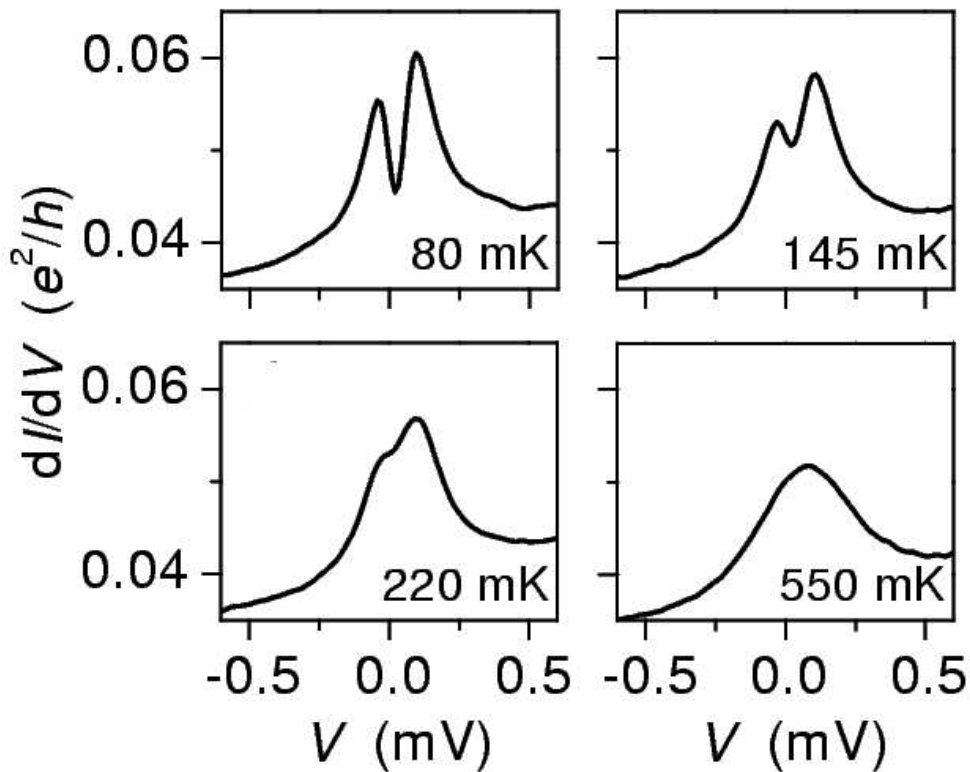


Figure 5.4: Differential conductance as a function of V of a nanotube QD [59]. The splitting of the zero bias anomaly can nicely be explained by a QD coupled to ferromagnetic leads. The splitting disappears when the temperature T is increased. We could qualitatively reproduce this behavior in an (unpublished) NRG-calculation.

5.2 Gate controlled spin splitting in the Kondo regime

In the above mentioned experiment of Nygaard *et al.* [59] also the gate voltage dependence of the splitting of the Kondo resonance was studied, see Fig. 5.5. Three typical classes of gate voltage dependence of this splitting were found, which the numerical study presented in this Section confirms.

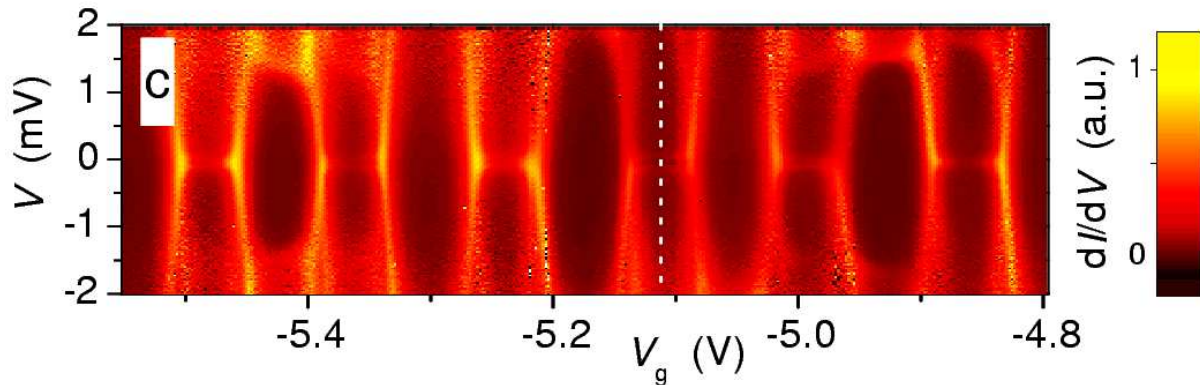


Figure 5.5: The gate voltage dependent spin splitting of the Kondo resonance as observed in the experiment of Nygaard *et al.* [59].

In the following paper (submitted to Phys. Rev. Lett.) we neither assume the leads DoS to be flat nor we disregard the Stoner splitting. The leads DoS of our choice can be found in Fig. 1 of the paper presented below. In contrast to the previous work [15] we really take the energy-dependence of the DoS into account. The chosen DoS corresponds to a dispersion as found for free electrons. From a methodological point of view this approach is more sophisticated than the iteration scheme introduced by Wilson [1]. Here, Wilson's iteration scheme [1] has to be extended to handle leads with an arbitrary DoS. The way how this can be achieved is described in Appendix A. Note that the spin-dependent DoS in the leads we use here (which is, by the way, not particle-hole symmetric) complicates the NRG-iteration dramatically, as spin-dependent hopping matrix elements *and* spin-dependent onsite energies along the Wilson chain have to be determined numerically. This is achieved by solving the equations introduced in Appendix A. As these matrix elements are decaying exponentially fast, their numerical determination requires rather advanced numerical techniques (for further information see Appendix A.2).

In this study we find that it is *not* sufficient to consider only the leads DoS at the Fermi energy $\rho_\sigma(\epsilon_F)$ for a proper description of the resulting splitting of the Kondo resonance. It turns out, instead, that *all* lead energies are necessary to describe the resulting splitting of the Kondo resonance properly - even though high energy states are logarithmically suppressed. For all choices of $\rho_\sigma(\omega)$ we find that one can tune the splitting of the Kondo resonance by means of an external gate voltage. Moreover we find that the Kondo resonance is fully recovered for a special choice of ϵ_d for a particular form of $\rho_\sigma(\omega)$ [see Fig. 1(c) of the

paper below]. This finding suggests the interesting possibility to mimic a local magnetic field inside a QD by means of an external gate voltage.

Gate-controlled spin-splitting in quantum dots with ferromagnetic leads in the Kondo regime

J. Martinek,^{1,3,6} M. Sindel,² L. Borda,^{2,4} J. Barnaś,^{3,5} R. Bulla,⁷ J. König,⁸ G. Schön,¹ S. Maekawa,⁶ and J. von Delft²

¹*Institut für Theoretische Festkörperphysik, Universität Karlsruhe, 76128 Karlsruhe, Germany*

²*Physics Department and Center for NanoScience, LMU München, 80333 München, Germany*

³*Institute of Molecular Physics, Polish Academy of Sciences, 60-179 Poznań, Poland*

⁴*Institute of Physics, TU Budapest, H-1521, Hungary*

⁵*Department of Physics, Adam Mickiewicz University, 61-614 Poznań, Poland*

⁶*Institute for Materials Research, Tohoku University, Sendai 980-8577, Japan*

⁷*Theoretische Physik III, Elektronische Korrelationen und Magnetismus, Universität Augsburg, Augsburg, Germany*

⁸*Institut für Theoretische Physik III, Ruhr-Universität Bochum, 44780 Bochum, Germany*

(Dated: July 9, 2004)

The effect of a gate voltage (V_g) on the spin-splitting of an electronic level in a quantum dot (QD) attached to ferromagnetic leads is studied in the Kondo regime using a generalized numerical renormalization group technique. We find that the V_g -dependence of the QD level spin-splitting strongly depends on the shape of the density of states (DOS). For one class of DOS shapes there is nearly no V_g -dependence, for another, V_g can be used to control the magnitude and sign of the spin-splitting, which can be interpreted as a local exchange magnetic field. We find that the spin-splitting acquires a new type of logarithmic divergence. We give an analytical explanation for our numerical results and explain how they arise due to spin-dependent charge fluctuations.

PACS numbers: 75.20.Hr, 72.15.Qm, 72.25.-b, 73.23.Hk

The manipulation of magnetization and spin is one of the fundamental processes in magneto-electronics and spintronics, providing the possibility of writing information in a magnetic memory [1], and also because of the possibility of classical or quantum computation using spin. In most situations this is realized by means of an externally applied, nonlocal magnetic field which is usually difficult to insert into an integrated circuit. Recently, it was proposed to control the magnetic properties, such as the Curie temperature of ferromagnetic semiconductors, by means of an electric field: In gated structures [2], due to the modification of carrier-density-mediated magnetic interactions, such properties can be modified by a gate voltage. In this Letter we propose to control the amplitude and sign of the spin-splitting of a quantum dot (QD) induced by the presence of ferromagnetic leads, only by using a gate voltage without further assistance of a magnetic field. To illustrate this effect we investigate the Kondo effect and its spin-splitting as a very sensitive probe of the spin state of the dot and the effective local magnetic field in the QD generated by exchange interaction with the ferromagnetic leads.

Recently, the possibility of the Kondo effect in a QD attached to ferromagnetic electrodes was widely discussed [3–9], and it was shown, that the Kondo resonance is split and suppressed in the presence of ferromagnetic leads [7, 8]. It was shown that this splitting can be compensated by an appropriately tuned external magnetic field, and the Kondo effect is thereby restored [7, 8]. In all previous studies of QDs attached to ferromagnetic leads [3–9] an idealized, flat, spin-independent DOS with spin-dependent tunneling amplitudes was considered. However, since the spin-splitting arises from renormalization

effects i.e. is a many-body effect, it depends on the *full* DOS-structure of the involved material, and not only on its value at the Fermi surface. In realistic ferromagnetic systems, the DOS shape is strongly asymmetric due to the Stoner splitting and the different hybridization between the electronic bands [1].

In this Letter we demonstrate that the gate voltage dependence of the spin-splitting of a QD level, resulting in a splitting and suppression of the Kondo resonance, is determined by the DOS structure and can lead to crucially different behaviours. We apply the numerical renormalization group (NRG) technique extended to handle bands of arbitrary shape. For one class of DOS-shapes, we find almost no V_g -dependence of the spin-splitting, while for another class the induced spin-splitting, which can be interpreted as the effect of a local exchange field, can be controlled by V_g . The spin-splitting can be fully compensated and its direction can even be reversed within this class. We explain the physical mechanism that leads to this behavior, which is related to the compensation of the renormalization of the spin-dependent QD levels induced by the electron-like and hole-like quantum charge fluctuations. Moreover we find that for the QD level close to the Fermi surface, the amplitude of the spin-splitting has a logarithmic divergence, indicating the many-body character of this phenomenon.

Model and method. – The Anderson model (AM) of a single level QD with energy ϵ_0 and Coulomb interaction U , coupled to ferromagnetic leads, is given by

$$H = \sum_{rk\sigma} \epsilon_{rk\sigma} c_{rk\sigma}^\dagger c_{rk\sigma} + \epsilon_0 \sum_{\sigma} \hat{n}_{\sigma} + U \hat{n}_{\uparrow} \hat{n}_{\downarrow} + \sum_{rk\sigma} (V_{rk} d_{\sigma}^\dagger c_{rk\sigma} + h.c.) - BS_z. \quad (1)$$

Here $c_{rk\sigma}$ and d_σ ($\hat{n}_\sigma = d_\sigma^\dagger d_\sigma$) are Fermi operators for electrons with momentum k and spin σ in the leads ($r = L/R$), and in the QD, V_{rk} is the tunneling amplitude, $S_z = (\hat{n}_\uparrow - \hat{n}_\downarrow)/2$, and the last term denotes the Zeeman energy of the dot. The energy ϵ_0 is experimentally controllable by V_g ($\epsilon_0 \simeq V_g$).

In order to discuss the gate voltage dependence of the QD level spin-splitting, we consider here a more realistic, both energy and spin dependent band structure [$\rho_{r\uparrow}(\omega) \neq \rho_{r\downarrow}(\omega)$], violating p-h symmetry $\rho_{r\sigma}(\omega) \neq \rho_{r\sigma}(-\omega)$, which leads to an energy dependent hybridization function $\Gamma_{r\sigma}(\omega) = \pi \sum_k \delta(\omega - \epsilon_{k\sigma}) V_{rk}^2 = \pi \rho_{r\sigma}(\omega) V_0^2$, where we take $V_{rk} = V_r$ to be constant. We apply the NRG method [10, 11] extended to handle arbitrary DOS shapes and asymmetry. To this end, the standard logarithmic discretization of the conduction band is performed for *each* spin component separately, with the bandwidths, $D_\uparrow = D_\downarrow = D_0$, chosen such that the total spectral weight is included in $[-D_0, D_0]$ for all values of V_g studied here (to avoid different systematic errors upon changing V_g).

Within each interval $[-\omega_n, -\omega_{n+1}]$ and $[\omega_{n+1}, \omega_n]$ (with $\omega_n = D_0 \Lambda^{-n}$) of the logarithmically discretized conduction band (CB) the operators of the continuous CB are expressed in terms of a Fourier series. Even though we allow for a non-constant conduction electron DOS, it is still possible to transform the Hamiltonian such that the impurity couples *only* to the zeroth order component of the Fourier expansion of each interval [12]. Dropping the non-constant Fourier-components of each interval [10, 11] then results in a discretized version of the Anderson model with the continuous spectrum in each interval replaced by a single fermionic degree of freedom (independently for both spin directions). Since we allow for an arbitrary DOS for *each* spin component σ (\uparrow, \downarrow) of the CB this mapping needs to be performed for each σ separately. This leads to the Hamiltonian:

$$H = \sum_\sigma \epsilon_\sigma \hat{n}_\sigma + U \hat{n}_\uparrow \hat{n}_\downarrow + \sqrt{\xi_{0\sigma}/\pi} \sum_\sigma [d_\sigma^\dagger f_{0\sigma} + f_{0\sigma}^\dagger d_\sigma] + \sum_{\sigma n=0}^{\infty} [\varepsilon_{n\sigma} f_{n\sigma}^\dagger f_{n\sigma} + t_{n\sigma} (f_{n\sigma}^\dagger f_{n+1\sigma} + f_{n+1\sigma}^\dagger f_{n\sigma})], \quad (2)$$

where $f_{n\sigma}$ are fermionic operators at the n th site of the Wilson chain, $\xi_{0\sigma} = 1/2 \int_{-D_0}^{+D_0} \Gamma_\sigma(\omega) d\omega$, $t_{n\sigma}$ denotes the hopping matrix elements, and $\epsilon_\sigma = \epsilon_0 - BS_z$. The absence of particle-hole symmetry leads to the appearance of non-zero on-site energies, $\varepsilon_{n\sigma}$ along the chain. In this *general* case no closed expression for the matrix elements $t_{n\sigma}$ and $\varepsilon_{n\sigma}$, both depending on the particular structure of the DOS via $\Gamma_\sigma(\omega)$, is known, therefore they have to be determined recursively. This requires rather advanced numerical methods, due to the exponentially fast decay of $t_{n\sigma}$ and $\varepsilon_{n\sigma}$ along the chain [13].

This method allows one to calculate the level occupation $n_\sigma \equiv \langle \hat{n}_\sigma \rangle$ and the spin-resolved single-particle

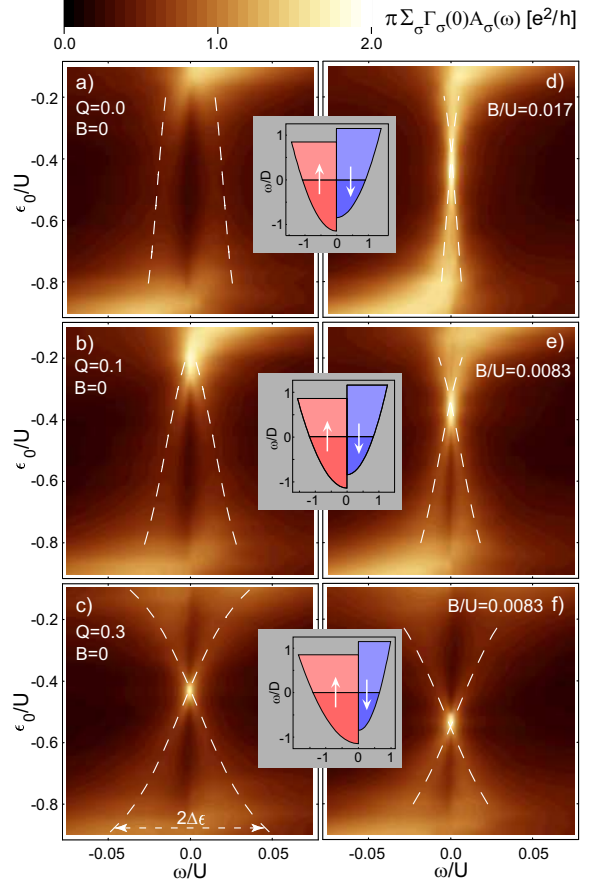


FIG. 1: (color online). V_g -dependence of the spin-splitting: Normalized spectral function $\pi \sum_\sigma \Gamma_\sigma(0) A_\sigma(\omega)$ as a function of energy ω and gate voltage ϵ_0 , for the three different DOS shapes (depicted in insets) characterized by a different Q , which modifies both the spin and p-h asymmetry: (a-c) for magnetic field $B = 0$, (d) $B/U = 0.017$, (e), and (f) $B/U = 0.0083$. The white dashed lines are obtained using Eq. (3). Here $U = 0.12D_0$, $\pi V_0^2 = UD/6$, $\Delta = 0.15D$ and $T = 0$. Inset: the scheme of the parabolic DOS shape for spin \uparrow (red) and \downarrow (blue).

spectral density $A_\sigma(\omega) = -\frac{1}{\pi} \text{Im} \mathcal{G}_\sigma^r(\omega)$, where $\mathcal{G}_\sigma^r(\omega)$ denotes a retarded Green's function. For symmetric coupling [$\Gamma_{L\sigma}(\omega) = \Gamma_{R\sigma}(\omega)$] the spin-resolved conductance takes the form $G_\sigma = \pi \frac{e^2}{h} \int_{-\infty}^{+\infty} d\omega \Gamma_\sigma(\omega) A_\sigma(\omega) (-\frac{\partial f(\omega)}{\partial \omega})$ where $f(\omega)$ is the Fermi function.

Spectral function and conductance. – Here, we focus our attention on $T = 0$ properties. We have analyzed several types of DOS shapes and found three typical classes of the V_g -dependence of the Kondo resonance splitting. Since our method enables us to perform NRG calculations for arbitrary band-shapes, we decide to choose an example which turns out to encom-

pass all three classes, namely $\rho_\sigma(\omega) = \frac{1}{2} \frac{3\sqrt{2}}{8} D^{-3/2} (1 + \sigma Q) \sqrt{\omega + D + \sigma\Delta}$, where $\omega \in [-D - \sigma\Delta, D - \sigma\Delta]$, $D_0 = D + \Delta$, [$\sigma \equiv 1(-1)$ for $\uparrow(\downarrow)$], a square-root shape DOS equivalent to a parabolic band (as for free electrons) with Stoner splitting Δ [14], and some additional spin asymmetry Q , which modifies the amplitude of the DOS [see Fig. 1(insets)].

In Fig. 1 we present the weighted spectral function $\tilde{A}(\omega) \equiv \pi e^2/h \sum_\sigma \Gamma_\sigma(0) A_\sigma(\omega)$, normalized such that for $\omega = 0$ it corresponds to the linear conductance $G = \tilde{A}(0)$, as a function of energy ω and ϵ_0 . We focus on a narrow energy window around the Fermi surface where the Kondo resonance appears; charge resonances are visible when ϵ_0 or $U + \epsilon_0$ approach the Fermi surface, namely at energies $\epsilon_0/U \gtrsim -0.1$ or $\lesssim -0.9$. Although the NRG method is designed to calculate equilibrium transport, one can still roughly deduce, from the spin-splitting of the Kondo resonance of the equilibrium spectral function $\tilde{A}(\omega)$, the splitting of the zero-bias anomaly ΔV in the non-equilibrium conductance $G(V)$, since $e\Delta V \sim 2\Delta\epsilon$ [7] ($\Delta\epsilon \equiv \tilde{\epsilon}_\uparrow - \tilde{\epsilon}_\downarrow$ is the splitting of the renormalized levels).

We present $\tilde{A}(\omega)$ for three DOS shapes depicted in the insets of Fig. 1: (i) $Q = 0$ (a,d), (ii) $Q = 0.1$ (b,e), and (iii) $Q = 0.3$ (c,f), with $2\Delta = 0.3D$ [15], leading to the three typical behaviors. Here the parameter Q tunes the spin and p-h asymmetry [see the definition of $\rho_\sigma(\omega)$] resulting in different behaviours (for a detailed discussion see the last section). For (i) we find nearly any ϵ_0 -dependence of the spin-splitting; for (ii), a strong ϵ_0 -dependence without compensation of the spin-splitting (i.e. no crossing), and for (iii) a strong ϵ_0 -dependence with a compensation (i.e. a crossing) and a change of the direction of the QD magnetization. The compensation (crossing) corresponds to the very peculiar situation where the Kondo effect (strong coupling fixed point) can be recovered in the presence of ferromagnetic leads without any external magnetic field. A behavior as presented in Fig. 1(a,b) was recently observed experimentally [16, 17], where indeed a variation of the gate voltage results in two split conduction lines $G(V, V_g)$ which are parallel for one case and converging for the other case, similar to our findings.

Effect of a magnetic field. – In Fig. 1(d,e,f) we show how a magnetic field B modifies the results of Fig. 1(a,b,c): in (i) the spin splitting can be compensated at a particular magnetic field B_{comp} (here $B_{\text{comp}}/U = 0.017$) and the Kondo effect is visible in a wide range of ϵ_0 ; for (ii), at $B/U = 0.0083$, the Kondo effect is recovered only at one particular ϵ_0 -value, which depends on the applied magnetic field; case (iii) shows that the crossing point shifts with B . Since B_{comp} can be viewed as a measure of the zero-field splitting, $\Delta\epsilon(B = 0, \epsilon_0) \simeq -B_{\text{comp}}(\epsilon_0)$, the ϵ_0 -dependence of $\Delta\epsilon$ can be measured by studying that of B_{comp} , for which one needs to measure the linear conductance $G(\epsilon_0, B)$ as a function of

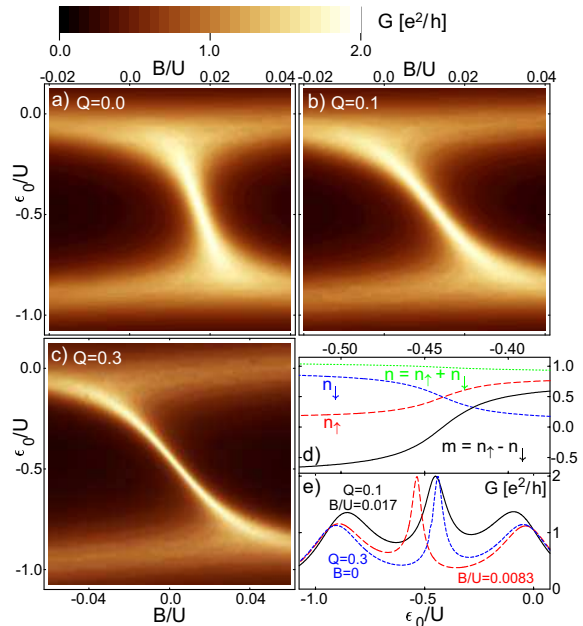


FIG. 2: (color online). The QD's linear conductance G as a function of gate voltage ϵ_0 and external magnetic field B for the DOS shapes (a), (b), and (c) as for Fig. 1(a), (b), and (c) respectively. (d) Spin-dependent occupancy n_σ of the dot level as a function of gate voltage ϵ_0 for the DOS shape as in Fig. 1(c) and $B = 0$. (d) The ϵ_0 -dependence of the total occupancy of the dot n and magnetization $m = n_\uparrow - n_\downarrow$ for the situation from Fig. 1(c). (e) The conductance G for the situations from Fig. 1(c - dashed), (d - solid), and (f - long dashed). Parameters U , Γ , and T as in Fig. 1.

both B and ϵ_0 . In Fig. 2(a-c) we plot $G(\epsilon_0, B)$ for the three bands of Fig. 1. The two horizontal ridges (resonances) in Fig. 2(a-c) correspond to quantum charge fluctuations (broadened QD level) of width $\sim \Gamma$. The lines with finite slope in Fig. 2(a-c) reflect the restored Kondo resonance and hence map out the ϵ_0 -dependence of $B_{\text{comp}}(\epsilon_0) = -\Delta\epsilon(\epsilon_0)$ when the magnetic field compensates the spin-splitting. Interestingly the spin-splitting and the corresponding B_{comp} tend to diverge ($|\Delta\epsilon| \rightarrow \infty$) when approaching the charging resonance, as is best visible in Fig. 2(c).

Such a finite slope in $G(\epsilon_0, B)$ was observed for a singlet-triplet transition Kondo effect in a two level QD (Fig.2(d) Ref. [18]). The corresponding transition leads to a characteristic maximum in the valley between two charging resonances (Fig.3(c) Ref. [18]), similarly as in our Fig. 2(e). In that system the effective spin asymmetry (assumed by our model) is realized by the asymmetry in the coupling of two QD levels [19].

In Fig. 2(d) we show how the occupation n_σ and the magnetic moment (spin) of the QD $m = n_\uparrow - n_\downarrow = 2\langle S_z \rangle$ change as a function of ϵ_0 for the situation of Fig. 1(c).

One finds that even though $B = 0$, it is possible to control the level spin-splitting of the QD, i.e. its spin, and thereby change the average spin direction of the QD from the parallel to anti-parallel alignment w.r.t. the lead's magnetization. This opens the possibility of controlling the QD's spin state by means of a gate voltage without further need of an external magnetic field, which is difficult to apply locally in practical devices.

Perturbative analysis. – One can understand the behavior presented in Fig. 1(a-c) by using Haldane's scaling method [20], where charge fluctuations are integrated out. This leads to a spin-dependent renormalization of the QD's level position $\tilde{\epsilon}_\sigma$ and a level broadening Γ_σ . In contrast to Ref. [7] we consider here the case of finite Coulomb interactions $U < \infty$, which means that also the doubly occupied state $|2\rangle$ is of importance. The spin-splitting is then given by $\Delta\epsilon \equiv \delta\epsilon_\uparrow - \delta\epsilon_\downarrow + B$, where

$$\delta\epsilon_\sigma \simeq -\frac{1}{\pi} \int d\omega \left\{ \frac{\Gamma_\sigma(\omega)[1-f(\omega)]}{\omega - \epsilon_\sigma} + \frac{\Gamma_{-\sigma}(\omega)f(\omega)}{\epsilon_{-\sigma} + U - \omega} \right\}. \quad (3)$$

The first term in the curly brackets corresponds to electron-like processes, namely charge fluctuations between a single occupied state $|\sigma\rangle$ and the empty $|0\rangle$ one, and the second term to hole-like processes, namely charge fluctuations between the states $|\sigma\rangle$ and $|2\rangle$. The amplitude of the charge fluctuations is proportional to Γ , which for $\Gamma \gg T$ determines the width of QD's levels. Eq. (3) shows that $\Delta\epsilon$ depends on the shape of $\Gamma_\sigma(\omega)$ for all ω , not only on its value at the Fermi surface. The dashed lines in Fig. 1(a-c) show $\pm\Delta\epsilon$ as a function of ϵ_0 [from Eq. (3)] for the same set of parameters as in the NRG calculation, and are in good agreement with the position of the (split) Kondo resonances observed in the latter. Eq. (3) shows that the dramatic changes observed in Fig. 1 upon changing Q are due to the modification of the p-h and spin asymmetry.

Eq. (3) predicts that even for systems with spin-asymmetric bands $\Gamma_\uparrow(\omega) \neq \Gamma_\downarrow(\omega)$, the integral can give $\Delta\epsilon = 0$, which corresponds to a situation where the renormalization of ϵ_σ due to electron-like processes are compensated by hole-like processes. An example is a system consisting of p-h symmetric bands, $\Gamma_\sigma(\omega) = \Gamma_\sigma(-\omega)$, for which there is no splitting of the Kondo resonance ($\Delta\epsilon = 0$) for the symmetric point, $\epsilon_0 = -U/2$. For real systems p-h symmetric bands cannot be assumed, however the compensation $\Delta\epsilon = 0$ is still possible, as in Fig. 1(c). Eq. (3) also shows that the characteristic energy scale of the spin-splitting is given by Γ rather than by the Stoner splitting Δ ($\Delta \gg \Gamma$), since the states far from the Fermi surface enter Eq. (3) only with a logarithmic weight. However, the Stoner splitting introduces a strong p-h asymmetry, so it can influence the character of gate voltage dependence significantly.

For a flat band $\Gamma_\sigma(\omega) = \Gamma_\sigma$, Eq. (3) can be integrated analytically. For $D_0 \gg U$, $|\epsilon_0|$ one finds: $\Delta\epsilon \simeq (P\Gamma/\pi) \text{Re}[\phi(\epsilon_0) - \phi(U + \epsilon_0)]$, where $P \equiv (\Gamma_\uparrow - \Gamma_\downarrow)/\Gamma$, $\phi(x) \equiv \Psi(\frac{1}{2} + i\frac{x}{2\pi T})$, and $\Psi(x)$ denotes the digamma

function. For $T = 0$, the spin-splitting is given by

$$\Delta\epsilon \simeq (P\Gamma/\pi) \ln(|\epsilon_0|/|U + \epsilon_0|), \quad (4)$$

showing a logarithmic divergence for $\epsilon_0 \rightarrow 0$ or $U + \epsilon_0 \rightarrow 0$. Since any sufficiently smooth DOS can be linearized around the Fermi surface, this logarithmic divergence occurs quite universally, as can be observed in log-linear versions (not shown) of Fig. 2(a-c). For finite temperature ($T > 0$) the logarithmic divergence for $\epsilon_0 \rightarrow 0$ or $\epsilon_0 \rightarrow -U$ is cut off, $\Delta\epsilon \simeq -\frac{1}{\pi} P\Gamma[\Psi(\frac{1}{2}) + \ln\frac{2\pi T}{U}]$, which is also important for temperatures $T \ll T_K$.

In conclusion, we demonstrated, using the extended NRG technique for general band shapes, the possibility of controlling the local exchange field and thereby the spin-splitting in a QD attached to ferromagnetic leads by means of the gate voltage. A new type of the logarithmic divergence of the QD's level spin-splitting was found, and attributed to spin-dependent charge fluctuations.

We thank T. Costi, L. Glazman, W. Hofstetter, B. Jones, C. Marcus, J. Nygård, A. Pasupathy, D. Ralph, A. Rosch, M. Vojta, and Y. Utsumi for discussions. This work was supported by the DFG under the CFN, 'Spintronics' RT Network of the EC RTN2-2001-00440, and Project OTKA T034243.

- [1] S. Maekawa and T. Shinjo, *Spin Dependent Transport in Magnetic Nanostructures*, Taylor & Francis (2002).
- [2] H. Ohno *et al.*, Nature (London) **408**, 944 (2000). D. Chiba *et al.*, Science **301**, 943 (2003).
- [3] N. Sergueev *et al.*, Phys. Rev. B **65**, 165303 (2002).
- [4] P. Zhang *et al.*, Phys. Rev. Lett. **89**, 286803 (2002).
- [5] B. R. Buřka *et al.*, Phys. Rev. B **67**, 024404 (2003).
- [6] R. Lopez *et al.*, Phys. Rev. Lett. **90**, 116602 (2003).
- [7] J. Martinek *et al.*, Phys. Rev. Lett. **91**, 127203 (2003).
- [8] J. Martinek *et al.*, Phys. Rev. Lett. **91**, 247202 (2003).
- [9] In Ref. [M. S. Choi *et al.*, Phys. Rev. Lett. **92**, 056601 (2004)] among other results the V_g -dependence of a QD coupled to ferromagnetic leads with a flat (p-h symmetric) DOS has been presented. However, the role of charge fluctuations in the absence of a spin-splitting, a sign change and a logarithmic divergence in the spin-splitting went unnoticed.
- [10] K.G. Wilson, Rev. Mod. Phys. **47** 773 (1975); T. A. Costi *et al.*, J. Phys.: Cond. Mat. **6**, 2519 (1994).
- [11] A. C. Hewson, *The Kondo Problem to Heavy Fermions*, Cambridge Univ. Press (1993).
- [12] R. Bulla *et al.*, J. Phys.: Condens. Matter **9**, 10463 (1997).
- [13] For more details see [N.-T. Tong *et al.*, in preparation].
- [14] K. Yosida, *Theory of Magnetism*, Springer (1996).
- [15] This value is in the range for typical ferromagnetic metals like *Ni*, *Co*, and *Fe* [D. A. Papaconstantopoulos, ed., *Handbook of the Band Structure of Elemental Solids*, Plenum Press (1986)].
- [16] J. Nygård and C. M. Markus (private commun.).
- [17] D. Ralph and A. Pasupathy (private commun.).
- [18] S. Sasaki *et al.*, Nature (London) **405**, 764 (2000).
- [19] D. Boese *et al.*, Phys. Rev. B **64**, 125309 (2001).
- [20] F. D. M. Haldane, Phys. Rev. Lett. **40**, 416 (1978).

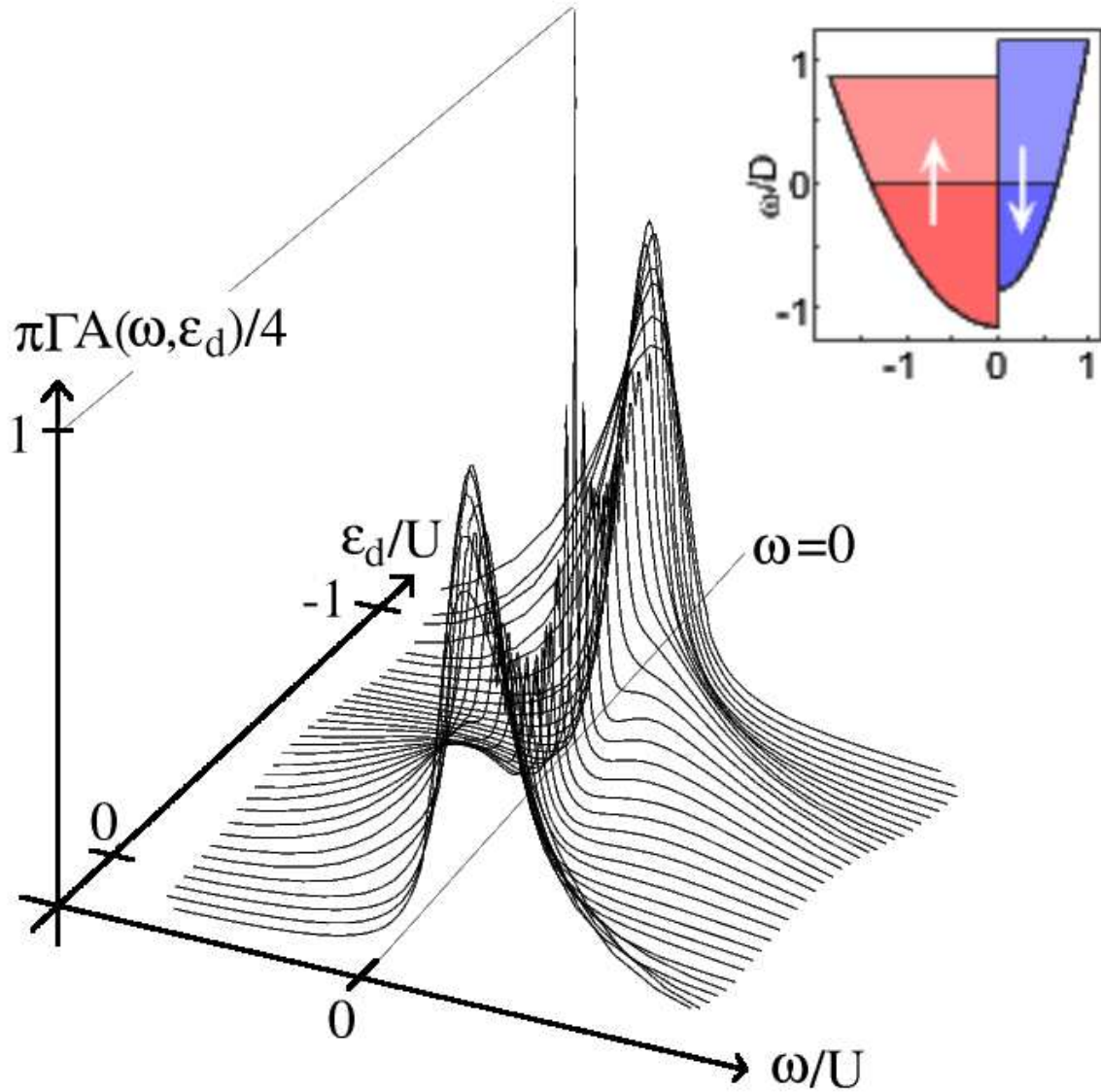


Figure 5.6: An alternative representation of the spectral function $A(\omega, \epsilon_d)$ of a QD connected to leads with a spin- and energy-dependent density of states (as shown in the inset). In contrast to a QD coupled to leads with a constant and spin-independent density of states, where a Kondo-plateau in $A(\omega = 0, \epsilon_d)$ is observed for $-U \lesssim \epsilon_d \lesssim 0$, a three peak structure in $A(\omega = 0, \epsilon_d)$ is found here. For that particular density of states, the splitting of the Kondo resonance, its full recovery and the resulting opposite splitting upon a variation of ϵ_d can be inferred. (Parameters are equivalent to Fig. 1(f) of Ref. [54]).

5.2.1 Comprehensive study dealing with QDs coupled to ferromagnetic leads

Currently we are working on a paper that summarizes the effects of a particular leads DoS on the Kondo resonance. Our goal is to study both the gate voltage and the polarization dependence of the Kondo resonance for the three classes of DoS presented below. In Fig. 5.7 these three classes of leads DoS are sketched.

The DoS sketched in (a) was studied in Section 5.1 without, however, analyzing the gate voltage dependence of the spin splitting. Even though this issue was already addressed in [60], we reexamine it here again, as its interpretation was in parts misleading.

The DoS corresponding to Fig. 5.7(b) has, so far not been studied at all. Our numerics confirms the expectation, based on poor man's scaling, that such a Stoner splitting leads to an logarithmically suppressed effective magnetic field.

The most general case is studied in case (c). Even though this case has already intensively been studied in Section 5.2 we will incorporate it in this comprehensive study.

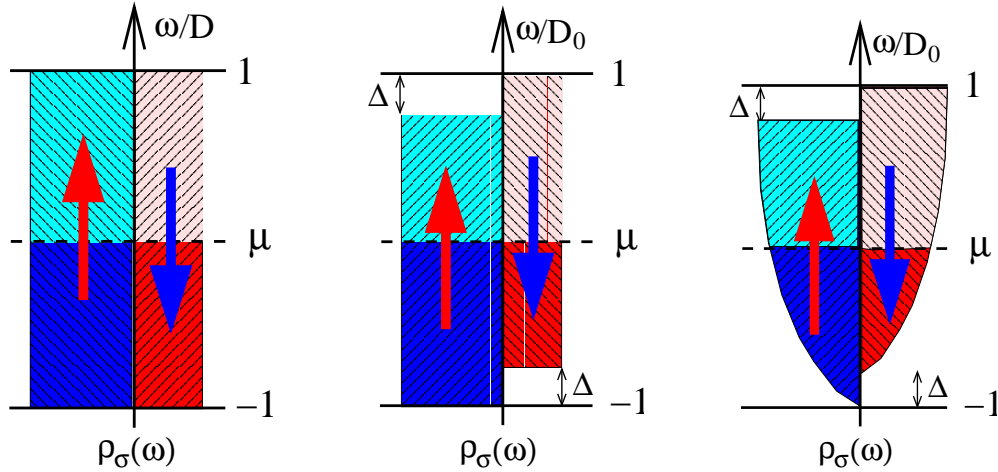


Figure 5.7: In a project we are currently working on we are studying the effect on the Kondo resonance for these three DoS classes. This study summarizes the studies presented above. Case (a) was investigated in [15] without investigating the gate voltage dependence of the spin splitting. The scenario with a finite Stoner-splitting, case (b), has so far not been investigated with NRG. Case (c) corresponds to a DoS as used in [54].

Chapter 6

Non-monotonic occupation in two-level QDs

In Chapter 3.2.4 we pointed out that an increase in Γ , i.e. an opening of the QD, results in a significant enhancement of T_K , see Eq. (3.29). This adjustment is sometimes required to reach the goal $T_K \lesssim T_{\text{exp}}$ (where T_{exp} is set by the fridge). However, when Γ becomes of the order of the level spacing Δ , $\Gamma \sim \Delta$, inter-orbital processes inside the QD might become relevant [61], i.e. a single-level AM does not properly describe the QD any more.

Indeed, recent experiments on a 'Kondo-QD' [8, 62]¹, observed an anomaly which can not be explained by means of a single-level AM. To be more specific: in Refs. [8, 62] Yang *et al.* observed an increase in the transmission phase ϕ of a QD in the Kondo valley by almost 2π (for detailed information see [8, 62]). This observation can not be explained in the framework of a single-level AM, as theoretically shown by Gerland *et al.* [33] (in Ref. [33] the transmission phase of a single-level AM was predicted to increase by π inside a Kondo valley). However, since the QD in [8, 62] is rather open (with a ratio $\Delta/\Gamma \approx 1-3$) it is very likely that a simple single-level AM is not capable of all processes involved in these experiments.

Motivated by these experiments [8, 62] and a theoretical study of Silva *et al.* [61] we initiated a study on a two-level AM. In contrast to Ref. [61], however, we studied a two-level QD including *interactions*.

In this studies we find, somehow surprisingly, a non-monotonic filling of the local levels upon lowering them w.r.t. the chemical potential of the leads. Naively one might expect, based on standard Coulomb blockade, that the QD levels should fill one after the other. It is the interplay between the relevant energy scales Δ , Γ_u (the coupling strength of the upper level), Γ_ℓ (the coupling strength of the lower level) and U that can lead to a non-monotonic filling of the two local levels, as presented below. Thus, the appropriate filling scheme of a more complicated QD depends strongly on the above mentioned parameters. Of course, in the limit $\Delta \gg \Gamma_u, \Gamma_\ell$ standard Coulomb blockade is recovered.

¹The parameters of the QDs in these experiments were: $U \approx 1.5\text{meV}$, $\Delta \approx 0.1-0.5\text{meV}$, $U/\Gamma \approx 1-10$, $T_K \approx 500\text{mK}$ and $T_{\text{exp}} = 50\text{mK}$.

As the observed non-monotonicity is due to interaction and not to spin effects, we first study this phenomenon with *spinless* electrons. The results of this study are shown below [27] (submitted to Phys. Rev. Lett.). A generalization of the findings presented below to the spinfull case is currently in preparation.

Charge oscillations in Quantum Dots

Michael Sindel,¹ Alessandro Silva,^{2,3} Yuval Oreg,³ and Jan von Delft^{1*}

¹*Physics Department and Center for NanoScience, LMU München, 80333 München, Germany*

²*Center for Materials Theory, Department of Physics and Astronomy, Rutgers University, Piscataway, NJ 08854, USA*

³*Department of Condensed Matter Physics, The Weizmann Institute of Science, Rehovot 76100, Israel*

(Dated: August 4, 2004)

We analyze the local level occupation of a spinless, interacting two-level quantum dot coupled to two leads by means of Wilson's numerical renormalization group method. A gate voltage sweep, causing a rearrangement of the charge such that the system's energy is minimized, leads to oscillations, and sometimes even inversions, in the level occupations. These charge oscillations can be understood qualitatively by a simple Hartree analysis. By allowing a relative sign in one tunneling matrix element between dot and leads, we extend our findings to more generic models.

PACS numbers: 73.63.Kv, 73.23.Hk, 72.10.-d

Introduction. - Small Quantum Dots (QD) are electron droplets confined in a small area [1] characterized by a relatively large level spacing Δ , and a comparably large charging energy U . The enhanced level spacing makes these systems ideal devices to study various physical phenomena [2] such as Coulomb Blockade (CB) [3] and the Kondo effect [4]. Moreover, QDs are of interest as the basic elements of spin qubit realizations [5].

In experimental realizations QDs are typically connected by tunnel barriers to metallic leads whose role is to feed the QD with electrons, as well as to allow for transport measurements through it. By changing the gate voltage applied to a plunger gate close to the QD, the single particle spectrum of the QD can be (rigidly and linearly) shifted downwards relative to the Fermi level in the leads. Correspondingly, the single particle levels in the QD would naively be expected to get occupied one by one, in order of increasing energy.

In this Letter, we show that this simple picture of the charging process is only an extreme limit of a much richer and interesting phenomenology. To demonstrate this, it suffices to consider a very simple model: we study a spinless, interacting two-level Anderson model (2LAM), consisting of a lower and an upper QD level ($\epsilon_\ell, \epsilon_u$) with level spacing $\Delta \equiv \epsilon_u - \epsilon_\ell$. (A possible experimental realization is discussed at the end; more general models, e.g. including spin, show effects similar to those described below.) We use both the numerical renormalization group (NRG) and a self-consistent Hartree approximation to calculate, at temperature $T = 0$, the evolution of the occupation of the single particle levels as a function of gate voltage.

The *generic picture* of the charging process emerging from our analysis is the following. For any finite coupling to the leads Γ ($\ll \Delta$), sweeping the levels towards the lead Fermi level (by tuning the gate voltage) causes the occupations of both, lower *and* upper, levels to *increase at comparable rates*. This process continues until one level takes over and becomes more occupied than the other. At this point the electron that occupies this level electrostatically repels the other level, pushing up its en-

ergy and emptying it. As a result the occupation of the other level *performs an oscillation* as the gate voltage is swept. The naive QD charging scheme, in which every step of the CB staircase is associated with the filling of *only one* single particle level in the QD, is only achieved when these charge oscillations are small, i.e. for $\Gamma \ll \Delta$. Below, we discuss in detail the physics of "charge oscillations" and the dependence of their amplitude and form on the system parameters. In particular, we discuss under which conditions the amplitude of these oscillations can be made so large as to cause an occupation inversion, i.e., lower level *less* occupied than upper level.

Model. - We consider a spinless 2LAM with Hamiltonian $\hat{\mathcal{H}} = \hat{\mathcal{H}}_d + \hat{\mathcal{H}}_\ell + \hat{\mathcal{H}}_r$. Two leads, identical, non-interacting and in equilibrium, are described by $\hat{\mathcal{H}}_\ell = \sum_{ka} \epsilon_{ka} c_{ka}^\dagger c_{ka}$, where c_{ka}^\dagger creates an electron with energy ϵ_k in lead $a = L, R$. The isolated QD is described by

$$\hat{\mathcal{H}}_d = \sum_{i=\ell, u} \epsilon_i d_i^\dagger d_i + U \hat{n}_\ell \hat{n}_u, \quad (1)$$

where d_i^\dagger creates an electron in the QD in level ϵ_i ($i = \ell, u$), measured w.r.t. the Fermi level defined by the leads, $\hat{n}_i = d_i^\dagger d_i$ is the number operator, and U is the charging energy, which we fix at $U = 0.2D$ throughout this Letter, $2D$ being the bandwidth. Finally, the tunneling between the QD and the leads is described by $\hat{\mathcal{H}}_{ld} = \sum_{kia} (V_{kia} c_{ka}^\dagger d_i + h.c.)$. We consider k -independent tunneling matrix elements $V_{kia} = V_{ia}$, which are L - R -symmetric in magnitude [6], $V_{uL} = V_{uR} = V_u$ and $V_{\ell L} = s V_{\ell R} = V_\ell$, but with a possible relative phase $s = \exp(i\phi)$ between the L and R matrix elements of the lower level [7]. Time reversal symmetry implies $\phi = 0, \pi$ (hence $s = \pm 1$). The corresponding bare level widths are $\Gamma_i = 2\pi\rho V_i^2$, where ρ is the density of states in the leads.

The two possible choices for $s = \pm 1$ lead to two distinct models (see Fig. 1): (i) for $s = +1$, both local levels couple to the same channel, namely the symmetric linear combination of the left and the right lead ($c_{kL} + c_{kR}$), while the antisymmetric combination ($c_{kL} - c_{kR}$) decouples completely; (ii) for $s = -1$, the upper and lower local

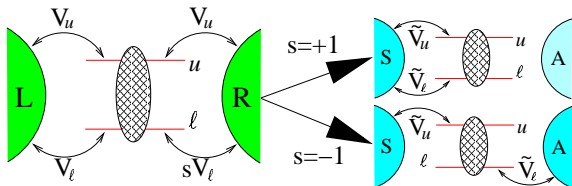


FIG. 1: Schematic depiction of the model. The sign s between the tunneling amplitudes V_{lR} and V_{lL} determines whether the two dot levels couple to the *same* (symmetric) channel ($s = +1$, upper mapping), or to two *different* channels ($s = -1$, lower mapping), with strength $\tilde{V}_i = \sqrt{2}V_i$, $i = \ell, u$.

levels couple to different channels, namely to the symmetric or antisymmetric combinations, respectively [8].

We shall denote the ground state expectation value of the occupation of level i by $n_i = \langle \hat{n}_i \rangle$, and parameterize the gate voltage by the average bare level position $\epsilon \equiv (\epsilon_\ell + \epsilon_u)/2$. For $\Gamma_\ell = \Gamma_u = \Gamma$, this parameterization reveals particle-hole symmetry [9] around $\epsilon^* = -U/2$, namely $n_u(\epsilon + \epsilon^*) = 1 - n_\ell(\epsilon^* - \epsilon)$, independent of Δ and Γ . If $\Gamma_\ell \neq \Gamma_u$, this symmetry is broken for both $s = \pm 1$.

Charge oscillations.— We start our analysis by considering equally coupled levels, $\Gamma_\ell = \Gamma_u = \Gamma$, and use NRG [10] to calculate the ϵ -dependence of n_i . Naively one may expect that if the QD is initially empty, the QD levels get occupied monotonically one by one as ϵ is decreased, the usual CB behavior. In other words, first the occupation of the lower level would be expected to increase monotonically as ϵ_ℓ crosses the Fermi level, and subsequently n_u would increase as $\epsilon_u + U$ approaches it. However, our NRG results [Fig. 2] show that this intuitive picture is valid only if the coupling to the leads is much smaller than the dot level spacing, $\Gamma \ll \Delta$. In particular, when $\Gamma \gtrsim \Delta$, n_ℓ and n_u show a *non-monotonic* ϵ -dependence, characterized by *charge oscillations* of n_u (or n_ℓ) when the lower (or upper) level crosses the Fermi level [11]. The oscillation in n_u occurs because as soon as the lower level begins to be occupied significantly, the system can gain charging energy by additionally filling the lower level and emptying the upper level (an analogous argument works for n_ℓ).

To explore how strongly these charge oscillations vary with Γ , Δ and how they are affected by the sign of s , we show in Fig. 2 the behavior of $n_i(\epsilon)$ for variable Γ and $s = \pm 1$, keeping Δ fixed (at $0.2U$). In the limit $\Gamma/\Delta \ll 1$ level ℓ becomes occupied rather suddenly (curve 1') when it crosses the Fermi level at $\epsilon = \Delta/2$, and similarly for the upper level at $\epsilon = -U - \Delta/2$ (curve 1). In addition to this typical CB behavior, we observe, even for the smallest Γ considered ($\Gamma = 0.1\Delta$), a tiny non-monotonicity or *charge oscillation* in n_u (n_ℓ) roughly at that ϵ where the occupation of the lower (upper) level increases sharply from 0 to 1. A gradual increase of Γ towards $\Gamma/\Delta \approx 1$ results in a strengthening of these charge oscillations. In

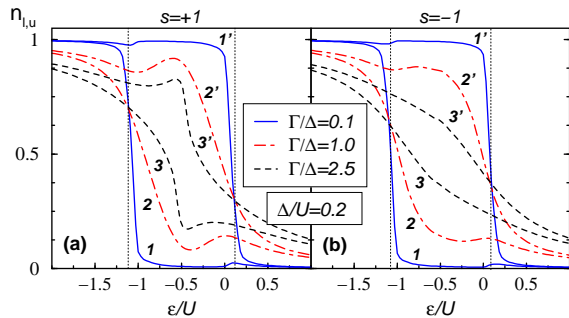


FIG. 2: NRG results for the occupation of the lower [n_ℓ , (curves 1' - 3')] and the upper level [n_u , (curves 1 - 3)] for fixed Δ and different values of Γ , for (a): $s = +1$ and (b): $s = -1$. The dotted lines indicate where the lower/upper level crosses the Fermi level, at $\epsilon = \Delta/2$ and $\epsilon = -U - \Delta/2$.

the limit $\Gamma/\Delta \gg 1$, Fig. 3 (c) and (d), the monotonic increase in the occupation is recovered, though the actual dependence of n_i on ϵ depends strongly on the sign of s .

Hartree approach.— A simple and qualitative understanding of the charge oscillations observed in our NRG results can be formulated in the framework of a self-consistent Hartree approximation (scHA), and studying the evolution of the Hartree levels as function of ϵ . This scheme accounts for the interaction by replacing the bare levels ϵ_i of the *noninteracting* problem, with the corresponding Hartree levels

$$\epsilon_i \rightarrow \epsilon_i^H = \epsilon_i + U n_{\bar{i}}, \quad (2)$$

where $\bar{i} = \ell/u$ if $i = u/\ell$. By integrating out the leads, we obtain the effective noninteracting dot Hamiltonian

$$\mathcal{H}_d^{\text{eff}} = \begin{pmatrix} \epsilon_u^H - i\Gamma_u & (-i\sqrt{\Gamma_u\Gamma_\ell})\delta_{s,+1} \\ (-i\sqrt{\Gamma_u\Gamma_\ell})\delta_{s,+1} & \epsilon_\ell^H - i\Gamma_\ell \end{pmatrix}. \quad (3)$$

The corresponding retarded dot Green's function, defined as $\mathcal{G}_{ij}^R(t) \equiv -i\theta(t)\langle \{d_i(t), d_j^\dagger(0)\} \rangle$, can be obtained exactly for both values of s , by solving the matrix equation $\mathcal{G}^R(\omega) = (\omega - \mathcal{H}_{\text{eff}})^{-1}$. To finally obtain the Hartree approximation for the *interacting* Green's function, one has to self-consistently calculate the average level occupation $n_i(\epsilon)$, using the $T = 0$ relation

$$n_i(\epsilon) = -\frac{1}{\pi} \int_{-\infty}^0 d\omega \text{Im} \mathcal{G}_{ii}^R(\omega, \epsilon). \quad (4)$$

Since the self-consistent Hartree equation (4) may have more than one solution, a criterion is needed to pick the correct one. To this end, we note that, for given ϵ , the system adjusts its local level occupations n_u and n_ℓ such that its total free energy $F_s(n_u, n_\ell)$ is minimized. Within the scHA approach, F_s can be obtained by integrating Eq. (4), so that the conditions for F_s to be extremal, $\partial F_s / \partial n_i = 0$, reproduce Eq. (4); we should then pick that solution of Eq. (4) for which the extremum is a *global*

minimum of F_s . In the case of *two* nearly degenerate minima, the scHA neglects the possibility of tunneling between them, and a different approach has to be considered. Nevertheless we find, somehow unexpectedly, that in the case of exactly degenerate minima, e.g. $\Delta = 0$, an average over the minima reproduces the NRG results rather accurately (see $s = -1$ parts of Figs. 3, 4).

For simplicity we implemented this strategy explicitly for $s = -1$, but not for $s = +1$, since for the latter $\mathcal{H}_d^{\text{eff}}$ is not diagonal, which makes the determination of F_{+1} very tedious. For $s = -1$, Eq. (4) yields the condition $n_i(\epsilon) = \frac{1}{2} - \frac{1}{\pi} \arctan\{(\epsilon_i + Un_i)/\Gamma_i\}$, and the corresponding free energy has the form

$$F_{-1} = Un_\ell n_u + \sum_{i=u,\ell} \left[\epsilon_i n_i - \frac{\Gamma_i}{\pi} \log(\sin \pi n_i) \right]. \quad (5)$$

Figs. 3 and 4 compare NRG with corresponding scHA results for $n_i(\epsilon)$. For $s = -1$, we minimized F_{-1} [Eq. (5)] and find remarkably good agreement between NRG and scHA. For $s = +1$, for which we did not determine F_{+1} , we show the results of a “naive scHA”, obtained by simply plotting a numerical solution of Eq. (4) and “hoping” (without checking) that it is the correct one. Clearly, the results so obtained cannot be trusted on their own merit; we present the naive scHA results nevertheless, to illustrate precisely this point: indeed, in Fig. 3(a,c) [for $\Gamma/\Delta > 1$] they do *not* agree well with NRG results.

In addition to providing a simple way to compute physical quantities, the scHA, and in particular the concept of Hartree levels [see insets of Fig. 3(b,d)], may be used to qualitatively understand how the physics of the charge oscillations depends on the various system parameters.

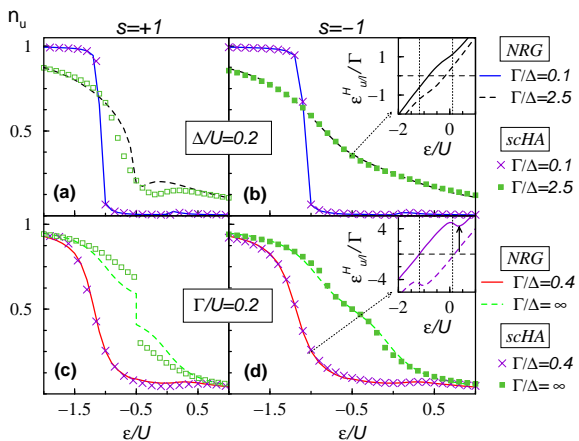


FIG. 3: Comparison of NRG and scHA results for $n_u(\epsilon)$, for fixed Δ and variable Γ [(a), (b)] or fixed Γ and variable Δ [(c), (d)]. The naive scHA used for $s = +1$ works well for $\Gamma/\Delta < 1$. Insets in (b) and (d): corresponding Hartree levels ϵ_ℓ^H and ϵ_u^H (dashed and solid lines), from Eq. (2). The arrow in (d) denotes the local minimum of ϵ_u^H at ϵ_0 .

Suppose that both Hartree levels are swept downwards, starting from ϵ well above the Fermi level. When the lower level comes within Γ_ℓ of the Fermi level, it begins to fill up and the upper Hartree level ϵ_u^H is pushed up by U , causing a charge oscillation in n_u . The latter will be stronger the larger n_u was before the oscillation, i.e., the larger the width (Γ_u) of the upper level, and the lower the value $\epsilon_u^H(\epsilon_0)$ of the upper Hartree level at its local minimum, say ϵ_0 (cf. Fig. 3). Indeed, if $\epsilon_u^H(\epsilon_0) \leq \Gamma_u$, then the upper level achieves a rather significant occupation before full occupation of the lower level (and corresponding emptying of the upper one), implying an increase in the amplitude of the corresponding charge oscillation. Moreover, since $\epsilon_u^H(\epsilon_0)$ is also the lower the more suddenly the lower level gets filled, a smaller Γ_ℓ also strengthens the charge oscillations. Thus, strong charge oscillations can be obtained quite generally by allowing $\gamma \equiv \Gamma_u/\Gamma_\ell \neq 1$. The above argument implies that n_u -oscillations are enhanced for $\gamma \gg 1$; by an analogous argument, with $\ell \leftrightarrow u$, n_ℓ -oscillations are strengthened for $\gamma \ll 1$.

Fig. 3 (c) and (d) include a special situation, namely $\gamma = 1$ and $\Delta = 0$, for which both $\epsilon_\ell = \epsilon_u$ and $\epsilon_\ell^H = \epsilon_u^H$. This causes a sudden jump for $s = +1$ in n_u (Fig. 3 c), but none for $s = -1$ (Fig. 3 d). To understand why, note that for $\Delta = 0$ and $s = +1$ the odd local combination ($d_u - d_\ell$) decouples from the leads; thus, its width is zero and hence its occupation increases abruptly when its energy drops below zero. On the other hand, for $s = -1$ the occupation increases gradually, since the width of the odd combination is comparable to that of the even one ($d_u + d_\ell$). A similar argument explains why for small but non-zero Δ/Γ (odd level almost decoupled for $s = +1$) as in Fig. 2, curves 3 and 3', the charge oscillations are still observable for $s = +1$ but not for $s = -1$.

Occupation inversion.— Interestingly, when either $\gamma \ll 1$ or $\gamma \gg 1$, the lower and the upper Hartree levels might actually cross each other (see inset Fig. 4d), leading to an inverted occupation [Figs. 4(a) to 4(f)].

Since the bare energy levels are separated by the level spacing Δ , the conditions $Un \gtrsim \Delta$ and $\max(\Gamma_\ell, \Gamma_u) \gtrsim \Delta$ must be met to achieve such an occupation inversion. Figs. 4(a) to 4(f) show how the asymmetry ($\gamma \neq 1$) of the couplings affects the occupation of level ℓ and u (dashed and solid lines) both for $s = \pm 1$, leading to an inversion of the occupation within a certain range of ϵ .

Our discussion of occupation inversion generalizes a recent related study by Silvestrov and Imry [12]. In an attempt to understand the origin of repeated and abrupt phase lapses observed in the transmission phase of a multilevel QD [13], they studied a multilevel model consisting of one level (say u with coupling Γ_u) strongly coupled to the leads and at least one additional weakly coupled level (say ℓ with coupling Γ_ℓ). They considered the particular case $\Gamma_u \gg \Delta \gg \Gamma_\ell \rightarrow 0$, and compared the energies of the configuration $(n_u, n_\ell) = (1, 0)$ to that of $(n_u, n_\ell) = (0, 1)$ in second order perturbation the-

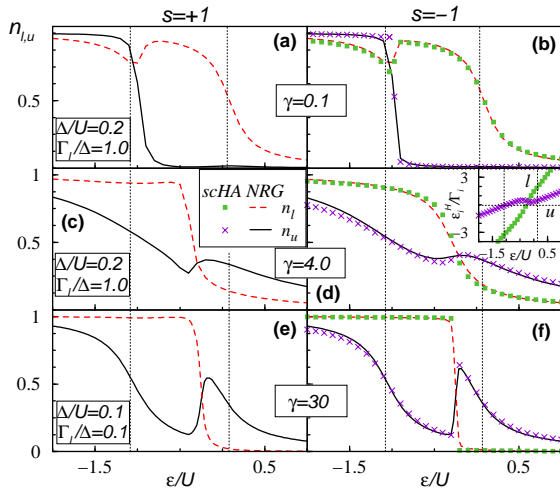


FIG. 4: (a)-(f): $\gamma \neq 1$ results in an *inversion* of the occupation for a certain range of ϵ . The scHA results (crosses, boxes) for $s = -1$ (where F_{-1} is known) agree well with NRG results (solid, dashed lines). For $\gamma > 1$ (< 1) the Hartree levels cross near the right (left) CB peak (see inset (d)) for $\gamma = 4$, implying an occupation inversion above (below) the corresponding crossings.

ory in the tunneling. Their results indicate that the system is able to sustain an occupation inversion until $\epsilon_u = -U / [\exp(2\pi\Delta/\Gamma_u) + 1] \approx -U/2$. Although we study this problem from an opposite point of view, i.e., we either solve it exactly by NRG or first solve the tunnel-coupling exactly and then treat the interaction self-consistently, the inversion range found in Ref. [12] coincides with the results [14] of this Letter.

Our analysis indicates that the example of Ref. [12] for occupation inversion is a special case of a more general phenomenon whose strength depends on γ : as γ is increased from 1 (where no occupation inversion occurs), (i) the range of gate voltages in which inversion occurs increases, with the inversion point moving towards the middle of the CB valley; and (ii) the maximal value reached by n_u right before the inversion increases gradually towards 1, i.e., the effect becomes more pronounced.

Experimental realization. — We expect that our predictions of the non-monotonicity of the charging of a 2LAM should be experimentally relevant (in spirit, if not in detail) for any quantum dot system containing orbital levels that are “nearly degenerate”, in the sense that their spacing is smaller than the level widths. One way of realizing the specific models studied here would be to use two capacitively coupled quantum dots, each with large level spacings, associating their topmost not-fully-occupied levels with ϵ_u and ϵ_l , and using a large magnetic field to lift the Zeeman degeneracy of each. The way in which the charges on these dots evolve with gate voltage, i.e., the evolution of $n_i(\epsilon)$, could then be measured experimentally using QPC’s serving as extremely sensitive

charge sensors, see e.g. Fig. 1 (a) of Ref. [15].

Summary. — We have studied the gate voltage dependence of the occupation of a spinless two-level Anderson model for the generic case of a relative sign s in the tunneling amplitude. We found a non-monotonic behavior in the occupation of the local levels, due to charging effects between electrons within the QD, and explained this effect in the framework of a self-consistent Hartree approximation. Remarkably, the occupations of the upper and lower levels can even be inverted if the level-to-lead couplings are sufficiently asymmetric. We expect similar effects to occur quite generally, for any quantum dot system having level spacings comparable to level widths.

We thank R. Berkovitz, L. Borda, Y. Gefen, U. Hartmann, M. Heiblum, F. Hekking, J. König, F. von Oppen, and G. Zarand for clarifying discussions. Financial support from SFB 631 of the DFG, CeNS, Minerva and DIP is gratefully acknowledged. While performing this work, we became aware of parallel work [16] that is closely related to ours.

* Correspondence to michael.sindel@physik.lmu.de

- [1] In GaAs-AlGaAs a QD of area $A \approx 0.1\mu\text{m} \times 0.1\mu\text{m}$ has $\Delta \approx 0.5\text{meV} \approx 6\text{K}$ and $U \approx 1.5\text{meV}$.
- [2] L.P. Kouwenhoven *et al.*, in *Mesoscopic Electron Transport*, edited by L.L. Sohn, L.P. Kouwenhoven, and G. Schön, NATO ASI Series (Kluwer, Dordrecht, 1997).
- [3] U. Meirav and E.B. Foxman, *Semicond. Sci. Technol.*, **10**, 255 (1995).
- [4] D. Goldhaber-Gordon *et al.*, *Nature* **391**, 156 (1998); L. I. Glazman and M. E. Raikh, *JETP Lett.* **47**, 452 (1988).
- [5] D. Loss and D.P. DiVincenzo, *Phys. Rev. A* **57**, 120 (1998).
- [6] For $V_{uR} = V_{lL} = 0$, our model includes the case of two dots (levels u, l) separately coupled to two leads (L,R).
- [7] A. Silva, Y. Oreg, Y. Gefen, *Phys. Rev. B* **66**, 195316 (2002), study an equivalent noninteracting model for $|V_{ia}| \equiv V, i = u, l, a = L, R$. See also O. Entin-Wohlman *et al.*, *Phys. Rev. B* **34**, 921 (1986); Q. Sun and T. Lin, *Euro. Phys. J. B* **5**, 913 (1998).
- [8] If we distinguish the symmetric and antisymmetric combination of the leads with an isospin index, the case $s = -1$ corresponds to an effective *single-level* Anderson model for (iso)spinful electrons, with (iso)spin-dependent couplings and an effective magnetic field Δ ; a model used to study a spinfull QD coupled to ferromagnetic leads [J. Martinek *et al.*, *Phys. Rev. Lett.* **91**, 247202 (2003)].
- [9] For $\Gamma_l = \Gamma_u$ (and both $s = \pm 1$), the system is particle-hole-symmetric under $c_k \rightarrow \tilde{c}_{-k}^\dagger$ and $d_i \rightarrow -\tilde{d}_i^\dagger$ where $\tilde{i} = l/u$ if $i = u/l$, implying $n_i \rightarrow (1 - \tilde{n}_i)$.
- [10] K.G. Wilson, *Rev. Mod. Phys.* **47**, 773 (1975).
- [11] After completion of this work, we became aware that small oscillations had been noted (but not studied systematically) by R. Berkovits, cond-mat/0306284.
- [12] P.G. Silvestrov and Y. Imry, *Phys. Rev. Lett.* **85**, 2565 (2000).
- [13] Schuster *et al.*, *Nature* **385**, 417 (1997).
- [14] $F_{-1}(0, 1) = F_{-1}(1, 0)$ determines this range.
- [15] D. Sprinzak *et al.*, *Phys. Rev. Lett.* **88**, 176805 (2002).
- [16] J. König and Y. Gefen, unpublished.

Chapter 7

Frequency-dependent transport in the Kondo regime

In this study (submitted to Phys. Rev. Lett.) we focus on the linear *AC conductance* $G(\omega) = G'(\omega) + iG''(\omega)$ (usually a complex quantity) of a single level QD (i.e. $\Delta/\Gamma \gg 1$). In typical experiments where Kondo correlations are important usually the linear DC conductance is measured. Therefore recent studies have mostly focused on this quantity. However, a measurement of the AC conductance has recently come into experimental reach [63].

Therefore, we generalize previous conductance studies in the Kondo regime to the AC case. For this sake we have to determine the complex quantity $G(\omega)$. Note that the DC conductance $G(\omega = 0)$ is purely real, $G(\omega = 0) = G'(\omega = 0)$. We use the Kubo formalism (see appendix F) to obtain a reliable, nonperturbative calculation of $G(\omega)$ which is reliable at all frequencies ω . This is because for sufficiently large values of ω , $\omega \gg U$, the charge on the island is fluctuating, so the used formalism has explicitly to allow for charge fluctuations.

We derive an approximate formula, a first order perturbation expansion of the result of Jauho *et al.* [64], for the linear AC conductance in the Kondo regime valid for frequencies ω much smaller than the charge-excitation energy $\Delta_c = \min\{|\epsilon_d|, |U + \epsilon_d|\}$. The validity of this formula is demonstrated by comparing it with the conductance calculated within the framework of the Kubo formalism.

The numerics reveals that $G'(\omega)$ has the same power laws as the spectral function $A(\omega)$ for frequencies $\omega \leq T_K$. This fact suggests that $A(\omega)$ and $G'(\omega)$ are related to each other. Indeed, the derived analytical formula (from [64]) allows us to relate both quantities in the limit of $|\omega| \ll \Delta_c$. This establishes a useful relation between the frequency-dependent conductance $G(\omega)$ and the spectral function $A(\omega)$.

Moreover, it was demonstrated in recent experiments of Deblock *et al.* [65] that it is feasible to measure the current fluctuations of a mesoscopic device at frequencies up to 90GHz. Motivated by this experiments we also calculate the frequency-dependent equilibrium current fluctuations $C(\omega)$. The fluctuation dissipation theorem (FDT) establishes a relation between the conductance $G(\omega)$ and the current fluctuations $C(\omega)$, which enables us

to establish a relation between the frequency-dependent noise $C(\omega)$ with the symmetrized spectral function $A_s(\omega)$ ¹ (which by itself is related to $G(\omega)$), for $|\omega| \ll \Delta_c$. This relation is of experimental relevance, as it allows one to extract the symmetrized equilibrium spectral function $A_s(\omega)$ (for $|\omega| < \Delta_c$, i.e. the Kondo peak) from a measurement of the frequency-dependent noise.

In our calculations we assume a time-dependent chemical potential in the leads. Since the leads are capacitively coupled to the local dot level one expects also an oscillating local level - an effect which we disregard as this capacitive coupling is a rather weak one. We study the effect of an alternating chemical potential of the left and right lead which is realized by applying an AC bias voltage (of frequency ω_{AC}). Experimentally the frequency of the (time-dependent) AC bias voltage has to be chosen such, that the Kondo scale can be detected, i.e. $\hbar\omega_{AC} \sim k_B T_K$. For a typical value of T_K , $T_K = 1\text{K}$, the frequency-dependent conductance $G(\omega)$ has thus to be determined for frequencies ω_{AC} up to $\sim 20\text{GHz}$.

¹For $|\omega| \ll \Delta_c$ this quantity is identical to $A(\omega)$ to a very good approximation.

Frequency-dependent transport through a quantum dot in the Kondo regime

M. Sindel,¹ W. Hofstetter,² J. von Delft,¹ and M. Kindermann²

¹*Physics Department and Center for NanoScience, LMU München, 80333 München, Germany*

²*Department of Physics, Massachusetts Institute of Technology, Cambridge MA 02139, USA*

(Dated: July 9, 2004)

We study the AC conductance and equilibrium current fluctuations of a Coulomb blocked quantum dot. A relation between the equilibrium spectral function and the linear AC conductance is derived which is valid for frequencies well below the charging energy of the quantum dot. Frequency-dependent transport measurements can thus give experimental access to the Kondo peak in the equilibrium spectral function of a quantum dot. We illustrate this in detail for typical experimental parameters using the numerical renormalization group method in combination with the Kubo formalism.

In the past years semiconductor quantum dots have gained considerable attention as tunable magnetic impurities [1]. Due to their small size, electronic transport through these structures is strongly influenced by the Coulomb blockade [2]. Quantum dots with an odd number of electrons display a well-known many-body phenomenon, the *Kondo effect* [3, 4], as predicted in [5]. In these systems, a single unpaired spin is screened at low temperatures, giving rise to an enhanced DC (zero-frequency) conductance at low bias voltage.

Theoretical studies have so far mostly focused on the DC conductance [5] and zero-frequency noise [6]. From the differential conductance dI/dV at finite bias voltage V one can obtain information about the Kondo resonance in the spectral density. Such measurements, however, yield only an *average* of the spectral density in a frequency window of width eV . Moreover, in a typical quantum dot coupled to two leads with comparable strength, they access only the spectral function under non-equilibrium conditions. It is known that in this case a finite bias suppresses the Kondo peak [7]. It has been demonstrated experimentally that an AC modulation of the gate or bias voltage has a similar effect [8, 9].

In this Letter we suggest that the Kondo resonance in the *equilibrium* spectral function can be measured by a frequency-dependent transport measurement. We derive a direct relation between the spectral function and the linear AC-conductance through a quantum dot. Alternatively, the Kondo peak can be measured by detecting equilibrium fluctuations in the current through the quantum dot at frequencies of the order of the Kondo temperature T_K . Such measurements have come into experimental reach with recent advances in the measurement of high-frequency current fluctuations [10]. Conductance measurements in the relevant frequency regime are challenging, mainly due to parasitic currents through hardly avoidable capacitances. One should, however, be able to extract the signal due to the current through the quantum dot from this background by an adiabatic change (much slower than the inverse Kondo temperature [11]) of gate voltage that drives the dot periodically into and out of the Kondo regime.

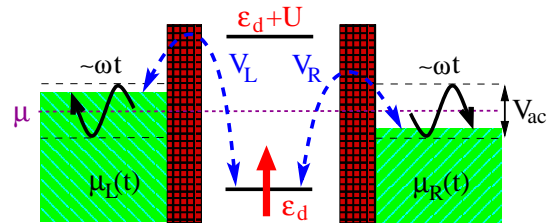


FIG. 1: The studied setup. We extend previous studies on the single-level Anderson model by allowing for time dependent chemical potential $\mu_\alpha(t) = \mu \pm (eV_{ac}/2) \cos \omega t$ in lead $\alpha \in \{L, R\}$.

We predict the frequency-dependence of the AC conductance and the equilibrium noise for typical experimental parameters. We apply the nonperturbative numerical renormalization group (NRG) [12] in combination with the Kubo formalism. This extends previous calculations which used perturbative methods [13]. It allows us to access the most interesting regime of frequencies of the order of the Kondo temperature for a device that exhibits a strong Kondo effect.

The exact correspondence between spectral function and AC-conductance holds only when charge fluctuations on the quantum dot are negligible. Using our rigorous NRG results, we verify that this condition is well satisfied for frequencies below the charging energy of the dot.

The setup that we study is shown in Fig. 1. At low energies, a Coulomb-blockaded quantum dot is well described by the single-level Anderson model

$$H = \sum_{\sigma} \epsilon_{d\sigma} d_{\sigma}^{\dagger} d_{\sigma} + U n_{d\uparrow} n_{d\downarrow} + \sum_{k\alpha\sigma} V_{\alpha} (d_{\sigma}^{\dagger} c_{k\alpha\sigma} + h.c.) + \sum_{\substack{k\sigma \\ \alpha \in \{L, R\}}} [\epsilon_k - \mu_{\alpha}(t)] c_{k\alpha\sigma}^{\dagger} c_{k\alpha\sigma}, \quad (1)$$

where the chemical potentials $\mu_{L(R)}(t) = \mu \pm (eV_{ac}/2) \cos \omega t$ for the left (right) lead include a time-dependent bias V_{ac} . We assume that the AC perturbation does not couple to electrons in the local level

d_σ ($n_{d\sigma} = d_\sigma^\dagger d_\sigma$). V_α couples the level d to electron states $c_{k\alpha\sigma}$ with momentum k and spin $\sigma = \pm 1$ in lead $\alpha \in \{L, R\}$. In the following, D denotes the conduction electron bandwidth. $\epsilon_{d\sigma} \equiv \epsilon_d + \sigma B^*/2$, $B^* = g\mu_B B$, is the energy of the local level, including the Zeeman shift in presence of a magnetic field B . U is the Coulomb repulsion of electrons on the dot.

Following [14] we relate the current I through the quantum dot to the local Green's function of the level d . For frequencies $\hbar\omega \ll \Delta_c$ much smaller than the charge

excitation energy $\Delta_c = \min\{|\epsilon_d|, |U + \epsilon_d|\}$, charge fluctuations on the quantum dot can be neglected and the currents flowing through the right and the left lead are equal to a good approximation: $I_L = -I_R$. It is then advantageous to write the total current as $I = (I_L - \lambda I_R)/(1 + \lambda)$, where $\lambda = \Gamma_L/\Gamma_R$, $\Gamma_\alpha = \pi\nu V_\alpha^2$ and ν is the conduction electron density of states. Expressing the currents I_L and I_R by the Green's function of d (see Eq. (15) in [14]), we find for energy-independent couplings Γ_α the current

$$I(\omega) = -\frac{2e^2 V_{ac}}{\hbar^2 \omega} \frac{\lambda}{1 + \lambda} \Gamma_R \int_{-\infty}^{\infty} dt e^{i\omega t} \int_{-\infty}^{\infty} dt_1 \int \frac{d\varepsilon}{2\pi} \text{Re} \left[e^{i\varepsilon(t-t_1)} (\sin \omega t - \sin \omega t_1) f(\varepsilon) \mathcal{G}^r(t, t_1) \right] + \mathcal{O}(V_{ac})^2 \quad (2)$$

in linear response to V_{ac} . Here $f(\varepsilon)$ is the equilibrium Fermi function of the leads and $\mathcal{G}^r(t_1, t_2) = -i\theta(t_1 - t_2)\langle\{d(t_1), d^\dagger(t_2)\}\rangle$ the retarded Green's function of d evaluated in equilibrium ($V_{ac} = 0$). From Eq. (2) we obtain the real (G') and imaginary (G'') parts of the linear conductance,

$$G'(\omega) = \frac{e^2}{2\hbar^2 \omega} \frac{\Gamma_L \Gamma_R}{\Gamma} \int d\varepsilon f(\varepsilon) [A(\varepsilon + \omega) - A(\varepsilon - \omega)], \quad (3)$$

$$G''(\omega) = \frac{e^2}{\hbar^2 \omega} \frac{\Gamma_L \Gamma_R}{\Gamma} \int \frac{d\varepsilon}{2\pi} f(\varepsilon) \left[-2\text{Re} \mathcal{G}^r(\varepsilon) + \text{Re} \mathcal{G}^r(\varepsilon + \omega) + \text{Re} \mathcal{G}^r(\varepsilon - \omega) \right], \quad (4)$$

where $\Gamma = \Gamma_L + \Gamma_R$ and $A(\omega) = -\frac{1}{\pi} \text{Im} \mathcal{G}^r(\omega)$ is the spectral function. At zero temperature $kT \ll \hbar\omega$ and in the presence of particle-hole symmetry [$A(\varepsilon) = A(-\varepsilon)$] Eq. (3) is readily inverted. This establishes a relation between $A(\omega)$ and $G'(\omega)$,

$$A(\omega) = \frac{\hbar^2}{e^2} \frac{\Gamma}{\Gamma_L \Gamma_R} \frac{\partial}{\partial \omega} [\omega G'(\omega)], \quad (5)$$

valid in the regime $\hbar\omega \ll \Delta_c$. By Eq. (5), the Kondo peak in the equilibrium spectral function can be extracted from a measurement of the AC-conductance through a quantum dot.

The frequency-dependent equilibrium current fluctuations (Johnson-Nyquist noise)

$$C(\omega) = \int_{-\infty}^{\infty} dt e^{i\omega t} [\langle I(0)I(t) \rangle - \langle I \rangle^2] \quad (6)$$

are related to the linear conductance by the fluctuation dissipation theorem (FDT)

$$C(\omega) = \frac{2\hbar\omega}{\exp(\hbar\omega/kT) - 1} G'(\omega). \quad (7)$$

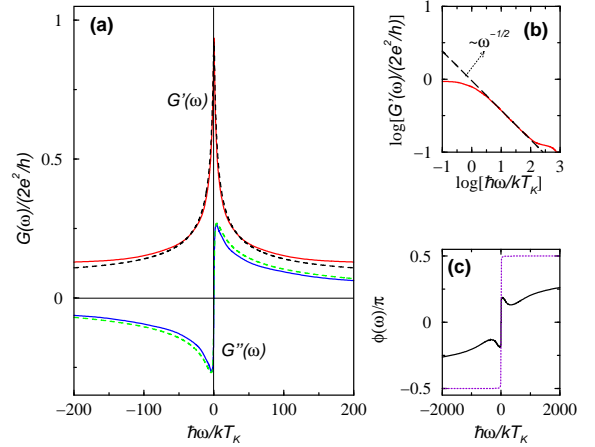


FIG. 2: (a) Real and imaginary parts of the AC conductance obtained via the Kubo approach (solid lines) and from the conductance formulas Eqs. (3) and (4) (dashed lines). Note the excellent agreement for frequencies $\hbar\omega \lesssim 100 kT_K$ ($\Delta_c \approx 600 kT_K$). (b) Doniach-Sunjić tails in $A(\omega)$ are responsible for the power law behavior (dashed line) in the conductance (solid line), $G'(\omega) \sim \omega^{-1/2}$, for frequencies $\hbar|\omega| \gg kT_K$. (c) Comparison of the frequency-dependent conductance phase $\phi(\omega)$ in the Kondo regime (solid line) (parameters $U = 0.12D$, $U/\Gamma = 6$, $\epsilon_d = -U/2$, $T = 0$) with that for a resonant level ($\epsilon_d = 0$) of width kT_K (dotted line).

Consequently, the spectral function can alternatively be inferred from a measurement of $C(\omega)$. At zero temperature, $kT \ll \hbar|\omega|$, we arrive at

$$A(|\omega|) = -\frac{\hbar}{2e^2} \frac{\Gamma}{\Gamma_L \Gamma_R} \frac{\partial}{\partial |\omega|} C(-|\omega|), \quad (8)$$

where we have again assumed particle-hole symmetry. Note that at zero temperature $C(\omega)$ is non-vanishing

only for $\omega < 0$, that is fluctuations have to be measured by probing absorption by the quantum dot. In [10] the measurement of current fluctuations at frequencies up to $\omega \simeq 100$ GHz has been reported. This frequency scale is of the same order of magnitude as the Kondo temperature in typical Kondo quantum dots [1]. It makes noise measurements a promising candidate for experimental studies of the Kondo peak in the spectral function of a quantum dot.

We turn now to a discussion of the frequency dependence of AC-conductance and equilibrium noise in a Kondo quantum dot with typical experimental parameters. We apply the numerical renormalization group (NRG), first used by Wilson to solve the Kondo problem [12]. This method is nonperturbative and does not suffer from low-energy divergences common to scaling approaches. In particular, it provides accurate results in the most interesting crossover regime $\hbar\omega \lesssim kT_K$. Within NRG we apply two independent approaches: Using the Kubo formula, we are able to calculate the conductance in the Anderson model Eq. (1) numerically exactly. On the other hand, using Eqs. (3) and (7), we obtain conductance and noise from the single-particle Green's function of the d level, that we determine by NRG as well. By comparing the two approaches we shall demonstrate the validity of the approximation underlying Eqs. (3) and (4) for frequencies of the order of the Kondo scale.

We apply the Kubo formalism following Izumida *et al.* [15]. We define an electric current from lead L to R as $\hat{I} = \frac{e}{2} [\langle \dot{N}_R \rangle - \langle \dot{N}_L \rangle]$, where $N_\alpha = \sum_{k\sigma} c_{k\alpha\sigma}^\dagger c_{k\alpha\sigma}$ is the total number of electrons in lead α and $\dot{N}_\alpha = \frac{i}{\hbar} [H, N_\alpha]$. Introducing a linear response tensor σ by $\langle \dot{N}_\alpha \rangle = \sigma_{\alpha\beta}(\omega) \mu'_\beta$, where $\mu'_{L(R)} = \pm (eV_{ac}/2) \cos \omega t$ is the time-dependent bias applied to the left (right) lead, the total linear AC conductance takes the form

$$G(\omega) = \frac{e^2}{4} [\sigma_{LL}(\omega) + \sigma_{RR}(\omega) - \sigma_{LR}(\omega) - \sigma_{RL}(\omega)]. \quad (9)$$

The complex response tensor σ can be written as $\sigma_{\alpha\beta}(\omega) = \frac{1}{i\omega} [K_{\alpha\beta}(\omega) - K_{\alpha\beta}(0)]$, where

$$K_{\alpha\beta}(\omega) = -\frac{i}{\hbar} \int_0^\infty dt e^{-\delta t + i\omega t} \langle [\dot{N}_\beta(0), \dot{N}_\alpha(t)] \rangle \quad (10)$$

with $\delta \rightarrow 0^+$. $\langle \dots \rangle$ in Eq. (10) refers to the equilibrium expectation value with respect to the Hamiltonian H with $V_{ac} = 0$. We evaluate this expression using NRG [12]. From the matrix elements of the current operator $\langle n | \hat{I} | m \rangle$ the imaginary part $K''_{\alpha\beta}$ is obtained directly while the real part $K'_{\alpha\beta}$ can be calculated via a Kramers-Kronig transformation.

In Fig. 2 we compare the conductance obtained from Eq. (3) with the result of the calculation in the Kubo formalism for $\epsilon_d = -U/2$ and $B = 0$. We find excellent agreement for frequencies below the charge gap Δ_c .

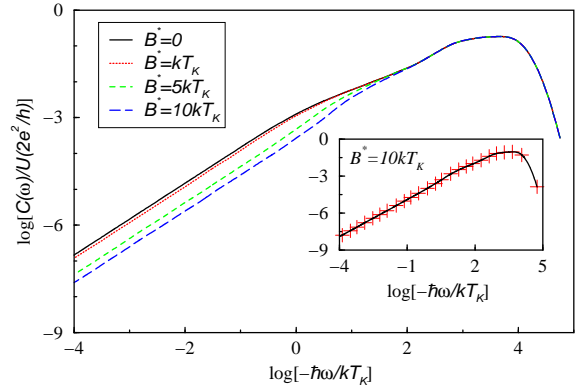


FIG. 3: The equilibrium current fluctuations $C(\omega)$ depend linearly on ω for $\hbar|\omega| \leq kT_K$ [17], as shown for various magnetic fields B . The inset shows that the fluctuations are spin-independent even in presence of a finite magnetic field B^* ($B^* = 10kT_K$, (red) crosses: $\sigma = \uparrow$, (black) solid line: $\sigma = \downarrow$). Parameters: $U = 0.12D$, $U/\Gamma = 6$, $\epsilon_d = -U/2$, $T = 0$.

Moreover the large frequency ($\hbar\omega \gg kT_K$) asymptotes of the conductance reveal a decay of $G'(\omega) \sim \omega^{-1/2}$ [Fig. 2 (b)]. This is expected as a consequence of the Doniach-Sunjić tails of the spectral function [16] together with Eq. (5). The deviation of $G'(\omega)$ from the unitary limit (by $\sim 6\%$) is due to systematic numerical errors accumulating in the NRG procedure. Fig. 2(c) shows the frequency-dependent phase $\phi(\omega)$ of the linear conductance, $G(\omega) = |G(\omega)| e^{i\phi(\omega)}$.

The frequency-dependence of the equilibrium noise obtained by a direct numerical evaluation of Eq. (6) within NRG is plotted in Fig. 3. As one expects, the fluctuations reach a maximum for frequencies $\hbar\omega \sim U$. The linear behavior $C(\omega) \sim \omega$ at small ω is a manifestation of the Fermi-liquid nature of a screened Kondo impurity. Fig. 3 also shows how a finite magnetic field B suppresses low-frequency equilibrium fluctuations. The inset demonstrates that at low frequencies the noise for spin-up and spin-down electrons is identical, even in the presence of a magnetic field. This is because an impurity with large charging energy $\Delta_c \gg \Gamma$ is half-filled: $\langle n_\uparrow \rangle + \langle n_\downarrow \rangle = 1$. As a consequence of the Friedel sum rule [18], the spectral densities at the Fermi energy ϵ_F for spin-up and spin-down electrons $A_{\uparrow/\downarrow}(\epsilon_F) \propto \sin^2(\pi \langle n_{\uparrow/\downarrow} \rangle)$ are then equal.

We now use Eq. (8) to extract the spectral function A from the numerical current noise data of Fig. 3 where charge fluctuations on the dot have been taken into account. The results are shown in Fig. 4. They nicely demonstrate the splitting and the suppression of the Kondo peak upon increasing the external field B . A comparison with the spectral function directly calculated by NRG confirms that Eq. (8) does indeed work very well for frequencies $\hbar\omega \ll \Delta_c$. In particular, our method reproduces the Kondo peak in the spectral function accu-

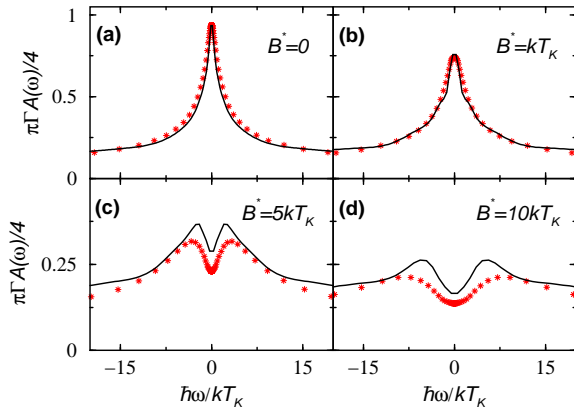


FIG. 4: Spectral function $A(\omega)$, extracted from the current noise $C(\omega)$ via Eq. (8) (lines) and calculated directly by NRG (stars) for different values of the magnetic field B . Eq. (8) captures the Kondo peak in $A(\omega)$ very well, including suppression and splitting in presence of a magnetic field B .

rately. Due to intrinsic broadening in the NRG which affects both $A(\omega)$ and $C(\omega)$, Eq. (8) becomes less accurate for finite B .

Having demonstrated that neglecting charge fluctuations in deriving Eqs. (5) and (8) is very well justified, we comment on another limitation of our approach. Calculating the linear response of the quantum dot, we have assumed the bias voltage in a conductance measurement to be small. While this in itself is not a problem, one might worry, however, that due to the finite frequency of V_{ac} extra decoherence processes would make the limit of linear response very restrictive. The decoherence rate τ of the dot's spin due to the oscillating bias voltage for $\hbar\omega \gg kT_K$ can be estimated [19] as

$$\frac{\hbar\tau^{-1}}{kT_K} \sim \left(\frac{eV_{ac}}{kT_K}\right)^2 \frac{kT_K}{\hbar\omega} \frac{1}{[\ln(\hbar\omega/kT_K)]^2}. \quad (11)$$

For the Kondo physics not to be disrupted by V_{ac} , we need $\hbar\tau^{-1}/kT_K \ll 1$. Eq. (11) shows that this condition can be easily fulfilled by the usual requirement $eV_{ac} \ll kT_K$. We expect that this statement remains true for frequencies of the order of T_K . We conclude that transport is described accurately by our linear response conductance for voltages that are much smaller than the Kondo temperature.

In conclusion, we have studied AC transport through a quantum dot in the Kondo regime, using the numerical renormalization group technique in combination with the Kubo formalism. We have expressed linear conductance and equilibrium current fluctuations in terms of the single-particle Green's function. This relation becomes exact at low frequencies, when charge fluctuations on the dot can be neglected. It has been shown to work

very well for frequencies of the order of the Kondo scale. This opens up the exciting possibility of measuring the *equilibrium* Kondo resonance directly in a transport measurement.

Acknowledgements: We would like to thank S. Amasha, L. Borda, M. Kastner, and A. Kogan for valuable discussions, and L. Glazman for comments on the manuscript. M.S. and J.v.D. acknowledge financial support from SFB 631 of the DFG and CeNS. W.H. has been supported by a Pappalardo fellowship; M.K. by the Cambridge-MIT Institute Ltd.

- [1] L. Kouwenhoven and L. Glazman, *Physics World* **14**, 33 (2001).
- [2] L.P. Kouwenhoven *et al.* in *Mesoscopic Electron Transport*, eds. L.L. Sohn, L.P. Kouwenhoven, and G. Schön, NATO ASI Series E, vol. 345, pp. 105-214 (Kluwer, Dordrecht, 1997).
- [3] A.C. Hewson, *The Kondo Problem to Heavy Fermions*, Cambridge University Press, Cambridge (1993).
- [4] D. Goldhaber-Gordon *et al.*, *Nature* **391**, 156 (1998); S.M. Cronenwett *et al.*, *Science* **281**, 540 (1998); F. Simmel *et al.*, *Phys. Rev. Lett.* **83**, 804 (1999); J. Schmid *et al.*, *Phys. Rev. Lett.* **84**, 5824 (2000); W. G. van der Wiel *et al.*, *Science* **289**, 2105 (2000).
- [5] L.I. Glazman and M.E. Raikh, *Sov. Phys. JETP Lett.* **47**, 452 (1988); T.K. Ng, P.A. Lee, *Phys. Rev. Lett.* **61**, 1768 (1988).
- [6] Y. Meir and A. Golub, *Phys. Rev. Lett.* **88**, 116802 (2002); B. Dong and X.I. Lei, *J. Phys.: Cond. Mat.* **14**, 4963 (2002); R. Lopez and D. Sanchez, *Phys. Rev. Lett.* **90**, 116602 (2003).
- [7] J. Paaske, A. Rosch, J. Kroha, P. Wölfle, *cond-mat/0401180*.
- [8] J. Elzerman *et al.*, *J. Low Temp. Phys.* **118**, 375 (2000).
- [9] A. Kogan, S. Amasha, and M.A. Kastner, *Science* **304**, 1293 (2004).
- [10] R. Deblock, E. Onac, L. Gurevich, and L. P. Kouwenhoven, *Science* **301**, 203 (2003).
- [11] P. Nordlander, M. Pustilnik, Y. Meir, N. S. Wingreen, and D. C. Langreth, *Phys. Rev. Lett.* **83**, 808 (1999).
- [12] K. G. Wilson, *Rev. Mod. Phys.* **47**, 773 (1975); T.A. Costi, A.C. Hewson, and V. Zlatić, *J. Phys.: Cond. Mat.* **6**, 2519 (1994); W. Hofstetter, *Phys. Rev. Lett.* **85**, 1508 (2000).
- [13] R. López, R. Aguado, G. Platero, and C. Tejedor, *Phys. Rev. B* **64**, 075319 (2001).
- [14] A.-P. Jauho, N.S. Wingreen and Y. Meir, *Phys. Rev. B* **50**, 5528 (1994).
- [15] W. Izumida, O. Sakai, and Y. Shimizu, *J. Phys. Soc. Jpn.* **66**, 717 (1997).
- [16] S. Doniach and M. Sunjić, *J. Phys. C: Solid State Phys.* **3**, 285 (1970).
- [17] T_K corresponds to the frequency at which the spin spectral function takes its maximum.
- [18] D.C. Langreth, *Phys. Rev.* **150**, 516 (1966).
- [19] A. Kaminski, Yu.V. Nazarov, and L.I. Glazman, *Phys. Rev. B* **62**, 8154 (2000).

Chapter 8

Kondo correlations in optical experiments

Recent photoluminescence (PL) experiments [2] revealed that it is feasible to measure the absorption and emission spectrum of a single self-assembled QD (an InAs QD embedded in a GaAs semiconductor). It was found that an illumination of the semiconducting QD with photons (of energy $h\nu$) triggers transitions inside the QD where an electron from the valence band (VB) level is elevated to the conduction band (CB) (or vice versa). Hereby an excited state, an exciton (electron-hole pair), is created (or destroyed). In an absorption (emission) experiment the QD *absorbs* (*emits*) a photon of energy $h\nu$ by creating (destroying) an excitonic state, say X .

The spatial confinement of the QD results in a discrete level structure inside the QD. An external gate voltage can rigidly shift the internal level structure leading to a filling (emptying) of the QD. The gate voltage dependence of optical transitions, as found in Ref. [2] [see Fig. 8.1(top panel)], can be understood, by identifying a particular value of the gate value with a particular excitonic state. Here a single exciton with n extra electrons in the CB, for instance, is named X^{n-} . The lower panel of Fig. 8.1 shows the discrete PL signals found in [2] which stem from the excitons X , X^{1-} , X^{2-} , ... realized upon successively lowering the gate voltage.

Indeed, the transitions observed in the PL experiment (PL counts vs. the gate voltage), shown in the top panel of Fig. 8.1, can be nicely explained by an atom-like electronic level structure inside the QD. The lower right panel of Fig. 8.1 nicely illustrates the involved states. The filling scheme suggested there quantitatively describes *all* observed PL-signals. For instance, the two appearing lines for the decay of the X^{2-} state can be understood very well when one identifies the two possible decay channels of this state: after the exciton has decayed, two electrons are left in the CB - one electron in the s - and another one in the p -level. These two electrons have either (i) parallel or (ii) anti-parallel spins. In case (ii) the excited state can immediately relax to the ground state of the system (the s level being doubly occupied). In case (i), however, a spin-flip event of the p -electron is required before the system can relax into its ground state. Therefore one expects a long-living state, i.e. a sharp signal, in case (i) and a short living one (correspondingly a broad signal) for case

(ii).

The expectation that case (ii) has a smaller amplitude and is broader w.r.t. case (i) can be clearly seen in the experiment. In summary: PL-experiments reveal an atom-like electronic level structure of the QD.

The possibility of tuning the QDs filling by an external gate voltage enables one to address interesting optical transitions within this experiment. We are particularly interested in a scenario when the wetting layer surrounding the dot is filled with electrons and hybridizes with the local level in the dot. In this case an interesting optical transition between a strongly correlated 'Kondo' and an uncorrelated 'non-Kondo' state is possible. To study this effect we investigate the simplest transition that fulfills this requirement, namely the absorption experiment where an initially singly occupied CB (left panel of Fig. 8.2) becomes doubly occupied under creation of an exciton (right panel of Fig. 8.2). For this sake we study an extended AM, consisting of a local VB level and a local CB level which is coupled to a lead, as sketched in Fig. 8.2. Additionally, we introduce a Coulomb attraction between VB holes and CB electrons in the QD which accounts for the exciton binding energy U_{exc} . In the unphysical limit $U_{\text{exc}} = 0$, where the VB is completely decoupled from the CB, we find that the absorption spectrum is determined by the local density of states of the QD. Even though this limiting case is unphysical, it provides a good check of the accuracy of the involved numerics.

For finite values of U_{exc} we observe two rather dramatic new features: firstly, the threshold energy below which no photons are absorbed, say ω_0 , shows a marked, monotonic shift as a function of U_{exc} . Secondly, as U_{exc} is increased, the absorption spectrum shows a tremendous increase in peak height. In fact, the absorption spectrum diverges at the threshold energy ω_0 , in close analogy to the well-known X-ray edge absorption problem. Exploiting analogies to the latter, we propose and numerically verify an analytical expression for the exponent that governs this divergence, in terms of the absorption-induced change in the average occupation of the local conduction band level.

The work presented here (to be submitted to Phys. Rev. B) has already partly been published in the Diploma thesis of Rolf Helmes, a diploma-student of Prof. Jan von Delft.

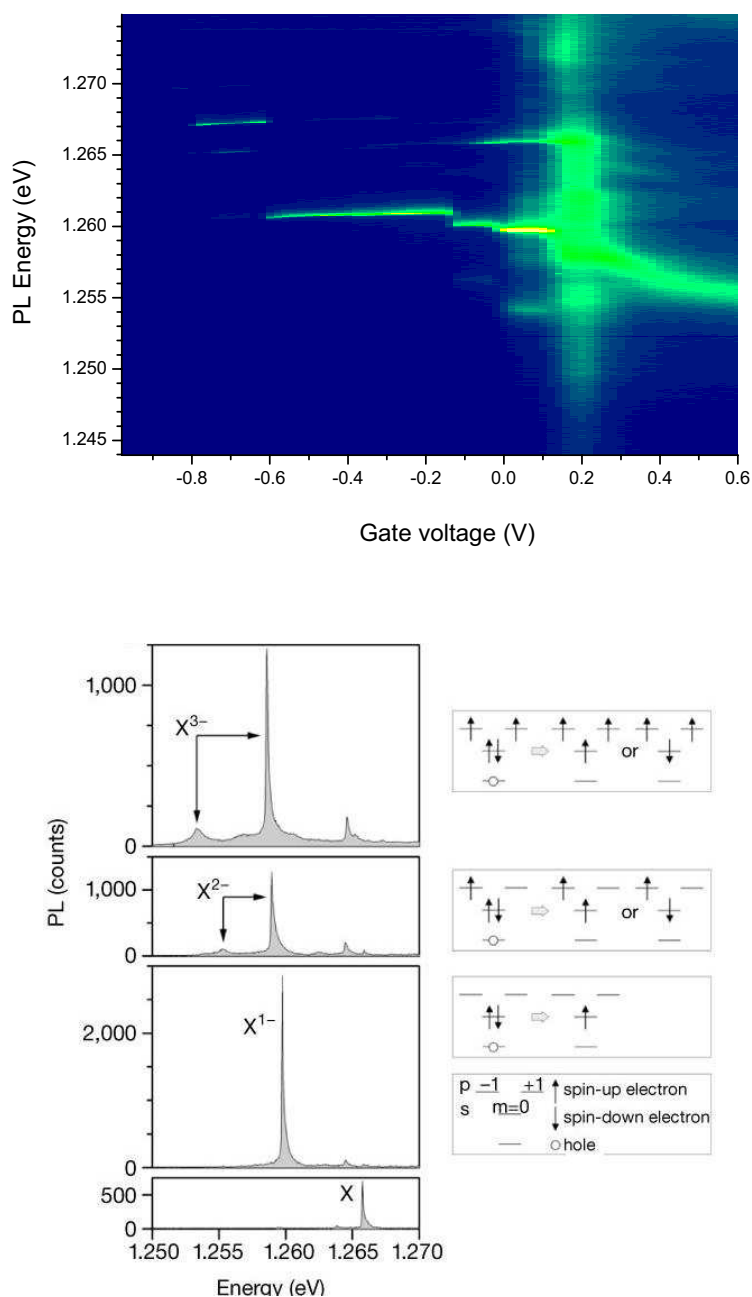


Figure 8.1: Top: The PL energy vs. gate voltage characteristics shows sharp distinct PL signals that can be nicely explained by an atom-like electronic level structure in the semiconductor QD. An external gate voltage allows for a controlled filling of the CB of the QD one by one. An excitonic state with n excess charges is named X^{n-} . [Photo: courtesy of A. Hoegle (LMU)]. Bottom left: PL vs. energy plots for the distinct gate voltage regions found in the top panel (e.g. the lowest plot corresponds to a gate voltage $-0.8\text{V} \lesssim V_G \lesssim -0.6\text{V}$). Bottom right: The filling scheme shown on the right explains the *sharp* observed PL signals very well. Thus, the PL experiment serves as direct evidence for the atom-like electronic level structure inside the QD. Figure taken from [2].

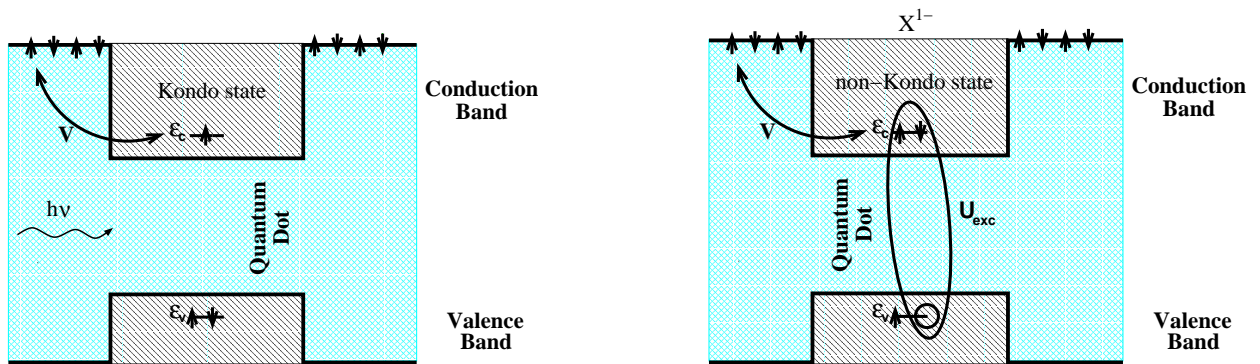


Figure 8.2: Sketch of an absorption process. The left panel shows the initial state (a singly occupied CB). An incoming photon of energy $h\nu$ excites an electron from the VB into the CB. The resulting (final) state, X^{1-} , is shown in the right panel. Here we consider a scenario where the wetting layer (surrounding the dot) is filled and hybridizes with the electrons inside the dot. This example marks a transition from a strongly correlated ('Kondo') into an uncorrelated ('non-Kondo') state, as marked in the figure. Since the mass of the holes in the VB is significantly larger than the electron mass in the CB we disregard the coupling between the VB holes and the lead electrons.

Anderson-Excitons: the effect of a Fermi sea on emission and absorption spectra

R. W. Helmes,¹ M. Sindel,¹ L. Borda,^{1,2} and J. von Delft¹

¹ *Physics Department and Center for NanoScience, LMU München, 80333 München, Germany*

² *Institute of Physics, TU Budapest, H-1521, Hungary*

(Dated: October 21, 2004)

Recent experiments measuring the emission of exciton recombination in a self-organized single quantum dot (QD) have revealed that novel effects occur when the wetting layer surrounding the QD becomes filled with electrons, because the resulting Fermi sea can hybridize with the local electron levels on the dot. Motivated by these experiments, we study an extended Anderson model, which describes a local conduction band level coupled to a Fermi sea, but also includes a local valence band level. We are interested, in particular, on how many-body correlations resulting from the presence of the Fermi sea affect the emission and absorption spectra. Using Wilson's Numerical Renormalization Group, we calculate the zero-temperature emission (absorption) spectrum of a QD which ends up in (starts from) a strongly correlated Kondo ground state. We predict two features: Firstly, the threshold energy ω_0 - above which no photon is emitted (below which no photon is absorbed) - shows a marked, monotonic shift as a function of the exciton binding energy U_{exc} . Secondly, we find that the spectrum shows a power law divergence, with an exponent that can be understood by analogy to the well-known X-ray edge absorption problem.

PACS numbers: Valid PACS appear here

I. INTRODUCTION

Recent optical experiments^{1,2} using self-assembled InAs quantum dots (QDs), embedded in GaAs, showed that it is feasible to measure the absorption and emission spectrum of a single QD. In emission spectrum measurements, an electron-hole pair (exciton) created by laser excitation recombines inside the QD, whereby a photon is emitted which is measured. In absorption spectrum measurements, on the other hand, photons are absorbed inside the QD by exciton excitation.

Due to spatial confinement, the QD possesses a charging energy and a discrete energy level structure, which can be rigidly shifted with respect to the Fermi energy by varying an external gate voltage V_g . Therefore V_g allows for an experimental control of the number of electrons in the QD, which in turn determines the energy of the absorbed and emitted photons. Indeed, the optical data show a distinct V_g -dependence and justify the assumption of a discrete energy level structure of the QD¹.

In the experimental set-up, depicted in Fig. 1, the InAs QDs are surrounded by an InAs mono-layer, called 'wetting layer' (WL), like islands in an ocean. Above a certain value of V_g , the conduction band of delocalized states of this WL begins to be filled, forming a two-dimensional Fermi sea of delocalized electrons, i. e. a two-dimensional electron gas (2DEG). The 2DEG hybridizes with localized states of the QD, leading to anomalous emission spectra which could not be explained by only considering the discrete level structure of the QD¹.

Motivated by these experiments, here we investigate the optical properties of a QD coupled to a Fermi sea, at temperatures sufficiently small that Kondo correlations can occur ($T=0$). The Kondo effect in a QD has already been detected in transport experiments^{3,4}, where it leads to an enhanced linear conductance. So far the Kondo

effect in QDs has been studied almost exclusively in relation to transport properties. The experiments of Refs.^{1,2} open the exciting possibility to study the Kondo effect in optical experiments.

In optics, the Kondo effect has to the best of our knowledge been discussed theoretically only with respect to non-linear and shake-up processes in a QD^{5,6}. In this paper we investigate the absorption and emission spectra of a QD. We are especially interested in optical transitions (examples are shown in Fig. 4 below) for which the QD starts in or ends up in a strongly correlated Kondo ground state, and will investigate how the Kondo correlations affect the observed line shapes. In Ref.⁷ the emission spectrum in the Kondo regime has already been studied, however with methods which only produce qualitative results.

The paper is organized as follows: In Section II, we extend the standard Anderson model⁸ by including a local valence band level (LVBL) containing the holes. In contrast to Refs.^{1,2} we consider only one local conduction band level (LCBL) to simplify the calculations. In Section III, we explain how Wilson's numerical renormalization group (NRG) method⁹ can be adapted to calculate the emission and absorption spectrum of the QD. In Section IV, we present the results of our calculations and predict two rather dramatic new features. Firstly, the threshold energy above which no photon is emitted or below which no photon is absorbed, respectively, say ω_0 , shows a marked, monotonic shift as a function of the exciton binding energy U_{exc} ; we give a qualitative explanation of this behaviour by considering the interplay of various relevant energy scales. Secondly, as U_{exc} is increased, the emission and absorption spectra show a tremendous increase in peak height. In fact, the absorption spectrum shows a power law divergence at the threshold energy ω_0 , in close analogy to the well-known X-ray edge absorption

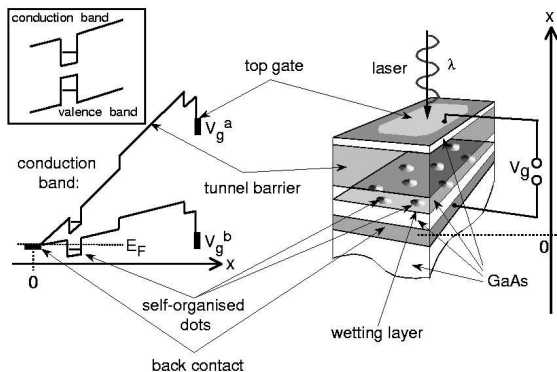


FIG. 1: Right hand side: experimental setup used in Refs.^{1,2} (Picture: courtesy of the group of K. Karrai.) [bottom to top: GaAs substrate (2000 nm), highly doped GaAs back contact (20 nm, zero-point of x-axis), GaAs tunnel barrier (20 nm), InAs mono-layer, forming the wetting layer, together with the QDs, GaAs layer (30 nm), AlAs/GaAs tunnel barrier (~ 100 nm), GaAs (4nm), NiCr top gate]. The gate voltage V_g , applied between the back contact and the top gate, drives no current through the system, since the contacts are separated by two tunnel barriers. Left hand side: position-dependence (in x-direction) and energy-dependence of the lower conduction band edge of the layered structure for two different gate voltages V_g^a and V_g^b ; the different band gaps of each material result in jumps at the corresponding interfaces. Since the InAs band gap is smaller than that of GaAs, there is a dip in the band gap at the GaAs-InAs interface, resulting in QDs with localized conduction and valence band states. The number of localized electrons trapped in the QD can be controlled by V_g , which shifts the energy levels with respect to the Fermi energy E_F (set by the back contact). Inset: holes can be trapped as well due to the bump of the upper band edge of the valence band at the position of the QDs. Irradiation by laser light excites electron-hole pairs (excitons) inside the GaAs layer, which migrate and become trapped in the InAs QDs. Finally they recombine by emitting photons, whose emission spectrum is detected.

problem¹⁰. Exploiting analogies to the latter, we propose and numerically verify an analytical expression for the exponent that governs this divergence, in terms of the absorption-induced change in the average occupation of the LCBL. Conclusions are given in Section V.

II. MODEL

The experimental setup used in Refs.^{1,2}, which inspired our analysis, is depicted in Fig. 1 (see Fig. caption for details). To model this system, we consider an Anderson-like model⁸ for a QD, with localized conduction and valence band levels, coupled to a band of delocalized conduction electrons stemming from the WL. Our model is similar in spirit, if not in detail, to that proposed in Refs.^{7,11}. It consists of six terms, illustrated in Fig. 2:

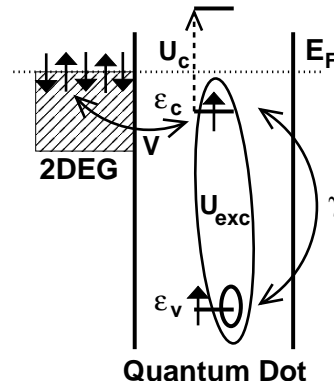


FIG. 2: Model of a semiconductor QD, consisting of one LCBL and one LVBL, with energies ϵ_c and ϵ_v , respectively. The Coulomb repulsion of two electrons in the LCBL has the strength U_c . The coupling between the LCBL and the 2DEG is parametrized by the tunnelling matrix element V . Crucial for the model is the Coulomb attraction between holes in the LVBL and electrons in the LCBL, which has a strength U_{exc} . The excitation of electrons from the LVBL to the LCBL (by photon absorption) and the relaxation of electrons from the LCBL to the LVBL (by photon emission) is considered as a perturbation with a strength γ .

$$\mathcal{H} = \mathcal{H}_0 + \mathcal{H}_{pert}, \quad (1)$$

where

$$\mathcal{H}_0 = \mathcal{H}_c + \mathcal{H}_v + \mathcal{H}_{U_{exc}} + \mathcal{H}_{WL} + \mathcal{H}_{c-WL}. \quad (2)$$

We consider one LCBL with energy ϵ_c and one LVBL with energy ϵ_v , originating from the conduction or valence band of the InAs QD, respectively. Note that ϵ_v is smaller than ϵ_c by the order of the band gap; since this difference is at least two orders of magnitude larger than all other relevant energy scales, its precise value is not important, except for setting the overall scale for the threshold for absorption or emission processes.

Since one LCBL is sufficient to produce the effects of present interest, we will, in contrast to Refs.^{1,2}, disregard further local levels to simplify the calculations¹².

The LCBL and the LVBL are described by \mathcal{H}_c and \mathcal{H}_v , respectively,

$$\begin{aligned} \mathcal{H}_c &= \sum_{\sigma} \epsilon_c \hat{n}_{c\sigma} + U_c \hat{n}_{c\uparrow} \hat{n}_{c\downarrow}, \\ \mathcal{H}_v &= \sum_{\sigma} \epsilon_v \hat{n}_{v\sigma} + U_v (1 - \hat{n}_{v\uparrow})(1 - \hat{n}_{v\downarrow}), \end{aligned} \quad (3)$$

where $\hat{n}_{c\sigma} \equiv c_{\sigma}^{\dagger} c_{\sigma}$ and $\hat{n}_{v\sigma} \equiv v_{\sigma}^{\dagger} v_{\sigma}$. Here the Fermi operators c_{σ}^{\dagger} and v_{σ}^{\dagger} create a spin- σ electron in the LCBL or in the LVBL, respectively. The parameters U_c and U_v are Coulomb repulsion energies which have to be paid if the LCBL is occupied by two electrons or if the LVBL is

empty, respectively. Since states with two holes are very highly excited states independent of the value of U_v [due to the band gap], the actual value of U_v has no influence on the results. The term

$$\mathcal{H}_{U_{\text{exc}}} = - \sum_{\sigma, \sigma'} U_{\text{exc}} \hat{n}_{c\sigma} (1 - \hat{n}_{v\sigma'}) \quad (4)$$

accounts for the exciton binding energy: the Coulomb attraction between each electron in the LCBL and each hole in the LVBL lowers the energy of the system by U_{exc} .

The 2DEG formed in the WL is described by

$$\mathcal{H}_{\text{WL}} = \sum_{k, \sigma} \epsilon_k l_{k\sigma}^\dagger l_{k\sigma}, \quad (5)$$

where the Fermi operator $l_{k\sigma}^\dagger$ creates a delocalized spin- σ electron with wave vector k . The hybridization between the LCBL and the 2DEG is described by

$$\mathcal{H}_{c\text{-WL}} = \sum_{k, \sigma} V \left(l_{k\sigma}^\dagger c_\sigma + c_\sigma^\dagger l_{k\sigma} \right), \quad (6)$$

where the tunneling matrix element V was assumed to be real and energy-independent. The hybridization between the LCBL and the 2DEG is henceforth parametrized by $\Gamma \equiv \pi \rho_F V^2$, where ρ_F is the density of states (DOS) of the 2DEG at E_F ; we assume a flat and normalized DOS with bandwidth D . Since in the considered experiments^{1,2}, the mass of the (heavy) holes is significantly larger than the mass of the electrons, we neglect the hybridization between the LVBL and the 2DEG.

The last part of the Hamiltonian,

$$\mathcal{H}_{\text{pert}} = \gamma \sum_{\sigma} (c_\sigma^\dagger v_\sigma + v_\sigma^\dagger c_\sigma), \quad (7)$$

describing the excitation (first term) and the annihilation (second term) of excitons in the QD by photon absorption or photon emission, respectively, is considered as a perturbation of the system. The constant γ describes the strength of the coupling of the transitions to the photon field. Treating this term perturbatively is valid as long as the coupling strength to the photon field given by the constant γ is small compared to the Kondo temperature T_K , see below, the smallest energy scale in our studies, $|\gamma| \ll T_K$.

For the scenario of a local spinfull level coupled to a Fermi sea, the Kondo effect occurs if the temperature $T < T_K$ and the average occupancy of the local level is roughly one, i. e. in our case $\langle \hat{n}_c \rangle = \sum_{\sigma} \langle \hat{n}_{c\sigma} \rangle \simeq 1$, known as the 'local moment regime' (LMR). Here T_K is given by

$$T_K \equiv (U_c \Gamma / 2)^{1/2} e^{\pi \epsilon_c (\epsilon_c + U_c) / 2 \Gamma U_c}, \quad (8)$$

see Ref.¹³. If $T < T_K$, T_K is the only relevant energy scale in the problem. The Kondo effect introduces a quasi-particle peak, the Kondo resonance, at the Fermi energy

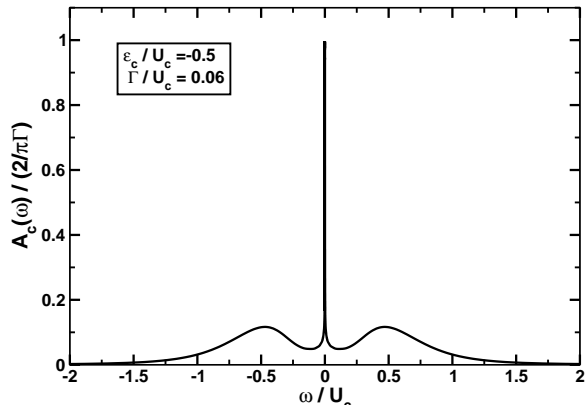


FIG. 3: The normalized¹⁵ local density of states $A_c(\omega)$ of the LCBL in the Kondo regime, with $\epsilon_c = -U_c/2$. The Kondo effect results in a resonance at the Fermi energy E_F . There are side peaks of the singly (doubly) occupied local level at $\omega = \mp U_c/2$ of a level width 2Γ .

E_F in the local density of states (LDOS) $A_c(\omega)$,

$$A_c(\omega) = \sum_{f, \sigma} \left[\left| \langle f | c_\sigma^\dagger | G \rangle \right|^2 \delta(\omega - (E_f - E_G)) + \left| \langle G | c_\sigma^\dagger | f \rangle \right|^2 \delta(\omega + (E_f - E_G)) \right], \quad (9)$$

see Fig. 3. Here $|G\rangle$ and $|f\rangle$ are eigenstates of \mathcal{H}_0 with energy E_G and E_f , respectively, where $|G\rangle$ is the ground state. The LDOS $A_c(\omega)$ of the LCBL is a well-known function which was first calculated with the NRG by Costi et al.¹⁴, and has been studied frequently since.

In transport experiments at $T < T_K$, the Kondo effect causes the 'zero bias anomaly', an enhanced conductance due to the quasi particle peak at E_F . Here we will investigate how the Kondo effect affects the emission and absorption spectrum¹⁶.

Fig. 4(a) and Fig. 4(b) show examples of absorption and emission processes to be studied in this paper. For both examples the QD is tuned such that the LCBL is initially singly occupied, $\langle \hat{n}_c \rangle = 1$, i. e. in the LMR and therefore gives rise to a strongly correlated Kondo state for $T \lesssim T_K$.

In the absorption process, Fig. 4(a), a photon excites an electron from the LVBL into the LCBL. Due to the exciton binding energy, the LCBL is 'pulled down' by the value of U_{exc} . Thus the occupation of the LCBL in the final state can have any value between one and two, depending on the value of U_{exc} relative to the charging energy U_c of the LCBL. If the final occupation is not in the LMR, the Kondo-state is lost.

In the emission process, Fig. 4(b), an electron from the LCBL recombines with a hole in the LVBL, thereby emitting a photon. In contrast to the absorption process, here the occupation of the LCBL decreases since the exciton binding energy is lost in the final state. Again the

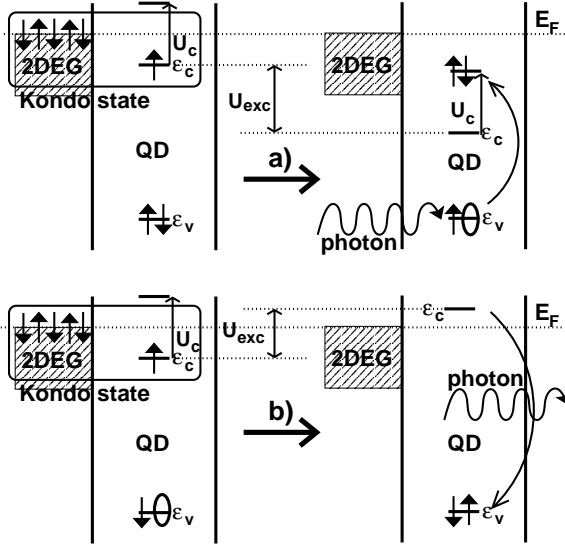


FIG. 4: QD (cf. Fig. 2) tuned such that the LCBL is initially (left hand side) singly occupied. (a) Photon absorption process, inducing a transition from a state without hole and a singly occupied LCBL (Kondo state) to a state with one hole and a doubly occupied LCBL (non-Kondo state). As indicated, the occupation of the LCBL in the final state is determined by the value of $\epsilon_c - U_{exc} + U_c$ relative to E_F . (b) Photon emission process, inducing a transition between a state with hole and a singly occupied LCBL (Kondo state) to a state without hole and empty LCBL.

Kondo state is lost if the final occupation is not in the LMR.

III. METHOD

To calculate the emission and absorption spectra, we use Fermi's Golden Rule for the transition rate out of an initial state $|i\rangle$, normalized to γ ,

$$\alpha_i(\omega) = \frac{2\pi}{|\gamma|^2} \sum_f |\langle f | \mathcal{H}_{\text{pert}} | i \rangle|^2 \delta(\omega - (E_f - E_i)), \quad (10)$$

where $|i\rangle$ and the possible final states $|f\rangle$ are eigenstates of \mathcal{H}_0 , cf. Eq. (1), with energy E_i and E_f , respectively.

No analytical method is known to calculate both the eigenenergies of \mathcal{H}_0 and all matrix elements $\langle i | \mathcal{H}_{\text{pert}} | f \rangle$ exactly. Here we calculate them with Wilson's Numerical Renormalization Group (NRG) method⁹, a numerically essentially exact method¹⁷.

A. Block structure of Hamiltonian

Since \mathcal{H}_0 commutes with $\hat{n}_{v\sigma}$, the number of holes in the LVBL is conserved. Thus it is convenient to write the

unperturbed Hamiltonian \mathcal{H}_0 in the basis $|\Psi\rangle_{c+WL} \otimes |\Psi\rangle_v$, where $|\Psi\rangle_{c+WL}$ denotes a product state of the LCBL and the 2DEG, and $|\Psi\rangle_v$ denotes a state of the LVBL. In this particular basis the unperturbed Hamiltonian \mathcal{H}_0 reads

$$\mathcal{H}_0 = \begin{pmatrix} |0\rangle_v & |\uparrow\rangle_v & |\downarrow\rangle_v & |\uparrow\downarrow\rangle_v \\ \mathcal{H}_{v0} & 0 & 0 & 0 \\ 0 & \mathcal{H}_{v\uparrow} & 0 & 0 \\ 0 & 0 & \mathcal{H}_{v\downarrow} & 0 \\ 0 & 0 & 0 & \mathcal{H}_{v\uparrow\downarrow} \end{pmatrix}, \quad (11)$$

where the Hamiltonians

$$\begin{aligned} \mathcal{H}_{v0} &= \mathcal{H}_{c-WL} + \mathcal{H}_{WL} + \mathcal{H}_c - \sum_{\sigma} 2U_{exc} \hat{n}_{c\sigma} + U_v, \\ \mathcal{H}_{v\uparrow} &= \mathcal{H}_{c-WL} + \mathcal{H}_{WL} + \mathcal{H}_c - \sum_{\sigma} U_{exc} \hat{n}_{c\sigma} + \epsilon_v, \\ \mathcal{H}_{v\uparrow\downarrow} &= \mathcal{H}_{c-WL} + \mathcal{H}_{WL} + \mathcal{H}_c + 2\epsilon_v \end{aligned} \quad (12)$$

act only on states $|\Psi\rangle_{c+WL}$. Since we have not included a magnetic field in our model, $\mathcal{H}_{v\uparrow} = \mathcal{H}_{v\downarrow}$.

Absorption (A) and emission (E) processes (see Fig. 4) involve transitions between different blocks of Eq. (11):

$$\begin{aligned} A: & |G\rangle = |G\rangle_{c+WL} \otimes |\uparrow\downarrow\rangle_v \rightarrow |f\rangle = |f\rangle_{c+WL} \otimes |\sigma\rangle_v \\ E: & |g\rangle = |g\rangle_{c+WL} \otimes |\sigma\rangle_v \rightarrow |f\rangle = |f\rangle_{c+WL} \otimes |\uparrow\downarrow\rangle_v, \end{aligned} \quad (13)$$

where $|G\rangle$ is the ground state of \mathcal{H}_0 , $|G\rangle_{c+WL}$ the corresponding ground state of $\mathcal{H}_{v\uparrow\downarrow}$ and $|g\rangle_{c+WL}$ is the ground state of $\mathcal{H}_{v\sigma}$ and $\sigma = \uparrow, \downarrow$. Since absorption is described by $\mathcal{H}_{\text{pert}} = \gamma c_{\sigma}^{\dagger} v_{\sigma}$, $|f\rangle$ is a state of the block $\mathcal{H}_{v\sigma}$. Emission is described by $\mathcal{H}_{\text{pert}} = \gamma v_{\sigma}^{\dagger} c_{\sigma}$, thus here $|f\rangle$ is a state of the block $\mathcal{H}_{v\uparrow\downarrow}$.

To calculate the absorption spectrum, cf. Fig. 4(a), we insert $|G\rangle$ for $|i\rangle$ in Eq. (10). Then $\alpha_G(\omega)$ gives the probability per time unit for the transition from $|G\rangle$ to any final state $|f\rangle$ of $\mathcal{H}_{v\sigma}$ [containing one hole], equivalent to the probability per time unit that a photon with frequency ω is absorbed, which is the desired absorption spectrum $\alpha_G(\omega)$, divided by $|\gamma|^2$. The actual value of γ is not important, since it does not affect the shape of the absorption function, but only its height. The same argument applies to the emission spectrum, cf. Fig. 4(b). Here, one needs to insert $|g\rangle$ for $|i\rangle$ in Eq. (10).

To employ the NRG to calculate $\alpha_i(\omega)$ via Eq. (10), one has to overcome a technical problem. The NRG is a numerical iterative procedure, where the energy spectrum is truncated in each iteration [besides the first few iterations]. In standard NRG implementations, transitions from or to highly excited states can only be calculated qualitatively rather than quantitatively. In our case we need to compute transitions to or from states of the blocks $\mathcal{H}_{v\sigma}$, see Eq. (13), which are highly excited since they are separated by the order of the band gap from states of $\mathcal{H}_{v\uparrow, \downarrow}$, see Section II. We solve this problem by keeping the same number of states for the blocks $\mathcal{H}_{v\sigma}$ and $\mathcal{H}_{v\uparrow, \downarrow}$ in each NRG iteration, which is in principle the same as running two NRG iterations for both blocks at the same time. This approach is similar to the one used by Costi et al.¹⁸, who studied a problem analogous to ours.

B. Limiting case of vanishing excitation binding energy ($U_{\text{exc}} = 0$)

To check the accuracy of the modified NRG method, we begin by considering the limiting case of vanishing exciton binding energy, $U_{\text{exc}} = 0$. We will show that for this particular case the emission and absorption spectra are related to the local spectral function.

For $U_{\text{exc}} = 0$ the LVBL is decoupled from the LCBL and the 2DEG, see Eq. (4). Therefore, we can decompose the states in the same way as above, $|\Psi\rangle = |\Psi\rangle_{\text{c+WL}} \otimes |\Psi\rangle_{\text{v}}$, and write the total energy can be written as a sum, $E = E_{\text{c+WL}} + E_{\text{v}}$. Thus, using Eqs. (10) and (13), the absorption and emission spectrum can be written as

$$\begin{aligned} \alpha_{\text{G}}(\omega) &= 2\pi \sum_{f,\sigma} |{}_{\text{c+WL}}\langle f|c_{\sigma}^{\dagger}|\text{G}\rangle_{\text{c+WL}}|^2 \cdot \\ &\quad \delta(\omega - (E_{f,\text{c+WL}} - E_{\text{G},\text{c+WL}}) - \Delta\omega), \\ \alpha_{\text{g}}(\omega) &= 2\pi \sum_{f,\sigma} |{}_{\text{c+WL}}\langle f|c_{\sigma}|\text{g}\rangle_{\text{c+WL}}|^2 \cdot \\ &\quad \delta(\omega - (E_{f,\text{c+WL}} - E_{\text{G},\text{c+WL}}) + \Delta\omega). \end{aligned} \quad (14)$$

Here $\Delta\omega \equiv E_{f,\text{v}} - E_{\text{G},\text{v}} = -\epsilon_{\text{v}}$ represents a constant shift.

To compare the LDOS with the absorption and emission spectrum, we divide it as $A_{\text{c}}(\omega) = A_{\text{c}}^{+}(\omega) + A_{\text{c}}^{-}(\omega)$ with

$$\begin{aligned} A_{\text{c}}^{+}(\omega) &= \sum_{f,\sigma} \left[|{}_{\text{c+WL}}\langle f|c_{\sigma}^{\dagger}|\text{G}\rangle_{\text{c+WL}}|^2 \right. \\ &\quad \left. \delta(\omega - (E_{f,\text{c+WL}} - E_{\text{G},\text{c+WL}})) \right] \text{ for } \omega > 0, \\ A_{\text{c}}^{-}(\omega) &= \sum_{f,\sigma} \left[|{}_{\text{c+WL}}\langle \text{G}|c_{\sigma}^{\dagger}|f\rangle_{\text{c+WL}}|^2 \right. \\ &\quad \left. \delta(\omega + (E_{f,\text{c+WL}} - E_{\text{G},\text{c+WL}})) \right] \text{ for } \omega < 0. \end{aligned} \quad (15)$$

Since the operator c_{σ}^{\dagger} does not change the state of the VB, the sum in Eq. (15) runs only over states $|f\rangle$ of $\mathcal{H}_{\text{v}\uparrow\downarrow}$.

To compare Eqs. (14) with Eqs. (15), note that for $U_{\text{exc}} = 0$ the blocks of the Hamiltonian (11) are degenerate (aside from a constant shift), $\mathcal{H}_{\text{v}\sigma} = \mathcal{H}_{\text{v}\uparrow\downarrow}$, and thus $|\text{G}\rangle_{\text{c+WL}} = |\text{g}\rangle_{\text{c+WL}}$. Therefore

$$\begin{aligned} \alpha_{\text{G}}(\omega) &= 2\pi A_{\text{c}}^{+}(\omega - \Delta\omega), \\ \alpha_{\text{g}}(\omega) &= 2\pi A_{\text{c}}^{-}(-\omega - \Delta\omega). \end{aligned} \quad (16)$$

Therefore, for $U_{\text{exc}} = 0$, we can calculate the absorption and emission spectra in two different ways: firstly, with the modified NRG procedure and secondly, via Eq. (16) with $A_{\text{c}}(\omega)$ obtained from the NRG as well. We find an excellent agreement between both approaches.

IV. RESULTS

In Section III B we showed that for $U_{\text{exc}} = 0$ the absorption or emission spectrum are related to the LDOS.

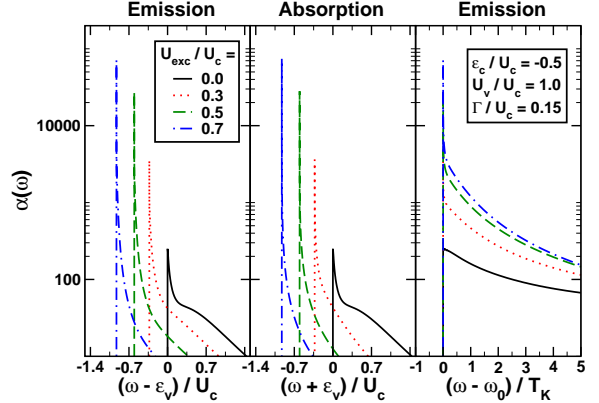


FIG. 5: Emission and absorption spectra for different values of U_{exc} ($\epsilon_{\text{c}}/U_{\text{c}} = -0.5, U_{\text{v}}/U_{\text{c}} = 1.0$ and $\Gamma/U_{\text{c}} = 0.15$). An increase in U_{exc} results in a monotonic shift of the threshold-energy ω_0 of the emission and absorption spectra and in an increase in height at ω_0 . The right panel shows the divergence of the emission spectrum at the threshold energy ω_0 normalized to T_{K} ($T_{\text{K}}/U_{\text{c}} = 0.020$, extracted from Eq. (8)).

We start from this well-understood limiting case and study how the absorption and emission spectra behave upon increasing U_{exc} . We use the modified NRG procedure, described in Section III, to calculate the emission and absorption spectra $\alpha_i(\omega)$ perturbatively, see Eq. (10). The results are shown in Fig. 5. We see two striking behaviors: Firstly, there is a tremendous increase in height for both the absorption and emission spectra. In fact, we find that the spectra diverge at the threshold energy ω_0 , the energy below which no photon is emitted or absorbed, respectively, in close analogy to the well-known X-ray edge absorption problem. Secondly, the threshold energy ω_0 shows a marked, monotonic shift as a function of the exciton binding energy U_{exc} .

A. Exponent of the power-law divergence

Let us first study the height of the spectra. For energies ω near the threshold energy ω_0 , $\omega \rightarrow \omega_0$, we find a power-law divergence for both¹⁹ the emission and the absorption spectra,

$$\alpha(\omega) \sim \left(\frac{1}{\omega - \omega_0} \right)^{\beta}, \quad \omega \rightarrow \omega_0. \quad (17)$$

To extract the exponent β from our numerical results we have determined the slope of the emission and absorption spectra in a double logarithmic plot. An example is shown in Fig. 6, where the absorption spectrum is plotted for varying U_{exc} .

Remarkably we find an universal behavior of the expo-

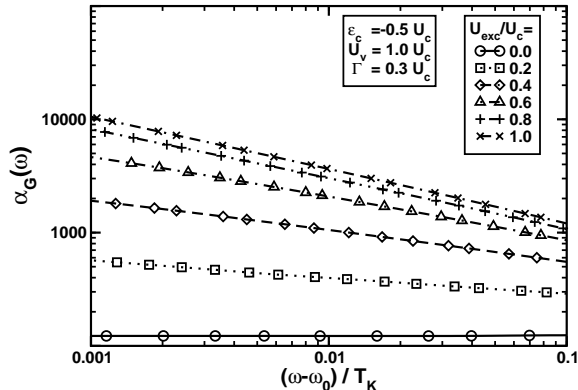


FIG. 6: Asymptotic behavior ($\omega \rightarrow \omega_0$) of the shifted absorption spectra normalized to T_K ($T_K/U_c = 0.10$, extracted from Eq. (8)). For energies $\omega - \omega_0 < 0.1T_K$ we find the power-law behavior as predicted in Eq. (17). The exponent β increases as U_{exc} is increased. The lower bound of $\alpha_G(\omega)$ is set by the number of NRG iterations (here: $\omega - \omega_0 \approx 10^{-3}T_K$ for 50 iterations).

ment β , given by the following equation,

$$\beta = \Delta n - \frac{(\Delta n)^2}{2}, \quad (18)$$

where $\Delta n \equiv \langle n_c \rangle_g - \langle n_c \rangle_G$. Here $\langle n_c \rangle_G$ and $\langle n_c \rangle_g$ denote the average occupation of the states $|G\rangle$ and $|g\rangle$, respectively, see Section III. [Note that for $\omega \rightarrow \omega_0$, $|g\rangle \rightarrow |G\rangle$ and $|G\rangle \rightarrow |g\rangle$ are the critical transitions in the case of emission and absorption, respectively. Since Δn is the same for both transitions, we find the same exponent β for both absorption and emission for a given choice of parameters.] At $U_{\text{exc}} = 0$, we have $\Delta n = 0$, since $|G\rangle_{c+\text{WL}} = |g\rangle_{c+\text{WL}}$, see Section III. As U_{exc} increases, $\langle n_c \rangle_g$ and thus Δn is also increased, since the Coulomb attraction between the hole and the electrons in the LCBL pulls down the LCBL to an effective value $\tilde{\epsilon}_c = \epsilon_c - U_{\text{exc}}$ [note that $|g\rangle$ is an eigenstate of $\mathcal{H}_{v\sigma}$, whereas $|G\rangle$ is an eigenstate of $\mathcal{H}_{v\uparrow\downarrow}$ and thus independent of U_{exc}].

The exponent β has been extracted for different values of ϵ_c . For each value of ϵ_c we have varied Δn between 0 and ~ 0.8 by varying U_{exc} between 0 and U_c . The results are shown in Fig. 7. We find a very good agreement between the results extracted from the NRG and the universal behavior predicted in Eq. (18): all data points nicely collapse onto the curve predicted by Eq. (18).

The numerical results presented in Fig. 5 should thus be interpreted in the following way: for $U_{\text{exc}} = 0$ we have $\Delta n = 0$ and thus $\beta = 0$, which gives a finite height of the emission and the absorption spectrum at the threshold [in fact the height is 2π times the height of the corresponding LDOS, see Section III]. As soon as we choose

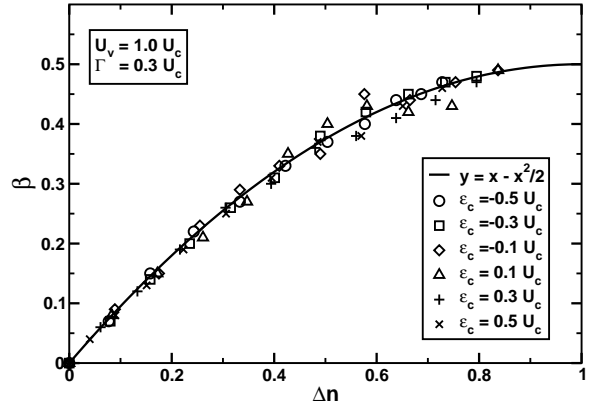


FIG. 7: The exponent β of the power-law divergence extracted from the NRG results for different values of ϵ_c (symbols) coincides very well with the formula for β given by Eq. (18) (solid line), indicating that β is determined only by Δn . Here Δn has been varied between 0 and ~ 0.8 by varying U_{exc} between $0U_c$ and $1U_c$ in steps of $0.1U_c$, where the values of ϵ_c and U_{exc} have been varied (U_{exc}/U_c has been varied between 0.0 and 1.0 in steps of 0.1).

values of $U_{\text{exc}} > 0$, we find $\beta > 0$, leading to an infinite height of the emission and the absorption spectrum, which cannot be resolved by the numerical data. However, with increasing U_{exc} the exponent β also increases, resulting in a steeper slope of the peak at the threshold, which leads to a higher peak in the numerical results.

An explanation for the universal behavior given by Eq. (18) can be given by studying the analogy between the physics presented in this paper and the well-known X-ray edge absorption problem. A result analogous to Eq. (17) was found by Schotte and Schotte²⁰, where the absorption spectrum was studied for the X-ray edge problem. [In Ref.²⁰ all results are presented for the absorption spectrum. However, by rewriting Eq. (7) in Ref.²⁰ for emission, their results can be applied to the emission spectrum as well. Keeping that in mind, we will focus only on the absorption spectrum in the following, but the argumentation can easily be applied to the emission spectrum as well.] In Ref.²⁰ an expression for the exponent β is derived using arguments relating phase-shifts and local screening charges,

$$\beta = 1 - \sum_{\sigma} N_{\sigma}^2, \quad (19)$$

where N_{σ} is the 'effective number of electrons' [which is not necessarily an integer], with spin σ , which flow away from the local level in the absorption process. We can use this result to analyze our absorption spectra, too, since the system behaves like a Fermi liquid for $T = 0$. Thus arguments based on the relation between phase shifts and screening charges do apply.

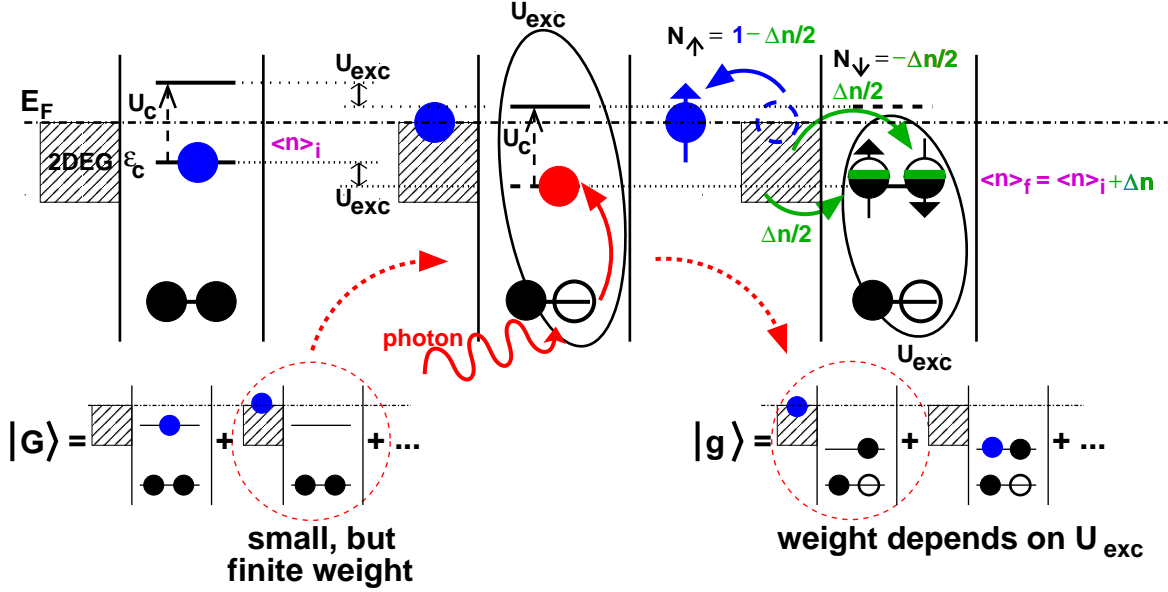


FIG. 8: Illustration of an example for the absorption process $|G\rangle \rightarrow |g\rangle$, the relevant absorption process for energies ω close to the threshold ω_0 : in the initial state $|G\rangle$ (left panel) the LVBL is doubly and the LCBL is singly occupied ($\langle n_c \rangle_G = 1$, since $\epsilon_c = -U_c/2$ in the example). The state $|G\rangle$ is a superposition with contributions from states with empty and singly occupied LCBL (bottom left), where the contribution with empty LCBL has small but finite weight. In the depicted absorption process a photon causes the promotion of an electron of the LVBL to the LCBL (middle panel), leading to a transition from the contribution with empty LCBL to a state with one hole and singly occupied LCBL, which is a contribution to the state $|g\rangle$ (right panel) [the weight of the contribution depends on the value of U_{exc} , see text]. Thus one electron with spin σ flows away from the QD (blue), adding one unit of charge to N_σ (charge with spin σ flowing *away* from the QD in the absorption process). The Coulomb attraction in the state $|g\rangle$ between the hole in the LVBL and the electrons in the LCBL pulls down the level ϵ_c to an effective value $\bar{\epsilon}_c = \epsilon_c - U_{exc}$ resulting in an increase of the average occupation $\langle n_c \rangle_g$ of the LCBL by Δn compared to $\langle n_c \rangle_G$. The charge Δn flows towards the QD, thus $\Delta n/2$ has to be subtracted from N_σ and $N_{\bar{\sigma}}$ (with $\bar{\sigma} = \{\downarrow, \uparrow\}$ for $\sigma = \{\uparrow, \downarrow\}$).

To see that Eqs. (18) and (19) are equivalent, we will now study the absorption process $|G\rangle \rightarrow |g\rangle$ [relevant absorption process at threshold] and count the charges N_σ . It is helpful to consider an example for the process $|G\rangle \rightarrow |g\rangle$, shown in Fig. 8, where the initial state $|G\rangle$ is the strongly correlated Kondo ground state with singly occupied LCBL. The state $|G\rangle$ is a superposition of states with different occupation of the LCBL, where the contribution of the state with empty LCBL is small but finite (depicted at the bottom of Fig. 8). If the operator $c_\sigma^\dagger v_\sigma$ [the part of $\mathcal{H}_{\text{pert}}$ corresponding to absorption] is applied to $|G\rangle$, this contribution results in a state with one hole and singly occupied LCBL. Thus one electron with spin σ flows away from the QD (illustrated in blue in Fig. 8), adding one unit of charge to N_σ . This contribution to the final state $c_\sigma^\dagger v_\sigma |G\rangle$ is a part of the state $|g\rangle$, which also has contributions from states with empty, singly and double occupied LCBL (bottom of Fig. 8). The weight of the contribution with singly occupied LCBL to $|g\rangle$ depends on U_{exc} : the Coulomb attraction

of the hole in $|g\rangle$ pulls down the LCBL to the effective value $\bar{\epsilon}_c$ resulting in an increase of the average occupation $\langle n_c \rangle_g$ of the LCBL by Δn compared to $\langle n_c \rangle_G$, see above. As U_{exc} is increased, the charge Δn [which screens the Coulomb potential of the hole] and thus the weight of the contribution to $|g\rangle$ with doubly occupied LCBL also increases, whereas the weight of the state with singly occupied LCBL decreases. The charge Δn flows towards the QD, thus $\Delta n/2$ has to be subtracted from N_σ and $N_{\bar{\sigma}}$ (with $\bar{\sigma} = \{\downarrow, \uparrow\}$ for $\sigma = \{\uparrow, \downarrow\}$). [Another possibility for a transition from $|G\rangle$ to $|g\rangle$ starts from the contribution to $|G\rangle$ with a singly occupied LCBL and ends up in a contribution of $|g\rangle$ with double occupied LCBL. One receives the same amount of charge for N_σ and $N_{\bar{\sigma}}$ if one argues that one unit of charge with spin σ has to leave the doubly occupied LCBL and the charge Δn has to flow into the LCBL to reach the average occupation $\langle n_c \rangle_g = \langle n_c \rangle_G + \Delta n$.] Picking up all contributions to N_σ and $N_{\bar{\sigma}}$ to calculate the exponent β via Eq. (19), one gets $\beta = 1 - (1 - \Delta n/2)^2 - (\Delta n/2)^2 = \Delta n - (\Delta n)^2/2$, which

is the result expected from Eq. (18).

A similar argument has been used in^{18,21}, where the local spectral function of the Anderson was studied.

B. Behavior of the threshold energy ω_0

Let us now switch to the second effect observed, the monotonic shift of the threshold energy ω_0 . The threshold energy for both emission and absorption is given by $\omega_0 = E_g - E_G$, where $\mathcal{H}_0|G\rangle = E_G|G\rangle$ and $\mathcal{H}_0|g\rangle = E_g|g\rangle$, as explained in Section III. The shift can be understood by considering a mean-field estimate of the relevant energies E_G and E_g ,

$$E_G \approx 2\epsilon_v + \epsilon_c \langle n_c \rangle_G + \frac{1}{4} U_c \langle n_c \rangle_G^2,$$

$$E_g \approx \epsilon_v + \epsilon_c \langle n_c \rangle_g + \frac{1}{4} U_c \langle n_c \rangle_g^2 - U_{\text{exc}} \langle n_c \rangle_g. \quad (20)$$

The average occupations $\langle n_c \rangle_G$ and $\langle n_c \rangle_g$ can be calculated by the NRG as well. Eq. (20) allows for a rough estimate of the threshold energy ω_0 ,

$$\omega_0 = E_g - E_G$$

$$\approx -\epsilon_v + \epsilon_c (\langle n_c \rangle_g - \langle n_c \rangle_G)$$

$$+ \frac{1}{4} U_c (\langle n_c \rangle_g^2 - \langle n_c \rangle_G^2) - U_{\text{exc}} \langle n_c \rangle_g. \quad (21)$$

The results for ω_0 shown in Fig. 9 reveal a good agreement between the threshold energy extracted from the emission and absorption spectra calculated with NRG (solid line) and the estimation given by Eq. (21). In the latter approach $\langle n_c \rangle_G$ and $\langle n_c \rangle_g$ have been determined via the NRG, see top panel of Fig. 9 [note that $\langle n_c \rangle_G = \text{const.}$ with $\langle n_c \rangle_G = \langle n_c \rangle_g$ at $U_{\text{exc}}=0$]. We find a linear behavior of ω_0 as a function of U_{exc} for those values of U_{exc} where $\langle n_c \rangle_g$ stays approximately constant. For this sake three regions of constant occupation are identified, region I ($\langle n_c \rangle_g \sim 0$), II ($\langle n_c \rangle_g \sim 1$) and III ($\langle n_c \rangle_g \sim 2$). As expected by considering the last term in Eq. (21), we observe the slope of $\omega_0(U_{\text{exc}})$ to be 0 in region I, to be -1 in region II and to be -2 in region III, respectively.

The cross-over regions (dotted lines in Fig. 9), where $\langle n_c \rangle_g$ changes between 0 and 1 (I \rightarrow II) or between 1 and 2 (II \rightarrow III), on the other hand, show non-trivial behavior of ω_0 . In these regions the terms in Eq. (9) compete with each other, which explains the non-linear behavior (note that in these regions $\langle n_c \rangle_g$ is a function of U_{exc} as well).

V. CONCLUSIONS

Motivated by experimental results^{1,2}, the aim of this paper was to calculate the emission and absorption spectra of a QD in the strongly correlated Kondo ground-state. We have studied an extended Anderson model including a local valence band level and a local conduction band level which is coupled to a Fermi-sea (2DEG),

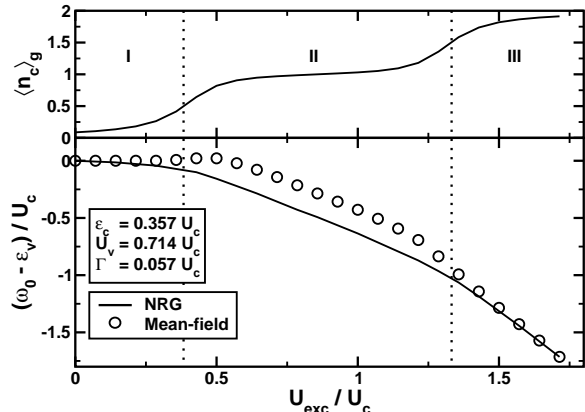


FIG. 9: Behavior of the threshold energy as a function of U_{exc} . Upper panel: average occupation of the LCBL $\langle n_c \rangle_g$ of the state $|g\rangle$, see Eq. (13). Three distinct regimes are identified: empty orbital (I), LMR (II) and full orbital (III) regime, where the LCBL is empty, singly or doubly occupied, respectively. Since the Coulomb attraction between an hole in the LVBL and the electrons in the LCBL 'pulls down' the LCBL [$\tilde{\epsilon}_c = \epsilon_c - U_{\text{exc}}$], an increase in U_{exc} bears the same effect for $\langle n_c \rangle_g$ as a decrease in ϵ_c . Lower panel: threshold energy ω_0 versus U_{exc} extracted from the NRG results (solid) and obtained from the mean-field estimate (circles), Eq. (21), where $\langle n_c \rangle_g$ of the upper panel has been used.

see Section II. For the academic limiting case of a vanishing exciton binding energy, $U_{\text{exc}} = 0$, we could relate the emission and absorption spectrum to the well known local density of states of the local conduction band, see Section III. Starting from this limit case, we have studied the spectra for arbitrary values of U_{exc} . Using the NRG method, we have produced our main result, Fig. 5, which shows two rather dramatic features: Firstly, we noticed a tremendous increase in height of the emission absorption spectrum as U_{exc} is increased. In fact, the spectra show a power-law divergence at the threshold energy, the energy below which no photon is absorbed or the energy above which no photon is emitted, respectively. Remarkably the exponent of the divergence depends only on Δn , the difference in occupation of the local conduction band level between the initial and final states for transitions at the threshold. We showed that the universal behavior of the exponent can be explained by considering the X-ray edge problem, which stands in close analogy to the physics presented in this paper. Secondly, for increasing U_{exc} there is a marked shift of the threshold energy, which can be understood on a mean field level.

In the present generation of experiments^{1,2}, the wetting layer forms a 2DEG only for values of the gate voltage V_g for which several local conduction band levels are occupied (not only one, as assumed in the present paper). However, we expect²² that future generations of samples could be produced for which the assumptions of

our model, namely one LCBL with presence of a 2DEG, are fulfilled.

Acknowledgments

We wish to thank M. Kroner, S. Seidel, A. Högele and K. Karrai of the group Karrai, R. Bulla, T. Costi and A.

Rosch for helpful discussions. This work was supported by the DFG under the SFB 631 and under the CFN, 'Spintronics' RT Network of the EC RTN2-2001-00440.

-
- ¹ R. J. Warburton, C. Schäflein, D. Haft, F. Bickel, A. Lorke, K. Karrai, J. M. Garcia, W. Schoenfeld, and P. M. Petroff, *Nature* **405**, 926 (2000).
- ² K. Karrai, R. J. Warburton, C. Schulhauser, A. Högele, B. Urbaszek, E. J. McGhee, A. O. Govorov, J. M. Garcia, B. D. Gerardot, and P. M. Petroff, *Nature* **427**, 135 (2004).
- ³ D. Goldhaber-Gordon, H. Shtrikman, D. Mahalu, D. Abusch-Magder, U. Meirav, and M. A. Kastner, *Nature* **391**, 156 (1998).
- ⁴ S. M. Cronenwett, T. H. Oosterkamp, and L. P. Kouwenhoven, *Science* **281**, 540 (1998).
- ⁵ T. V. Shahbazyan, I. E. Perakis, and M. E. Raikh, *Phys. Rev. Lett.* **84**, 5896 (2000).
- ⁶ K. Kikoin and Y. Avishai, *Phys. Rev. B* **62**, 4647 (2000).
- ⁷ A. O. Govorov, K. Karrai, and R. J. Warburton, *Phys. Rev. B* **67**, 241307 (2003).
- ⁸ P. W. Anderson, *Phys. Rev.* **124**, 41 (1961).
- ⁹ K. G. Wilson, *Rev. Mod. Phys.* **47**, 773 (1975).
- ¹⁰ P. Nozieres and C. T. de Dominicis, *Phys. Rev.* **178**, 1097 (1969).
- ¹¹ R. J. Warburton, B. T. Miller, C. S. Dürr, C. Bödefeld, K. Karrai, J. P. Kotthaus, G. Medeiros-Ribeiro, P. M. Petroff, and S. Huant, *Phys. Rev. B* **58**, 16221 (1998).
- ¹² In the present generation of experiments, the WL forms a 2DEG only for V_g -values for which *several* local conduction band levels are occupied (not only one, as assumed in the present paper). However, we expect²² that future generations of samples could be produced for which the assumptions of our model, namely one LCBL in the presence of a 2DEG, are fulfilled.
- ¹³ A. M. Tsvetlick and P. B. Wiegmann, *Adv. Phys.* **32**, 453 (1983).
- ¹⁴ T. A. Costi, A. C. Hewson, and V. Zlatic, *J. Phys. Condens. Matter* **6**, 2519 (1994).
- ¹⁵ D. C. Langreth, *Phys. Rev.* **150**, 516 (1966).
- ¹⁶ For our numerical calculations, we use $|\epsilon_c|, U_c \ll D$, but this is not an essential assumption to realize the Kondo effect, which can also occur for $U_c \gg D$, as long as $\langle \hat{n}_c \rangle \simeq 1$.
- ¹⁷ To obtain a continuous spectrum $\alpha_i(\omega)$, the δ -functions in Eq. (10), associated with the sum over discrete final states, have to be properly 'broadened', see Refs.^{14,23}.
- ¹⁸ T. A. Costi, P. Schmitteckert, J. Kroha, and P. Wölfle, *Phys. Rev. Lett.* **73**, 1275 (1994).
- ¹⁹ One might expect that the absorption and emission spectrum are related by the particle-hole symmetry. However, the Hamiltonian \mathcal{H}_0 , Eq. (2), has no particle-hole symmetry: The operators $J^+ \equiv c_\uparrow^\dagger c_\downarrow^\dagger$, $J^- = (J^+)^\dagger$ and $J_z = [J^+, J^-]$ compose a SU(2) algebra, where $J_z = c_\uparrow^\dagger c_\uparrow + c_\downarrow^\dagger c_\downarrow$ is proportional to the charge operator and thus commutes with the Hamiltonian. There is particle-hole symmetry if J^+ commutes with the Hamiltonian. In our case $[\mathcal{H}_0, J^+] = (-2\epsilon_c - U_c + 2U_{\text{exc}} \sum_\sigma (1 - n_{\nu\sigma})) c_\uparrow^\dagger c_\downarrow^\dagger$. Thus the Hamiltonian can only be particle-hole symmetric for one particular choice of $n_{\nu\sigma}$, i. e. different blocks of \mathcal{H}_0 , see Eq. (11) cannot be particle-hole symmetric at the same time.
- ²⁰ K. D. Schotte and U. Schotte, *Phys. Rev.* **185**, 509 (1969).
- ²¹ T. A. Costi, J. Kroha, and P. Wölfle, *Phys. Rev. B* **53**, 1850 (1996).
- ²² K. Karrai, private communications.
- ²³ R. Bulla, T. A. Costi, and D. Vollhardt, *Phys. Rev. B* **64**, 045103 (2001).

Chapter 9

Summary and outlook

In this thesis we have been focusing on zero-temperature properties of QD-systems. The different QD-systems that we analyzed were modeled by the Anderson impurity model, a model that is extremely well suited to describe QD-physics. In the limit of small temperatures correlation effects are crucial. Consequently, we employed Wilson's numerical renormalization group method, which is essentially a numerical exact method for the determination of the low-temperature properties of the various models we studied. We expect our predictions to be observed in (future) experiments.¹

Table 9.1 shows four different classes of impurity models we were solving in this thesis. One can categorize these classes by the number of (spinfull) *levels* inside the impurity and the number of (spinfull) *channels* the impurity couples to. In particular, the number of channels the (complex) impurity couples to sets a serious restriction for the numerical solution of a particular model.² Within each of those classes particular symmetries can be exploited. As stressed in Appendix C the use of symmetries is essential for an accurate determination of the quantities one is interested in. As this symmetries depend on the particular model under study we do not refine Table 9.1 w.r.t. particular symmetries here.

Whereas in this thesis, we only considered QDs coupled to fermionic baths,³ the NRG-method is *not* restricted to fermionic baths. The 'bosonic' NRG, developed by Bulla *et al.* [66], overcomes this restriction. This generalization of the NRG-method is a new path one should definitely follow. It opens the exciting possibility to study models, such as the spin boson model (see [66]), which are, for instance, relevant in the context of quantum-computation [22].

The code that was programmed during my PhD-studies is rather flexible. Therefore it allows for the solution of various problems (dealing with fermionic baths) without changing

¹The spin splitting of the Kondo resonance for a QD contacted to ferromagnetic leads has already, in agreement with our predictions, been observed [55] (see also [59]).

²It is the number of coupled channels that governs the growth-rate of the Hilbert space in the course of the NRG-iteration.

³In Chapter 6 and 7 we solved models up to four different fermionic baths, (two different channels each carrying a spin index).

	1 channel	2 channel
1 level	Chapter 5, 8	Chapter 7
2 level	Chapter 6	Chapter 6

Table 9.1: The table classifies the models that have been solved in Part II of this thesis. Models that fall into one of these classes can, in principle, be solved with the NRG-code that was produced within my PhD-studies. Since the symmetries one should exploit depend crucially on the model one is studying we do not refine this table by including possible symmetries.

the structure of it.

In a recent experiment on single wall carbon nanotubes [67], for instance, a fascinating feature of a sixfold split Kondo resonance (in presence of a finite magnetic field) has been observed. In this experiment, carried out at TU Delft (Netherlands), the nanotube was tuned such that it behaves, in absence of a magnetic field, as a two-fold degenerate QD⁴ coupled to two distinct channels. Once the relevant model of this experiment is identified, it is rather straightforward to use the developed code to compute the (level and spin resolved) spectral functions of the system, which enables one to gain a deeper understanding of the experimental results.

⁴It turns out that a magnetic field couples differently to the spin and the orbital degree of freedom, leading to a difference between the Zeeman and the orbital splitting.

Part III

Appendix

Appendix A

Derivation of the NRG-equations

In the early 1970's K.G. Wilson succeeded to construct a nonperturbative solution of the Kondo Model (KM) [1]. The crucial step in Wilson's procedure was the mapping of the free conduction electrons (that surround the impurity) onto a chain, the *Wilson chain*. Krishna-murthy *et al.* [31], [47] extended this procedure to the Anderson Model (AM) [25] in the early 1980's.

In contrast to Wilson and Krishna-murthy *et al.*, who assumed a flat conduction band (CB),¹ we consider here a CB with a *spin*- and *energy*-dependent density of states (DoS) $\rho_\sigma(\epsilon)$ [the energy dispersion in the CB $\epsilon_{\mathbf{k}\sigma}$ is related to $\rho_\sigma(\epsilon)$ via $\rho_\sigma(\epsilon) = \sum_{\mathbf{k}} \delta(\omega - \epsilon_{\mathbf{k}\sigma})$]. For this sake the iteration scheme used in [1] has to be generalized for a CB with an *arbitrary* DoS $\rho_\sigma(\epsilon)$. To establish this generalization we follow Bulla [68], [69] and Hofstetter [70]:²

For simplicity the mapping of the single level AM,

$$\hat{\mathcal{H}}_{AM} = \hat{\mathcal{H}}_d + \underbrace{\sum_{\mathbf{k}\sigma} \epsilon_{\mathbf{k}\sigma} c_{\mathbf{k}\sigma}^\dagger c_{\mathbf{k}\sigma}}_{\hat{\mathcal{H}}_{CB}} + \underbrace{\sum_{\mathbf{k}\sigma} V_{\mathbf{k}\sigma} \left(c_{\mathbf{k}\sigma}^\dagger d_\sigma + d_\sigma^\dagger c_{\mathbf{k}\sigma} \right)}_{\hat{\mathcal{H}}_{ld}}, \quad (\text{A.1})$$

on the Wilson chain will be described below. As explained in Eq. (3.7), the AM consists of three parts, the CB $\hat{\mathcal{H}}_{CB}$, the tunneling part $\hat{\mathcal{H}}_{ld}$ and the impurity part $\hat{\mathcal{H}}_d$ which does not need to be specified here. The operators d_σ and $c_{\mathbf{k}\sigma}$ denote the impurity and CB operators [actually the symmetric linear combination of the left and right lead (called $\alpha_{s\mathbf{k}\sigma}$ in part I, see Section 3.1)] which obey Fermi statistics (with σ describing the z-component of spin orientation), respectively. The corresponding mapping of an impurity that couples to N channels³ - the case $N = 1$ is shown here - can easily be obtained via a generalization of the procedure outlined below. In Chapter 6, for instance, the mapping for $N = 2$ had to be performed.

¹ The bandwidth D of the CB is the natural energy scale; for a flat and normalized CB the DoS is given by: $\rho(\epsilon) = \sum_\sigma \rho_\sigma(\epsilon) = \frac{1}{2D}$, since $\sum_\sigma \int_{-D}^D d\epsilon \rho_\sigma(\epsilon) = 1$.

² An impurity that couples to an arbitrary DoS is of particular importance in DMFT-applications [26].

³ $c_{\mathbf{k}\sigma} \rightarrow c_{\mathbf{k}i\sigma}$, $i \in \{1, \dots, N\}$. Note, however, that a single level impurity couples effectively to one channel only (as a unitary transformation [16] reveals).

A.1 Manipulation of the CB

A continuous representation of $\hat{\mathcal{H}}_{CB}$ and $\hat{\mathcal{H}}_{\ell d}$ is more convenient for the derivation of the NRG-mapping [69]. To achieve this, we replace the \mathbf{k} -sums in Eq. (A.1) by a continuous representation

$$\hat{\mathcal{H}}_{CB} = \sum_{\sigma} \int_{-1}^1 d\epsilon g_{\sigma}(\epsilon) a_{\epsilon\sigma}^{\dagger} a_{\epsilon\sigma}, \quad (\text{A.2})$$

$$\hat{\mathcal{H}}_{\ell d} = \sum_{\sigma} \int_{-1}^1 d\epsilon h_{\sigma}(\epsilon) (d_{\sigma}^{\dagger} a_{\epsilon\sigma} + \text{h.c.}). \quad (\text{A.3})$$

In Eq. (A.2) an isotropic energy representation of the CB (with band edge $D = 1$, i.e. $|\epsilon| \leq 1$) with a generalized *dispersion* $g_{\sigma}(\epsilon)$ has been introduced. Accordingly, a generalized *hybridization* function $h_{\sigma}(\epsilon)$ was inserted in Eq. (A.3). The continuous CB-operators $a_{\epsilon\sigma}$ obviously have to obey Fermi statistics $\{a_{\epsilon\sigma}, a_{\epsilon'\sigma'}^{\dagger}\} = \delta(\epsilon - \epsilon')\delta_{\sigma,\sigma'}$. The equivalence of the discrete and continuous version of $\hat{\mathcal{H}}_{AM}$ [i.e. between Eq. (A.1) and Eqs. (A.2), (A.3)] is established if the effective action on the impurity degree of freedom is identical in both representations. Given that the functions $g_{\sigma}(\epsilon)$ and $h_{\sigma}(\epsilon)$ obey the relation

$$\frac{\partial g_{\sigma}^{-1}(\epsilon)}{\partial \epsilon} [h_{\sigma}(g_{\sigma}^{-1}(\epsilon))]^2 = \rho_{\sigma}(\epsilon) [V_{\sigma}(\epsilon)]^2, \quad (\text{A.4})$$

where $g_{\sigma}^{-1}(\epsilon)$ is the inverse of $g_{\sigma}(\epsilon)$, this requirement is fulfilled and the discrete and the continuous representation of the AM are identical (see Eq.(10) of [69]).

Obviously, there are many possibilities to satisfy Eq. (A.4). One possibility is to choose the dispersion $g_{\sigma}(\epsilon) = g_{\sigma}^{-1}(\epsilon) = \epsilon$ and the generalized hybridization $h_{\sigma}(\epsilon) = \sqrt{\Delta_{\sigma}(\epsilon)}/\pi$, with ϵ -dependent hybridization $\Delta_{\sigma}(\epsilon) \equiv \pi \rho_{\sigma}(\epsilon) [V_{\sigma}(\epsilon)]^2$ (other possibilities can, for instance, be found in [69]). For reasons that will become clear below, this choice is well suited for a constant (or at least sufficiently smooth) hybridization $\Delta_{\sigma}(\epsilon)$. For a hybridization with a strong energy-dependence [71], however, the functions $g_{\sigma}(\epsilon)$ and $h_{\sigma}(\epsilon)$ are chosen differently [still satisfying Eq. (A.4)]. An example of the latter case is given in Fig. A.1(a) [the corresponding functions $g_{\sigma}(\epsilon)$ and $h_{\sigma}(\epsilon)$ are sketched in Fig. A.1(b)].

Eq. (A.3) reveals that the impurity couples to *all* energy scales of the problem, i.e. infinitely many degrees of freedom. Wilson's original idea, a *logarithmic* discretization of the CB, allowed him to transform $\hat{\mathcal{H}}_{\ell d}$ into a tractable form. The logarithmic discretization resolves low-energy states with a high accuracy, but does not simply disregard high energy states of the CB, as shown in Fig. A.1(a). By introducing a discretization parameter Λ ($\Lambda > 1$) Wilson divided the CB into energy intervals ranging between $[-\Lambda^{-n}; -\Lambda^{-(n+1)}[$ and $]\Lambda^{-(n+1)}; \Lambda^{-n}]$, $n \in \mathbb{N}_0$. In each logarithmic interval a Fourier Series

$$\Psi_{np}^{\pm}(\epsilon) = \begin{cases} \frac{1}{\sqrt{d_n}} e^{\pm i\omega_n p \epsilon} & \text{if } \Lambda^{-(n+1)} < \pm \epsilon \leq \Lambda^{-n}; \quad p \in \mathbb{Z} \\ 0 & \text{else} \end{cases} \quad (\text{A.5})$$

is defined where the superscript \pm labels wave functions defined for positive/negative energies. The subscripts n and p mark the interval and the harmonic index of the Fourier

expansion. Note that the width of the n -th interval $d_n = \Lambda^{-n}(1 - \Lambda^{-1})$ determines the fundamental Fourier frequency $\omega_n = 2\pi/d_n$ of that interval. The expansion (A.5) now

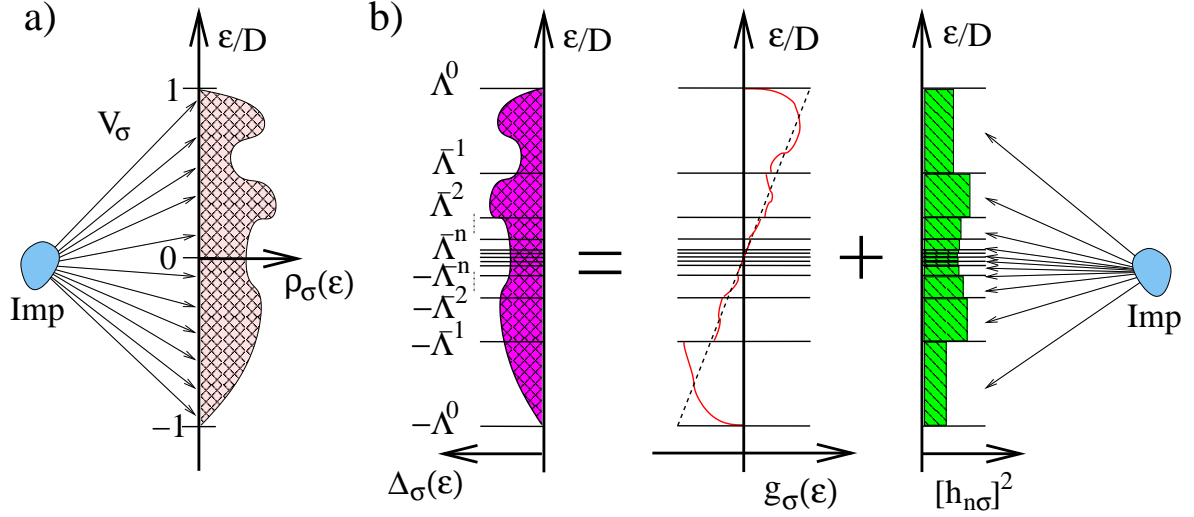


Figure A.1: (a) Since the impurity couples to *all* energies, the CB is logarithmically discretized (with discretization parameter Λ). (b) For an energy-dependent hybridization $\Delta_\sigma(\epsilon)$ (left) one chooses the generalized hybridization $h_\sigma(\epsilon) = h_{n\sigma}^\pm$ to be constant in each logarithmic interval; for this choice only the ($p = 0$)-component of the CB couples to the impurity (right panel). The corresponding dispersion $g_\sigma(\epsilon)$, sketched in the middle panel (solid line), follows from solving Eq. (A.4). For reference the linear dispersion $g_\sigma(\epsilon) = \epsilon$ (dashed line) is plotted as well.

allows one to replace the continuous operators $a_{\epsilon\sigma}$ in $\hat{\mathcal{H}}_{CB}$ and $\hat{\mathcal{H}}_{ld}$ [cf. (A.2) and (A.3)] by discrete ones,

$$a_{\epsilon\sigma} = \sum_{np} [a_{np\sigma} \Psi_{np}^+(\epsilon) + b_{np\sigma} \Psi_{np}^-(\epsilon)]. \quad (\text{A.6})$$

A *discrete* set of anti-commuting operators $a_{np\sigma}$ and $b_{np\sigma}$ [note: $\{a_{np\sigma}, a_{n'p'\sigma'}^\dagger\} = \delta_{nn'} \delta_{pp'} \delta_{\sigma\sigma'}$ and analogously for $b_{np\sigma}$] with harmonic index p and spin σ ,

$$a_{np\sigma} = \int_{-1}^1 d\epsilon [\Psi_{np}^+(\epsilon)]^* a_{\epsilon\sigma}, \quad (\text{A.7})$$

$$b_{np\sigma} = \int_{-1}^1 d\epsilon [\Psi_{np}^-(\epsilon)]^* a_{\epsilon\sigma}, \quad (\text{A.8})$$

that act on the n -th positive or negative logarithmic interval is defined hereby.

A.1.1 Transformation of $\hat{\mathcal{H}}_{ld}$

We start the derivation of the NRG-equations by a transformation of the tunneling part $\hat{\mathcal{H}}_{ld}$ of the AM. Inserting the expansion (A.6) into Eq. (A.3) yields

$$\hat{\mathcal{H}}_{ld} = \sum_{np\sigma} \left\{ \left[d_{\sigma}^{\dagger} \left(a_{np\sigma} \int_{\Lambda^{-(n+1)}}^{\Lambda^{-n}} d\epsilon h_{\sigma}(\epsilon) \Psi_{np}^{+}(\epsilon) + b_{np\sigma} \int_{-\Lambda^{-n}}^{-\Lambda^{-(n+1)}} d\epsilon h_{\sigma}(\epsilon) \Psi_{np}^{-}(\epsilon) \right) \right] + \text{h.c.} \right\}. \quad (\text{A.9})$$

Henceforth, we take the generalized hybridization function $h_{\sigma}(\epsilon)$ to be constant [69] in *all* logarithmic intervals, $h_{\sigma}(\epsilon) \rightarrow h_{n\sigma}^{\pm}$, see Fig. A.1(b), which ensures that the impurity couples to *s*-waves only, i.e. to the ($p = 0$)-contributions (Riemann-Lebesgue Lemma) [70]. Consequently the harmonic index p can be dropped in Eq. (A.9). This particular choice of the generalized hybridization function, the *averaged* hybridization function

$$h_{n\sigma}^{+} \equiv \begin{cases} \sqrt{\frac{1}{dn} \int_{\Lambda^{-(n+1)}}^{\Lambda^{-n}} d\epsilon \rho_{\sigma}(\epsilon) [V_{\sigma}(\epsilon)]^2} & \text{if } \Lambda^{-(n+1)} < \epsilon \leq \Lambda^{-n} \text{ ,} \\ 0 & \text{else} \end{cases}, \quad (\text{A.10})$$

$$h_{n\sigma}^{-} \equiv \begin{cases} \sqrt{\frac{1}{dn} \int_{-\Lambda^{-n}}^{-\Lambda^{-(n+1)}} d\epsilon \rho_{\sigma}(\epsilon) [V_{\sigma}(\epsilon)]^2} & \text{if } -\Lambda^{-n} < \epsilon \leq -\Lambda^{-(n+1)} \text{ ,} \\ 0 & \text{else} \end{cases}, \quad (\text{A.11})$$

forces us to adjust the generalized dispersion $g_{\sigma}(\epsilon)$ such that Eq. (A.4) still holds. In general, as indicated in Fig. A.1(b), this results in a nonlinear generalized dispersion $g_{\sigma}(\epsilon)$. Inserting Eqs. (A.10) and (A.11) into Eq. (A.9) simplifies $\hat{\mathcal{H}}_{ld}$ considerably

$$\hat{\mathcal{H}}_{ld} = \sqrt{\frac{1}{\pi}} \sum_{\sigma} \left[d_{\sigma}^{\dagger} \sum_n \overbrace{(\gamma_{n\sigma}^{+} a_{n\sigma} + \gamma_{n\sigma}^{-} b_{n\sigma})}^{\sim f_{0\sigma}} + \text{h.c.} \right], \quad (\text{A.12})$$

with $\gamma_{n\sigma}^{+} \equiv \sqrt{\int_{\Lambda^{-(n+1)}}^{\Lambda^{-n}} d\epsilon \Delta_{\sigma}(\epsilon)}$ and $\gamma_{n\sigma}^{-} \equiv \sqrt{\int_{-\Lambda^{-n}}^{-\Lambda^{-(n+1)}} d\epsilon \Delta_{\sigma}(\epsilon)}$, respectively. As indicated in Eq. (A.12), it is convenient to define a fermionic operator $f_{0\sigma}$ (with $\{f_{0\sigma}, f_{0\sigma'}^{\dagger}\} = \delta_{\sigma\sigma'}$), which has the form

$$f_{0\sigma} \equiv \frac{1}{\sqrt{\vartheta_{0\sigma}}} \sum_n (\gamma_{n\sigma}^{+} a_{n\sigma} + \gamma_{n\sigma}^{-} b_{n\sigma}), \quad (\text{A.13})$$

with $\vartheta_{0\sigma} = \sum_n [(\gamma_{n\sigma}^{+})^2 + (\gamma_{n\sigma}^{-})^2] = \int_{-1}^1 \Delta_{\sigma}(\epsilon) d\epsilon$. The operator $f_{0\sigma}^{\dagger}$ creates a spin σ electron in the maximally localized state (which is essentially the conduction electron field on the impurity site), equivalent to the *zeroth* site of the Wilson chain, see Fig. A.2. In the limit of constant hybridization, $\Delta_{\sigma}(\epsilon) = \Delta_{\sigma}$, Eq. (A.13) reproduces the well-known result [31], $f_{0\sigma} = \sum_{n=0}^{\infty} \sqrt{d_n/2} (a_{n\sigma} + b_{n\sigma}) = \sqrt{(1 - \Lambda^{-1})/2} \sum_{n=0}^{\infty} \Lambda^{-n/2} (a_{n\sigma} + b_{n\sigma})$.

We insert the maximally localized state into Eq. (A.12) and finally obtain

$$\hat{\mathcal{H}}_{ld} = \sum_{\sigma} \left[\sqrt{\frac{\vartheta_{0\sigma}}{\pi}} (d_{\sigma}^{\dagger} f_{0\sigma} + \text{h.c.}) \right]. \quad (\text{A.14})$$

Eq. (A.14) nicely illustrates that the impurity couples to a *single* fermionic degree of freedom only, the zeroth site of the Wilson chain. To fully map $\hat{\mathcal{H}}_{AM}$ on a linear chain, however, still $\hat{\mathcal{H}}_{CB}$ needs to be transformed properly. We focus on this issue in the next Section.

A.1.2 Transformation of $\hat{\mathcal{H}}_{CB}$

When we insert the expansion (A.6) into Eq. (A.2) the CB-Hamiltonian $\hat{\mathcal{H}}_{CB}$ reads

$$\hat{\mathcal{H}}_{CB} = \sum_{\sigma} \int_{-1}^1 d\epsilon g_{\sigma}(\epsilon) \left\{ \sum_{npp'} [a_{np\sigma}^{\dagger} [\Psi_{np}^{+}(\epsilon)]^{*} a_{np'\sigma} \Psi_{np'}^{+}(\epsilon) + b_{np\sigma}^{\dagger} [\Psi_{np}^{-}(\epsilon)]^{*} b_{np'\sigma} \Psi_{np'}^{-}(\epsilon)] \right\}. \quad (\text{A.15})$$

Though only ($p = 0$)-contributions couple *directly* to the impurity [remember that we chose constant hybridization $h_{n\sigma}^{\pm}$, see Eqs. (A.10) and (A.11)], ($p \neq 0$)-contributions might become important via an indirect coupling to the impurity [via the ($p = 0$)-mode]. Therefore two contributions remain in the pp' -sum of Eq. (A.15): $\sum_{p=0,p'} [\dots] = [\dots]_{p=0,p'=0} + \sum_{p' \neq 0} [\dots]_{p=0}$.

The first term of this sum ($p = p' = 0$), which we label $\hat{\mathcal{H}}_{CB}^{(1)}$, reduces Eq. (A.15) to

$$\hat{\mathcal{H}}_{CB}^{(1)} = \sum_{n\sigma} [\zeta_{n\sigma}^{+} a_{n\sigma}^{\dagger} a_{n\sigma} + \zeta_{n\sigma}^{-} b_{n\sigma}^{\dagger} b_{n\sigma}], \quad (\text{A.16})$$

with the general expression $\zeta_{n\sigma}^{+} = (1/d_n) \int_{\Lambda^{-(n+1)}}^{\Lambda^{-n}} d\epsilon g_{\sigma}(\epsilon)$ and $\zeta_{n\sigma}^{-} = (1/d_n) \int_{-\Lambda^{-n}}^{-\Lambda^{-(n+1)}} d\epsilon g_{\sigma}(\epsilon)$. Note the following: since the single-particle energies of the CB electrons $\zeta_{n\sigma}^{\pm}$ depend only on the *integral* over the logarithmic intervals an exact knowledge of $g_{\sigma}(\epsilon)$ [which can be inferred from Eq. (A.4)] is not required.

Bulla *et al.* [69] showed that for the particular choice taken here [$h_{\sigma}(\epsilon) \rightarrow h_{n\sigma}^{\pm}$ in each logarithmic interval], the single-particle energies $\zeta_{n\sigma}^{\pm}$ are given by

$$\zeta_{n\sigma}^{+} \equiv \frac{\int_{\Lambda^{-(n+1)}}^{\Lambda^{-n}} d\epsilon \epsilon \Delta_{\sigma}(\epsilon)}{\int_{\Lambda^{-(n+1)}}^{\Lambda^{-n}} d\epsilon \Delta_{\sigma}(\epsilon)}, \quad (\text{A.17})$$

$$\zeta_{n\sigma}^{-} \equiv \frac{\int_{-\Lambda^{-n}}^{-\Lambda^{-(n+1)}} d\epsilon \epsilon \Delta_{\sigma}(\epsilon)}{\int_{-\Lambda^{-n}}^{-\Lambda^{-(n+1)}} d\epsilon \Delta_{\sigma}(\epsilon)}. \quad (\text{A.18})$$

A comparison between the general expression for $\zeta_{n\sigma}^{+}$ and Eq. (A.17) reveals that the dispersion is indeed nonlinear here, $g_{\sigma}(\epsilon) = \epsilon \left\{ [d_n \Delta_{\sigma}(\epsilon)] / \left[\int_{\Lambda^{-(n+1)}}^{\Lambda^{-n}} d\epsilon \Delta_{\sigma}(\epsilon) \right] \right\}$.

For constant hybridization $\Delta_{\sigma}(\epsilon) = \Delta_{\sigma}$ the linear dispersion [$g_{\sigma}(\epsilon) = \epsilon$] is recovered within this more general framework. Also the result for $\hat{\mathcal{H}}_{CB}$ of Krishna-murthy *et al.* [31] [who assumed $\Delta_{\sigma}(\epsilon) = \Delta$; see Eq. (2.12) of [31]], $\hat{\mathcal{H}}_{CB}^{(1)} = \frac{1}{2} (1 + \Lambda^{-1}) \sum_{n\sigma} \Lambda^{-n} (a_{n\sigma}^{\dagger} a_{n\sigma} - b_{n\sigma}^{\dagger} b_{n\sigma})$, i.e. $\zeta_{n\sigma}^{\pm} = \pm \frac{1}{2} (1 + \Lambda^{-1}) \Lambda^{-n}$, is recovered in this more general scheme.

The second contribution to the (pp') -sum, $\sum_{p' \neq 0} [\dots]_{p=0}$, couples off-diagonal angular momenta. This term, labeled by $\hat{\mathcal{H}}_{CB}^{(2)}$, takes the form

$$\hat{\mathcal{H}}_{CB}^{(2)} = \sum_{n\sigma} \left\{ \sum_{p' \neq 0} \left[\overbrace{a_{np=0\sigma}^\dagger a_{np'\sigma}}^{I_1} \left(\int_{\Lambda^{-(n+1)}}^{\Lambda^{-n}} d\epsilon g_\sigma(\epsilon) [\Psi_{np=0}^+(\epsilon)]^* \Psi_{np'}^+(\epsilon) \right) + \right. \right. \\ \left. \left. + \overbrace{b_{np=0\sigma}^\dagger b_{np'\sigma}}^{I_2} \left(\int_{-\Lambda^{-n}}^{-\Lambda^{-(n+1)}} d\epsilon g_\sigma(\epsilon) [\Psi_{np=0}^+(\epsilon)]^* \Psi_{np'}^+(\epsilon) \right) \right] \right\}. \quad (\text{A.19})$$

Note that the mapping of the AM on the Wilson chain is still exact at this stage ($\hat{\mathcal{H}}_{CB} = \hat{\mathcal{H}}_{CB}^{(1)} + \hat{\mathcal{H}}_{CB}^{(2)}$), with $h_\sigma(\epsilon)$ and $g_\sigma(\epsilon)$ satisfying Eq. (A.4). In particular, Eq. (A.19) stresses that a complete description of the CB includes *all* possible angular momenta p .

We analyze the importance of $\hat{\mathcal{H}}_{CB}^{(2)}$ by computing the integral I_1 in Eq. (A.19) for the particular case of a linear dispersion (which results in: $I_2 = -I_1$):⁴ inserting Eq. (A.5) into I_1 results in

$$I_1 = \frac{1}{d_n} \int_{\Lambda^{-(n+1)}}^{\Lambda^{-n}} d\epsilon \epsilon \exp(i\omega_n p' \epsilon) = \frac{1}{d_n} \left\{ \exp(i\omega_n p' \epsilon) \left[-(\omega_n p')^{-2} + \epsilon (i\omega_n p') \right] \right\} \Big|_{\Lambda^{-(n+1)}}^{\Lambda^{-n}}$$

which finally reduces to

$$I_1 = \frac{1 - \Lambda^{-1}}{2\pi i p'} \Lambda^{-n} \exp[2\pi i p' / (1 - \Lambda^{-1})] \quad (\text{A.20})$$

[see also Eq. (2.10) of [31]].

We conclude from Eq. (A.20) that $\hat{\mathcal{H}}_{CB}^{(2)}$ becomes less and less important for Λ approaching 1. Wilson showed [1] that the $p \neq 0$ contributions, i.e. $\hat{\mathcal{H}}_{CB}^{(2)}$, can be dropped to a very good approximation for $\Lambda = 2$, which was mostly used in this thesis.⁵

From now on we will disregard $\hat{\mathcal{H}}_{CB}^{(2)}$, which is like dropping a small perturbation in $\hat{\mathcal{H}}_{CB}$. The first *approximation* we use is therefore

$$\hat{\mathcal{H}}_{CB} \approx \hat{\mathcal{H}}_{CB}^{(1)}, \quad (\text{A.21})$$

i.e. we replace Eq. (A.2) by Eq. (A.16).

⁴The reasoning also holds for an arbitrary dispersion, see [69].

⁵The approximation works still pretty good for bigger values of Λ , e.g. $\Lambda = 3$.

A.2 Mapping of the CB onto a semi-infinite chain

To solve $\hat{\mathcal{H}}_{AM}$ numerically, it is convenient to bring $\hat{\mathcal{H}}_{CB}$, Eq. (A.16), into tridiagonal form, see Fig. A.2, i.e. to map $\hat{\mathcal{H}}_{CB}$ onto a semi-infinite chain (the Wilson chain $\hat{\mathcal{H}}_{WC}$),

$$\underbrace{\sum_{n=0\sigma}^{\infty} (\zeta_{n\sigma}^+ a_{n\sigma}^\dagger a_{n\sigma} + \zeta_{n\sigma}^- b_{n\sigma}^\dagger b_{n\sigma})}_{\hat{\mathcal{H}}_{CB}} = \underbrace{\sum_{n=0\sigma}^{\infty} \left[\epsilon_{n\sigma} f_{n\sigma}^\dagger f_{n\sigma} + t_{n\sigma} (f_{n\sigma}^\dagger f_{n+1\sigma} + f_{n+1\sigma}^\dagger f_{n\sigma}) \right]}_{\hat{\mathcal{H}}_{WC}}. \quad (\text{A.22})$$

For this mapping (see e.g. [72]) we use the tridiagonalization procedure developed by Lánczos [73] with diagonal matrix elements $\epsilon_{n\sigma}$ and off-diagonal ones $t_{n\sigma}$ [70].

The tridiagonalization procedure of Lánczos allows us to determine $\hat{\mathcal{H}}_{CB} |\Psi_{n\sigma}\rangle$, where $|\Psi_{n\sigma}\rangle = f_{n\sigma}^\dagger |0\rangle$ denotes a one-particle state (with Fock vacuum $|0\rangle$, $n \in \mathbb{N}_0$),⁶

$$\begin{aligned} \hat{\mathcal{H}}_{CB} |\Psi_{n\sigma}\rangle &= \overbrace{\langle \Psi_{n\sigma} | \hat{\mathcal{H}}_{CB} | \Psi_{n\sigma} \rangle}_{\epsilon_{n\sigma}} |\Psi_{n\sigma}\rangle + \overbrace{\langle \Psi_{n-1\sigma} | \hat{\mathcal{H}}_{CB} | \Psi_{n\sigma} \rangle}_{t_{n-1\sigma}} |\Psi_{n-1\sigma}\rangle \\ &\quad + \overbrace{\langle \Psi_{n+1\sigma} | \hat{\mathcal{H}}_{CB} | \Psi_{n\sigma} \rangle}_{t_{n\sigma}} |\Psi_{n+1\sigma}\rangle. \end{aligned} \quad (\text{A.23})$$

We can immediately identify the matrix elements $\epsilon_{n\sigma}$, $t_{n-1\sigma}$ and $t_{n\sigma}$ by comparing Eq. (A.23) with the ansatz (A.22). Eq. (A.23) nicely illustrates that the n -th site of the Wilson chain is only connected to its two neighboring sites, the $(n-1)$ -th and the $(n+1)$ -th site of the chain. It can also nicely be seen that the recursive determination of the fermionic operators $f_{n\sigma}$ involves the calculation of the onsite energies and the hopping matrix elements along the Wilson chain. Below, the derivation of the corresponding recursion relations is summarized.

The single-particle operator $f_{n\sigma}$ that acts on the n -th site of the Wilson chain is given by the ansatz

$$f_{n\sigma} = \sum_{m=0}^{\infty} (u_{nm\sigma} a_{m\sigma} + v_{nm\sigma} b_{m\sigma}), \quad (\text{A.24})$$

with coefficients $u_{nm\sigma}$ and $v_{nm\sigma}$ that need to be determined recursively.

The initial values $u_{0m\sigma}$ and $v_{0m\sigma}$ are immediately found by comparing the ansatz (A.24) with $f_{0\sigma}$ as given in (A.13),

$$u_{0m\sigma} = \frac{\gamma_{m\sigma}^+}{\sqrt{\vartheta_{0\sigma}}}, \quad v_{0m\sigma} = \frac{\gamma_{m\sigma}^-}{\sqrt{\vartheta_{0\sigma}}}. \quad (\text{A.25})$$

An inversion of the ansatz (A.24) leads to $a_{n\sigma} = \sum_{m=0}^{\infty} u_{mn\sigma} f_{m\sigma}$ and $b_{n\sigma} = \sum_{m=0}^{\infty} v_{mn\sigma} f_{m\sigma}$. When we insert $a_{n\sigma}$ and $b_{n\sigma}$ in the l.h.s. of Eq. (A.22) and compare corresponding $f_{n\sigma}$ operators on both sides of this equation we obtain

$$\sum_{m=0}^{\infty} (\zeta_{ms}^+ u_{nm\sigma} a_{m\sigma}^\dagger + \zeta_{ms}^- v_{nm\sigma} b_{m\sigma}^\dagger) = \epsilon_{n\sigma} f_{n\sigma}^\dagger + t_{n\sigma} f_{n+1\sigma}^\dagger + t_{n-1\sigma} f_{n-1\sigma}^\dagger. \quad (\text{A.26})$$

⁶ $f_{0\sigma}$ was already given in Eq. (A.13); see Eq. (A.24) for the general definition of $f_{n\sigma}$.

In particular, the ($n = 0$)-comparison in Eq. (A.26) (which reflects the comparison of the $f_{0\sigma}$ operators) yields

$$\sum_{m=0}^{\infty} \left(\frac{\zeta_{m\sigma}^+ \gamma_{m\sigma}^+}{\sqrt{\vartheta_{0\sigma}}} a_{m\sigma}^\dagger + \frac{\zeta_{m\sigma}^- \gamma_{m\sigma}^-}{\sqrt{\vartheta_{0\sigma}}} b_{m\sigma}^\dagger \right) = \epsilon_{0\sigma} f_{0\sigma}^\dagger + t_{0\sigma} f_{1\sigma}^\dagger, \quad (\text{A.27})$$

where Eq. (A.25) has already been inserted.

Since the operators $f_{n\sigma}$ obey Fermi-statistics, $\{f_{n\sigma}, f_{n'\sigma'}^\dagger\} = \delta_{nn'} \delta_{\sigma\sigma'}$, the anticommutator of the r.h.s. of Eq. (A.27) with $f_{0\sigma}$ yields $\{\epsilon_{0\sigma} f_{0\sigma}^\dagger + t_{0\sigma} f_{1\sigma}^\dagger, f_{0\sigma}\} = \epsilon_{0\sigma}$. The corresponding anticommutator of the l.h.s. of Eq. (A.27) with $f_{0\sigma}$ as given in (A.13),⁷ finally leads to the relation

$$\epsilon_{0\sigma} = \frac{1}{\vartheta_{0\sigma}} \sum_m \left[\zeta_{m\sigma}^+ (\gamma_{m\sigma}^+)^2 + \zeta_{m\sigma}^- (\gamma_{m\sigma}^-)^2 \right]. \quad (\text{A.28})$$

The initial hopping matrix element $t_{0\sigma}$ can now easily be determined from Eq. (A.27) by computing the anticommutator $\{\epsilon_{0\sigma} f_{0\sigma}^\dagger + t_{0\sigma} f_{1\sigma}^\dagger, \epsilon_{0\sigma} f_{0\sigma} + t_{0\sigma} f_{1\sigma}\} = (\epsilon_{0\sigma})^2 + (t_{0\sigma})^2 = \sum_m \left\{ \left(\frac{\zeta_{m\sigma}^+ \gamma_{m\sigma}^+}{\sqrt{\vartheta_{0\sigma}}} a_{m\sigma}^\dagger + \frac{\zeta_{m\sigma}^- \gamma_{m\sigma}^-}{\sqrt{\vartheta_{0\sigma}}} b_{m\sigma}^\dagger \right), \left(\frac{\zeta_{m\sigma}^+ \gamma_{m\sigma}^+}{\sqrt{\vartheta_{0\sigma}}} a_{m\sigma} + \frac{\zeta_{m\sigma}^- \gamma_{m\sigma}^-}{\sqrt{\vartheta_{0\sigma}}} b_{m\sigma} \right)^\dagger \right\}$. As $\epsilon_{0\sigma}$ is known we obtain $t_{0\sigma}$ as

$$(t_{0\sigma})^2 = \frac{1}{\vartheta_{0\sigma}} \left\{ \sum_m \left[(\zeta_{m\sigma}^+)^2 (\gamma_{m\sigma}^+)^2 + (\zeta_{m\sigma}^-)^2 (\gamma_{m\sigma}^-)^2 \right] - \sum_m \left[\zeta_{m\sigma}^+ (\gamma_{m\sigma}^+)^2 + \zeta_{m\sigma}^- (\gamma_{m\sigma}^-)^2 \right] \right\}. \quad (\text{A.29})$$

When we insert Eqs. (A.13), (A.28) and (A.29) into Eq. (A.27) and compare this with the ansatz for $f_{1\sigma}^\dagger$, Eq. (A.24), we obtain

$$u_{1m\sigma} = \frac{\gamma_{m\sigma}^+}{\sqrt{\vartheta_{0\sigma}} t_{0\sigma}} (\zeta_{m\sigma}^+ - \epsilon_{0\sigma}), \quad (\text{A.30})$$

$$v_{1m\sigma} = \frac{\gamma_{m\sigma}^-}{\sqrt{\vartheta_{0\sigma}} t_{0\sigma}} (\zeta_{m\sigma}^- - \epsilon_{0\sigma}). \quad (\text{A.31})$$

Following the above argumentation one finally obtains the spin-dependent onsite energies $\epsilon_{n\sigma}$ and hopping matrix elements $t_{n\sigma}$ at the n -th site of the Wilson chain as

$$\epsilon_{n\sigma} = \sum_m \left[(u_{nm\sigma})^2 \zeta_{m\sigma}^+ + (v_{nm\sigma})^2 \zeta_{m\sigma}^- \right], \quad (\text{A.32})$$

$$(t_{n\sigma})^2 = \sum_m \left[(u_{nm\sigma})^2 (\zeta_{m\sigma}^+)^2 + (v_{nm\sigma})^2 (\zeta_{m\sigma}^-)^2 \right] - (t_{n-1\sigma})^2 - (\epsilon_{n\sigma})^2, \quad (\text{A.33})$$

with the coefficients of the single-particle operator $f_{n+1\sigma}$, defined in Eq. (A.24),

$$u_{n+1m\sigma} = \frac{1}{t_{n\sigma}} \left[(\zeta_{m\sigma}^+ - \epsilon_{n\sigma}) u_{nm\sigma} - t_{n-1\sigma} u_{n-1m\sigma} \right], \quad (\text{A.34})$$

$$v_{n+1m\sigma} = \frac{1}{t_{n\sigma}} \left[(\zeta_{m\sigma}^- - \epsilon_{n\sigma}) v_{nm\sigma} - t_{n-1\sigma} v_{n-1m\sigma} \right]. \quad (\text{A.35})$$

⁷Note that the discrete operators $a_{n\sigma}$ and $b_{n\sigma}$ are anticommuting as well.

Even though, only the matrix elements along the Wilson chain ($\epsilon_{n\sigma}$ and $t_{n\sigma}$) are finally required, it is crucial to determine the coefficients $u_{n+1m\sigma}$ and $v_{n+1m\sigma}$ as well, since $\epsilon_{n\sigma}$ and $t_{n\sigma}$ depend on these coefficients, see Eqs. (A.32) and (A.33).

Note: the mapping of the CB onto the Wilson chain does not change electron-hole symmetry (as it is a unitary transformation). The Wilson chain, given in Eq. (A.22), consists only of hopping matrix elements $t_{n\sigma}$ and onsite energies $\epsilon_{n\sigma}$. Thus an electron-hole symmetric hybridization $\Delta_\sigma(\epsilon)$ implies that all onsite energies along the Wilson chain vanish, $\epsilon_{n\sigma} = 0 \forall n \in \mathbb{N}_0$. More rigorously the reasoning goes as follows: for an electron-hole symmetric hybridization [$\Delta_\sigma(\epsilon) = \Delta_\sigma(-\epsilon)$] the relations $\zeta_{n\sigma}^+ = -\zeta_{n\sigma}^-$ and $\gamma_{n\sigma}^+ = \gamma_{n\sigma}^-$ are valid, thus $\epsilon_{0\sigma} = 0$ [Eq. (A.28)]. This results in $u_{1m\sigma} = -v_{1m\sigma}$ what leads to $\epsilon_{1\sigma} = 0$ [Eq. (A.32)]. From Eqs. (A.34) and (A.35) one realizes that this leads to $u_{2m\sigma} = -v_{2m\sigma}$ which results in $\epsilon_{2\sigma} = 0$ etc. .

We shall make a final remark here about the numerical solution of the above mentioned equations: since the band energies are exponentially decaying in the course of the iteration one has to use reliable numerical routines (i.e. arbitrary-precision Fortran routines [69]) to solve for the coefficients ($u_{nm\sigma}$, $v_{nm\sigma}$) and matrix elements ($t_{n\sigma}$, $\epsilon_{n\sigma}$).

A.3 Iterative numerical diagonalization

When we rename the impurity operator $d_\sigma \equiv f_{-1\sigma}$ the AM takes a particular compact form

$$\hat{\mathcal{H}}_{AM} = \hat{\mathcal{H}}_d + \overbrace{\sum_{n=-1,\sigma}^{\infty} \left[t_{n\sigma} \left(f_{n\sigma}^\dagger f_{n+1\sigma} + f_{n+1\sigma}^\dagger f_{n\sigma} \right) + \epsilon_{n+1\sigma} f_{n+1\sigma}^\dagger f_{n+1\sigma} \right]}^{\hat{\mathcal{H}}_{CB} + \hat{\mathcal{H}}_{\ell d}}, \quad (\text{A.36})$$

with the coupling between the impurity and the CB $t_{-1\sigma} \equiv \sqrt{\frac{\vartheta_{0\sigma}}{\pi}}$ [see Eq. (A.14)], the kinetic energy ($\propto t_{n\sigma}$) [see Eq. (A.33)] and the onsite energy ($\propto \epsilon_{n\sigma}$) [see Eq. (A.32)] of the CB, written in form of the Wilson chain. Note that there is no possibility of a spin-flip event along the chain. The Hamiltonian (A.36) is valid for an arbitrary energy- and spin-dependent hybridization function $\Delta_\sigma(\epsilon)$, it is therefore a generalization of the one obtained by Krishna-murthy *et al.* [see Eq. (2.14) of [31]]. For the particular case considered by Krishna-murthy *et al.* [31] ($\Delta_\sigma(\epsilon) = \Delta$, i.e. flat and spin-independent bands), their result is recovered with

$$t_{n\sigma} = \frac{1}{2}(1 + \Lambda^{-1})\Lambda^{-n/2} \overbrace{\frac{1 - \Lambda^{-n-1}}{\sqrt{(1 - \Lambda^{-2n-1})(1 - \Lambda^{-2n-3})}}}^{\xi_n^K} \quad (\text{A.37})$$

and $\epsilon_{n\sigma} = 0 \forall n \in \mathbb{N}_0$.

The obtained 'chain-Hamiltonian', depicted in Fig. A.2, can be solved by iterative diagonalization. In the limit of an infinite long Wilson chain the AM is recovered,

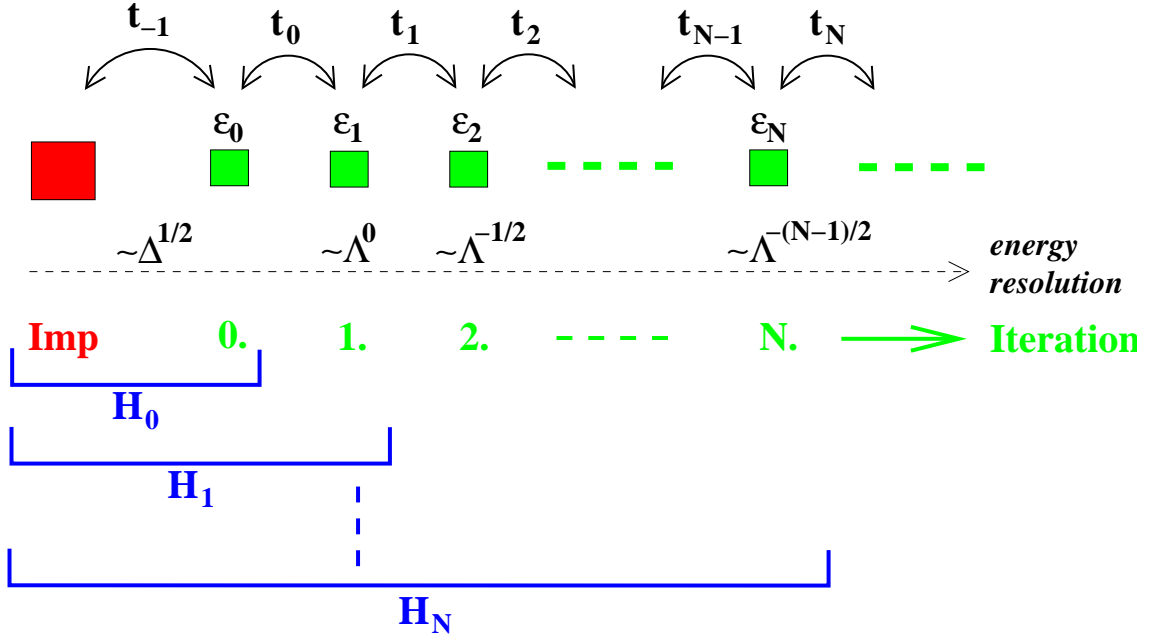


Figure A.2: The Wilson chain can be iteratively diagonalized, since only neighboring sites are coupled with each other. One proceeds by first diagonalizing H_N , the Hamiltonian that describes the system consisting of the impurity and the first N sites of the Wilson chain, then setting up H_{N+1} [via Eq. (A.40)] by coupling H_N to the $(N+1)$ -th site of the chain and restarting the diagonalization procedure. Along the chain the energy resolution increases since smaller and smaller energies ($\sim \Lambda^{-(N-1)/2}$ in the N -th iteration) are coupled to H_N . The t_N 's are the exponentially decaying tunneling matrix elements and the ϵ_N the onsite energies along the chain. For symmetric hybridization, $\Delta(\epsilon) = \Delta(-\epsilon)$, $\epsilon_N = 0 \forall N \in \mathbb{N}_0$.

$$\hat{\mathcal{H}}_{AM} = \lim_{N \rightarrow \infty} \Lambda^{-(N-1)/2} \hat{H}_N \quad (\text{A.38})$$

with the Hamiltonian \hat{H}_N that contains the first N sites of the Wilson chain

$$\hat{H}_N = \Lambda^{(N-1)/2} \left\{ \hat{\mathcal{H}}_d + \sum_{n=-1, \sigma}^{N-1} \left[t_{n\sigma} \left(f_{n\sigma}^\dagger f_{n+1\sigma} + f_{n+1\sigma}^\dagger f_{n\sigma} \right) + \epsilon_{n+1\sigma} f_{n+1\sigma}^\dagger f_{n+1\sigma} \right] \right\}. \quad (\text{A.39})$$

Indeed, Eq.(A.39) coincides with the formula found by Krishna-murthy *et al.* [Eq.(2.18) of [31]] for $\Delta_\sigma(\epsilon) = \Delta$.

Eq. (A.39) allows us to set up the NRG-iteration, heavily used in this thesis

$$\hat{H}_{N+1} = \sqrt{\Lambda} \hat{H}_N + \Lambda^{N/2} \sum_{\sigma} \left[t_{N\sigma} \left(f_{N\sigma}^\dagger f_{N+1\sigma} + f_{N+1\sigma}^\dagger f_{N\sigma} \right) + \epsilon_{N+1\sigma} f_{N+1\sigma}^\dagger f_{N+1\sigma} \right]. \quad (\text{A.40})$$

The latter equation defines a transformation R that (i) relates effective Hamiltonians on successive lower energy scales with each other and (ii) couples only neighboring sites along

the (Wilson) chain ($H_{N+1} = R[H_N]$).⁸

Note that the energy resolution in the N -th iteration is of order $\sim \Lambda^{-(N-1)/2}$, see also Fig. A.2. The rescaling factor $\Lambda^{(N-1)/2}$ in Eq. (A.39) ensures that \hat{H}_N contains numbers that are $\sim \mathcal{O}(1)$, i.e. numerically “good” numbers. \hat{H}_N is an *effective* Hamiltonian that captures the physics at a temperature $k_B T/D \sim \Lambda^{-(N-1)/2}$. Lower temperatures are reached when one proceeds along the Wilson chain.

In the course of the iteration one solves the Schrödinger equation iteratively, i.e. one computes the eigenstates and corresponding eigenenergies of \hat{H}_N . The exponential decay of the matrix elements $t_{N\sigma}$ and $\epsilon_{N\sigma}$ is crucial for the success of the iteration scheme (A.40).

The iteration scheme (A.40) becomes particularly transparent in matrix-notation,

$$\hat{H}_{N+1} = \begin{matrix} |0\rangle_{N+1} \\ |\uparrow\rangle_{N+1} \\ |\downarrow\rangle_{N+1} \\ |\uparrow\downarrow\rangle_{N+1} \end{matrix} \begin{pmatrix} |0\rangle_{N+1} & |\uparrow\rangle_{N+1} & |\downarrow\rangle_{N+1} & |\uparrow\downarrow\rangle_{N+1} \\ \sqrt{\Lambda}\hat{H}_N^d & t_{N\uparrow}f_{N\uparrow}^\dagger & t_{N\downarrow}f_{N\downarrow}^\dagger & 0 \\ t_{N\uparrow}f_{N\uparrow} & \sqrt{\Lambda}\hat{H}_N^d + \epsilon_{N+1\uparrow} & 0 & t_{N\downarrow}f_{N\downarrow}^\dagger \\ t_{N\downarrow}f_{N\downarrow} & 0 & \sqrt{\Lambda}\hat{H}_N^d + \epsilon_{N+1\downarrow} & -t_{N\uparrow}f_{N\uparrow}^\dagger \\ 0 & t_{N\downarrow}f_{N\downarrow} & -t_{N\uparrow}f_{N\uparrow} & \sqrt{\Lambda}\hat{H}_N^d + \sum_\sigma \epsilon_{N+1\sigma} \end{pmatrix}.$$

Here each entry represents a (truncated) matrix which is written in the basis where \hat{H}_N is diagonal, \hat{H}_N^d .

Since the Hilbert space is growing exponentially fast when one proceeds along the chain a truncation is necessary. Thus, one only keeps the lowest lying eigenstates of \hat{H}_N (typically ~ 1000) in each iteration. This is achieved by diagonalizing \hat{H}_N , $\hat{H}_N \rightarrow \hat{H}_N^d$, sorting it w.r.t. increasing eigenenergies and finally truncating it.

The NRG-iteration for the KM is identical to the one for the AM (with identical $\epsilon_{n\sigma}$ and $t_{n\sigma}$). The only thing that needs to be adjusted is the initial Hamiltonian \hat{H}_0 . For the KM the coupling between the impurity and the zeroth site of the Wilson chain is $\sim J$ (the Kondo coupling) (and not $\sim \sqrt{\Delta}$ as for the AM).

A.4 Results of the iterative diagonalization

As explained above, before the Hamiltonian \hat{H}_N is coupled to the next site of the chain, it is diagonalized, $\hat{H}_N^d |\Psi_n\rangle_N = E_n^N |\Psi_n\rangle_N$. The knowledge of the n -th eigenstate $|\Psi_n\rangle_N$ (in the N -th iteration) and its corresponding eigenenergy E_n^N enables us to calculate physical quantities at a scale $\omega_N \sim \Lambda^{-(N-1)/2}D$. Additionally, the calculation of an expectation value of an operator \hat{O} requires the knowledge of the corresponding matrix elements (in the basis of \hat{H}_N^d ; see Section 4.1) of this operator.

The calculation of dynamic quantities (see also Section 4.1), such as the spectral function $A_\sigma(\omega)$, defined as $A_\sigma(\omega) = -\frac{1}{\pi} \Im [\mathcal{G}_\sigma^R(\omega)]$, with the retarded Green's function $\mathcal{G}_\sigma^R(t) = -i\theta(t) \langle \{d_\sigma(t), d_\sigma^\dagger(0)\} \rangle$, requires even more tricks. The spectral function obtained

⁸For constant hybridization one obtains from Eq. (A.37): $t_{N\sigma} \rightarrow \Lambda^{-N/2}$ for $N \rightarrow \infty$.

in the N -th iteration $A_\sigma^N(\omega)$ takes the following form in Lehmann representation [74]

$$A_\sigma^N(\omega, T) = \sum_{nm} \left[\frac{e^{-\beta E_m^N} + e^{-\beta E_n^N}}{Z_N(T)} \right] |{}_N\langle \Psi_n | d_\sigma^\dagger | \Psi_m \rangle_N|^2 \delta(\omega - (E_n^N - E_m^N)). \quad (\text{A.41})$$

Two problems arise from the way Eq. (A.41) is written: (i) what is the 'optimal' way of replacing the δ -functions in Eq. (A.41)? An important question since one is interested in computing the *continuous* spectral function $A_\sigma(\omega, T)$ (see Appendix B.1). (ii) How should one mix the matrix elements in the spectral function $A_\sigma^N(\omega, T)$ to obtain the best possible spectral function of the system $A_\sigma(\omega, T)$? We comment on this issue in Appendix B.2.

Appendix B

How to obtain continuous dynamic functions

It was pointed out in Section 4.1 that dynamic quantities, such as the spectral function $A(\omega, T)$ [see Eq. (4.5)], can be written as a sum of δ -functions; the spectral function corresponding to the N -th NRG-iteration, for instance, can be found in Eq. (A.41). Figure B.1 shows the eigenspectrum of the N -th iteration (horizontal lines) with possible transitions (indicated by the arrows), i.e. non zero matrix elements ${}_N\langle\Psi_n|d_\sigma^\dagger|\Psi_m\rangle_N$, for (a) $T = 0$ and (b) $T \neq 0$. Note that for $T \neq 0$ transitions between excited states are possible.

Since the typical energy scale in the N -th iteration is ω_N , $A^N(\omega, T)$ contains mostly transitions at this energy scale, i.e. $A^N(\omega, T) \sim A(\omega_N, T)$. Information about bigger (smaller) energies in $A(\omega, T)$ are obtained at an earlier (later) stage of the iteration procedure.

Our final goal, namely to obtain a continuous spectral function $A(\omega, T)$ ($\omega \in [-D; D]$), is achieved when the following two problems are resolved: (i) δ -functions appearing in $A^N(\omega, T)$, see Eq. (A.41), have been broadened properly and (ii) spectral functions A^N of different iterations have been combined appropriately as explained above [i.e. $\sum_N A^N \sim A(\omega)$].

Task (i) will be resolved in Section B.1, task (ii) in Section B.2.

B.1 The broadening of the δ -functions

The broadening of the δ -functions by gaussians or lorentzians suggests itself, as the identities $\delta(c - \epsilon) = \lim_{\sigma \rightarrow 0} \frac{1}{\sigma\sqrt{2\pi}} e^{-(c-\epsilon)^2/(2\sigma^2)}$ or $\delta(c - \epsilon) = \lim_{\sigma \rightarrow 0} \frac{1}{\pi} \frac{\sigma}{(c-\epsilon)^2 + \sigma^2}$ [76] hold, respectively. It turns out, however, that dynamic quantities (such as the spectral function) are very sensitive to the properties of the corresponding broadening-functions. Based on some properties of the spectral function, such as (i) the height of the spectral function at the Fermi energy $A(\omega = 0, T = 0)$ (Friedel-sum-rule), (ii) the accuracy of the relation $n(T = 0) = \int_{-\infty}^0 d\omega A(\omega, T = 0)$ [the (thermodynamically computed) occupation $n(T = 0)$ is known with high precision] and (iii) the width of the atomic resonances (which is Γ),

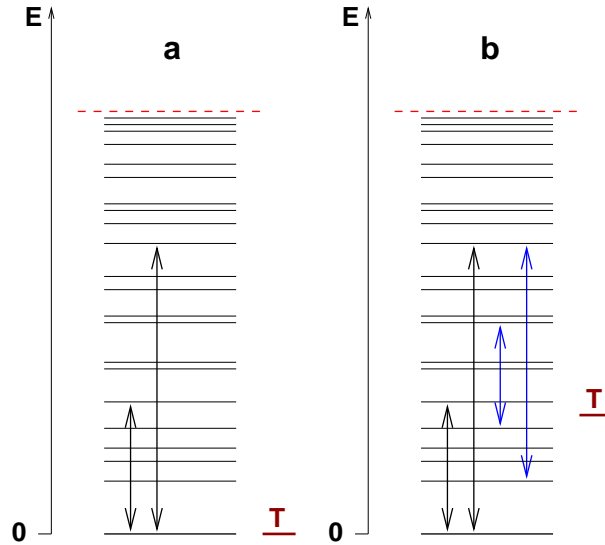


Figure B.1: Possible transitions that contribute to $A^N(\omega, T = 0)$ (a) and $A^N(\omega, T \neq 0)$ (b). Here all energies are measured w.r.t. the ground state energy of the N -th iteration. Note the following: (i) for finite temperatures the possibility of transitions between excited states exists and (ii) an additional energy scale T comes into play. Therefore one should stop the NRG-iteration once the energy resolution $\sim \Lambda^{-(N-1)/2}$ is comparable to T . The dashed lines in (a) and (b) mark the cutoff in the energy spectrum which arises from the truncation of highly excited states. Figure taken from [75].

one can decide which broadening-function is preferable.

It turns out that it is favorable to replace the appearing δ -functions by gaussians rather than lorentzians. This is because gaussians, in contrast to lorentzians, decay exponentially fast. Sakai *et al.* [77] showed that a gaussian adopted to the logarithmic grid used in the NRG-scheme, i.e. a logarithmic gaussian, has even better properties than the 'usual' gaussian has. Fig. B.2 shows a comparison between both functions: the logarithmic gaussian is not symmetric around its center, in contrast to the 'usual' gaussian. It can be inferred from Fig. B.2 that logarithmic gaussians suppress low energies even more than 'usual' gaussians do. Since these energies are resolved at later iterations this suppression makes them preferable w.r.t. 'usual' gaussians.

Consequently appearing δ -functions are broadened by a logarithmic gaussian [75]

$$\delta(c - \epsilon) \rightarrow \frac{e^{-\sigma^2/4}}{\sigma \epsilon \sqrt{\pi}} e^{-\frac{(\ln(c) - \ln(\epsilon))^2}{\sigma^2}}, \quad (\text{B.1})$$

with positive energies ϵ and c [for negative energies Eq. (B.1) has to be adjusted correspondingly]. In typical NRG-calculations we use $\sigma \approx 0.6$.

To improve our intuition of the gaussian and the logarithmic gaussian we compute their width here: at energies $c \pm \sigma\sqrt{2}$ the 'usual' gaussian has decayed to $1/e$ of its maximal

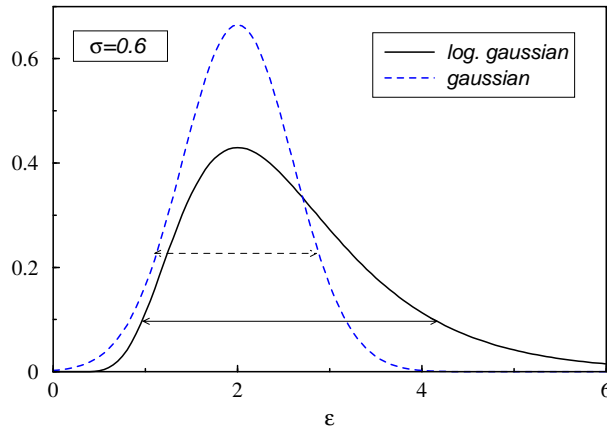


Figure B.2: Logarithmic gaussian [solid; see Eq. (B.1)] vs. 'usual' gaussian (dashed) for $c = 2$ and $\sigma = 0.6$. The logarithmic gaussian is not symmetric around its center c ; it has comparably more weight at higher energies than a 'usual' gaussian does. Note that the width of the logarithmic gaussian (see text) scales with its center, whereas the width of the gaussian is determined by σ only.

value, its width is thus $\sim \sigma$. A logarithmic gaussian, however, decays to $1/e$ of its maximal value at energies $c \pm \delta c$, with $\delta c = c(e^{\pm\sigma} - 1)$. This implies that its width scales with the value of its center c .

B.2 How to combine information from different iterations

To illustrate problem (ii) we use the spectral function $A(\omega)$ as a showcase. A good summary about this topic is given in an article of Bulla *et al.* [75].

One way to obtain a continuous spectral function $A(\omega)$ is to analyze the sum of the N -th NRG-iteration, $A^N(\omega, T = 0) = \sum_n |{}_N\langle n | d^\dagger | 0 \rangle_N|^2 \delta(\omega - (E_n^N - E_0^N))$ at a frequency $\bar{\omega}_N$ which is *typical* for the N -th iteration, say $\bar{\omega}_N = c \omega_N$ (typically $c \approx 2$; $\omega_N = \Lambda^{-(N-1)/2}$). In this scheme, the spectral function of the N -th iteration is replaced by the averaged value at frequency $\bar{\omega}_N$, $A^N(\omega) \rightarrow \bar{A}^N(\bar{\omega}_N)$. One chooses c such that it corresponds to a state with an energy that lies roughly in the middle of the N -th cluster (by cluster we mean the set of *all* possible transitions included in the N -th iteration). Rather big (small) values of c are better described at an earlier (later) stage of the iteration. The continuous spectral function $A(\omega)$ is finally obtained by connecting the 'averaged' points $(\bar{\omega}_N; \bar{A}^N(\bar{\omega}_N))$. In this approach one does not have to worry about the issue of over-counting the matrix elements of the spectral function since consecutive intervals are evaluated separately. This issue is relevant for the procedure outlined below.

The second possibility to evaluate $A(\omega, T)$ is to *first* combine information of the relevant

matrix elements from neighboring clusters, say the N -th and $(N + 2)$ -th cluster (to avoid even/odd oscillations), and *finally* to broaden the combined spectrum. This procedure was suggested by Bulla *et al.* [75]. As shown in Fig. B.3, one combines the matrix elements of the N -th (which contains *all* relevant matrix elements of previous clusters) and the $(N + 2)$ -th cluster such that one finally obtains a mixed cluster that includes information of both original clusters. To do so one embarks the following strategy: those energies of the N -th cluster that are not contained in the $(N + 2)$ -th cluster are just copied in the mixed cluster. Correspondingly energies of the $(N + 2)$ -th cluster that are not contained in the N -th cluster are copied in the mixed cluster. For this sake relevant energies ω_{\min}^{N+2} , ω_{\min}^N and ω_{\max}^{N+2} (see Fig. B.3) have to be identified. Formally, matrix elements with energies $\epsilon > \omega_{\max}^{N+2}$ or $\epsilon < \omega_{\min}^N$ are copied in the mixed cluster.

The energy region where the N -th and $(N+2)$ -th cluster overlap is combined with appropriate weighting of the contributions stemming from the two initial regions. Double-counting of matrix elements is avoided by introducing a weighting function whose weight increases (or decreases) linearly between 0 and 1 (or 1 and 0) for $\omega_{\min}^N \leq \epsilon \leq \omega_{\max}^{N+2}$, as shown in Fig. B.3. As the $(N + 2)$ -th cluster describes smaller energies better than the N -th cluster does, it is appropriate that the weighting function of the $(N+2)$ -th cluster has its maximum weight at ω_{\min}^N (the contrary holds for the N -th cluster). After completing this procedure a set of all relevant (properly weighted) matrix elements (still at discrete energies) for the $(N + 2)$ -th iteration is obtained.

The spectral function $A(\omega, T)$ is finally obtained by broadening all δ -functions of the final cluster. In this approach, every δ -peak is broadened which has the substantial advantage w.r.t. the first procedure that the parameter c does not have to be chosen in this scheme. This approach, introduced for finite temperature calculations first, works very well in the $T = 0$ limit, too. To summarize: in contrast to the previous approach, here one broadens the full (combined) spectrum and one does not average over a cluster.

Below we want to comment on some technical details of the broadening procedure. As the logarithmic gaussian is restricted to positive (or negative) energies (cf. Fig. E.1) it is important to introduce a broadening scheme that interpolates between negative and positive energies. In the finite temperature broadening scheme suggested by Bulla *et al.* [75] a lorentzian is used for broadening the δ -functions at energies $|\epsilon| < 4T$. For $|\epsilon| > 4T$ the δ -functions are broadened by the logarithmic gaussians introduced in Eq. (B.1).¹ Therefore the δ -functions are approximated by

$$\delta(c - \epsilon) \rightarrow \begin{cases} \frac{1}{\pi} \frac{\sigma}{(c-\epsilon)^2 + \sigma^2}, & |\epsilon| < 4T, \quad \sigma = 0.6T, \\ \frac{e^{-\sigma^2/4}}{\sigma|\epsilon|\sqrt{\pi}} e^{-\frac{(\ln(|\epsilon|) - \ln(|\epsilon|))^2}{\sigma^2}}, & |\epsilon| > 4T, \quad \sigma = 0.3. \end{cases}$$

Finally we want to show a plot of the matrix elements of neighboring clusters. In the histogram Fig. B.4 matrix elements of the N -th and $(N + 2)$ -th cluster are plotted versus the typical energy of the N -th cluster $\Lambda^{-(N-1)/2}D$. It can be nicely inferred from this figure that the $(N + 2)$ -th cluster contains excitations at smaller energies than the N -th cluster. For

¹Note that the logarithmic gaussians are restricted to positive (negative) frequencies for $c > 0$ ($c < 0$).

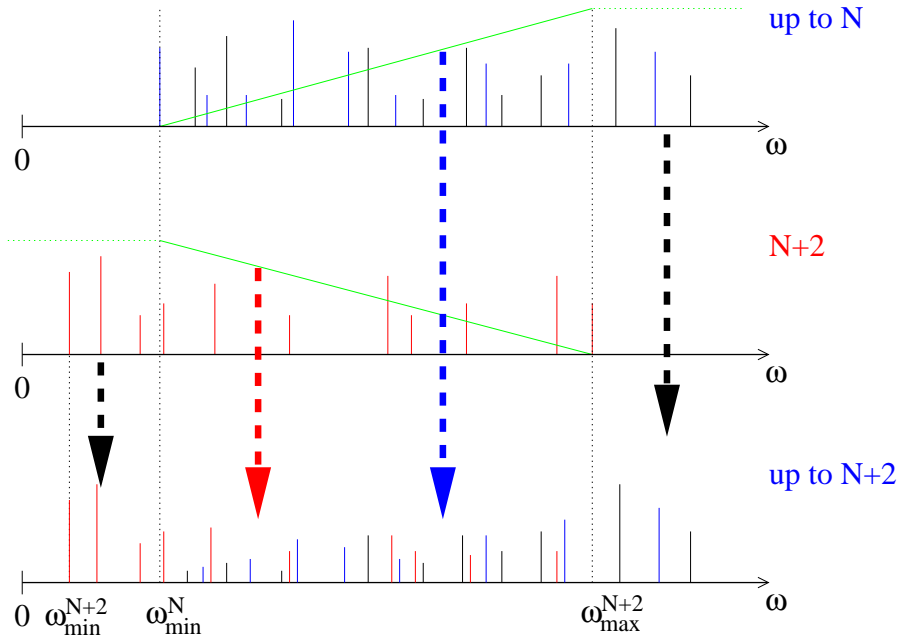


Figure B.3: The initial cluster contains information about all (even) iterations up to the N -th iteration. The combination of this cluster with the $(N + 2)$ -th cluster, schematically depicted, results in a cluster that contains all relevant information up to the $(N + 2)$ -th iteration. The vertical lines correspond to relevant matrix elements (obtained via NRG) that one needs to combine to achieve a continuous spectral function. Relevant energies in this scheme are: the biggest energy of a non-vanishing matrix element of the $(N + 2)$ -th iteration ω_{\max}^{N+2} and the corresponding smallest energies of the N -th and $(N + 2)$ -th iteration ω_{\min}^N and ω_{\min}^{N+2} . The linear weighting functions ensure that the obtained spectral function does not suffer from double counting of involved matrix elements.

this particular example, Fig. B.4 reveals that there are just a few nonzero matrix elements within each cluster. Additional to this, one realizes that the absolute value of the matrix elements decreases in the course of the iteration. This histogram is an important tool to find out which of the above mentioned two procedures of combing the matrix elements is better suited to obtain a smooth dynamical function.

Given the individual clusters contain many nonzero matrix elements, the procedure suggested by Bulla *at al.* [75] is preferable. For only a few matrix elements within each cluster (as shown in Fig. B.4), however, the first suggested method turns out to be more successful [78].

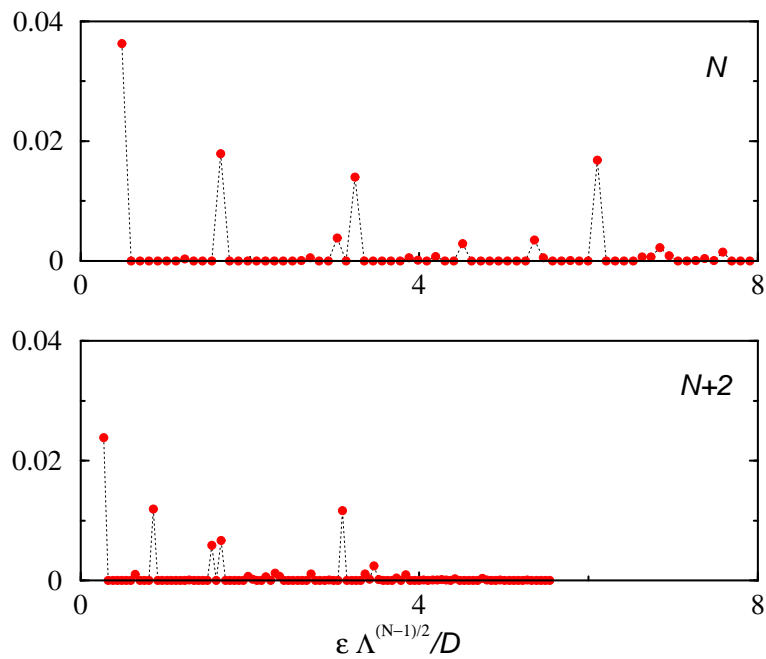


Figure B.4: Matrix elements of the Kubo operator (see Appendix F) in the case of a calculation done for one level coupled to two leads (two channels) (as used in [7]). The odd channel decouples in this particular example. Therefore there are only a few nonzero matrix elements of this operator left. Note that the procedure suggested in Fig. B.3 is not successful here, since the different clusters contain only a few nonzero matrix elements. Here, the evaluation of a continuous function according to the first described procedure is more successful.

Appendix C

Symmetries in the NRG-scheme

The most time-consuming steps of the NRG-iteration are the iterative numerical diagonalizations of (truncated) Hamiltonians \hat{H}_N of size $(\mathcal{N}_N \times \mathcal{N}_N)$ and the following unitary transformations of *all* relevant operators. Since both processes scale like \mathcal{N}_N^3 it is crucial to identify symmetries of the problem which enables us to divide the full Hilbert space into smaller subspaces. This ensures that the model one is interested in can be solved with sufficient precision (set by the value of \mathcal{N}_N) while keeping the computational time tolerable. Especially when one studies more complicated models, such as two channel models, the use of symmetries is essential.

An additional reason why one should use the symmetries of a model is the following: as mentioned in Appendix A, the Hilbert space along the Wilson chain is growing exponentially fast. To circumvent this problem a truncation scheme (a pure energy criterion) is introduced where only the lowest lying eigenstates of the system are kept. This truncation scheme, however, might introduce 'artificial perturbations' in the NRG-iteration. For instance, if one does not use the full spin symmetry (present in absence of a magnetic field; for details see below), one can introduce an 'artificial magnetic field' during the truncation process by dividing spin multiplets. One can get rid of these 'artificial perturbations' by implementing the corresponding symmetry.

Neither the impurity part $\hat{\mathcal{H}}_d$ nor the chain part of the NRG-iteration (A.40) creates or annihilates an electron. The total charge of a system that contains the impurity and the first N sites of the Wilson chain, Q_N (normalized to half-filling),

$$\hat{Q}_N = \sum_{\sigma, n=0}^N (f_{n\sigma}^\dagger f_{n\sigma} - 1) + (d_\sigma^\dagger d_\sigma - 1), \quad (\text{C.1})$$

is therefore a conserved quantity within the NRG-procedure, formally $[\hat{Q}_N, \hat{\mathcal{H}}_N] = 0$ $\forall N \in \mathbb{N}_0$. From $[\hat{Q}_N, \hat{\mathcal{H}}_N] = 0$ follows that $\hat{\mathcal{H}}_N$ has to be diagonal in Q_N ; therefore the full Hilbert space of the N -th iteration can be decomposed into subspaces sorted w.r.t. all possible charge quantum-numbers Q_N . Thus it is convenient to add a *charge* label to an

arbitrary state of the N -th iteration $|\Psi\rangle_N = |\Psi; Q_N\rangle_N$.

Even though one is tempted to introduce also a total spin symmetry S , we do not implement this symmetry, as it is broken in presence of a finite magnetic field B (which is often used in our studies). If one would, however, want to use this symmetry, one has to compute Clebsch-Gordan coefficients to be able to use reduced matrix elements.¹ In presence of a finite magnetic field in z -direction, however, the z -component of the spin \hat{S}_N^z , defined as

$$\hat{S}_N^z = \frac{1}{2} \sum_{n=0}^N \left(f_{n\uparrow}^\dagger f_{n\uparrow} - f_{n\downarrow}^\dagger f_{n\downarrow} + d_{\uparrow}^\dagger d_{\uparrow} - d_{\downarrow}^\dagger d_{\downarrow} \right), \quad (\text{C.2})$$

is still conserved, $[\hat{S}_N^z, \hat{\mathcal{H}}_N] = 0$. Note that this symmetry is broken if the possibility of a spin-flip event along the chain exists or if an additional magnetic field in x or y direction is present. Given this symmetry exists, the Hilbert space of the N -th iteration can be further decomposed. In this case the states are labeled by their total charge and the z -component of the total spin $|\Psi\rangle_N = |\Psi; Q_N, S_N^z\rangle_N$.

In case of two-level impurities, as studied e.g. in [27], one might introduce additional symmetries such as a 'symmetric' and an 'antisymmetric' charge quantum number, \hat{Q}_N^s and \hat{Q}_N^{as} , respectively, given the system can be separated into a symmetric and an antisymmetric subsystem. When these conditions are met, it is convenient to write an arbitrary state as $|\Psi\rangle_N = |\Psi; Q_N^s, Q_N^{\text{as}}, S_N^z\rangle_N$.

¹ For $B = 0$ the eigenstates of $\hat{\mathcal{H}}_N$ are eigenstates of the operators \hat{Q}_N , $(\hat{\mathbf{S}}_N^2)$ and \hat{S}_N^z . In absence of a magnetic field one can label the eigenstates of $\hat{\mathcal{H}}_N$ with $|\Psi; Q_N, S_N, m_N^s\rangle_N$.

Appendix D

The density matrix Numerical Renormalization Group (DM-NRG)

The traditional NRG-scheme inherits only *one* energy scale (corresponding to the effective temperature of the N -th iteration $\sim \Lambda^{-N/2}$). In cases where different energy scales are involved serious problems arise, as outlined in Ref. [4]. If a finite magnetic field is present, for instance, the energy scale $\omega_{\text{magn}} \sim g\mu_B B$ is a relevant energy scale as well. A cure of this problem was invented by Hofstetter [4], who proposed a generalization of the traditional NRG-method.

As a magnetic field (with characteristic energy ω_{magn}) affects the spectral function $A(\omega, T)$ on *all* frequencies ω , it was shown in Ref. [4] that one has to distinguish carefully between the two scales ω and ω_{magn} . For $B \neq 0$ the expectation value of an operator can *not* be calculated by 'just' combining the matrix elements as suggested in Appendix B. The scheme one should use instead is Hofstetter's 'DM-NRG' procedure [4].

The fundamental new idea within this approach is that any expectation value is calculated by considering the density matrix ρ which contains information of the full system.

Indeed, as shown in [4], this more sophisticated treatment has only consequences (in particular on 'high-energy' features) when more than one energy scale is relevant - else the 'DM-NRG'-method coincides with the traditional method on *all* energy scales.

In presence of a magnetic field one would naively expect the following: at high energies a tiny perturbation (e.g. a small magnetic field) does not affect the spectrum at first glance. However, this small perturbation might break the spin symmetry of the ground state leading to a finite polarization of the impurity and therefore result in a remarkable effect at high energies. As shown in Fig. D.1, a finite magnetic field (due to a finite spin-polarization in the leads) results in a systematic redistribution of spectral weight from the lower to the upper atomic level. The 'traditional' NRG-scheme (lower panel in Fig. D.1) is not capable of this effect.

Hofstetter [4] realized that in such a scenario it is crucial to start with the correct ground state (which is the one in presence of a magnetic field), the *real* many-body ground state of the system, to observe the behavior anticipated above. Therefore the DM-NRG-method consists of two stages:

First the usual NRG-procedure is run until the strong coupling fixed point is reached, say at the energy T_{N^*} . At this energy the density matrix of the system $\hat{\rho}$,

$$\hat{\rho} = \frac{1}{Z} \sum_m e^{-E_m^{N^*}/(k_B T_{N^*})} |m\rangle_{N^*} \langle m|, \quad (\text{D.1})$$

with $Z = \sum_m e^{-E_m^{N^*}/(k_B T_{N^*})}$, is constructed. Here $E_m^{N^*}$ are the eigenenergies of the eigenstates $|m\rangle_{N^*}$ of \hat{H}_{N^*} . $\hat{\rho}$ fully describes the physical state of the system. In particular, the (retarded) equilibrium Green's function takes the form

$$\mathcal{G}_\sigma^R(t) = -i\theta(t) \text{tr} [\hat{\rho} \{d_\sigma(t), d_\sigma^\dagger(0)\}]. \quad (\text{D.2})$$

In the DM-NRG-scheme one uses Eq. (D.2) instead of Eq. (4.7) to compute $A(\omega, T)$ [related to \mathcal{G}_σ^R via Eq. (4.5)], i.e. the spectral function is evaluated by using the correct reduced density matrix $\hat{\rho}^{\text{red}}$. As shown in [4] the reduced density matrix is obtained by splitting the Wilson chain into a smaller cluster of length N ($N < N^*$) and an environmental part which contains the remaining degrees of freedom.

In practice, one has to store all unitary transformations (up to the N^* -th iteration) that lead to the *real* ground state, evaluate the density matrix at this iteration, and then evaluate the expectation value given in Eq. (D.2) backwards (i.e. $\forall N \in \mathbb{N}_0, N < N^*$). In the course of this 'backwards-iteration' the reduced density matrices are obtained by tracing out the environmental degrees of freedom. Consequently one deals with a triple sum at every iteration step N ($N < N^*$) and finally obtains the spectral function of the N -th iteration as

$$\begin{aligned} A_\sigma^N(\omega, T_{N^*}) &= \sum_{i,j,m} \langle j | d_\sigma^\dagger | m \rangle_N \langle j | d_\sigma^\dagger | i \rangle_N \rho_{im,N}^{\text{red}} \delta(\omega - (E_j^N - E_m^N)) \\ &+ \sum_{i,j,m} \langle m | d_\sigma^\dagger | j \rangle_N \langle i | d_\sigma^\dagger | j \rangle_N \rho_{im,N}^{\text{red}} \delta(\omega - (E_i^N - E_j^N)). \end{aligned} \quad (\text{D.3})$$

Since we only keep the matrix elements of d^\dagger , we wrote the last expression in the corresponding form. It is worthwhile mentioning that in the DM-NRG-approach transitions between excited states are allowed which are forbidden in 'traditional' zero-temperature NRG-calculations. Thus, both terms in Eq. (D.3) contribute at positive *and* negative frequencies to $A_\sigma^N(\omega, T_{N^*})$.

For the spin correlation function, introduced in Eq. (4.10), one obtains a similar formula

$$\begin{aligned} \chi_N''(\omega) &= \pi \sum_{i,j,m} \langle m | S^z | j \rangle_N \langle j | S^z | i \rangle_N \rho_{im,N}^{\text{red}} \delta(\omega - (E_j^N - E_m^N)) \\ &- \pi \sum_{i,j,m} \langle m | S^z | j \rangle_N \langle j | S^z | i \rangle_N \rho_{im,N}^{\text{red}} \delta(\omega - (E_i^N - E_j^N)), \end{aligned} \quad (\text{D.4})$$

in the framework of the DM-NRG-method.

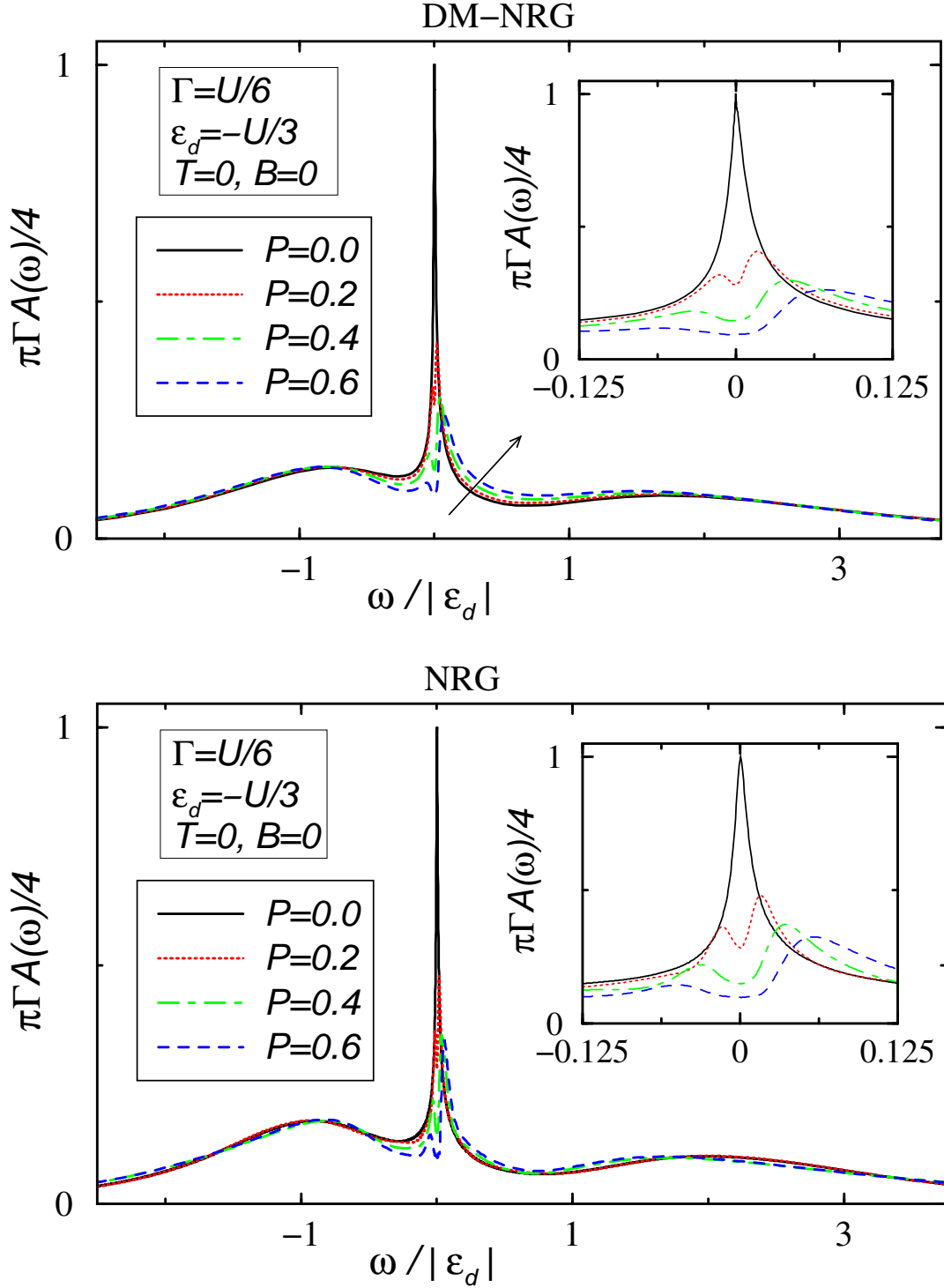


Figure D.1: Spectral function $A(\omega, T = 0)$ of a QD coupled to polarized leads with varying lead polarization P [15] once computed with the DM-NRG (top) and for comparison with the usual NRG-method (bottom). As discussed in [15], finite P has similar effects as an applied magnetic field, leading to a systematic shift (indicated by the arrow in the upper plot) of spectral weight to the upper atomic level. The spectral functions computed via the DM-NRG nicely show this behavior while those computed with the 'conventional' NRG-method are not capable of this shift. For small energies, both methods are essentially identical.

Appendix E

Kramers-Kronig (KK) relation

The KK-relations [79] establish a relation between the real and the imaginary part of a causal function¹ $\kappa(\omega) = \Re[\kappa(\omega)] + i\Im[\kappa(\omega)]$, $\omega \in \{-\infty, \infty\}$,

$$\Re[\kappa(\omega)] = \frac{1}{\pi} \mathcal{P} \int_{-\infty}^{\infty} \frac{\Im[\kappa(\omega')]}{\omega' - \omega} d\omega', \quad (\text{E.1})$$

$$\Im[\kappa(\omega)] = -\frac{1}{\pi} \mathcal{P} \int_{-\infty}^{\infty} \frac{\Re[\kappa(\omega')]}{\omega' - \omega} d\omega', \quad (\text{E.2})$$

where $\mathcal{P} \int_{-\infty}^{\infty} \frac{\Im[\kappa(\omega')]}{\omega' - \omega} d\omega' = \lim_{\epsilon \rightarrow 0} \left[\int_{-\infty}^{-\epsilon} \frac{\Im[\kappa(\omega')]}{\omega' - \omega} d\omega' + \int_{\epsilon}^{\infty} \frac{\Im[\kappa(\omega')]}{\omega' - \omega} d\omega' \right]$ denotes the principal value of the corresponding integrals. In cases when one is interested in *both*, real and imaginary part of a causal function, it suffices to compute only one of them. The corresponding conjugated part can be obtained from relation (E.1) or (E.2), respectively. However, the computation of the principal value (with high precision) makes the KK-transformation a nontrivial numerical task.

We follow an idea of Bulla [5] for performing the KK-transformation here. In the course of NRG the imaginary part of an arbitrary causal function, say $\Im[\kappa(\omega)]$, is given (before broadening) as a sum of matrix elements α_n at energies p_n , $\Im[\kappa(\omega)] = \sum_n \alpha_n \delta(\omega - p_n)$.² Since the integration is a linear operation, there are obviously two possibilities for the KK-transformation of $\Im[\kappa(\omega)]$: (i) one *first* sums up the broadened δ -functions (leading to a continuous function) and *afterwards* performs the KK-transformation, $\Re[\kappa(\omega)] = [\sum_n \alpha_n \delta(\omega - p_n)]^{KK}$ or (ii) one performs the KK-transformation of all δ -functions *before* summing them up, $\Re[\kappa(\omega)] = \sum_n \alpha_n [\delta(\omega - p_n)]^{KK}$.

Since typical functions of our interest, like $\Im[\mathcal{G}^R(\omega)]$, reveal sharp features around the Fermi energy (Kondo resonance) it is much harder to obtain the KK-transformed following approach (i). For this reasons we follow the second approach.

Let us consider the causal function $\Im[\kappa_1(\omega)] = \delta(\omega - p_n)$, a single delta function at energy p_n . The complex function $\kappa_1(z)$, $\kappa_1(z = \omega + i\eta) = \left(-\frac{1}{\pi}\right) \int_0^{\infty} d\omega' \frac{\delta(\omega' - p_n)}{z - \omega'}$, $z \in \mathbb{C}$

¹Such as the retarded Green's function $\mathcal{G}^R(\omega)$.

²Note: $\Im[\mathcal{G}^R(\omega)] \sim \sum_n |\langle n | d^\dagger | 0 \rangle|^2 \delta(\omega - p_n)$, i.e. a sum of δ -functions.

and $\eta \rightarrow 0^+$, is easily obtained by analytic continuation. We know from Appendix B that the broadening of the δ -peak works best when one replaces them by logarithmic gaussians $\delta(\omega - p_n) \rightarrow \frac{e^{-b^2/4}}{bp_n\sqrt{\pi}} \exp\left[-\frac{(\ln\omega - \ln p_n)^2}{b^2}\right]$, centered at the *positive* energy p_n (analogously for $p_n < 0$) with $b \approx 0.6$. It is convenient to write the logarithmic gaussian as a function f that only depends on ω/p_n , $\frac{1}{p_n} \frac{e^{-b^2/4}}{b\sqrt{\pi}} \exp\left[-\frac{(\ln(\omega/p_n))^2}{b^2}\right] = \frac{1}{p_n} f\left(\frac{\omega}{p_n}\right)$, thus

$$\kappa_1(z = \omega + i\delta) = \left(-\frac{1}{\pi}\right) \int_0^\infty d\omega' \frac{\frac{1}{p_n} f\left(\frac{\omega'}{p_n}\right)}{z - \omega'}. \quad (\text{E.3})$$

By means of the definitions $x' \equiv \frac{\omega'}{p_n}$, $x \equiv \frac{\omega}{p_n}$ and $\delta' \equiv \frac{\eta}{p_n}$ we can therefore compute both the real and the imaginary part of $\kappa_1(z)$

$$\Re[\kappa_1(z = \omega + i\delta)] = \left(-\frac{1}{\pi}\right) \frac{1}{p_n} \overbrace{\int_0^\infty dx' f(x') \frac{x - x'}{\delta'^2 + (x - x')^2}}^{g(x)} = -\frac{g(x)}{\pi p_n}, \quad (\text{E.4})$$

$$\Im[\kappa_1(z = \omega + i\delta)] = \left(-\frac{1}{\pi}\right) \frac{1}{p_n} \underbrace{\left[-\int_0^\infty dx' f(x') \frac{\delta'}{\delta'^2 + (x - x')^2}\right]}_{h(x)} = -\frac{h(x)}{\pi p_n}, \quad (\text{E.5})$$

with the function $f(x)$ (defined for $x > 0$ only)³ given as

$$f(x) = \frac{e^{-b^2/4}}{b\sqrt{\pi}} \exp\left[-\frac{(\ln x)^2}{b^2}\right]. \quad (\text{E.6})$$

The functions that describe the real and the imaginary part of $\kappa_1(z)$, namely $g(x)$ and $h(x)$, cf. Eqs. (E.4) and (E.5) have to be determined for sufficiently small δ' , chosen such that the integrals in Eqs. (E.4) and (E.5) have converged (typically $\delta' \approx 0.01$). Note that the required convergence makes an adjustment of δ' necessary when the value of b in the logarithmic gaussian is changed. The big advantage of this treatment is that one has to compute (numerically) the function $g(x)$ for any given b , with an accordingly adjusted δ' , only once. Consequently we store the function $g(x)$ for the most relevant values of b on the hard disk.

Finally we remark on an anomaly: although the logarithmic gaussians are confined to positive or negative frequencies, their KK-transformed, obtained from $g(x)$, see Eq. (E.4), are not restricted to those intervals, see Fig. E.1.

³Note: for $x \leq 0$ Eq. (E.6) is not defined, thus we define $f(x) = 0 \forall x \leq 0$.

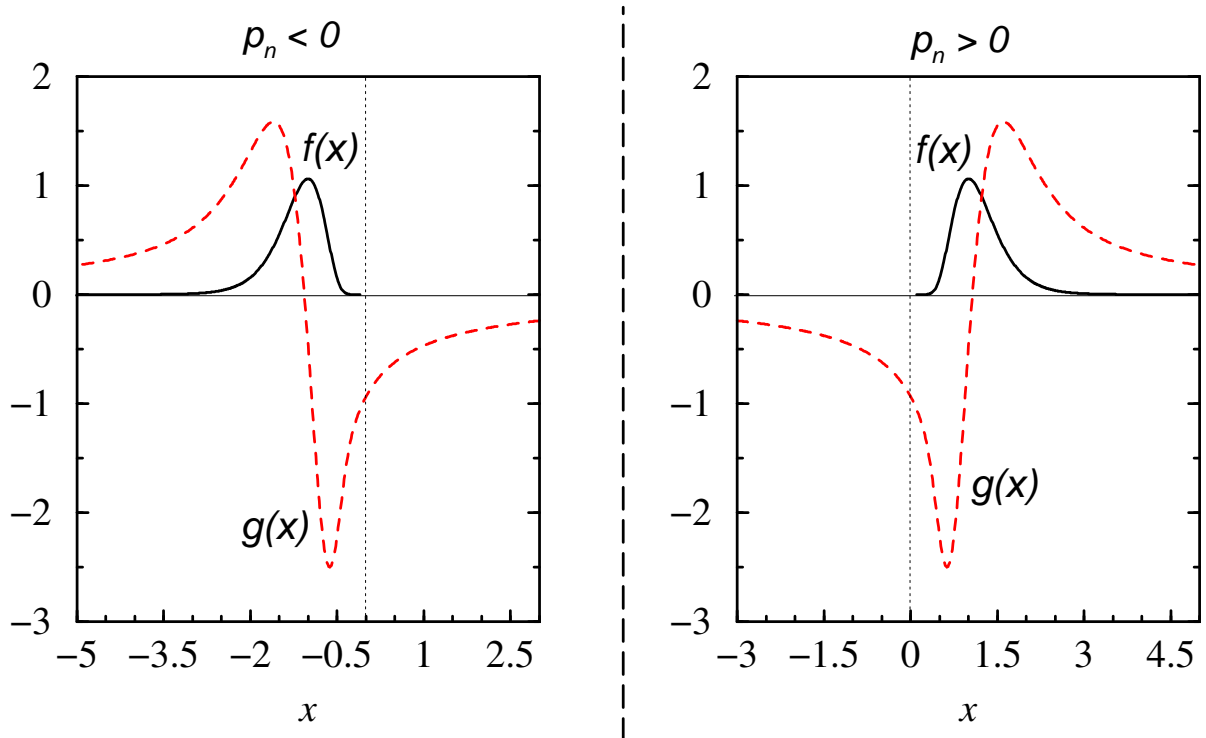


Figure E.1: KK-transformation of the logarithmic gaussian, Eq. (E.6), $f(x)$ (for $b = 0.50$) for the case of $p_n > 0$ and $p_n < 0$. $g(x)$, defined in Eq. (E.4), is shown for both cases as well (with $\delta' = 0.001$). In contrast to $f(x)$, its KK-transformed, $g(x)$, is finite for positive *and* negative energies.

Appendix F

Kubo formalism

The linear conductance through an interacting region can be calculated for an *arbitrary* impurity contacted to a left and a right lead within the Kubo formalism [6]. In contrast to the formula developed by Meir and Wingreen [80], where the conductance G through an interacting region is related to $\Im[\mathcal{G}^R]$, the condition of proportional coupling ($\Gamma_L \propto \Gamma_R$) is not required for the Kubo approach. In particular, in multi-level QDs with a relative sign in the tunneling matrix elements between the different levels, the condition of proportional coupling is not met, see e.g. the $s = -1$ case in [27].

Since the conductance is calculated in a *nonlocal* way within the Kubo formalism, one really has to perform a 'two-channel' calculation (which means that the system size increases by a factor of 16 in each step of the NRG-iteration) when one uses this approach.

The Kubo formalism allows one to relate the linear conductance with the current-current correlator, see Izumida *et al.* [6]. Obviously the operator $\hat{K}^* = \hat{N}_L - \hat{N}_R = \frac{i}{\hbar}[\hat{\mathcal{H}}, \hat{N}_L - \hat{N}_R]$, with $\hat{N}_L = \sum_{k\sigma} c_{k\sigma L}^\dagger c_{k\sigma L}$ and $\hat{N}_R = \sum_{k\sigma} c_{k\sigma R}^\dagger c_{k\sigma R}$ [with Fermi operators $c_{k\sigma L}$ ($c_{k\sigma R}$) of the left (right) lead], is of particular interest within this formalism. Since only the tunneling part of \mathcal{H} does not commute with $\hat{N}_L - \hat{N}_R$, one obtains $\hat{K}^* = \frac{i}{\hbar}[\hat{\mathcal{H}}_{\ell d}, \hat{N}_L - \hat{N}_R]$. As shown in Section 3.1, it is often convenient to work in the symmetric/antisymmetric basis described by the Fermi operators $\alpha_{sk\sigma}$ and $\alpha_{ak\sigma}$ [as defined in Eq. (3.6)]. In this basis \hat{K}^* has the form

$$\hat{N}_L - \hat{N}_R = \sum_{k,\sigma} (c_{k\sigma L}^\dagger c_{k\sigma L} - c_{k\sigma R}^\dagger c_{k\sigma R}) = \sum_{k\sigma} (\alpha_{ak\sigma}^\dagger \alpha_{sk\sigma} + \alpha_{sk\sigma}^\dagger \alpha_{ak\sigma}). \quad (\text{F.1})$$

We illustrate this procedure by looking at the case of a two level, two channel problem with a relative minus sign in one tunneling matrix element, as studied in Ref. [27]. In the symmetric/antisymmetric basis $\hat{\mathcal{H}}_{\ell d}$ takes the form $\hat{H}_{\ell d} = \sum_{k,\sigma} \tilde{V}_1 (d_{1\sigma}^\dagger \alpha_{sk\sigma} + \text{h.c.}) + \tilde{V}_2 (d_{2\sigma}^\dagger \alpha_{ak\sigma} + \text{h.c.})$ ($d_{i\sigma}$ are the Fermi operators of the impurity level i , $i = \{1, 2\}$, and $\tilde{V}_i = \sqrt{2}V_i$ are the corresponding tunneling matrix elements), which finally leads to

$$\hat{N}_L - \hat{N}_R = \frac{i}{\hbar} \sum_{k\sigma} [\tilde{V}_1 (d_{1\sigma}^\dagger \alpha_{ak\sigma} - \alpha_{ak\sigma}^\dagger d_{1\sigma}) + \tilde{V}_2 (d_{2\sigma}^\dagger \alpha_{sk\sigma} - \alpha_{sk\sigma}^\dagger d_{2\sigma})]. \quad (\text{F.2})$$

Note, even though the operator $\hat{N}_L - \hat{N}_R$ is purely imaginary, we can use real matrices to compute Eq. (F.2).

F.1 Derivation of the Kubo formula

When a *small* bias voltage is applied across a QD, a current is driven through the system. Here we compute the *linear* conductance G through an interacting QD which is connected to leads of chemical potentials $\mu_L = eV/2$ and $\mu_R = -eV/2$, respectively (shown in Fig. F.1).

Consequently the system consists of an equilibrium part (the equilibrium Anderson model

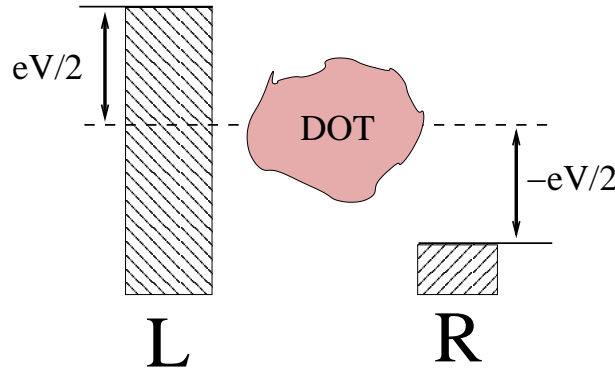


Figure F.1: The leads connected to the QD have different chemical potentials which drives a current through the QD. An overall potential difference of magnitude V is applied on the QD. Note that V has to be sufficiently small to justify the use of linear response theory.

$\hat{\mathcal{H}}_{\text{eq}}$) and an additional perturbation, $\hat{\mathcal{H}}_{\text{sys}} = \hat{\mathcal{H}}_{\text{eq}} + \hat{\mathcal{H}}'$, $\hat{\mathcal{H}}' = -N_L\mu_L - N_R\mu_R$. Since we consider the perturbation $\hat{\mathcal{H}}'$ to be small, we use first order perturbation theory in $\hat{\mathcal{H}}'$ (linear response theory) to compute G . The introduction of a linear response tensor σ , $\langle \dot{N}_\alpha \rangle = \sum_\beta \sigma_{\alpha\beta} \mu_\beta$ (with $\alpha/\beta = L/R$), allows us to write $G(\omega)$ as

$$G(\omega) = \frac{\langle I(\omega) \rangle}{V} = \frac{e}{V} \frac{\langle \dot{N}_L \rangle - \langle \dot{N}_R \rangle}{2} = \frac{e^2}{4} [\sigma_{LL}(\omega) + \sigma_{RR}(\omega) - \sigma_{LR}(\omega) - \sigma_{RL}(\omega)]. \quad (\text{F.3})$$

To compute $\sigma_{\alpha\beta}$, we first compute $\langle \dot{N}_\alpha(t) \rangle$ for arbitrary times (see [40], Appendix B)¹ and then take the expectation value $\langle \dot{N}_\alpha(t=0) \rangle$. The steady state conductance is thus related to

$$\langle \dot{N}_\alpha(t=0) \rangle = \frac{1}{i\hbar} \text{tr} \left\{ \int_{-\infty}^{t=0} [-N_\beta, \rho_{\text{eq}}] \dot{N}_\alpha(-t') \mu_\beta dt' \right\} = \int_{-\infty}^{t=0} \sigma_{\alpha\beta}(0-t') \mu_\beta, \quad (\text{F.4})$$

¹ In linear response theory, the change $\Delta A(t)$ of an observable A due to a (time dependent) perturbation $V(t) = BF(t)$ is given as $\langle \Delta A(t) \rangle = \frac{1}{i\hbar} \text{tr} \int_{-\infty}^t [B, \rho_{\text{eq}}] A(t-t') F(t') dt'$. Here we are interested in a time-independent perturbation, an applied bias voltage.

which implies

$$\sigma_{\alpha\beta}(t') = \frac{1}{i\hbar} \text{tr} \left\{ [-N_\beta, \rho_{eq}] \dot{N}_\alpha(t') \right\} = \frac{-1}{i\hbar} \text{tr} \left\{ [N_\beta, \rho_{eq}] e^{\frac{i}{\hbar} \hat{\mathcal{H}}_{eq} t'} \dot{N}_\alpha e^{-\frac{i}{\hbar} \hat{\mathcal{H}}_{eq} t'} \right\}. \quad (\text{F.5})$$

Here $\rho_{eq} = \frac{1}{Z} e^{-\beta \hat{\mathcal{H}}_{eq}}$ denotes the density matrix of the unperturbed Hamiltonian. The cyclic property of the trace allows us to write the frequency-dependent conductivity $\sigma_{\alpha\beta}(\omega)$, the Fourier transformed of Eq. (F.5), in the following way

$$\sigma_{\alpha\beta}(\omega) = \lim_{\delta \rightarrow 0^+} \frac{i}{\hbar} \text{tr} \left\{ \int_0^\infty e^{i\omega t - \delta t} \underbrace{e^{-\frac{i}{\hbar} \hat{\mathcal{H}}_{eq} t} [N_\beta, \rho_{eq}] e^{\frac{i}{\hbar} \hat{\mathcal{H}}_{eq} t} \dot{N}_\alpha}_{\chi(t)} dt \right\}. \quad (\text{F.6})$$

To simplify notation we will skip the $\lim_{\delta \rightarrow 0^+}$ henceforth. Integrating Eq. (F.6) by parts yields

$$\begin{aligned} \sigma_{\alpha\beta}(\omega) &= \frac{i}{\hbar} \left\{ \frac{e^{i\omega t - \delta t}}{i\omega - \delta} \text{tr}(\chi(t)) \Big|_0^\infty - \int_0^\infty dt \frac{e^{i\omega t - \delta t}}{i\omega - \delta} \text{tr} \left[\left(\frac{-i}{\hbar} \hat{\mathcal{H}}_{eq} \right) e^{-\frac{i}{\hbar} \hat{\mathcal{H}}_{eq} t} [N_\beta, \rho_{eq}] e^{\frac{i}{\hbar} \hat{\mathcal{H}}_{eq} t} \dot{N}_\alpha \right. \right. \\ &\quad \left. \left. + e^{-\frac{i}{\hbar} \hat{\mathcal{H}}_{eq} t} [N_\nu, \rho_{eq}] \left(\frac{i}{\hbar} \hat{\mathcal{H}}_{eq} \right) e^{\frac{i}{\hbar} \hat{\mathcal{H}}_{eq} t} \dot{N}_\alpha \right] \right\} \\ &= \frac{i}{\hbar} \left\{ \frac{-1}{i\omega - \delta} \text{tr}([N_\nu, \rho_{eq}] \dot{N}_\alpha) - \frac{1}{i\omega - \delta} \int_0^\infty dt e^{i\omega t - \delta t} \left[\text{tr} \left(\left(\frac{-i}{\hbar} \hat{\mathcal{H}}_{eq} \right) [N_\beta, \rho_{eq}] \dot{N}_\beta(t) \right) \right. \right. \\ &\quad \left. \left. + \text{tr} \left(\dot{N}_\alpha(t) [N_\beta, \rho_{eq}] \left(\frac{i}{\hbar} \hat{\mathcal{H}}_{eq} \right) \right) \right] \right\}. \quad (\text{F.7}) \end{aligned}$$

We rewrite the terms $\text{tr} \left\{ \left(\frac{-i}{\hbar} \hat{\mathcal{H}}_{eq} \right) [N_\beta, \rho_{eq}] \dot{N}_\alpha(t) \right\} = -\frac{i}{\hbar} \text{tr} \left\{ \rho_{eq} \dot{N}_\beta(t) \hat{\mathcal{H}}_{eq} N_\beta - \rho_{eq} \hat{\mathcal{H}}_{eq} N_\beta \dot{N}_\alpha(t) \right\}$ and $\text{tr} \left\{ \dot{N}_\alpha(t) [N_\beta, \rho_{eq}] \left(\frac{i}{\hbar} \hat{\mathcal{H}}_{eq} \right) \right\} = \frac{i}{\hbar} \text{tr} \left\{ \rho_{eq} \dot{N}_\alpha(t) N_\beta \hat{\mathcal{H}}_{eq} - \rho_{eq} N_\beta \hat{\mathcal{H}}_{eq} \dot{N}_\beta(t) \right\}$ in Eq. (F.7) and finally obtain the frequency-dependent linear conductivity

$$\begin{aligned} \sigma_{\alpha\beta}(\omega) &= \frac{i}{\hbar} \left\{ \frac{-1}{i\omega - \delta} \text{tr} \left([N_\beta, \rho_{eq}] \dot{N}_\alpha \right) \right. \\ &\quad \left. - \frac{1}{i\omega - \delta} \int_0^\infty dt e^{i\omega t - \delta t} \text{tr} \left(\rho_{eq} \left[\frac{i}{\hbar} [\hat{\mathcal{H}}_{eq}, N_\beta] \dot{N}_\alpha(t) - \dot{N}_\alpha(t) \frac{i}{\hbar} [\hat{\mathcal{H}}_{eq}, N_\beta] \right] \right) \right\} \\ &= \frac{i}{\hbar} \left[\frac{-1}{i\omega - \delta} \text{tr} \left([N_\beta, \rho_{eq}] \dot{N}_\alpha \right) - \frac{1}{i\omega - \delta} \int_0^\infty dt e^{i\omega t - \delta t} \left\langle [\dot{N}_\beta, \dot{N}_\alpha(t)] \right\rangle_{eq} \right]. \quad (\text{F.8}) \end{aligned}$$

Analogously to [6] we define $K_{\alpha\beta}(\omega) \equiv \frac{-i}{\hbar} \int_0^\infty dt e^{i\omega t - \delta t} \left\langle [\dot{N}_\beta(0), \dot{N}_\alpha(t)] \right\rangle_{eq}$ which enables us to simplify Eq. (F.8)

$$\sigma_{\alpha\beta}(\omega) = \frac{1}{i\omega} \{ K_{\alpha\beta}(\omega) - K_{\alpha\beta}(0) \}, \quad (\text{F.9})$$

with $K_{\alpha\beta}(0) = \frac{i}{\hbar} \text{tr} \left\{ [N_\beta, \rho_{eq}] \dot{N}_\alpha \right\}$. Note that the *complex* causal function $K_{\alpha\beta}(\omega) = K'_{\alpha\beta}(\omega) + iK''_{\alpha\beta}(\omega)$ is obtained by averaging over the *unperturbed* system. When one inserts a complete set of states, it is straightforward to perform the integration² that is necessary to obtain $K_{\alpha\beta}(\omega)$

$$\begin{aligned}
K_{\alpha\beta}(\omega) &= \frac{-i}{\hbar} \int_0^\infty dt e^{i\omega t - \delta t} \sum_{n,m} \left(\langle n | \rho_{eq} \dot{N}_\beta | m \rangle \langle m | e^{\frac{i}{\hbar} \hat{\mathcal{H}}_{eq} t} \dot{N}_\alpha e^{-\frac{i}{\hbar} \hat{\mathcal{H}}_{eq} t} | n \rangle \right. \\
&\quad \left. - \langle m | \rho_{eq} e^{\frac{i}{\hbar} \hat{\mathcal{H}}_{eq} t} \dot{N}_\alpha e^{-\frac{i}{\hbar} \hat{\mathcal{H}}_{eq} t} | n \rangle \langle n | \dot{N}_\beta | m \rangle \right) \quad (\text{F.10}) \\
&= \frac{-i}{\hbar} \sum_{n,m} \int_0^\infty dt e^{i\omega t - \delta t} e^{\frac{i}{\hbar} (E_m - E_n) t} \left[\frac{1}{Z} (e^{-\beta E_n} - e^{-\beta E_m}) \right] \langle n | \dot{N}_\beta | m \rangle \langle m | \dot{N}_\alpha | n \rangle \\
&= \frac{-i}{\hbar} \frac{1}{Z} \sum_{n,m} (e^{-\beta E_n} - e^{-\beta E_m}) \langle n | \dot{N}_\beta | m \rangle \langle m | \dot{N}_\alpha | n \rangle \int_0^\infty dt e^{\frac{i}{\hbar} (\hbar\omega - (E_n - E_m)) t - \delta t} \\
&= \frac{1}{Z} \sum_{n,m} (e^{-\beta E_n} - e^{-\beta E_m}) \frac{(E_m - E_n + \hbar\omega) - i\hbar\delta}{(E_m - E_n + \hbar\omega)^2 + (\hbar\delta)^2} \langle n | \dot{N}_\beta | m \rangle \langle m | \dot{N}_\alpha | n \rangle.
\end{aligned}$$

Eq. (F.10) yields $K'_{\alpha\beta}(\omega) = \sum_{n,m} \left[\frac{e^{-\beta E_n} - e^{-\beta E_m}}{Z} \right] \langle n | \dot{N}_\beta | m \rangle \langle m | \dot{N}_\alpha | n \rangle \frac{\hbar\omega - (E_n - E_m)}{(\hbar\omega - (E_n - E_m))^2 + (\hbar\delta)^2}$ and $K''_{\alpha\beta}(\omega) = \sum_{n,m} \left[\frac{e^{-\beta E_n} - e^{-\beta E_m}}{Z} \right] \langle n | \dot{N}_\beta | m \rangle \langle m | \dot{N}_\alpha | n \rangle \frac{-\hbar\delta}{(\hbar\omega - (E_n - E_m))^2 + (\hbar\delta)^2}$ (with $\delta \rightarrow 0^+$) resulting in³

$$K'_{\alpha\beta}(\omega) = - \sum_{n,m} \left[\frac{e^{-\beta \epsilon_m} - e^{-\beta \epsilon_n}}{Z} \right] \langle n | \dot{N}_\beta | m \rangle \langle m | \dot{N}_\alpha | n \rangle \frac{1}{\hbar\omega - (\epsilon_n - \epsilon_m)} \quad (\text{F.11})$$

$$K''_{\alpha\beta}(\omega) = \pi \sum_{n,m} \left[\frac{e^{-\beta \epsilon_m} - e^{-\beta \epsilon_n}}{Z} \right] \langle n | \dot{N}_\beta | m \rangle \langle m | \dot{N}_\alpha | n \rangle \delta(\hbar\omega - (\epsilon_n - \epsilon_m)). \quad (\text{F.12})$$

Obviously the functions $K'_{\alpha\beta}(\omega)$ and $K''_{\alpha\beta}(\omega)$ have the following symmetries: $K'_{\alpha\beta}(\omega) = K'_{\alpha\beta}(-\omega)$ and $K''_{\alpha\beta}(\omega) = -K''_{\alpha\beta}(-\omega)$ ⁴ implying

$$K'_{\alpha\beta}(0) \neq 0 \quad (\text{F.13})$$

$$K''_{\alpha\beta}(0) = 0. \quad (\text{F.14})$$

Even though we can only compute $K''_{\alpha\beta}(\omega)$, but not $K'_{\alpha\beta}(\omega)$ within the framework of NRG, we can access $K'_{\alpha\beta}(\omega)$ by performing a KK-transformation (see Appendix E) of $K''_{\alpha\beta}(\omega)$ [as

² $\int_0^\infty dt e^{\frac{i}{\hbar} (\hbar\omega - (E_n - E_m)) t - \delta t} = \hbar \frac{i(E_m - E_n + \hbar\omega) + \delta\hbar}{(E_m - E_n + \hbar\omega)^2 + (\hbar\delta)^2}$

³ $\pi\delta(\alpha) = \lim_{a \rightarrow 0} \frac{a}{\alpha^2 + a^2}$

⁴For $T = 0$ an integration of $K''_{\alpha\beta}(\omega)$ results in: $\int_{-\infty}^\infty d\omega K''_{\alpha\beta}(\omega) = \pi \langle 0 | [\dot{N}_\alpha, \dot{N}_\beta] | 0 \rangle$, with the ground state of the unperturbed system $|0\rangle$. Note that $[\dot{N}_\alpha, \dot{N}_\beta] = 0$ (trivially for $\alpha = \beta$; in the case $\alpha \neq \beta$ the conservation of charge, $\dot{N} = 0$, with $N = N_L + N_R$, yields $\dot{N}_\alpha = -\dot{N}_\beta$ confirming the assertion). The accuracy of the numerics can be checked, since $\int G''(\omega) d\omega$ should give an exact zero; the numerical value we obtain is $\sim 10^{-4}$, i.e. it is in excellent agreement with this sum-rule.

$K_{\alpha\beta}(\omega)$ is a *causal* function]

$$K'_{\alpha\beta}(\omega) = \frac{1}{\pi} \mathcal{P} \int_{-\infty}^{\infty} \frac{K''_{\alpha\beta}(\omega')}{\omega' - \omega} d\omega', \quad (\text{F.15})$$

$$K''_{\alpha\beta}(\omega) = -\frac{1}{\pi} \mathcal{P} \int_{-\infty}^{\infty} \frac{K'_{\alpha\beta}(\omega')}{\omega' - \omega} d\omega', \quad (\text{F.16})$$

with the principal value \mathcal{P} of the integral. Finally Eq. (F.10) simplifies to

$$\sigma_{\alpha\beta}(\omega) = \frac{1}{i\omega} (K'_{\alpha\beta}(\omega) - K'_{\alpha\beta}(0) + iK''_{\alpha\beta}(\omega)) \quad (\text{F.17})$$

with its real-part $\sigma'_{\alpha\beta}(\omega)$ (directly obtained from NRG)

$$\sigma'_{\alpha\beta}(\omega) = \frac{K''_{\alpha\beta}(\omega)}{\omega} \quad (\text{F.18})$$

and its imaginary part [obtained via a KK-transformation of $K''_{\alpha\beta}(\omega)$]

$$\sigma''_{\alpha\beta}(\omega) = -\frac{K'_{\alpha\beta}(\omega) - K'_{\alpha\beta}(0)}{\omega}. \quad (\text{F.19})$$

Thus, the *frequency* dependent conductance [7] is, substituting (F.9) in (F.3), $G(\omega) \sim \frac{K(\omega) - K(0)}{\omega}$, where $K(\omega) = K_{LL}(\omega) + K_{RR}(\omega) - K_{LR}(\omega) - K_{RL}(\omega)$. $G'(\omega)$ can thus be written as

$$\frac{G'(\omega)}{\frac{2e^2}{h}} = \frac{\pi}{4} \left\{ \frac{\pi \sum_{n,m} \left[\frac{e^{-\beta E_m} - e^{-\beta E_n}}{Z} \right] \left| \langle n | (-\hat{K}) | m \rangle \right|^2 \delta(\hbar\omega - (E_n - E_m))}{\hbar\omega} \right\}. \quad (\text{F.20})$$

The definition

$$\mathcal{W}(\omega) \equiv \pi \sum_{n,m} \left[\frac{e^{-\beta E_m} - e^{-\beta E_n}}{Z} \right] \left| \langle n | (-\hat{K}) | m \rangle \right|^2 \delta(\hbar\omega - (E_n - E_m)) \quad (\text{F.21})$$

allows us to write $G''(\omega)$ as the KK-transformed of $G'(\omega)$ [see Eq. (F.19)],

$$\frac{G''(\omega)}{\frac{2e^2}{h}} = -\frac{\pi}{4} \left\{ \frac{[\mathcal{W}(\omega)]^{KK} - [\mathcal{W}(0)]^{KK}}{\hbar\omega} \right\}. \quad (\text{F.22})$$

The operator $\hat{K} = \frac{\hbar}{i} \hat{K}^*$, used in Eqs. (F.20) and (F.22), was defined in the introduction of this Appendix (remember $\hat{K}^* \sim [\hat{\mathcal{H}}_{\ell d}, \hat{N}_L - \hat{N}_R]$). Phase and absolute value of the linear conductance, ϕ and $|G(\omega)|$, are given as

$$\phi = \arctan \left(-\frac{[\mathcal{W}(\omega)]^{KK} - [\mathcal{W}(0)]^{KK}}{\mathcal{W}(\omega)} \right) \quad (\text{F.23})$$

$$\frac{|G(\omega)|}{\frac{2e^2}{h}} = \frac{\pi/4}{|\hbar\omega|} \sqrt{[\mathcal{W}(\omega)]^2 + \left\{ [\mathcal{W}(\omega)]^{KK} - [\mathcal{W}(0)]^{KK} \right\}^2}. \quad (\text{F.24})$$

The (numerical) strategy we use is the following: after we implement the operator \hat{K} , which allows us to determine $\mathcal{W}(\omega)$ [see Eq. (F.20)], we take its KK-transformed, $[\mathcal{W}(\omega)]^{KK}$, which determines $G''(\omega)$, see Eq. (F.22).

When one is only interested in the *DC conductance* G the delicate limit $G = \lim_{\omega \rightarrow 0} G(\omega)$ has to be computed. Due to the properties of the real and the imaginary part of $K_{\alpha\beta}$ [cf. Eqs. (F.13) and (F.14); $K'_{\alpha\beta}$ is an even whereas $K''_{\alpha\beta}$ is an odd function] the DC conductance is purely real.

Part IV

Miscellaneous

Bibliography

- [1] K.G. Wilson. *The renormalization group: Critical phenomena and the Kondo problem*. Rev. Mod. Phys. **47**, 773–840 (1975).
- [2] R.J. Warburton, C. Schäflein, D. Haft, F. Bickel, A. Lorke, K. Karrai, J.M. Garcia, W. Schoenfeld and P.M.Petroff. *Optical emission from a charge-tunable quantum ring*. Nature **405**, 926–929 (2000).
- [3] Gerald D. Mahan. *Many-Particle Physics*. Plenum New York, N.Y. 2nd edition 1993.
- [4] W. Hofstetter. *Generalized Numerical Renormalization Group for Dynamical quantities*. Phys. Rev. Lett. **85**, 1508–1511 (2000).
- [5] R. Bulla. *About the KK transformation*. private communication (2002).
- [6] W. Izumida, O. Sakai and Y. Shimizu. *Many Body Effects on Electron Tunneling through Quantum Dots in an Aharonov-Bohm Circuit*. J. Phys. Soc. Jpn. **66**, 717 – 726 (1997).
- [7] M. Sindel, W. Hofstetter, J. von Delft and M. Kindermann. *Frequency-dependent transport through a quantum dot in the Kondo regime*. Electronic Archive, xxx.lanl.gov, cond-mat/0406312 (2004).
- [8] Yang Ji, M. Heiblum, D. Sprinzak, D. Mahalu and H. Shtrikman. *Phase Evolution in a Kondo-Correlated System*. Science **290**, 779–783 (2000).
- [9] D. Böse, W. Hofstetter and H. Schöller. *Interference and interaction effects in multi-level quantum dots*. Phys. Rev. B **64**, 125309–1 – 125309–4 (2001).
- [10] A. W. Holleitner, R. H. Blick, A. K. Hüttel, K. Eberl and J. P. Kotthaus. *Probing and Controlling the Bonds of an Artificial Molecule*. Science **297**, 70–72 (2002).
- [11] L.P. Kouwenhoven, T.H. Osterkamp, M. Eto, D.G. Austing, T. Honda and S. Tarucha. *Excitation Spectra of Circular, Few-Electron Quantum Dots*. Science **278**, 1788–1792 (1997).

- [12] J. von Delft and D.C. Ralph. *Spectroscopy of Discrete Energy Levels in Ultrasmall Metallic Grains*. Physics Report **345**, 61–173 (2001).
- [13] L.I. Glazman and M. Pustilnik. *Coulomb Blockade and Kondo Effect in Quantum Dots*. "New Directions in Mesoscopic Physics", eds. R. Fazio, V.F. Gantmakher, and Y. Imry (Kluwer, Dordrecht) pages 93–115 (2003).
- [14] Y. Meir, N.S. Wingreen and P.A. Lee. *Transport through a strongly interacting electron system: Theory of periodic conductance oscillations*. Phys. Rev. Lett. **66**, 3048–3051 (1991).
- [15] J. Martinek, M. Sindel, L. Borda, J. Barnas, J. König, G. Schön and J. von Delft. *Kondo Effect in the Presence of Itinerant-Electron Ferromagnetism Studied with the Numerical Renormalization Group Method*. Phys. Rev. Lett. **91**, 247202–1 – 247202–4 (2003).
- [16] L. I. Glazman and M. E. Raikh. *Resonant Kondo transparency of a barrier with quasilocal impurity states*. Sov. Phys.–JETP **47**, 452 (1988).
- [17] T.K. Ng and P.A. Lee. *On-Site Coulomb Repulsion and Resonant Tunneling*. Phys. Rev. Lett. **61**, 1768 – 1771 (1988).
- [18] D. Goldhaber-Gordon, H. Shtrikman, D. Mahalu, D. Abusch-Magder, U. Meirav and M.A. Kastner. *Kondo effect in a single-electron transistor*. Nature **391**, 156–159 (1998).
- [19] D. Goldhaber-Gordon, J. Göres, M.A. Kastner, H. Shtrikman, D. Mahalu and U. Meirav. *From the Kondo Regime to the Mixed-Valence Regime in a Single-Electron Transistor*. Phys. Rev. Lett. **81**, 5225–5228 (1998).
- [20] W.G. van der Wiel, S. de Franceschi, T. Fujisawa, J.M. Elzerman, S. Tarucha and L.P. Kouwenhoven. *The Kondo Effect in the Unitary Limit*. Science **289**, 2105–2108 (2000).
- [21] D. C. Langreth. *Friedel sum rule for Anderson's Model of Localized Impurity States*. Phys. Rev. **150**, 516 (1966).
- [22] D. Loss and D.P. DiVincenzo. *Quantum computation with quantum dots*. Phys. Rev. A **57**, 120 – 126 (1998).
- [23] S.M. Cronenwet, T.H. Oosterkamp and L.P. Kouwenhoven. *A Tunable Kondo Effect in Quantum Dots*. Science **281**, 540–544 (1998).
- [24] J. Schmid, J. Weis, K. Eberl and K. von Klitzing. *A Quantum Dot in the Limit of Strong Coupling to Reservoirs*. Physica B **256**, 182–185 (1998).
- [25] P.W. Anderson. *Localized Magnetic States in Metals*. Phys. Rev. **124**, 41–53 (1961).

- [26] W. Metzner and D. Vollhardt. *Correlated Lattice Fermions in $d = \infty$ Dimensions*. Phys. Rev. Lett. **62**, 324–327 (1988).
- [27] M. Sindel, A. Silva, Y. Oreg and J. von Delft. *Charge oscillations in Quantum Dots*. Electronic Archive, xxx.lanl.gov, cond-mat/0408096 (2004).
- [28] W. Hofstetter and H. Schöller. *Quantum Phase Transition in a Multi-Level Dot*. Phys. Rev. Lett. **88**, 016803–1 – 016803–4 (2002).
- [29] T.A. Costi, A.C. Hewson and V. Zlatic. *Transport coefficients of the Anderson model via the numerical renormalization group*. J. Phys. Cond. Matter **6**, 2519–2558 (1994).
- [30] J.R. Schrieffer and P.A. Wolff. *Relation between the Anderson and Kondo Hamiltonians*. Phys. Rev. **149**, 491–492 (1966).
- [31] H.R. Krishna-murthy, J.W. Wilkins and K.G. Wilson. *Renormalization-group approach to the Anderson model of dilute magnetic alloys. I. Static properties for the symmetric case*. Phys. Rev. B **21**, 1003–1043 (1980).
- [32] M. Pustilnik and L.I. Glazman. *Kondo effect induced by a magnetic field*. Phys. Rev. B **64**, 045328–1 – 045328–15 (2001).
- [33] U. Gerland, J. von Delft, T.A. Costi and Y. Oreg. *Transmission Phase Shift of a Quantum Dot with Kondo Correlations*. Phys. Rev. Lett. **84**, 3710–3713 (2000).
- [34] P. Brouwer. *Lecture Notes*. <http://people.ccmr.cornell.edu/brouwer/p636/kondo.pdf> Cornell University 2003.
- [35] J.J. Sakurai. *Modern Quantum Mechanics*. Addison Wesley Reading, Massachusetts 1994.
- [36] S. Kehrein. *The Flow Equation Approach to Many-Particle Systems*. Habilitation Universität Augsburg 2001.
- [37] W.G. van der Wiel. *Electron transport and coherence in semiconductor quantum dots and rings*. PhD thesis Technical University Delft, The Netherlands 2002.
- [38] J. Kondo. *Resistance Minimum in Dilute magnetic Alloys*. Progress of theoretical physics **32**, 37 (1964).
- [39] L.P. Kouwenhoven and L. Glazman. *Revival of the Kondo effect*. Physics World **14**, 33–38 (2001).
- [40] A.C. Hewson. *The Kondo Problem to heavy Fermions*. Cambridge University Press Cambridge 1993.
- [41] D. Haldane. *Scaling Theory of the Asymmetric Anderson Model*. Phys. Rev. Lett. **40**, 416–419 (1978).

- [42] P.W. Anderson. *A poor man's derivation for the scaling laws of the Kondo problem*. J. Phys. C **3**, 2436–2441 (1970).
- [43] J. von Delft. *Kondo Effect in Quantum Dots*. Euro summer School on Condensed Matter, Lancaster University, UK; <http://www.lancs.ac.uk/users/esqn/windsor04/program.htm> (2004).
- [44] J. Martinek, Y. Utsumi, H. Imamura, J. Barnas, S. Maekawa, J. König and G. Schön. *Kondo effect in quantum dots coupled to ferromagnetic leads*. Phys. Rev. Lett. **91**, 127203–1 – 127203–4 (2003).
- [45] N.W. Ashcroft and N.D. Mermin. *Solid State Physics*. Saunders College Philadelphia 1976.
- [46] K. Wilson and J. Kogut. *The Renormalization Group and the ϵ Expansion*. Phys. Rep. **12**, 75–200 (1974).
- [47] H.R. Krishna-murthy, J.W. Wilkins and K.G. Wilson. *Renormalization-group approach to the Anderson model of dilute magnetic alloys. II. Static properties for the asymmetric case*. Phys. Rev. B **21**, 1044–1083 (1980).
- [48] S.R. White. *Density matrix formulation for quantum renormalization groups*. Phys. Rev. Lett. **69**, 2863 – 2866 (1992).
- [49] A.M. Tsvelik and P.B. Wiegmann. *Exact results in the theory of Magnetic Alloys*. Adv. Phys. **32**, 453–713 (1983).
- [50] P.B. Wiegmann and A.M. Tsvelik. *Exact Solution of the Anderson Model (I-II)*. J. Phys. C **16**, 2281 (1983).
- [51] T.A. Costi and A.C. Hewson. *Transport Coefficients of the Anderson model*. J. Phys. Cond. Matter **5**, 361–368 (1993).
- [52] R. Bulla, A.C. Hewson and T. Pruschke. *Numerical Renormalization Group Calculations for the Self-energy of the impurity Anderson model*. J. Phys. Cond. Matter **10**, 8365–8380 (1998).
- [53] W. Liang, M. P. Shores, M. Bockrath, J. R. Long and H. Park. *Kondo resonance in a single-molecule transistor*. Nature **417**, 725–729 (2002).
- [54] J. Martinek, M. Sindel, L. Borda, J. Barnas, R. Bulla, J. König, G. Schön, S. Maekawa and J. von Delft. *Gate-controlled spin-splitting in quantum dots with ferromagnetic leads in the Kondo regime*. Electronic Archive, xxx.lanl.gov, cond-mat/0406323 v1 (2004).
- [55] A.N. Pasupathy, R.C. Bialczak, J. Martinek, J.E. Grose, L.A.K. Donev, P.L. McEuen and D.C. Ralph. *The Kondo Effect in the Presence of Ferromagnetism*. Science **306**, 86–89 (2004).

- [56] D. Ralph. *Mn atoms contacted to Mn leads*. private communication (2003).
- [57] M.R. Buitelaar, T. Nussbaumer and C. Schönenberger. *Quantum Dot in the Kondo Regime Coupled to Superconductors*. Phys. Rev. Lett. **89**, 256801(1)–256801(4) (2002).
- [58] K. Tsukagoshi, B. W. Alpebaer and H. Ago. *Coherent Transport of electron spin in a ferromagnetically contacted carbon nanotube*. Nature **572**, 572–574 (1999).
- [59] J. Nygaard, W.F. Koehl, N. Mason, L. DiCarlo and C. M. Marcus. *Zero-field splitting of Kondo resonances in a carbon nanotube quantum dot*. Electronic Archive, xxx.lanl.gov, cond-mat/0410467v1 (2004).
- [60] M.S. Choi, D. Sanchez and R. Lopez. *Kondo Effect in a Quantum Dot Coupled to Ferromagnetic Leads: A Numerical Renormalization Group Analysis*. Phys. Rev. Lett. **92**, 056601–1 – 056601–4 (2004).
- [61] A. Silva, Y. Oreg and Y. Gefen. *Signs of quantum dot-lead matrix elements: The effecton transport versus spectral properties*. Phys. Rev. B **66**, 195316–1 – 195316–10 (2002).
- [62] Yang Ji, M. Heiblum and H. Shtrikman. *Transmission Phase of a Quantum Dot with Kondo Correlation near the Unitary Limit*. Phys. Rev. Lett. **88**, 076601–1 – 076601–4 (2002).
- [63] A. Kogan, S. Amasha and M.A. Kastner. *Photon-Induced Kondo Satellites in a Single-Electron Transistor*. Science **304**, 1293–1295 (2004).
- [64] A.-P. Jauho, N.S. Wingreen and Y. Meir. *Time-dependent transport in interacting and noninteracting resonant-tunneling*. Phys. Rev. B **50**, 5528–5544 (1994).
- [65] R. Deblock, E. Onac, L.Gurevich and L.P. Kouwenhoven. *Detection of Quantum Noise from an Electrically Driven Two-Level System*. Science **301**, 203–206 (2003).
- [66] R. Bulla, N.-H. Tong and M. Vojta. *Numerical Renormalization Group for Bosonic Systems and Application to the Subohmic Spin-Boson Model*. Phys. Rev. Lett. **91**, 170601 – 170604 (2003).
- [67] P. Jarillo-Herrero, Jing Kong, H.S.J. van der Zant, C. Dekker, L.P. Kouwenhoven and S. DeFrancheschi. *Multi-level Kondo and Orbital Spectroscopy in Carbon Nanotubes*. private communication; to be published in Science (2004).
- [68] R. Bulla. *Entwicklung neuer Methoden zur Untersuchung des Anderson-Modells*. Dissertation Universität Regensburg 1994.
- [69] R. Bulla, Th. Pruschke and A.C. Hewson. *Anderson impurity in pseudo-gap Fermi systems*. J. Phys. Cond. Matter **9**, 10463–10474 (1997).

- [70] W. Hofstetter. *Renormalization Group Methods for Quantum Impurity Systems*. Dissertation Universität Augsburg 2000.
- [71] K. Chen and C. Jayaprakash. *X-ray-edge singularities with nonconstant density of states: A renormalization-group approach*. Phys. Rev. B **52**, 14436–14440 (1995).
- [72] R. Bulla, H.-J. Lee, N.-H. Tong and M. Vojta. *Numerical Renormalization Group for Quantum Impurities in a Bosonic Bath*. Electronic Archive, xxx.lanl.gov, cond-mat/0407559 (2004).
- [73] C. Lanczos. *An Iteration Method for the Solution of the Eigenvalue Problem of Linear Differential and Integral Operators*. J. Res. Natl. Bur. Stand. **45**, 255 (1950).
- [74] R. Bulla. *The Numerical Renormalization Group Method for correlated electrons*. Adv. Solid State Phys. **40**, 169–182 (2000).
- [75] R. Bulla, T. A. Costi and D. Vollhardt. *Finite temperature numerical renormalization group study of the Mott-transition*. Phys. Rev. B **64**, 045103–045111 (2001).
- [76] I.N. Bronstein, K.A. Semendjajew, G. Musiol and H. Muhlig. *Taschenbuch der Mathematik*. Verlag Harri Deutsch Frankfurt am Main 1993.
- [77] O. Sakai, Y. Shimizu and T. Kasuya. *Single-Particle and Magnetic Excitation Spectra of Degenerate Anderson Model with finite f-f Coulomb Interaction*. J. Phys. Soc. Jpn. **58**, 3666 (1989).
- [78] W. Hofstetter. *Discussion about relevant schemes to obtain a continuous function via NRG*. private communication (2004).
- [79] D. Pines and P. Nozieres. *The Theory Of Quantum liquids, Vol I*. W.A. Benjamin, Inc. New York, N.Y. 1966.
- [80] Y. Meir and N.S. Wingreen. *Landauer Formula for the Current through Interacting Electron Region*. Phys. Rev. Lett. **68**, 2512–2515 (1992).

List of Publications

The results presented in this thesis have been published in the following papers:

1. *Kondo Effect in the Presence of Itinerant-Electron Ferromagnetism Studied with the Numerical Renormalization Group Method*
J. Martinek, M. Sindel, L. Borda, J. Barnas, J. König, G. Schön, and J. von Delft
Phys. Rev. Lett. **91**, 247202 (2003)
2. *Gate-controlled spin-splitting in quantum dots with ferromagnetic leads in the Kondo regime*
J. Martinek, M. Sindel, L. Borda, J. Barnas, R. Bulla, J. König, G. Schön, S. Maekawa, and J. von Delft
submitted to Phys. Rev. Lett., cond-mat/0406323
3. *Charge oscillations in Quantum Dots*
M. Sindel, A. Silva, Y. Oreg, and J. von Delft
submitted to Phys. Rev. Lett., cond-mat/0408096
4. *Frequency-dependent transport through a quantum dot in the Kondo regime*
M. Sindel, W. Hofstetter, J. von Delft, and M. Kindermann
submitted to Phys. Rev. Lett., cond-mat/0406312
5. *Anderson-Excitons: the effect of a Fermi sea on emission and absorption spectra*
R.W. Helmes, M. Sindel, L. Borda, and J. von Delft
to be submitted to Phys. Rev. B

Acknowledgements

I am grateful to my adviser, Prof. Jan von Delft, for providing guidance and direction for my research over the last three years. His critical questions were crucial to gain a deeper understanding of the physics behind the different problems. Thanks for teaching me how to give a good talk and how to write scientific publications. I am very grateful for the possibility of going to conferences and schools, to work with varying collaborators on different projects and the open atmosphere at our chair.

In particular I want to thank Prof. Walter Hofstetter for co-refereeing this thesis and the possibility of working on common projects with him.

Deep gratitude goes to my friend László Borda who tolerated me as an office mate and taught me the powerful numerical technique I used in my thesis.

Without the support, help and ideas of my excellent collaborators (and friends), I found during the last years, the thesis wouldn't have been possible. Thanks to Ralf Bulla, Theo Costi, Silvano De Franceschi, Yuval Gefen, Markus Kindermann, Jürgen König, Johann Kroha, Florian Marquardt, Jan Martinek, Yuval Oreg, Achim Rosch, Alessandro Silva and Gergely Zárand.

Moreover I would like to thank Udo Hartmann, Theresa Hecht, Rolf Helmes and Markus Storz for critical reading of the thesis.

Thanks to all members of our group during the last years: Andreas Friedrich, Rong Lu, Frank Wilhelm, Ulrich Zülicke, Uli Schollwöck, Alexander Khaetskii, Corinna Kollath, Dominique Gobert, Robert Dahlke, Henryk Gutmann, Hamed Saberi, Andreas Wechselbaum, Michael Möckel, Johannes Ferber, Konstanze Jähne, Igor Gazuz and Stephane Schoonover with whom I spent a great time in Munich.

I would like to thank my family, in particular my parents, for their continuous support over all the years. Special thanks goes to my girl friend Angelika who kept supporting me. Thanks!

Financial support through the DFG Program “Festkörperbasierte Quanteninformationsverarbeitung: Physikalische Konzepte und Materialaspekte” (SFB 631) is acknowledged.

Deutsche Zusammenfassung

Die vorliegende Arbeit umfasst eine Reihe theoretischer Studien, die sich mit verschiedenen Aspekten von Quantenpunkten beschäftigen.

Kleine Quantenpunkte mit grossen Niveauabständen lassen sich sehr gut mit Hilfe des nach P.W. Anderson benannten Störstellenmodelles beschreiben. Da wir in der vorliegenden Arbeit in erster Linie dieses Modell benutzen, erwarten wir, dass unsere Vorhersagen experimentell nachweisbar sind.⁵ Es sei hier bemerkt, dass sich alle Parameter der oben beschriebenen Quantenpunkte durch externe Gatterspannungen experimentell einstellen lassen.

In besonderer Weise interessieren wir uns für den Temperaturbereich, unterhalb dessen ein lokaler Elektronenspin (im Quantenpunkt) stark mit den ihn umgebenden Leitungselektronen (in den Zuleitungen) wechselwirkt. Dieser Temperaturbereich wird durch die sogenannte Kondo Temperatur T_K festgelegt (d.h. $T < T_K$). Zur exakten Berechnung verschiedener Transporteigenschaften von Quantenpunkten für Temperaturen $T < T_K$ benutzen wir die von Wilson entwickelte numerische Renormierungsgruppenmethode [1].

Der vorliegenden Dissertation stellen wir eine allgemeine Einleitung zur Physik von Quantenpunkten, mit besonderer Betonung auf den Kondo Effekt in Quantenpunkten, voran. Darüber hinaus beinhaltet der erste Teil eine Einführung in die von uns verwendete numerische Renormierungsgruppenmethode.

Der zweite Teil dieser Arbeit, der Hauptteil, ist in die folgenden verschiedenen Studien aufgeteilt:

(i) Wir analysieren die Eigenschaften eines 'Kondo' Quantenpunktes, der an spinpolarisierte Zuleitungen gekoppelt ist. Es stellt sich heraus, dass die Spin-Polarisierung der Zuleitungen zu einer Aufspaltung und einer Unterdrückung der Kondo Resonanz führt. Wir erweitern unsere Studien auf den Fall eines Quantenpunktes, der an Zuleitungen mit einer beliebigen Zustandsdichte koppelt. Für diesen Fall untersuchen wir die Gatterspannungsabhängigkeit der Kondo Resonanz.

(ii) Wir untersuchen das Füllungsverhalten eines spinlosen Anderson Modells das zwei lokale Niveaus besitzt als Funktion der Gatterspannung. Wir identifizieren Parameterbereiche, in denen sich die beiden betrachteten Niveaus nicht monoton füllen, wenn sie relativ zur Fermi-Energie der Zuleitungen abgesenkt werden. Für asymmetrisch gekoppelte Niveaus finden wir sogar eine Besetzungsinversion, d.h. für einen bestimmten Gatterspannungsbereich ist das energetisch höher liegende Niveau stärker besetzt als das energetisch

⁵Die theoretische Studie in Kapitel 5.1 wurde bereits experimentell nachgewiesen, siehe [55].

niedriger liegende Niveau. Das gefundene Verhalten erklären wir mit Hilfe eines selbstkonsistenten Hartree Ansatzes.

(iii) Wir berechnen den frequenzabhängigen Leitwert eines Quantenpunktes im Kondo Regime unter Benutzung der Kubo Formel. Wir leiten eine analytische Formel ab, die eine Beziehung zwischen dem frequenzabhängigen Leitwert und der (lokalen) Gleichgewichts-Spektralfunktion herstellt. Das Fluktuations-Dissipations Theorem gestattet es uns, eine Beziehung zwischen Stromrauschen und der (lokalen) Gleichgewichts-Spektralfunktion aufzustellen.

(iv) Emissionsexperimente in selbstorganisierten Quantenpunkten [2] motivierten uns, optische Übergänge zwischen 'Kondo' und 'Nicht-Kondo' Zuständen zu untersuchen. Zu diesem Zwecke verallgemeinern wir das üblicherweise verwendete Anderson Modell. Wir finden, dass sich sowohl das Emissions- als auch das Absorptionsspektrum durch eine Analogie mit dem 'X-ray edge' Problem erklären lassen.

Der dritte Teil dieser Arbeit enthält Herleitungen, die für das Verständnis der vorliegenden Arbeit von grosser Bedeutung sind.

Der vierte Teil dieser Dissertation enthält sonstige Informationen.

Curriculum vitae

Name: Michael Sindel

born: June 26th, 1974 in Rothenburg ob der Tauber

School: 1980 - 1984: Primary school in Schillingsfürst
1984 - 1993: Reichsstadt-Gymnasium, Rothenburg o.d.T.
06/1993: Abitur

Studies: 10/1994 - 06/1998: Study of Lehramt für Realschule (subjects: mathematics and physics) at the University of Würzburg
06/1998: 1. Staatsexamen für das Lehramt an Realschulen
04/1998 - 08/2000: Study of physics at the University of Würzburg
10/1999: Vordiplom in physics (University of Würzburg)
09/2000 - 10/2001: Study of physics at Rutgers,
The State University of New Jersey, New Brunswick
10/2001: Master of Science (Rutgers, State University of New Jersey)
10/2001 - 12/2004: Ph.D. studies in Theoretical Condensed Matter Physics,
supervised by Prof. Dr. Jan van Delft,
Ludwig-Maximilians-University, München

Theses: “Vertauschung von Grenzprozessen von Funktionen einer Veränderlichen”
supervised by Dr. L. Neckermann at Mathematisches Institut,
University of Würzburg (Zulassungsarbeit 1998)
“Two Patch Model for Transport Properties of Optimally and Overdoped Cuprates”
supervised by Prof. Dr. G. Kotliar at the Center for Materials Theory,
Rutgers, State University of New Jersey (Master Thesis 2001)